Planetary Resonance Dynamics and Chaos:

Numerical Stability Study of Habitable Terrestrial Planets in Extrasolar Planetary Systems

A Dynamical Analysis of the HD70642 and HD4208 Planetary Systems

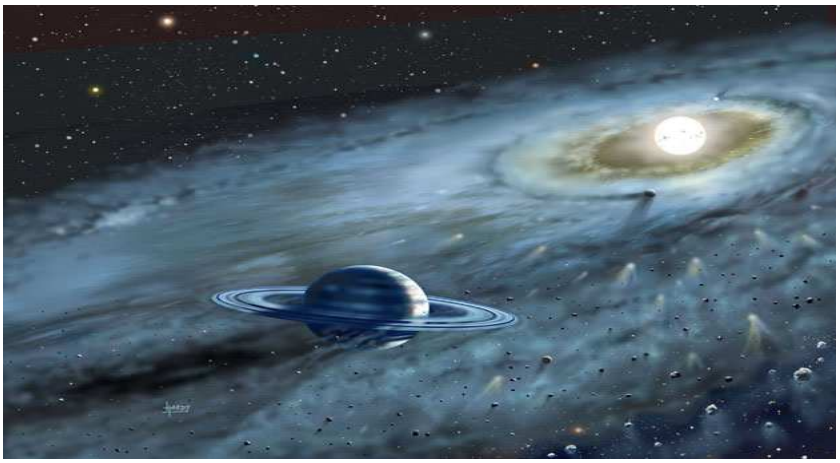

A Master Thesis in

Celestial Mechanics and Dynamical Astronomy

by

Tobias Cornelius Hinse

Niels Bohr Institute - University of Copenhagen

April 2006

The title page picture is taken from the "Astronomy Picture of the Day" archive available at http://antwrp.gsfc.nasa.gov/. Credits: David A. Hardy, ROE, ATC, NSF, NASA. The following descriptive text has been taken from http://antwrp.-gsfc.nasa.gov/apod/ap021011.html.
Picture explanation:
"One of the brightest stars on the sky likely has planets. Fomalhaut, actually the 17th brightest star in the night sky, is a mere 22 light-years away but only a fraction of the age of our Sun. Recent observations in far infrared light with a detector cooled to near zero kelvins indicate a dust disk surrounding Fomalhaut that has both a hole in the center and a warped edge. Now the hole in the center indicates that dust has fallen onto interior planets – possibly like the Earth – while the warp at the edge indicates the gravitational pull of a planet like Jupiter or Saturn. The discovery image was taken with the SCUBA instrument through the James Clerk Maxwell Telescope in Hawaii, USA. The above (ed. on the front page) illustration shows what the Fomalhaut dusty planetary system might look like from near the large planet."

This thesis is submitted for evaluation in accordance with the requirements for obtainment of the degree Candidata Scientiarum in Astronomy at the Niels Bohr Institute, University of Copenhagen (www.nbi.dk, www.ku.dk).

External Supervisor:

Dr. René Michelsen
DTU, Technical University of Denmark
(rene@astro.ku.dk)

Internal Supervisor:

Prof. Dr. Uffe Gråe Jørgensen
NBI, Niels Bohr Institute, University of Copenhagen
(uffegj@nbi.dk)

Tobias Cornelius Hinse
Niels Bohr Institute, University of Copenhagen
(tobiash@astro.ku.dk)

Table of Contents

Abstract

In this thesis, we present numerical results[1] from planet-particle simulations within extrasolar planetary systems. Orbital stability properties of hypothetic terrestrial planets (modelled as test particles) within the habitable zone of the Solar like stars HD70642 and HD4208 are investigated. The three-body problem is considered as the fundamental model and the effect of giant planet gravitational perturbations on orbital Kepler elements of a terrestrial planet are studied within a giant planet orbit parameter survey. Short- and long-term integration ($10^6 - 10^9$ years) of the equation of motion are considered in simulations.

The habitable zone for each system is determined from a one-dimensional atmosphere model for an Earth-mass planet in thermal equillibrium (Kasting et al., 1993). Zonal habitable boundaries provide constraints on Kepler parameters within (a, e)-space.

Independent numerical methods using symplectic and interpolation algorithms are used to study dynamical characteristics of the system. The MEGNO indicator is used to measure the chaotic nature of the time evolution of Kepler orbital elements. Stability properties of terrestrial planets are inferred by directly considering the dynamics of 2×10^3 test particles. A dynamically cold (i.e $e = 0$) distribution of particles with random mean anomalies is used as initial conditions. For the giant planet, we consider orbit eccentricity and planet mass as the variable parameters within a parameter survey.

Orbital mean-motion resonances are identified to cause eccentricity excitations of particles. For some choices of giant planet orbital elements, numerical simulations shows particle removal by either ejections or accretion as a result of close encounters. This is a dynamical consequence of repeated resonance perturbations and global chaotic dynamics, resulting in gap formation within the initial particle population. Numerical results allow a general conclusion on the possibility of habitable terrestrial like planets within the current population of observed giant planets. Upper bounds on giant planet orbit eccentricity ($e_{max} = 0.16$) are determined for both systems. Results suggest that giant planets are best located in the outer region on circular orbits in a planetary system in order to render terrestrial habitable planets on a stable orbit. However, giant planets on circular orbits with semi-major axis $a \simeq 1.7$ AU exhibit a stable configuration for the terrestrial planet, in order to be confined to within the habitable zone.

This kind of numerical dynamical stability analysis will help future satellite search missions for habitable terrestrial planets, by providing a mission targeting list of exosystems with a high probability in harboring terrestrial planets on dynamically stable orbits within the habitable zone.

[1]Results of this work has been presented as a poster (cf. appendix B) at the annual DPS/AAS conference in Cambridge (UK), September 2005 (Hinse & Jørgensen, BAAS, vol. 37, p.3, 2006).

Acknowledgements

The realisation and completion of this thesis relies on the help of a number of fine individuals, for which I would like to express my profound gratitudes.

First, I would like to thank Dr. René Michelsen for countless discussions on various theoretical aspects within the field of Celestial Mechanics and planet dynamics. It is amazing and fascinating, what one can extract from Newton's $1/r^2$-law. He was the first to draw my attention on the importance of resonance phenomena within planet formation and evolution - especially within the context of extrasolar planetary systems.

Next, my special gratitude goes to the specialists within the field on chaotic planetary dynamics theory and numerical celestial mechanics. I owe much of my gained knowledge within Celestial Mechanics and planet dynamics to them. This thesis would not exist without their support and scientific expertise.

First, I would like to thank Dr. K. Gózdziewski from the Torun Center of Astronomy, Poland for providing me his numerical algorithm for the calculation of the MEGNO/Lyapunov chaos indicator. In addition, he supported me in various technical aspects of the code with detailed explanations and comments.

Second, but on an equal basis, I would like to thank Dr. Seppo Mikkola from Tuorla Observatory, Turku University, Finland for kindly providing me with various numerical algorithms for the fast and efficient computation of planetary orbits. In addition, he provided me with his lecture notes on modern aspects in numerical celestial mechanics from which I learned the proper machinery of the numerical code in order to circumvent the usage of a "black box".

During the thesis period, Drs. Mikkola and Gózdziewski patiently answered all my email requests in great details within what is possible without having "pencil & paper" nearby at hand for proper explanations. Seppo, I hope to have the opportunity to visit you at the Tuorla Observatory at some future time ;-).

In addition, I would like to thank Drs. A. Erikson, K. Gózdziewski, H. Rauer, U. G. Jørgensen and S. Mikkola for their efforts in supporting my future plans within the field of Solar System dynamics and Celestial Mechanics leading towards a PhD scholarship.

Also, I would like to thank Drs A. Erikson and H.Rauer at the German Aerospace Center - Institute for Planetary Science, Berlin-Adlershof for their persistent support and hospitality during and after my visiting period as a guest student.

For financial support to enable my participation at the DPS conference (Cambridge, UK, Sept. 2005), I would like to thank Prof. Dr. Uffe G. Jørgensen. He is that person, who opens doors and who is always willing to listen.

For computer/programming related support, I gained much of my knowledge within UNIX/Linux programming and tips & tricks from Jakob Hunsballe. His expertise is, to my opinion, enormous and I learned a lot from him during the thesis period. Also, I'm greatful for conversations with fellow students at the Astronomical Department.

Of most importance, my warmthly and hartiest gratitude goes to my mum for always believing, supporting and realising my plans, everlasting asking me "when do you submit?" and for the daily morning calls during the most challenging periods of thesis writing.

Introduction, thesis outline and units

One of the most exciting astronomical advances in the last few years has been the discovery of planets around other stars - known as extrasolar planetary systems. The recent discoveries of planets outside the Solar System have opened a hole new branch within the field of observational and theoretical astrophysics. The search for other planets is motivated by our deep interest to understand their formation mechanisms and, by analogy, to gain an improved understanding of the formation of our own Solar System.

For many centuries, philosophers and scientist have theorised about the formation of planets and the existence of planets outside the Solar System, including possible habitable planets. Kant (1755) and Laplace (1796) hypothesised that the planets of the Solar System formed from a flattend gaseous disk in differential rotation about the Sun. In *De l'Infinito, Universo e Mondi*, Giordano Bruno (1584) argued that the universe was infinite and that it contained an infinite number of worlds, all inhabited by intelligent beings.

Only in modern times, with the revolutionary discovery of planets around other stars can we now test their hypothesis and quantify it. In particular, the most exciting question is the quest to discover life beyond Earth: does there exist a planet, habitating biological lifeforms, in orbit within a life-supporting envirmonment around a Sun-like star?

Some of the extrasolar planetary systems (EPS), nearly similar to the orbital structure of the Solar System, have been observed and studied for the existence of possible Earth like planets. Promissing candidates are 47 Ursae Majoris, 51 Pegasi and 55 Cancri. All are multi-planetary systems containing 2-3 giant Jupiter-like planets in different orbits around their central host star. Whether life could have emerged on a extrasolar Earth within any of these systems depends on several dynamical factors (in evolutionary order): 1) planetary embryo interactions with an initial gas disk 2) formation of giant planets 3) gravitational interactions between planets and protoplanetary embryos on timescales comparable to the lifetime of the systems hoststar and 4) the spin-stability of extrasolar Earths will depend on the masses and proximity of neighboring satellites or moons. To first order, a key ingredient is whether extrasolar terrestrial planetary orbits dynamically remain confined long enough within the habitable zone in order for life to form and develop.

Recently, a few planets have been confirmed observed at comparable large orbital distances. 14Herb, HD30177b, HD33636b, HD39091b, Gl777Ab and HD 72659 are all systems with a single massive planet orbiting their central host beyond 3 AU with moderate large eccentricities ($e = 0.5$). An interesting candidate is HD70642, containing a single giant planet orbiting a solar-like star on a near-circular orbit ($e = 0.1$), with a mean distance of 3.3 AU. This system resembles our Solar System more closely and it is natural to ask whether this system can harbor terrestrial

planets in its inner regions.

At present, we cannot give a definitive answer to this question since the detection of terrestrial planets is beyond the resolving capabilities of current telescope technology. However, future space missions like COROT (CSNR, ESA), DARWIN and GAIA (ESA), the Terrestrial Planet Finder (NASA) mission or SIM (NASA), will be able to explore remote star systems through either astrometric and/or transit effects (COROT, SIM, GAIA), direct imaging (DARWIN, TPF) or even spectroscopy of planets that might show evidence of biological activity in their atmosphere (CH_4, O_3 and O_2).

Within this thesis I outline fundamental aspects of planetary dynamics and present a dynamical analysis of initial conditions on orbit parameters for the existence of a possible Earth like planet within the habitbale zone of the HD70642 extrasolar planetary system. Basically, the three-body equation of motion (expressed in inertial coordinates $\boldsymbol{\eta}$)

$$m_i \ddot{\boldsymbol{\eta}}_i = k^2 \sum_{j=1, j\neq i}^{3} m_i m_j \frac{\boldsymbol{\eta}_j - \boldsymbol{\eta}_i}{|\boldsymbol{\eta}_j - \boldsymbol{\eta}_i|^3} \qquad i, j = 1, 2, 3 \tag{1}$$

is studied within the parameter space of observed orbital elements using the overall principle: *what happens, if ...* ? The full 3-body planetary and the restricted n-particle problem is considered. Stability and the chaotic nature of terrestrial planetary orbits in the habitable zone after the dissipation of a gas-dust disk is investigated numerically evaluating only gravitational interactions. Theoretical investigations of this kind will help future search missions for habitable planets by providing a mission targeting list of potential terrestrial planets on dynamical stable orbits.

Thesis outline, notation and units

This thesis is structured into 8 chapters, reflecting the main natural approach during the thesis period.

Chapter 1

The first chapter presents a review of a literature study within the field of the detection, observation and properties of extrasolar planets, formation of terrestrial planets; their habitability and stability within the terrestrial region in extrasolar planetary systems.

Chapter 2

In this chapter, we introduce basic concepts within astrodynamics and celestial mechanics. Properties of the two-body problem are discussed and basic terms and notations are defined. The geometrical content of Kepler's orbital elements are explained. In particular, we introduce Gauss's f and g function and discuss the numerical solution of Kepler's equation and introduce the Delauney variables.

Chapter 3

This chapter concerns aspects of perturbation theory. The three-body problem is introduced and properties of it are discussed. The concept of Jacobi coordinates are reviewed. They are of most importance in the development of numerical algorithms. The perturbation function is analysed and classes of perturbations occuring within planetary interactions are discussed. For analytic purposes the Lagrange equations represents the foundation for further analysis and represents differential equations for the time evolution of the Kepler elements. Finally, we introduce Gauss's form of perturbations and study the origin of changes in orbital parameters by considering a small perturbing force.

Chapter 4

Methods of numerical integration of the equations of motion are presented and discussed. This chapter reviews the basic theory of symplectic integration widely used within numerical celestial mechanics and planet dynamics. Numerical tests are performed and presented for the accuracy and reliability of the adopted numerical algorithms.

Chapter 5

In order to study the chaotic aspects within the three-body problem with application to stability studies of terrestrial planets within extrasolar planetary systems, the MEGNO indicator is introduced as a fast numerical method to test the presence of chaotic dynamics. The concept of Lyapunov stable orbits are discussed and introduced leading to the maximum Lyapunov exponent. The numerical code for calculating the MEGNO is outlined and tested against known results within the literature.

Chapter 6

Orbital parameters for the systems under study are presented based on observations using the radial velocity technique. The one-planet Kepler fitting technique

to observations is outlined. In addition, the concept of the habitable zone and the corresponding boundaries within (a, e)-space is introduced and explained.

Chapter 7

Results are presented obtained from numerical simulations. MEGNO stability maps are derived for the systems HD70642 and HD4208. Initial conditions for a parameter survey are given. The dynamical evolution of 2×10^3 particles under the presenece of giant planet perturbations are obtained by direct integration of the equations of motion. Particles are initially distributed within the habitable zone of the systems. Results from both short-term and long-term simulations are presented. Dynamical aspects between the systems are compared and discussed.

Chapter 8

This final chapter concludes the thesis.

Notation and units

The notation within the thesis follows the classic notation employed within the field of celestial mechanics. Vector quantities are denoted by **boldsymbols** (i.e $\boldsymbol{r}_i$, for the heliocentric position vector of the ith body). The time rate of change of a quantity $\boldsymbol{r}_i$, is denoted by $\dot{\boldsymbol{r}}_i$. References are quoted in the format (author(s), (publ. year)) and are listed in within the bibliography section at the end of the thesis.

Numerical simulations are performed using the *Gaussian system of units* traditionally used within planetary dynamics and celestial mechanics. Within this system masses[2] are measured in units of solar masses ($M_\odot$), distances are measured in astronomical units (AU) and time is measured in Julian days (d). This convention forces the Newtonian gravitational constant to be $\sqrt{G} = k$, where k is the Gaussian gravitational unit with numerical value $k = 0.01720209895$ $(\mathrm{AU}^3\mathrm{d}^{-2})^{1/2}$ (Danby, 1988, p.146). For numerical reasons, we set $k = 1$ by using a modified unit of time within the calculations.

[2]Frequently, masses of observed extrasolar planets are given in units of Jupiters mass ($M_{jup} \sim 300\ M_\oplus$, where $M_\oplus$ is one Earth mass.

Chapter 1

Extrasolar and terrestrial planets

1.1 Detection and properties of extrasolar planets

At the time of writing, the discovery of about 107 extrasolar planetary systems has been announced[1], and there are several systems containing more than one known planet. The first planet to be discovered being the 51 Pegasi system (Mayor and Queloz (1995)) and the first multi-planetary system being the υ Andromedae system, where three planets have currently been detected (Lissauer (1999)). Compared to the planets within the Solar System, these new planets were discovered to be in very different orbit configurations. Fig. 1.2 shows the range in semi-major axis of the known extrasolar planets. We discuss briefly the current detection techniques of these planets, and their properties.

1.1.1 Detection techniques

Although the existence of extrasolar planets have been reported, no planets have yet been directly imaged. All the detections so far have been by indirect methods, which infer the presence of the planet by either the *dynamical* or *photometric* effects caused by the orbiting planet on the host star (cf. Perryman (2000)).

The majority of the presently known extrasolar planets have been detected by the '*radial velocity*' technique. The gravitational effect of a planet in orbit causes a small velocity signature wobble in the motion of the star in the center-of-mass frame. Accurate Doppler shift spectroscopic measurements (today, sensitive to measure radial wobble-motions as small as $1\mathrm{ms}^{-1}$) can detect this wobbling motion along the line-of-sight velocity component. A time series of a sufficiently amount of observations enable the planetary orbit to be determined by the process of Keplerian orbit

[1] see for example http://exoplanets.org/ or http://www.obspm.fr/encycl/encycl.html for monthly updates and news

fitting. In the case for multi-planet systems the mutual gravitational interactions must be included into the fitting procedure (Chambers and Laughlin, 2001). In this way spectroscopic analysis can determine the orbital period P, the semi-major axis a and eccentricity e of a planet. As the Doppler shift only is a measure of the line-of-sight velocity component, the radial velocity method is unable of determining the orbital inclination to the observers line of sight i, and hence the actual mass m_{pl} is not determined. Only the minimum ('projected') planetary mass $m_{pl} \sin i$ can be measured. Geometric arguments leads to a statistical *average* value of $\sin i = \sqrt{1/2}$ with $i = \pm\pi/4$, which gives an average estimate of the real value of m_{pl} for random orientations of the orbital plane. In addition, the apsidal longitude[2] ω of the orbit can also be determined. This method is affected by observational bias, a systematic selection effect that favours the detection of giant planets in small-distance orbits. Extended periods of observation time will enable more distant planets to be detected, as is the case for the present occurence of giant planets on(in) distant orbits.

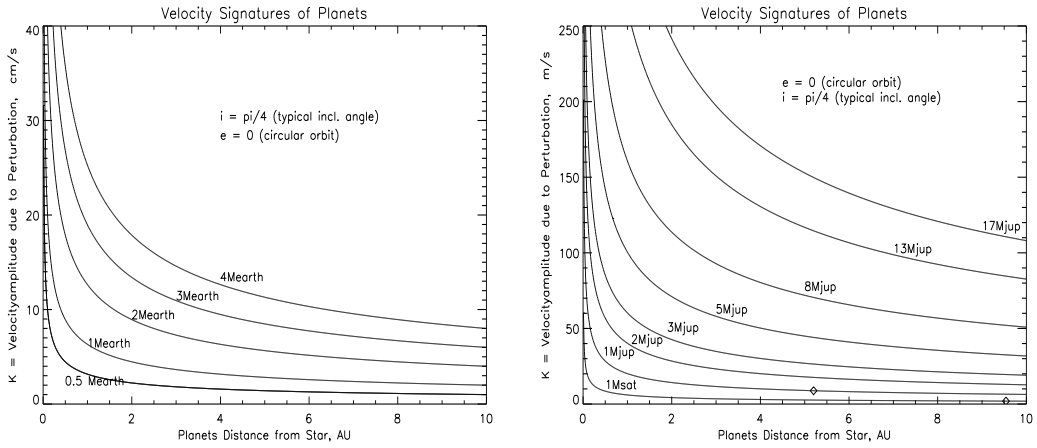

Figure 1.1: Induced velocity signature on a Sun-like star as a function of planetary mass (where M_{Earth} and M_{jup} is the mass of Earth and Jupiter) and distance for circular ($e = 0$) orbits and $i = \pi/4$, where i measures the inclination of the orbital planet with the line-of-sight. Left panel: Induced signature profiles of sub- to super-Earths at various distances. Right panel: Induced signature profiles of giant Jovian planets at various distances.

If the inclination of the orbital plane of the planet coincides with the observers line of sight, the planet will periodically pass in front of the star. These planetary transits cause a small but observable dip (of about 1%) in the intensity of light emitted from the star for a moderate giant planet. This is the '*photometric transit*' method. Currently, extrasolar transits have been confirmed in only two systems.

[2]geometrical interpretations of orbital elements will be discussed in chapter 2

The first transiting planets was found in orbit around HD209458 by Charbonneau et al. (2000), a planet previously detected by the radial velocity technique. More recently, a planet around the star OGLE-TR-56 was discovered by the transit method, and subsequently confirmed by Konacki et al. (2003) using the radial velocity technique. Lightcurve analysis of photometric time series observations can determine the orbital period P, the semi-major axis a, the radius of the planet R_{pl} and the orbital inclination to the observers line of sight i. Combined with radial velocity measurements, the absolute planetary mass m_{pl}, can be extracted with this method.

The detection of terrestrial planets in extrasolar planetary systems with these techniques is beyond the current sensitivity limit for both spectroscopic and photometric measurements. Fig. 1.1 shows the velocity signature of a star as a function of planet mass and distance for cicular planetary orbits. In order to detect a second Earth radial velocity measurements should be accurate to as small as 0.1 ms^{-1}, which is beyond the current sensitivity and which also impose additional detection problems, because of stellar surface movements with this velocity.

A third and very promising technique for the detection of Earth sized planets from ground based observations is the *gravitational microlensing* method. Its quantification is based on the general relativistic effects of light within a gravitational field. A gravitational field bends light and acts like a lens. If the lens star is orbited by a planet (lensing object), it cause an asymmetric amplification in the intensity profile of the background star (the lensed object or source), as a function of time. Again, by a fitting procedure and an appropiate lens model, absolute values of planetary mass m_{pl}, semi-major axis a and orbital period P, can be measured. Very recently, Bond et al. (2004) reported on an asymmetric microlensing event that can be best understood as the lens being an M-dwarf star orbited by a 1.5 Jupiter mass planet at an orbital distance of 3 AU. A major problem with this method is that detections are based on random alignments of stars with planets. Microlensing is a one-time event only, and follow-up observations are not possible. However, data acquisition by this method will contribute to a statistical analysis of extrasolar planetary properties.

1.1.2 Properties

The orbits of many extrasolar planets differ significantly from the orbits of the planets of the Solar System. With the exception of the low mass planets Mercury and Pluto, planets of the Solar System are all in near circular orbits ($e < 0.1$) around the Sun. Again with the exception of Pluto, the planets of the Solar System are almost co-planar, with orbital inclinations of less than 7 degrees relative to the orbital plane of Earth. Additionally, the terrestrial planets are located nearer the Sun at distances between 0.39 AU and 1.5 AU, and the large gaseous planets are placed further out at distances in the range 5.2 AU to 30 AU.

Many extrasolar planets detected so far are in significantly non-circular orbits around a Solar like G-star, with eccentricities in the range $0.01 < e < 0.9$ ($e = 0.93$ for HD80606b; Naef et al. (2001) and see Fig. 1.2). The projected minimum masses are in the range $0.1\ M_{jup} < m_{pl} \sin i < 12.0\ M_{jup}$. Jorissen et al. (2001) presents a statistical mass distribution, which shows that most of the planets have $m_{pl} < 12\ M_{jup}$.

Unexpectedly, some planets of near Jupiter mass have been observed to be in very small circular orbits with ($a = 0.04$ AU for HD83443b; Mayor et al. (2000)). These '*hot Jupiters*' are in low eccentric orbits circularized by tidal interaction with the host star and could not possibly have formed in situ at their observed locations (see Lin et al. (1996) for a discussion of the case of 51 Pegb).

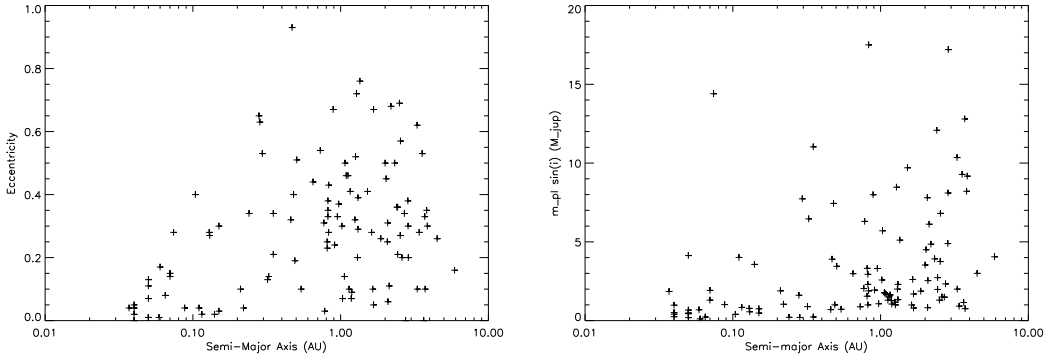

Figure 1.2: Population and global statistics of orbital parameters and minimum masses for observed extrasolar giant planets. Data are taken from http://vo.obspm.fr/exoplanetes/encyclo/-encycl.html.

Today, the most accepted mechanism for close-in hot Jupiters is *orbital migration*, a proces first proposed by Goldreich and Tremaine (1980). In general, gas giant planets are believed to form at distances much further from the star (around 5 AU for a Solar like star) and then have since migrated to their present positions via tidal interaction with the gaseous nebula from which they formed.

The large scatter of planets in high eccentric orbits, could be explained by dynamical interactions of *mean motion resonances*[3]. Two planets are in a mean motion resonance, if there exist a rational relation between their mean orbital velocities. The smaller the fraction the larger the dynamical interactions. One consequence of a mean motion resonance is the dynamical excitation of the eccentricities of the protoplanetary orbits (Chiang et al. (2001)), which may explain the observations of extrasolar planets in non-circular orbits. In fact, several systems have been observed

[3]to be discussed in a further section and formaly defined in chapter 2.

in a mean motion resonance: GJ876b and GJ876c (2:1), HD82943b and HD82943c (2:1), 55Cancrib and 55Cancric (3:1) and the 47 Ursae Majoris system (7:3). Eccentricity excitation over a long period of time could result in a break-up of the system with the ejection of a planet on a hyperbolic orbit. On the contrary, mean motion resonances can act as a stabilizing mechanism as it is the case for the Neptune-Pluto (3:2) mean motion resonance or the Floras-Jupiter (7:2) asteroid familiy within the Solar System.

1.2 Planet formation theory

The standard scenario for the formation of planets is that planets form in an accretion disk around the star called the protoplanetary disk. Modelling the structure and evolution of the disk is a highly complex matter and at present only constrained by observations of the Solar System, supplemented by recent observations of star-forming regions and circumstellar disks. The building-blocks of planets are kilometer-sized bodies called planetesimals. Planetesimals are formed by accretion of the surrounded material in the disk. This proces of planetary accretion controls the basic structure of a planetary system and the formation timescale of planets. The main question is, how likely is the formation of terrestrial planets? What is the effect on terrestrial planet formation in the presence of a giant planet? In the following, we present a brief overview of recent results (spanning the last 5-6 years) of our current understanding on how the terrestrial planet and cores of gas giants can be built up over many stages starting from condensates and dust grains within the protoplanetary disk.

1.2.1 Four stages of planet formation

Four stages for the formation of planets are currently distincted (see Lissauer (1993), for a review on general planet formation theory). Each stage, or evolutionary process, differentiates and the dynamical evolution is characterised by different physical properties in the disk environment and its subsequent evolution.

1. **Initial stage** - cloud contraction: Protoplanetary disks form from the gravitational collapse of cold rotating molecular clouds, containing the high angular momentum material not able to collapse into the star. Conservation of angular momentum requires the increase of the rotation rate as the cloud becomes smaller. The rotation naturally leads to the flattening of the rest of the cloud material into a disk configuration around the protostar. The initial temperature- and pressure gradient determines the chemical composition of the disk, as a function of radial distance from the star. Different species of gaseous elements start to condense at

various distances, along the mid-plane of the disk. Volatile elements condense in cold distant regions. The timescale for cloud contraction and nebula disk formation can be estimated from the free-fall time: $t_{ff} \sim 10^5$yrs.

2. **Early stage** - grain growth and runaway accretion: The stirring of the turbulent disk materials results in sub-collisions. The growth of sub-micron dust grains to larger agglomerates (cm-sized), is believed to occur via the hit-and-stick mechanism (Blum and Wurm (2000)). The collisional evolution of the growing aggregates is determined by the interaction of the particles with the disk gas, as long as the internal gravity is negligible. Thus, the growth process is highly dependent on the velocity dispersion induced by the turbulent disk. Large dispersions result in collisional fragmentation with no effective netgrowth of cm-sized particles. Relative velocities less than 1ms^{-1} are needed to form cm-sized particles. Unfortunately, higher relative velocities arise from chaotic laminar motions within the disk, preventing the sticking formation of larger grain agglomerates. Recently, a possible solution to reduce the relative velocity is the formation and presence of rotating dust-trapping disk vortices (Johansen et al. (2004)). Within a local disk vortice, relative velocities between grains are small since they all rotate in the same direction. Eventually, km-sized planetesimals form by the accretion of cm- and m-sized bodies. Some planetesimals grows faster than others, initiating a runaway process due to an increased gravitational focusing (see for example Kokubo and Ida (2002) and backtracing references therein). As planetesimals grow, they start to gravitationally interact with each other. The subsequent evolution is now determined by gravitational interactions and collisional processes. The material density profile determines the amount of planetesimals formed at various distances.

3. **Middle stage** - oligarchic growth of protoplanets: The dynamical evolution of the protoplanetary disk is mainly determined by the presence of several tenth of planetary embryos (Moon- to Mars-sized protoplanets) ranging from the inner regions (1 AU) to the outer regions (5 AU). Collisions causes an equipartition of orbital energy and leads to a polarization of mass distribution: a few large bodies on low eccentric and low-inclined orbits in a swarm of much smaller planetesimals with high eccentricity and inclination. In addition, gas drag acts as a damping mechanism and results in a decrease of the velocity dispersion of km-sized planetesimals. This reduces the relative velocities between protoplanets and planetesimals, favouring the further growth of planetary embryos. The accretion of planetesimals to protoplanets takes place all over the disk. Because of an enhanced material density beyond the ice-condensation line (5 AU for the proto Solar System), protoplanets with several Earth-masses start to accrete the surrounding gas and form gasgiant planets (Pollack et al. (1996)). The gravitational effect of the giant planet perturbations on the inner region terrestrial protoplanets causes the orbits to become crossing orbits on

a timescale of $10^5 - 10^6$ years.

4. **Late stage** - perturbations and crossing orbits: The final stage follows the paradigm - survival of the biggest. Cumulative gravitational perturbations leads to radial mixing of protoplanets. Crossing orbits enhances the chance of giant impacts to form the final survivors within a newly formed Solar System. The size, number and type of giant impacts which a protoplanet experiences can have a profound effect on the final characteristics of a planet. The subsequent evolution of possible stable orbits is now determined by pure gravitational n-body interactions and by secular resonant perturbations among possible gas giant planets. A highly chaotic process. A left-over remnant gasdisk could damp the excited eccentricities of the final planets. The timescale for the formation of terrestrial planets is on the order $10^7 - 10^8$ years.

1.2.2 Terrestrial planet formation

In the following we focus on the middle- and late-stage scenarios for the formation of terrestrial planets within the Solar System. Numerical n-body simulations on the final accretion stage of terrestrial planets has been investigated intensively the last few years. With the increased availability of computational resources and the invention of fast and accurate n-body algorithms, a qualitative dynamical picture of planetary late stage evolution can be obtained spanning over time scales of up to 10^8 years. Investigation on orbital stability of Earth like planets within selected extrasolar systems have been performed, and a discussion will be postponed to a later section. For now, we ask the question on the possibility and conditions that terrestrial planets actually *can* form and the question of the origin of *water* on Earth.

Among the first to investigate terrestrial planet formation were Wetherill (1996) and Chambers and Wetherill (1998). The latter considered a three dimensional model of a late stage disk, populated with 56 planetary embryos initially spaced at 1.2 AU $< a <$ 2.0 AU. Mutual gravitational interactions, inelastic collisions, external giant planet perturbations and various disk surface densities have been included into the model. Various combinations of initial conditions have been investigated. The simulations typically produce several terrestrial planets on isolated orbits interior to 2 AU, with eccentricities and inclinations substantially larger than the present observed time-averaged values (see A-series simulations in Fig. 1.3) within the Solar System.

This result was reproduced by Agnor et al. (1999), using roughly the same initial conditions. In these simulations, several sub-Earth planets were formed within the terrestrial region. One possible explanation for the eccentricity excess of the final simulated planets, is the low number of initial planetary embryos. A larger number will result in a higher collision frequency acting as a dynamical friction effect result-

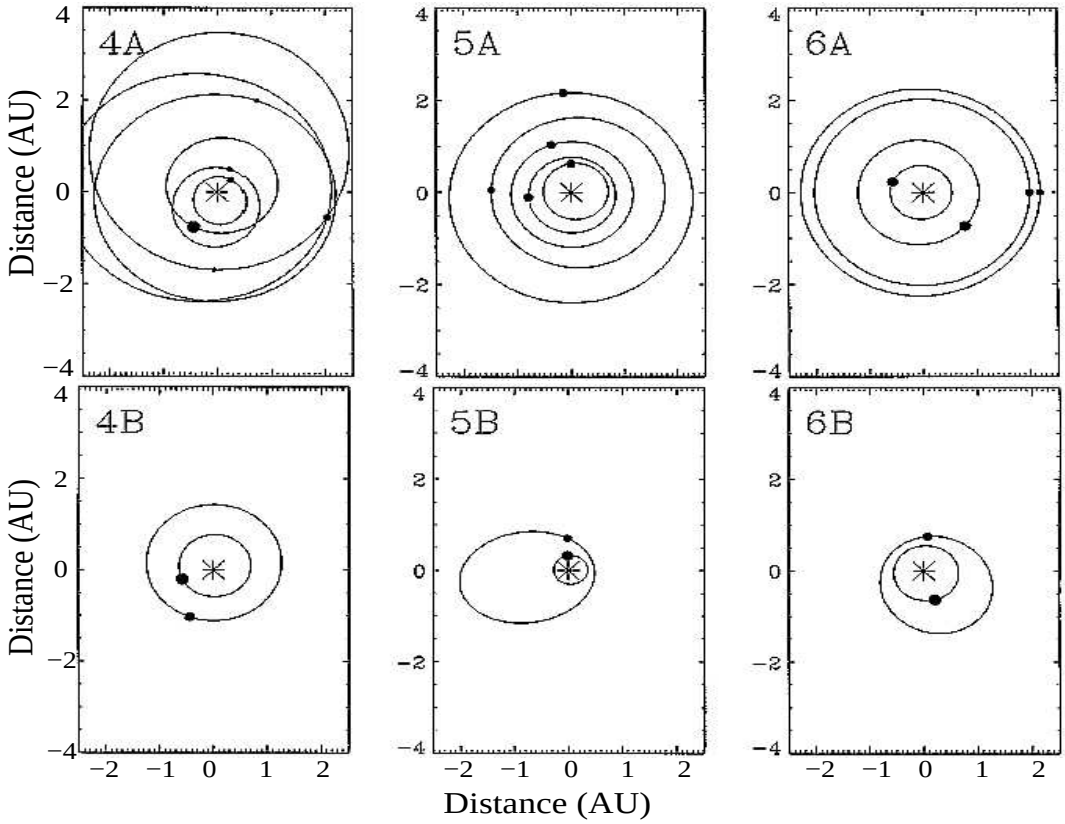

Figure 1.3: Final orbits of surviving terrestrial planets after 10^8 years (reproduced from (Chambers and Wetherill, 1998, Fig. 17,18)). Upper panel (A-series): Jupiter and Saturn are not included in the simulations. Parameterrange: 4A: $0.10 < e_{4A} < 0.49$, 0.52 AU $< a_{4A} <$ 2.57 AU, $2° < i_{4A} < 34°$ and $0.08 M_\oplus < m_{4A} < 2.2 M_\oplus$. 5A: $0.06 < e_{5A} < 0.08$, 0.61 AU $< a_{5A} <$ 2.28 AU, $2° < i_{5A} < 5°$ and $0.35 M_\oplus < m_{5A} < 0.96 M_\oplus$. 6A: $0.05 < e_{6A} < 0.06$, 0.58 AU $< a_{6A} <$ 2.25 AU, $3° < i_{6A} < 8°$ and $0.41 M_\oplus < m_{6A} < 1.29 m_\oplus$. Lower panel (B-series): Jupiter and Saturn are included after 10^7 years with present orbital parameters. Parameterrange: 4B: $0.09 < e_{4B} < 0.13$, 0.68 AU $< a_{4B} <$ 1.27 AU, $2° < i_{4B} < 6°$ and 1.01 $M_\oplus < m_{4B} <$ 1.85 $M_\oplus$. 5B: $0.09 < e_{5B} < 0.12$, 0.31 AU $< a_{5B} <$ 1.27 AU, $15° < i_{5B} < 17°$ and 0.51 $M_\oplus < m_{5B} <$ 1.59 $M_\oplus$. 6B: $0.17 < e_{6B} <$ 0.29, 0.60 AU $< a_{6B} <$ 1.29 AU, $2° < i_{6B} < 6°$ and 0.51 $M_\oplus < m_{6B} <$ 1.59 $M_\oplus$.

ing in a damping of orbital eccentricity and inclination. By increasing the number of initial planetary embryos by a factor of two, Chambers (2001) managed to lower the final eccentricity and inclination of the final planets.

A second mechanism for the damping of orbital parameters is gas drag. By following the evolution of 4000 particles Kokubo and Ida (2000) demonstrated the formation of circular Earth like planets at 1 AU, within 10^5 years (see Fig. 1.4). In their simulations they included the effect of gas drag due to the disk nebula.

More realistic simulations need to include the gravitational influence of the giant

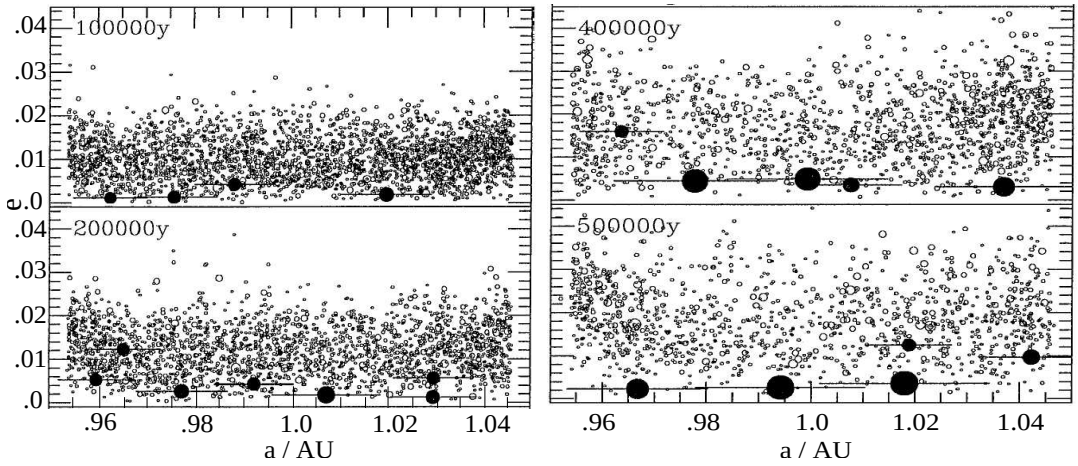

Figure 1.4: Formation of terrestrial planets (reproduced from (Kokubo and Ida, 2000, Fig. 7)). Simulation snapshots of a swarm of planetesimals at different times. Filled circles represent protoplanets with mass larger than 2×10^{24}kg. Horizontal lines represents the perihelion- and aphelion distance.

planets (Jupiter and Saturn) on planetesimals accretion. By adding the giant planets after 10^7 years, Chambers and Wetherill (1998) simulated the dynamical evolution of planetesimals over 10^8 years (see B-series simulations in Fig. 1.3). Kominami and Ida (2002, 2004) simulated the combined effect of giant planet perturbation and gas drag on the formation of terrestrial planets. Different mass distributions for the initial surface density profile where investigated and the disspation of the gas modelled by a damping parameter, measuring the strength of the damping as a function of time. In the majority of all simulations, they formed Earth planets in circular orbits at distances between ~ 0.5 AU and ~ 1.5 AU, although numerous Mars-sized planets remain uncollided in the final configurations.

The effect of giant planet eccentricity and migration, on planetary accretion in the terrestrial region where studied by Chambers and Cassen (2002); Chambers (2003) and Sleep (2001). The larger the eccentricity the smaller the perihelion distance, leading to a stronger gravitational interaction within the inner Solar System region. High-mass giant planets (two times Jupiter mass) on $e = 0.2$ eccentric orbits (i.e., four times Jupiters eccentricity) could account for a strong enough perturbation on terrestrial protoplanets, leading to a higher collision rate. In particular, eccentric giant-planet orbits leads to a significant excitation of terrestrial planetesimals on hyperbolic orbits, prohibiting the formation of Earth like planets. Numerical studies of the effect of giant-planet eccentricities in observed extrasolar systems has been performed by Thébault et al. (2002). For example, the terrestrial region within the ϵ Eridani system (see Appendix C for a list on orbital elements) turns out to be a

highly dynamical hostile region for the formation of protoplanets. In general, high eccentric giant planet orbits, tends to increase the planetesimal velocity dispersion, leading to fragmentation rather than accretion after collisions. A key parameter for a succesful accretion and formation of terrestrial planets is the *timing* of the formation of giant planets. According to the 'core-accretion' model (Pollack et al., 1996), the formation of giant planets requires about 10^7 years, in observational agreement with inferred lifetimes of gaseous disks around young stars (Briceño et al., 2001). Within that timespan, planetesimal accretion in the unperturbed inner region of a planetary system must form protoplanetary embryos, before the giant planets gravitational influence counteracts the accretion process.

1.2.3 Water worlds

According to current models of the early solar nebula environment, volatile elements like H_2O could *not* condense within the terrestrial regions to eventually form water, to be incorporated into the early Earth. This is attributable to a higher temperature at smaller heliocentric distances (initial stage). Therefore, the local building blocks of Earth were devoid of water. This raises the question of the source(s) of Earth's water and a possible delivery mechanism. A conservative estimate of Earth's present total water content is $\sim 5 \cdot 10^{-4} M_{\oplus}$.

Until recently, the *cometary late veneer* scenario were generally accepted for the delivery of H_2O on Earth (Owen and Bar-Nun, 1995). Planetesimals which formed in cooler regions within the solar nebula, accreted H_2O in its solid form. Perturbations by the giant planets excited the orbit eccentricity serving as a transport carrier mechanism to the inner terrestrial region of the early Solar System. At present, the remnants of these planetesimals are classified as comets, characterised by their high eccentric orbits. Linking the origin of H_2O on Earth to its source, is quantified by the ratio of the two stable isotopes of hydrogen - D/H ($^2H/^1H$). Spectroscopic measurements of the D/H ratio for three different comets, indicates that cometary water contain roughly twice as much deuterium relative to hydrogen as the Earth's mean ocean value. Therefore, it appears that H_2O delivery by cometary impacts could not have been the dominant source of Earth's water. It is estimated that, around 10% of the present amount of H_2O could have been delivered by cometary impacts.

Morbidelli et al. (2000) performed dynamical simulations of planet accretion to estimate the delivery efficiency and timescale for water bearing planetesimals. They present an alternative model for the origin of water on Earth based on different water reservoirs within the protoplanetary nebula disk. On the basis of their simulations, they showed that the main contributers of Earth's water content, is delivered by planetary embryo collisions in the middle and late stage of planet accretion process. Protoplanetary embryos originally formed in more hydrated ("wet") distant regions

at a location of the outer part of the asteroid belt, subsequently excited to crossing orbits leading to collisions with terrestrial planetary embryos. In the extreme, this scenario could be as efficient as delivering 10× the current amount of water.

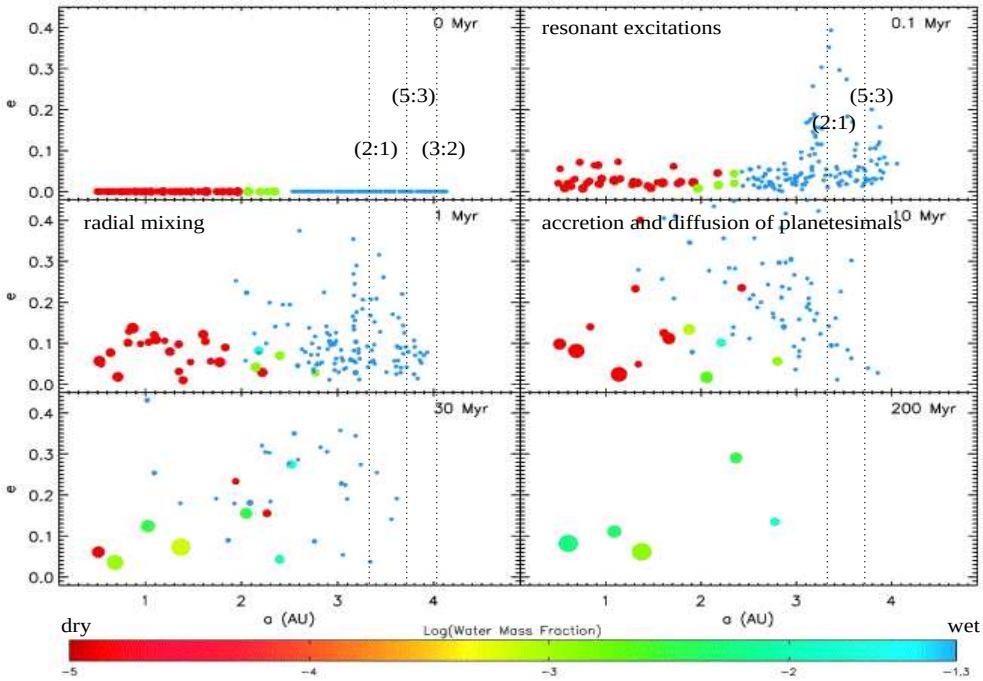

Figure 1.5: Simulation snapshots of the time evolution of planetesimals under the gravitational influence of a Jupiter mass planet (reproduced from Raymond et al. (2004, Fig. 3, p.7)). The initial radial distribution were divided into three regions according to the fractional water content (hydration). Dry: planetesimals at $a < 2$AU have a water content of 0.001% by mass. Wet: planetesimals at $a > 2.5$ AU, have a water content of 5% by mass and the intermediate planetesimals have a water content of 0.1%. Note: the radius of objects represents not the physical size. The final terrestrial planets at 1 AU have masses $0.4M_{\oplus}$ and $1M_{\oplus}$ and for reference the ($\log_{10}$) water mass fraction for Earth is -3.3 (green-yellow).

Recently, Raymond et al. (2004) presented simulations of the delivery of volatile elements to the terrestrial region as a function of Jupiters mass, eccentricity, semi-major axis and the density profile of solids within the protoplanetary disk. In particular, Fig. 1.5 shows the time evolution of a swarm of accreting hydrated planetesimals under the gravitational influence of a Jupiter mass planet. The distance of solid water condensation is called the *snow line*, and is in this simulation chosen to be located at $a \sim 5$AU for the initial stage solar nebula environment. Within the first 10^7 years, the main dynamical characteristics of *resonant excitation*, *radial mixing* and *diffusion* of planetesimals are exhibited during the middle and final stage of planetary evolution. Clearly, the 2:1 and 5:3 mean motion resonances with

Jupiter, are dominant in exciting the eccentricity within 10^5 years. In between 10^7 years and 3×10^7 years, hydrated planetesimals start to radially diffuse into the inner region, resulting into collisions with terrestrial planetary embryos. The end state water content of final terrestrial planets, are somewhat "wetter" compared to Earth (see figure caption for details). After $\sim 10^8$ years the evolution produces 2 - 3 Earth like *water worlds* on nearly circular orbits. In addition, Raymond et al. demonstrated that the efficiency of terrestrial planet formation decreases as the eccentricity of Jupiter increases. For eccentricities $e_{Jup} = 0.2$, the number of planetesimals decreases substantially by either collisions with the Sun or ejections on hyperbolic orbits. Again, large eccentricities of Jupiter's orbit acts as an effective depletion mechanism, preventing planet formation by planetesimal accretion.

It must be stressed, that constraints on model parameters adopted in these simulations are poorly determined by observations. An exact replica of the current Solar System configuration, or at least the terrestrial region, is almost not produced in any of the numerical simulations. The physical nature of the simulated accretion process is highly stochastic, involving chaos as the random variable. Identical initial conditions of disk- and protoplanet parameters results in different end states of a planetary system. In general, numerical models described here can predict only qualitatively the dynamics and the detailed endstates of planetary configurations is a matter of chance and not of deterministic and predictable physics. In order to get quantitatively statistical valid results on terrestrial planet formation, many numerical simulations must be done. Future studies will establish a deeper foundation on this topic. However, present day experiments by numerical simulations of planetary accretion process, indicates that terrestrial planets actually can form, although depending on orbit- and mass-parameters of possible giant planet(s).

1.3 Orbital resonances and chaotic motion

The geometry of the Solar System and some of its subsystems is highly structured by the presence of resonances. A detailed review of resonance phenomena within the Solar System is given by Peale (1976) and most recently by Malhotra (1998). The phenomenon of resonance is very efficient in changing orbit characteristic. The timescale involved for such changes is on the order of millions of years. The underlying kinematics of resonant orbits have interesting dynamical characteristics, exhibiting a source of both long term stability, transition to instability and chaotic diffusion. The forces characterising the dynamics are mainly of gravitational or tidal nature. For resonant orbits, the forces involved acts periodically at specific intervals of time. Hence small repetetive resonant perturbations accumulate over long timescales producing interesting and complex dynamical features of orbital evolution over long periods of time.

In general, resonances occurs if there exist a small numbered rational relationship or commensurability between frequencies or periods. The periods involved are due to either sidereal planetary or orbital rotation. Following Malhotra (1998) there exist three general types of resonance phenomena within the Solar System. The most simple case is the single body *spin-orbit* resonance for which two examples within the Solar System are: 1) the Moon wich has a rotational period equal to its orbital period and 2) Mercury being in a 3:2 spin-orbit resonance state. In addition, satellite moons of Jupiter and Saturn are observed to be in orbital resonances. If the periods involved are associated to orbital parameters only, then there exist an orbit-orbit resonance. Orbit-orbit resonances differentiate into two main types of resonances: a) *mean motion resonance* and b) *secular resonance*.

Mean motion resonances occurs if there exist a commensurability of the mean orbital angular velocities (or mean motions) between Solar System objects. If n_1 and n_2 measures the mean motion of two bodies, then they are said to be in a (near) $n_1 : n_2$ mean motion resonance if

$$\frac{n_1}{n_2} \simeq \frac{p+q}{p} \qquad \text{for } p,\ q \in \mathbb{Z}. \tag{1.1}$$

The rational number p is called the *order* of the resonance. As will be discussed later the mean motion is related to the spatial location of the body by Keplers third law of planetary motion. For a given orbiting body: the larger the mean orbital angular velocity the closer is its location to the central force field. High order mean motion resonances implicate therefore large mutual separation between two bodies in resonance. Fig. 1.6 represents some examples of known mean motion resonances within the Solar System and the satellite subsystem of Saturn.

Secular resonances involves commensurabilities between the time rate of change of the apsidal longitudes (precession rates of the orbits) of two planets (or a planet and an asteroid.). The timescales involved for the occurance of orbital changes are much larger compared to mean motion resonances, and within the Solar System there is a separation between the secular precession and orbital mean motion timescales.

Exceptions are observed within the asteroid belt where there exist a coupling between secular and mean motion resonances inducing chaotic dynamics for the motion of the asteroids. Such couplings are called *resonance overlap* and over large timescales acts as a destabilizing mechanism of the orbit (Lecar et al., 2001). In particular, the structure of the asteroid belt within the Solar System is characterised by gaps devoid of asteroids, known as *Kirkwood gaps* (see Fig. 1.9). The locations of the gaps are associated with mean motion commensurabilities with Jupiter. The most famous locations are the 4:1, 3:1, 5:2 and 7:3 mean motion resonances, located at 2.1 AU, 2.5 AU, 2.82 AU and 2.95 AU, respectively.

The presently accepted explanation of these gaps is based on the appearance of chaos induced by resonant overlaps between mean motion and secular resonances

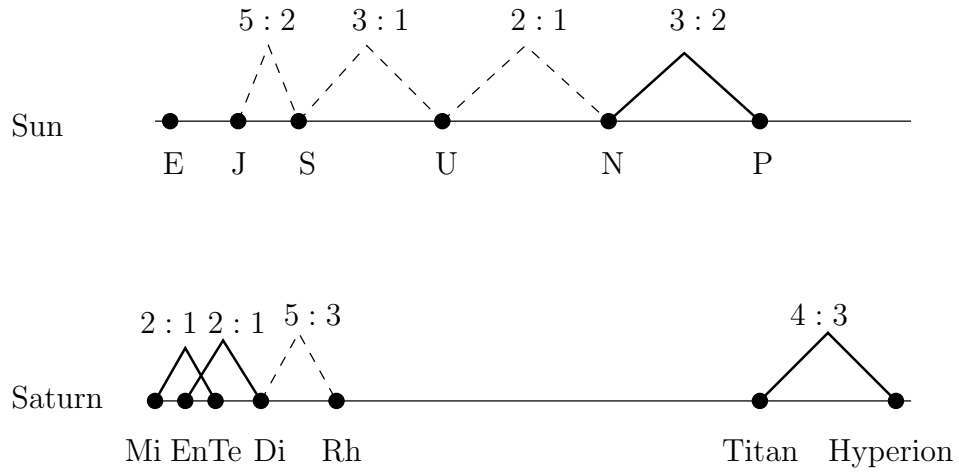

Figure 1.6: Mean motion resonances within the Solar System and the Saturnian satellite system. Exact resonances are indicated with solid lines and near resonances by dotted lines.Orbital Spacings are relative distances. The 5:2 near mean motion resonance between Jupiter and Saturn is called the *great inequality* and causes a modulation of the planets orbital elements on a $\sim$ 900 year timescale. The figure is extracted and reproduced from (Malhotra, 1998, Figure 4).

(Morbidelli and Moons, 1993b,a). Mean motion resonances have the characteristic to increase the eccentricity of the asteroid over a long period of time, also known as chaotic diffusion within the systems phase space. Excursions of the eccentricity have the effect of reaching the inner part of the Solar System, resulting in collisions or close encounters with Mars. Possible close encounter with Mars change the asteroids orbital parameters away from the 3:1 resonant location or completely remove it by impact absorbtion. The presence of secular resonances within mean motion resonances increase the effect of eccentricity pumping further. Thus, the combined effect of secular and mean-motion resonances provides a more efficient transport mechanism by which asteroids are capable of reaching the orbits of Earth and Venus resulting in a higher depletion rate of asteroids by either collisions or close encounters. This scenario could in addition explain the nessecary impactors for the late heavy bombardment phase of the early Solar System.

1.4 Habitability and the habitable zone

The ability of a planet for supporting life, or *habitability*[4], is based on our knowledge of life on Earth and on Earth's location within the Solar System. With the

[4]for a good introduction into the field of astrobiology, see the recent monograph by Gilmour and Sephton (2004)

general consensus among biologists that carbon-based life requires water for its self-sustaining chemical reactions, the search for habitable planets has therefore focused on identifying environments in which liquid water is stable over billions of years (Rampino and Caldeira, 1994). In particular, a strong argument that biological activity requires an aqueous environment, is that water is the major component of living tissues, accounting for 70% of their mass.

The presence of liquid water itself is not sufficient to produce and support life. The building blocks of life can be grouped into four different types: lipids (fats and oils), carbohydrates (carbon-compounds, sugars), proteins (enzymes) and nucleic acids (DNA, RNA). In addition, energy is required to synthesise molecules capable of generating organic compounds that may be biologically useful. The role played by liquid water, is to act as a solvent. It's polar chemical character enables different organic molecules to perform specific functions, due to their hydrophobic and hydrophilic nature - a profound property in the construction of the cell. Details on the emergence of simple prebiological organisms and the process of replication and subsequent evolution will not be discussed here. Instead we conclude that in general, liquid water appears to be an essential requirement for the formation of life on a habitable planet and the evolution of a Earth like biosphere (Kasting et al., 1993).

The long-term occurence of liquid water on a planet is mainly determined by the following key factors: a) the luminosity and surface temperature of the host star and b) geological and atmospheric properties of the terrestrial planet. In combination they determine a unique range from the host star for a planet to sustain liquid water. In the following, we focus on the circumstellar region known as the habitable zone.

The concept of the *habitable zone* (HZ), or the radial distance around a star in which planets might be able to maintain liquid water to eventual initiate and support life, has been discussed in the scientific literature for many years (Huang, 1959; Hart, 1979; Kasting et al., 1993). In order for liquid water to exist, the average temperature of the planetary surface must remain between 273 K and 373 K (if the surface pressure is $\sim$ 1 atm), at a sufficiently high atmospheric pressure to prevent sublimation of water to water vapour. The planets surface temperature is determined by the balance between a) incoming solar radiation and b) thermal emission from the planet's surface/atmosphere. To a first order, the recieved energy is strongly dependent on the stellar surface temperature and luminosity at a given time of the star's main-sequence phase. The amount of absorbed energy is dependent on physical properties and chemical composition of the planetary atmosphere. For example, the Earth upper atmosphere ozon layer absorbes high energy solar radiation at ultra violet wavelengths. Other possible environmental constraints that affect the habitability of a planet are the fractional covering ratio of water/land surface areas, planetary rotation/inclination and atmospheric circulation currents for the distribution of heat. Changes in planetary atmospheric properties, such as

escape of volatile gases into interplanetary space and chemical reactions with surface materials (plate tectonics and waethering), regulates the planetary surface temperature in a highly complex interaction mechanism. Establishing limits to the extent of a HZ requires a considerable understanding of the interaction processes on the planet in order for models to be accurate.

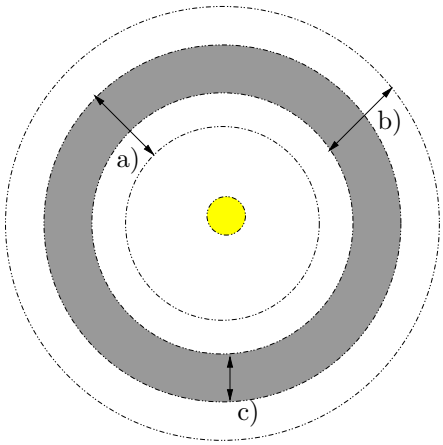

Figure 1.7: Concepts of the habitable zone: a) initial habitable zone at zero age main sequence (ZAMS), b) final or *current* habitable zone and c) the continouse habitable zone.

An additional constraint on the definition of the HZ is of temporal character. Variation in stellar luminosity associated with the stellar evolution of main sequence stars, introduces the concept of a *continously habitable zone* (CHZ). With time the stellar luminosity and surface temperature increases, resulting in a shift of the habitable zone radially outwards. The overlap between the initial habitable annulus and the final habitable annulus, is defined as the continuos habitable zone (gray area in Fig. 1.7). In order for a planet to be habitable during the star's entire main-sequence life time, it needs to be located and confined to within the CHZ. Again, Kasting et al. (1993) calculated the CHZ for various main sequence stars by using their climate model in combination with stellar evolution models in order to determine changes in stellar luminosity and effective temperature for different stellar spectral classes.

The existence of possible life bearing planets is limited to stars of spectral type F, G, K and M. The timescale for the developement of a biosphere is estimated to be 10^9 years. Stars with spectral type G and mid-to-early K are optimal candidates for harboring terrestrial planets, since the main sequence duration time is sufficiently long enough ($\sim 10^{10}$ years) for developing biological activity. A planet initially located outside (frozen) the HZ could become habitable as the outer boundary moves outwards with increasing luminosity.

1.5 Terrestrial planets in extrasolar planetary systems

Since the discovery of multiple-planetary systems, two questions became apparent for the orbital nature of these systems. First, the question regarding global dynamics and stability in order to constrain observed (fitted) orbital parameters as derived from radial velocity data of the observed giant planets and secondly, the possibility of the long-term existence of stable terrestrial planetary orbits, within the HZ. Currently, 12 multiple-planetary systems have been observed with planet configurations for potentially harboring Earth like planets. In the following, we discuss briefly on the possibility of the existence of terrestrial planets within 47 Ursae Majoris. This system gained much attention regarding dynamical stability simulations of terrestic planets, and stable orbits within the HZ could be well estabilished considering only the inner most planet in the model. However, by the recent discovery of a secondary outer planet, the previously confirmed stable regions were now delimited due to the additional gravitational influence of the secondary outer planet.

1.5.1 A case study review: 47 Ursae Majoris

The existence of a planet orbiting the G1V main sequence Solar-type star 47 Ursae Majoris (47 UMa), have been reported by Butler and Marcy (1996), by using the radial velocity technique. Subsequent observations of velocity measurements exhibited the existence of a second planet (Fischer et al., 2002). The HZ and orbital elements for the planets are listed in Table 1.1. The study of hypothetical terrestrial planets within 47 UMa is particular interesting, since it resembles the Solar System most closely among the known extrasolar planetary systems. The orbital period ratios for both systems are quite similar ($P_c/P_b \sim 2.39$ for 47 UMa vs. 2.49 for Jupiter-Saturn), and to within radial velocity measurement errors, the mass ratios are identical ($M_b/M_c \sim 3.34$ for 47 UMa vs. 3.34 for Jupiter-Saturn). The major differences between these two systems are the orbital periods and nominal masses of 47 UMa(b) and Jupiter. The orbital period of Jupiter is less than one-fourth that of Jupiter, and the nominal mass is ~ 2.5 times greater. The effects on orbital elements due to mutual perturbations are therefore expected to occure on shorter time scales.

The first attempt to estimate stability by introducing the concept of the HZ were done by Gehman et al. (1996), by considering the circular restricted three-body problem analytically (at that time only one planet, 47 UMa(b) was known to exist). They concluded that terrestrial planets could survive within an outer boundary of $a \leq 1.6$ AU, assuming circular orbits. Although, Gehman et al. proofed stable orbits within the HZ, analytic investigations neglects long-term dynamical effects

	47 Ursae Majoris		
Parameters	b-component	c-component	Range of HZ
a (AU)	2.09	3.73	-
e	0.061	0.005	-
ω (°)	172	127	-
$m_{pl} \sin i$ (M_{Jup})	2.54	0.76	-
P (days)	1089	2594	-
$R^{\text{ZAMS}}_{\text{inner}}$ (AU)	-	-	0.76
$R^{\text{ZAMS}}_{\text{outer}}$ (AU)	-	-	1.43
$R^{\text{now}}_{\text{inner}}$ (AU)	-	-	1.00
$R^{\text{now}}_{\text{outer}}$ (AU)	-	-	1.90

Table 1.1: Orbital parameters for planets and the extend of the habitable zone within 47 Ursae Majoris. Data are reproduced from (Fischer et al., 2002, table 2, p.1031) and (Jones and Sleep, 2002, Fig. 1, p.1017). The estimated age of 47 UMa is $\sim 7 \times 10^9$ years. R^{now} and R^{ZAMS} refers to the current and zero age main sequence boundary of the habitable zone.

such as resonant interactions and secular perturbations.

A more precise picture of the qualitative dynamics within the HZ, is obtained by solving the equations of motion using direct numerical integrations over long time scales. Jones et al. (2001) numerically studied the dynamical evolution of terrestrial planets as a function of the giant planet mass and eccentricity over 10^8 years. As a stability measure they used the Hill stability concept: a planetary system is Hill stable, if a pair of planets are forbidden to undergo close approaches for all time (at least within the simulation time). The outcome of a close encounter is almost always a hyperbolic or high eccentric orbit, ejecting the planet into interstellar space or producing collisions with the host star. The Hill sphere of a planet corresponds to the volume centered on the planet in which the gravitational attraction is larger than the star's tidal attraction; and therefore, the perturbations to the orbital elements are more significant. In addition, they require that the terrestrial orbit is confined to the HZ of the system, that is, confinement is taken to mean that the semimajor axis remain in the HZ at all times during a given integration. Although not adopted, they point out that an even tighter criterion is to additionally restrict the orbits in the HZ to some upper limit of the eccentricity. Their results are as follows: Regions located around the 2:1 ($a = 1.3$ AU) and 3:1 ($a = 1.0$ AU) mean motion resonance as well as for the outer boundary of the HZ were found to be unstable. Stable circular orbits at the inner ($a < 1.0$ AU) habitable region were found, for a minimum giant planet mass, considering only the dynamical effects of the inner giant planet as observed at that time.

Several stability investigations have been performed after the discovery of the

second outer giant planet. Noble et al. (2002b) noted that the gravitational effect of the outer planet on the stability of terrestrial planets at the inner edge of the habitable zone is negligible. However, they only considered dynamical simulations with short integration times ($\sim 10^2$ years), therefore not considering long-term orbital instabilities. Dynamical simulations over an extended period of time ($\sim 10^9$ years) have been done by Jones and Sleep (2002). Because of the evolved main sequence age of 47 UMa (estimated to $\sim 7 \times 10^9$ years), they searched for stable orbits within the CHZ (0.43 AU in width) as calculated by Kasting et al. (1993) and shown in Table 1.1. Their simulations show that gravitational perturbations by the outer planet, causes significant excursions in the variation of the inner giant planet's eccentricity, leading to larger instability regions within the CHZ. They found unstable orbits (the case of a close encounter) of terrestrial planets at the inner (~ 1.0 AU) and outer (~ 1.43 AU) boundary of the CHZ, where the inner unstable region is associated with the 3:1 mean motion resonance.

The presence of the secondary outer component also introduces, as we have seen, secular resonances involving the commensurabilities of the apsidal frequency between the inner giant and a terrestrial planet. Goździewski (2002) performed a stability analysis of the two planets within 47 UMa and studied the stability of Earth like planets within the HZ with emphasize on secular dynamics. In combination with the `MEGNO` chaos indicator, a straight forward stability criterion were adopted for different initial conditions, in which the maximum variation of the eccentricity and semi-major axis of the terrestrial planet were monitored during the time evolution of a simulation. The amount of chaoticity, for a given initial condition, is a measure of how erratic the system response to small changes in the initial conditions; thereby inferring a measure of stability. The analysis confirmed the unstable regions around the 2:1 and 3:1 mean motion resonances as determined by Jones et al.. In addition, the presence of the secular resonance narrows the stability region at the inner HZ(ZAMS), as were previously claimed stable by Jones et al.. Numerical simulations shows a large instability region between $a = 0.8 - 0.9$ AU at the 4:1 mean motion resonance, as a result of secular resonances. In addition, the outer edge of the HZ(now) becomes unstable from 1.35 AU, due to the close proximty of the inner giant planet. Recently, Ashgari et al. (2004) confirmed this result using a similar approach of stability analysis and determines stable orbits in the regions $1.05 \text{ AU} < a < 1.3 \text{ AU}$ and $0.65 \text{ AU} < a < 0.8$ AU.

In general, Goździewsky points out, that the dynamical structure of the HZ in 47 UMa recalls the analogy of the Asteroid belt in the Solar System were the combined effect of mean motion and secular resonances are responsible for the formation of prominent gaps in the distribution of asteroid orbital elements. The fact that no planet is observed within the asteroid belt, makes it reasonable to assume that the combination of mean motion and secular resonances counter acts the accretion process in order to form proto planets in the late stage accretion phase. Although,

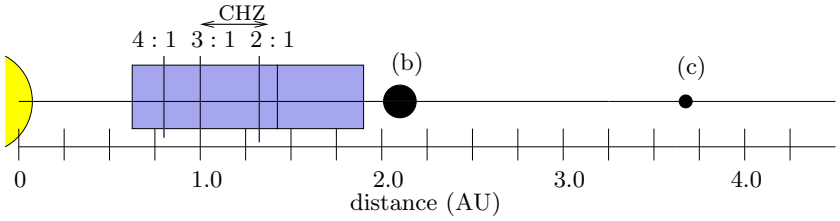

Figure 1.8: Main characteristics of 47 Ursae Majoris including the continouse habitable zone. The 4:1, 3:1 and 2:1 mean motion resonances with 47 UMa(b) are indicated.

an extended region of stability were found to harbor a possible Earth like planet, other regions of the HZ of 47 UMa seems to be dynamically hostile. Accretion simulations have been performed by Laughlin et al. (2002), addressing the question of how likely terrestrial planets could be formed within 47 UMa. Considering the time evolution of accreting proto-planet embryos embedded in a low- and high-mass disk, they concluded that final planets could only form within $a < 0.7$ AU, assuming the existence of the giant planets during the simulations. The depletion of planetesimals within the HZ, were dominated by the presence of secular resonances causing an excitation of orbit eccentricities. However, future space missions should certainly not avoid 47 Ursae Majoris for the search of possible Earth like planets due to the large extend of dynamically quiscent orbits of possible terrestrial planets within the CHZ.

1.6 Motivating question and problem statement

My motivation

The most interesting question, since the discovery of the first extrasolar planet, has been the speculation on the possibility of the existence of a second Earth like planet in orbit around a distant Sun like star. Current telescope technology is not capable of resolving a distant second Earth, thereby leaving us the option to theorise about the existence of Earth like planets within known extrasolar planetary systems using numerical techniques. For a given system, the question then is: given the orbital parameters of an *observed* extrasolar giant planet, is it possible for an Earth like planet to maintain a stable orbit within the HZ over the main sequence lifetime of the host star?

Numerical experiments, as we have seen, suggested in general that the dynamical evolution of particles initially located within the terrestrial region, were mainly dictatet by the orbital parameters of the external giant planet. External giant planets in eccentric orbits have the effect of 1) counteracting planetesimal accumulation and

2) destabilizing terrestrial orbits. In addition, multiplanetary systems containing two giant planets have the effect of inducing secular resonances, rendering specific regions to be dynamically unstable.

In order to fullfill the dynamical constraints for the selection of an extrasolar planetary system, I have adopted two selection criteria: 1) a giant planet in a sufficiently circular orbit and 2) with a sufficiently large orbital distance. Following these criteria the most promising candidate is the HD70642 planetary system. Within observation uncertainties, this system contains a $m \sin i = 2\ M_{jup}$ planet, orbiting a Solar like G5 star in a six year circular orbit with semimajor axis $a = 3.3$ AU. It was observed over a five year period by the Anglo-Australian Planet Search Group and reported by Carter et al. (2003).

The search for possible stable orbits within the HZ is furthermore motivated by comparing the orbital parameters of HD 70642b with a histogram distribution of the Solar System asteroid families (see Fig. 1.9). In addition to the Kirkwood gaps, the asteroid belt is characterised by three major locations with an enhanced density of asteroids (ex. at 2.3 AU, 2.6 AU and 3.1 AU). These regions matches mean motion resonances with Jupiter and are dynamically stable on time scales comparable to the Solar System age. The stabilizing mechanism is poorly understood and currently an active research field within Solar System dynamics. However, inferring the location of HD 70643b at 3.3 AU, we are enabled to calculate the orbits of some high order mean motion resonances within the HZ. Comparing the radial extent from Jupiter to the major asteroid families with HD70642 the following question is apparent: Is it possible that there exist dynamically quiscent regions within HD70642's habitable zone, maintained by high order mean motion resonances?

Problem statement

In order to fully understand whether or not there exist stable niches for a hypothetical Earth like planet within the habitbale zone of HD70642, we need to perform a parameter survey using a numerical n-body particle simulation algorithm. To a first approximation, we employ the following assumptions to represent the dynamics of an Earth like planet within HD70642:

i) The planets are considered as spherically symmetrical and non-rotating bodies (i.e each body can be considered as a point-mass object).

ii) The dynamics are based on Newtonian mechanics, i.e planets (point-masses) moves in the gravitational field of a central star, perturbing each other due to mutual gravitational interactions.

iii) Relativistic corrections are not included.

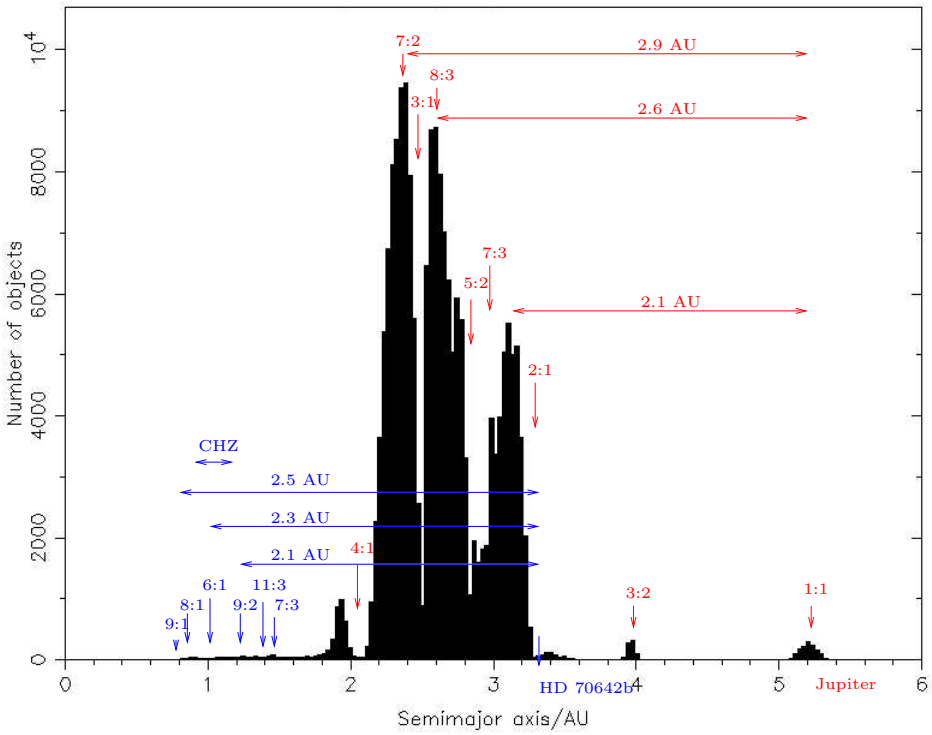

Figure 1.9: Histogram of asteroid distribution taken from data available from the Minor Planet Center (http://cfa-www.harvard.edu/iau/plot/OrbEls01.gif). Asteroids in mean motion resonance with Jupiter are labeled in red. Orbital distances in mean motion resonances with HD 70642b are labeled in blue.

iv) Any external perturbations (galactic potential, potential of nearby stars and the potential of possible asteroid rings and moons) of the system are assumed to be neglectible. No observations of such structures are currently evident.

v) The central star is considered to be a spherically symmetric, non-rotating (i.e no quadrupole moment, J_2) body.

vi) Neglection of massloss in any object (i.e isotropic massloss of the central star due to electromagnetic radiation and solar wind is neglected.

The simulation timespan should cover a substantial part of the main sequence lifetime of the host star. A statistical approach to the complex dynamical three-body problem is needed, since three-body dynamics is expected to exhibit chaotic behavior. Such a survey should scan over a large range of initial conditions within

the systems phase space. Although specific particle trajectories cannot be predicted over long times, average values based on many particle trajectories are in fact reproducible. This will enable us to make statements on the future evolution of particle trajectories. In general, the time evolution of orbital parameters should be monitored during the complete integration time for an analysis of the orbital behavior. By performing this study, we should be able to ascertain whether or not HD70642 could harbor an Earth like planet on a dynamically stable orbit within the habitable zone.

Chapter 2

Basic Concepts in Astrodynamics

2.1 Introduction

The most fundamental model within planetary dynamics is the two-body model or the *two-body Kepler problem*. A possible statement of the problem would be: given two mutual attracting massive objects m_1 and m_2, determine the future state in space at any time for a given set of initial conditions. Two important aspects of the two-body problem are 1) the existence of a complete analytic solution describing the general possibilities of motion and 2) its application to general perturbation theory, which can be treated as approximate two-body models. These approximations has been the starting point in obtaining theories for the motion of planets within the Solar System.

In this section, we will consider fundamental properties of the two-body problem and introduce basic astrodynamical concepts and terms necessary for an understanding of our further analysis. The orbital Kepler elements are introduced. They are convenient to characterize the relative two-body motion by quantities that describe the geometrical properties of the possible orbital motion. Some emphasis has been given on the analysis and exploration of numerical algorithms for the solution of Kepler's equation, as this topic became a first lesson within this thesis project. Limitations in their range of applications to orbital dynamics problems have been considered at the same time providing a deeper understanding of the machinery at play. They will be necessary for our numerical analysis of habitable planetary motion.

There exists various books for an introduction to the field of astrodynamics and celestial mechanics. The authors Danby (1988),Roy (1988), Boulet (1991),Prussing and Conway (1993) and Murray and Dermott (1999) are found to give the most complete picture of classic concepts. Modern celestial mechanics is introduced by the book of Morbidelli (2002a).

2.2 Properties of Keplerian motion

In the following, we consider the motion of two homogeneous spherically symmetric masses m_0 and m_1. Denoting the relative heliocentric position of m_1 from m_0 with $\boldsymbol{r}$, then by Newton's law of gravitation the *equation of relative motion* can be written as

$$\frac{d^2\boldsymbol{r}}{dt^2} = -\mu\frac{\boldsymbol{r}}{r^3}, \tag{2.1}$$

where $\mu = k^2(m_0 + m_1)$ is the *mass parameter* and k^2 is the Gaussian gravitational constant. In the following, we will treat planets as point masses, but most of the discussion will apply to a planet in orbit around a dynamical center given by a central massive star.

Constants of motion are useful to derive basic properties of the motion. Considering the motion in phase space geometrically, a constant of motion restricts the time evolution of the system onto a sub space, limiting the available phase space to a confined region. The first constant of motion for the two-body system is the orbital angular momentum $\boldsymbol{h}$. From eq. (2.1), we have

$$\frac{d\boldsymbol{h}}{dt} = \frac{d(\boldsymbol{r}\times\dot{\boldsymbol{r}})}{dt} = 0, \tag{2.2}$$

where $\dot{\boldsymbol{r}}$ is the relative velocity of m_2. The angular momentum points in the same direction for all time and constrains the motion of m_2 to an *orbital plane* in inertial space.

Introducing polar coordinates (r, θ) within the orbital plane coordinate system of m_2, eq.(2.1) of relative motion can be written as

$$\ddot{r} - r\dot{\theta}^2 = -\frac{\mu}{r^2}. \tag{2.3}$$

A complete solution of this second-order differential equation (2.1), requires the determination of six constants of motion[1]. Detailes on their derivation is found in Danby (1988), and in the following we only review the most important properties of two-body Keplerian motion. A general solution of the relative motion of m_1 (i.e of Eq. 2.1, is given by the following parametric representation of the orbit

$$r(\theta) = \frac{h^2/\mu}{1 + e\cos\big(\theta(t) - \omega\big)} \quad \text{with} \quad 0 \le \theta < 2\pi, \tag{2.4}$$

where h measures the magnitude of orbital angular momentum and the quantities e and ω are constants of integration, measuring the orbital *eccentricity* (amplitude or shape) and *argument of pericenter* (phase), respectively. The latter is interpreted as

[1] sometimes also called *integrals of motion*

an orbital phaseshift measured from a given reference direction at some initial epoch, and it plays a major role in the determination of the orbit within three dimensional space.

Referring to Fig. 2.1 and considering the case of elliptic motion, we have $h^2/\mu = a(1-e^2)$ and we introduce the *semimajor axis a* (orbital size) and the *true anomaly* $f(t)$, defined by $f(t) \equiv \theta(t) - \omega$ as the independent variable. The variable $\theta(t)$, is referred to as the *true longitude* and sometimes denoted as the argument of latitude. Within the language of celestial mechanics, an anomaly angle is measured with respect to the apsidal line or semimajor axis, and longitudes are referred to an arbitrary fixed direction. Three points in the elliptic orbit are of special interest. The minimum (*pericenter*) $q = a(1-e)$ and maximum (*apocenter*) $Q = a(1+e)$ distance of the orbital radius and $p = h^2/\mu$ the *semilatus rectum* when $f(t) = \pm\pi/2$. Furthermore, we define the orbital *mean motion* or mean orbital angular velocity

$$n \equiv \frac{2\pi}{T} = \sqrt{\frac{\mu}{a^3}}, \tag{2.5}$$

where T is the orbital period. The mean motion of the point mass is related to the orbit geometry, through Kepler's third law of planetary motion.
A second constant of motion is the orbital energy C of the point mass m_2 and is given by

$$\frac{v^2(t)}{2} - \frac{\mu}{r(t)} = C. \tag{2.6}$$

Here, v is the orbital velocity of m_2 relative to m_1 and the constant is called the *vis-viva integral*. We note that the orbital energy is independent of eccentricity and depends only on the semimajor axis.

Within gravitational orbit theory the vis-viva enery integral determines the nature of the orbit. Three possible types of planetary orbits are generally known and we classify orbits into either a *anomalyorbit*, *parabola* or *hyperbola*. Table 2.1 summarizes the characteristics of the orbit by either the energy constant, eccentricity parameter, orbital velocity or semimajor axis. These quantities are useful in determining a possible planet escape case. For elliptic motion the orbital energy is negative, implying that the point mass is bound to the attracting center. For a hyperbolic orbit the orbital energy is positive for $r \to \infty$, and the point mass proceeds infinitly away from the attracting center. For a parabolic orbit the point mass has enough energy to escape from the attracting center to infinite radius.

Considering the elliptic case, the velocity of m_2 is a maximum at pericenter ($f = 0$) and a minimum at apocenter ($f = \pi$). From eq. 2.6, we have for $r = q$ and

type of orbit	e	C	v^2	a
ellipse	$0 \leq e < 1$	$C = -\frac{\mu}{2a}$	$v^2 = \mu\left(\frac{2}{r} - \frac{1}{a}\right)$	$a > 0$
parabola	$e = 1$	$C = 0$	$v^2 = \frac{2\mu}{r}$	$1/a > 0$
hyperbola	$e > 1$	$C = \frac{\mu}{2a}$	$v^2 = \mu\left(\frac{2}{r} + \frac{1}{a}\right)$	$a < 0$

Table 2.1: Four possible conics for orbital motion. Circular motion is a special case of the ellipse when $e = 0$ and $r = a$. Bounded motion attracted to m_1 is indicated by a negative orbital energy of m_2, which is a function of semimajor axis.

$r = Q$ the pericentric v_p and apocentric v_a velocity

$$v_p = \frac{\mu}{a}\sqrt{\frac{1+e}{1-e}} \quad \text{and} \quad v_a = \frac{\mu}{a}\sqrt{\frac{1-e}{1+e}}. \tag{2.7}$$

We will use these relations later for the determination of proper initial conditions of an orbit with given eccentricity and unit semimajor axis.

2.2.1 The mean and eccentric anomalies

Although the solution given by eq. (2.4) is a closed-form solution, it only gives a parametric representation of the geometry of the orbit. The time parameter is not explicitly available for the determination of a position at a given time. In the general case ($e \neq 0$), the functions $\dot{f}(t)$ and $\dot{r}(t)$ are nonlinear in time and therefore of no practical use for a solution of our problem at hand. By introducing an auxiliary angle, linear in time and 2π-periodic, we are able to determine the position of a point mass at a given instant of time. Fig. 2.1 shows the geometry of the following discussion.

Considering the motion of a point mass within the orbit plane coordinate system with $\omega = 0$, we have the following relations

$$x(t) = a(\cos E(t) - e) \quad \text{and} \quad y(t) = a\sqrt{1-e^2}\sin E(t). \tag{2.8}$$

Here, we introduce the *eccentric anomaly* E, measuring the angle obtained by a line intersecting a point P located on an auxiliary circle with radius a. The apparent position P is the vertical projection of m_2 onto the circle. By this construction, the eccentric anomaly is 2π periodic and linear in time. From eq. (2.8) and using trigonometric identities, we obtain the following expression relating E to f

$$\tan\frac{f}{2} = \sqrt{\frac{1+e}{1-e}}\tan\frac{E}{2}. \tag{2.9}$$

This equation is very convenient in the use of coordinate conversion procedures. It avoids quadrant ambiguities for the angles involved, and is numerically stable even for small values of the eccentricity. The final equation of time evolution is given by *Keplers equation*

$$M \equiv n(t - \tau) = E - e \sin E, \tag{2.10}$$

where τ is the *time of pericenter passage* (or periastron date, if we consider planets in exoplanetary systems) and M the *mean anomaly* and have the interpretation of the angular displacement of a fictitious point mass moving at the mean angular rate n.

To summarize, the position at a particular time for a given orbit with semimajor axis a and eccentricity e is calculated as follows. Knowing M for the time t, and the eccentric anomaly E from solving Keplers equation, the position $r(t)$ and $f(t)$ are given by equations (2.8) and (2.9). Keplers equation is transcendental in the unknown variable E and obtaining a closed-form expression for E as a function of time, is impossible. Many attempts for its solution have been given over the past many years (Colwell, 1993) leading to modern developments of mathematics as a spin-off effect. Today, the solution is trivial using modern computers. In a later section, I consider a numerical solution based on the method of successive approximations by solving Kepler's equation iteratively using e and $M(t)$ as input parameters.

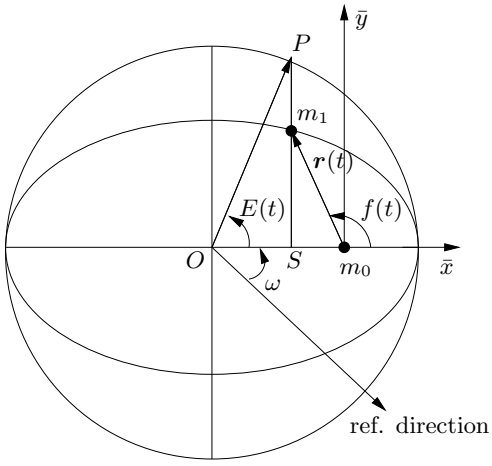

Figure 2.1: Geometric introduction of the eccentric anomaly. The fundamental reference system, is the orbit plane coordinate system $\bar{O}(\bar{x}, \bar{y})$.

2.2.2 Closed f and g expressions

In order to analytically determine the orbital position and velocity of a planet at a given time from initial coordinates and velocity components, we utilize the so-called closed f- and g-series, as originally invented by C. F. Gauss (originally, Gauss used the so-called f- and g-functions and for practical calculations these functions were truncated up to a desired order of accuracy). For any set of initial conditions, the f- and g-series represents an analytic closed solution to the two-body Kepler problem at any instant of time. Since these closed forms do not suffer from series truncation error, they maintain their accuracy when the computed position and velocities are separated by long intervals of time. The use of these functions needs a knowledge of the semimajor axis a, eccentricity e and the eccentric anomaly E, which can be provided by appropiate coordinate transformations and the numerical solution of Kepler's equation. Within this thesis, an important application of the f- and g- functions, is the testing of the accuracy of my numercial integration algorithm against known analytic solutions. The following algorithm is implemented as a subroutine within `FORTRAN90` and I list the source code in appendix A.1. A discussion of the equations of the f- and g- series and their derivation is given in nearly any book on celestial mechanics. The following treatment is based on Boulet (1991) and any details are referred within it.

Let $\boldsymbol{r}_0 = \boldsymbol{r}_0(t_0)$ and $\boldsymbol{v}_0 = \boldsymbol{v}_0(t_0)$ denote the Cartesian position and velocity vectors at time t_0 of a point mass in Keplerian motion. Then if $\boldsymbol{r}(t)$ and $\boldsymbol{v}(t)$ are the position and velocity vectors at any time t, there exists unique scalars f and g such that

$$\boldsymbol{r}(t) = f(t,t_0)\ \boldsymbol{r}(t_0) + g(t,t_0)\ \boldsymbol{v}(t_0), \tag{2.11}$$

$$\boldsymbol{v}(t) = \frac{\partial f(t,t_0)}{\partial t}\ \boldsymbol{r}(t_0) + \frac{\partial g(t,t_0)}{\partial t}\ \boldsymbol{v}(t_0). \tag{2.12}$$

The f-function have the property of being dimensionless, whereas g has the dimension of time. Both scalars plays the role of mapping a point mass's initial orbital state at time t_0, into a final state in the future at time t. A physical or geometrical interpretations for these functions does not exists and their introduction is of pure mathematical interest.

By splitting the problem into two parts, we first consider the position equation from which the velocity equation is easly obtained by time differentiation. Considering equation 2.11 in its component form,

$$x(t) = f(t,t_0)\ x_0 + g(t,t_0)\ \dot{x}_0, \tag{2.13}$$

$$y(t) = f(t,t_0)\ y_0 + g(t,t_0)\ \dot{y}_0, \tag{2.14}$$

where we have taken $\boldsymbol{r}_0 = (x_0, y_0)$ and $\boldsymbol{v}_0 = (\dot{x}_0, \dot{y}_0)$, we can solve this set of two simultanious linear equation for the scalar functions f and g and have

$$f(t,t_0) = \frac{1}{h}\Big(x(t)\ \dot{x}(t_0) - y(t)\ \dot{x}(t_0)\Big), \tag{2.15}$$

$$g(t,t_0) = \frac{1}{h}\Big(y(t)\ x(t_0) - x(t)\ y(t_0)\Big), \tag{2.16}$$

where $h = x(t_0)\ \dot{y}(t_0) - y(t_0)\ \dot{x}(t_0)$ measures the magnitude of the orbital angular momentum and is assumed to be non-zero. By the geometry and kinematical aspects of a particle in an elliptic orbit, as discussed in previous sections, the quantities $x(t), y(t), x(t_0), y(t_0)$ and $\dot{x}(t_0), \dot{y}(t_0)$ can be expressed in terms of the eccentric anomaly $E = E(t)$ and $E_0 = E(t_0)$ and we have the final closed form for the f- and g-functions and its time-derivative by the following relations

$$f(t,t_0) = \frac{a}{|\boldsymbol{r}_0|}\Big(\cos(E - E_0) - 1\Big) + 1, \tag{2.17}$$

$$g(t,t_0) = (t - t_0) + \frac{1}{n}\Big(\sin(E - E_0) - (E - E_0)\Big), \tag{2.18}$$

$$\frac{\partial f(t,t_0)}{\partial t} = -\frac{a^2 n}{|\boldsymbol{r}||\boldsymbol{r_0}|}\sin(E - E_0), \tag{2.19}$$

$$\frac{\partial g(t,t_0)}{\partial t} = \frac{a}{|\boldsymbol{r}|}\Big(\cos(E - E_0) - 1\Big) + 1. \tag{2.20}$$

In addition, the f- and g-functions and their derivatives can also be expressed in terms of the true anomaly by using eq. (2.8).

In practice, the computation of a future position and velocity at time t requires the knowledge of the initial conditions in terms of the elements $a, e, \omega, M(t_0)$ at time t_0. If the initial conditions are given in Cartesian coordinates, it will be necessary to transform then into Kepler elements. From equations (2.17)-(2.20), again we see that the main task is the computation of the eccentric anomaly from Kepler's equation. In addition, the initial timestep $\Delta t = t - t_0$, can be chosen arbitrary large without a reduction of accuracy (Mikkola, *private communication*, 2004). This completes the statement of the two-body problem having an analytic closed-form solution.

2.2.3 The orbit in space

Planetary motion is not confined to a fixed plane and the general motion of a point mass in three-dimensional space must be considered. The orientation of the orbit with respect to some reference plane, is determined by three angular elements. We refer to Fig.2.2 for a graphical representation of these elements.

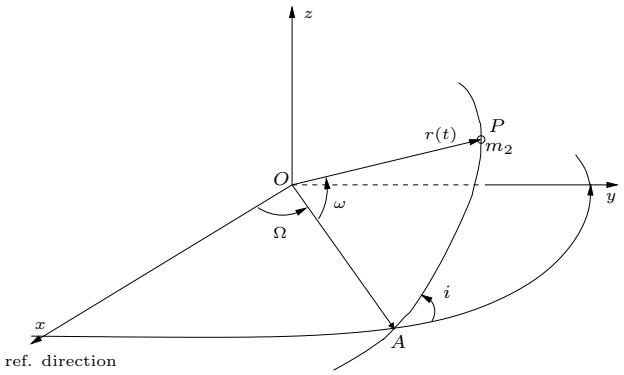

Figure 2.2: Graphical representation of the orbit in space. The line of intersection OA, is the direction of the ascending node or line of nodes. P denotes the pericenter and the line segment OP, is called the apsidal line. The point A is denoted as the ascending node.

Introducing a general coordinate system, the *orbital inclination*[2] i, is measured with respect to the (x, y)-plane and is defined within $0 \leq i \leq \pi$ in radian measure. The 2π periodic angle Ω, measured clockwise from the positive $x-$direction is the *longitude of ascending node*. Finally, we have the *argument of pericenter* ω, measured from the line called *ascending node* representing a line of intersection between the two planes involved. To fix ideas, the reference plane is defined as the orbital ecliptic plane of the Earth. The reference direction is then taken as the vernal equinox. As a result of precession and nutation the reference plane and direction is changing over time. Planetary motion is then referred to the mean ecliptic and equinox at a given epoch (usually taken as J1950 or J2000).

For reasons of avoiding singularities[3] within the classic set of elements, we introduce non-singular variables defined by (Murray and Dermott, 1999)

$$\varpi = \Omega + \omega \tag{2.21}$$

$$\lambda(t) = M(t) + \omega + \Omega. \tag{2.22}$$

While the former is called *longitude of perihelion* or *apsidal longitude* the latter is called the *mean longitude*. From this definition, the set $(a, e, i, \varpi, \Omega, \lambda(t))$ equally determines the position and velocity of a point mass.

In summary, the instantanouse position and velocity of a celestial point mass in space is determined by the following sets of orbital elements: $(a, e, i, \omega, \Omega, M(t, \tau))$ or $(a, e, i, \varpi, \Omega, \lambda(t))$. These elements are known as *osculating classic Kepler elements* or non-singular elements and reflects the phase space state of a point mass at an

[2]not to be confused with the line-of-sight inclination mentioned within chapter 1

[3]example: if $i = 0$, ω and M are not defined.

osculating time t. In chapter 3, we will consider the time variation of these elements under the action of a perturbating force. The osculating orbit is represented by the Kepler orbit of a point mass, if all perturbations were suddenly dissapearing.

2.3 Numerical solution of Kepler's equation

In the following, we return to a discussion on the solution of Kepler's equation using an iterative approach based on a Taylor series approximation. Our motivation for solving Kepler's equation is explained by the fact that general orbital dynamics require a large number of solutions to be calculated within numerical integrations. Procedures for coordinate transformation and the use of f- and g-functions are depending on a solution of Kepler's equation. The following algorithms are based on Danby (1988), urging the reader to perform numerical experiments as an exercise for the development of intuition and a necessary insight for possible numerical limitations for applications within orbital dynamics. We will take his word for good and conduct numerical experiments in the following discussion.

For a point mass in orbit with eccentricity e, and mean anomaly M, Keplers eq. (2.10) can be rewritten as

$$f(x) = x - e\sin(x) - M = 0, \tag{2.23}$$

and is identified as beeing nonlinear in x, i.e. no closed-form solution exists for which $E = E(M)$ can be written. Methods of numerical analysis provides iterative techniques for which a solution $E = x$ is determined by generating a sequence of approximations $\{x_n\}$, $n = 0, 1, 2, \ldots$. Three iterative methods will be considered and investigated for various input parameters. In general, we are interested in an algorithm which 1) converge to a solution and 2) is fast converging. This raises the following questions: for which values of (M, e) is convergence established, and how is the initial guess $x_0 = E_0$ to be chosen?

Let ϵ_n denote the error of the approximation x_n to the actual solution E, then $\epsilon_n + x_n = E$ and we generate a Taylor series expansion for $f(x)$ by

$$f(x) = f(x_n) + \epsilon_n f^{'}(x_n) + \frac{1}{2}\epsilon_n^2 f^{''}(x_n) + \frac{1}{6}\epsilon_n^3 f^{'''}(x_n) + \cdots = 0. \tag{2.24}$$

Finding iterative procedures using a Taylor series approach is practical, since high order derivatives of $f(x)$ are easily obtained from Kepler's equation. Retaining terms upto $\mathcal{O}(\epsilon_n)$, we have the first well known *Newton-Raphson* iterative procedure for $n = 0, 1, 2, \cdots$

$$x_{n+1} = x_n + \delta_n, \quad \text{with} \quad \delta_{n,1} \equiv x_n - \frac{f(x_n)}{f^{'}(x_n)}. \tag{2.25}$$

Retaining terms upto $\mathcal{O}(\epsilon_n^2)$ and using the symbolic notation $f(x_n) = f_n$, we get *Halley's* method defined as

$$x_{n+1} = x_n + \delta_{n,2}, \quad \text{with} \quad \delta_{n,2} \equiv -\frac{f_n}{f'_n + \frac{1}{2}\delta_n f''_n}. \tag{2.26}$$

Finally, considering terms upto $\mathcal{O}(\epsilon_n^3)$, we get a fourth order extension of Newtons method known as *improved Halley's* method and defined as

$$x_{n+1} = x_n + \delta_{n,3}, \quad \text{with} \quad \delta_{n,3} \equiv -\frac{f_n}{f'_n + \frac{1}{2}\delta_{n,2} f''_n + \frac{1}{6}\delta_{n,2}^2 f'''_n}. \tag{2.27}$$

Instructions for the algorithms 2.25-2.27, have been implemented within the IDL programming language and a complete program listing can be found within appendix A.4.

Each iteration algorithm have been investigated for convergence by considering the number of iterations $N = N(M, e)$ on a 70×70 grid of the (M, e) parameter space, where $0 \leq e < 1$ and $0 \leq M < 2\pi$. Each iteration procedure is repeated, until a solution is determined to a given desired accuracy given by $\texttt{ABS}(f_{n+1} - f_n) < \texttt{eps} = 10^{-12}$ using double precision[4] arithmetic or, terminated if a maximum number of iteration of $N = 20$ have been exceeded. The general tactics of choosing initial

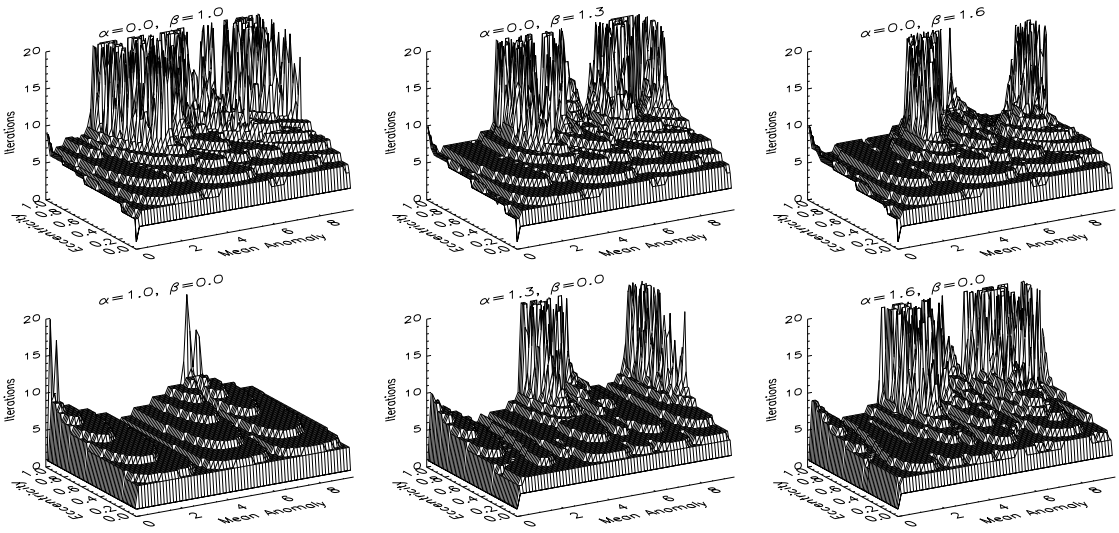

Figure 2.3: Plots showing the number of iterations required by solving Keplers equation, depending on the (M, e) plane for $(\alpha, \beta) = (0.0, 1.0); (0.0, 1.3); (0.0; 1.6)$ using the Newton-Raphson iteration algorithm (upper panel) and for $(\alpha, \beta) = (1.0, 0.0); (1.3, 0.0); (1.6, 0.0)$ (lower panel).

[4]Choosing `eps` larger than the machine precision

guesses of $x_0 = E_0$, is of the form

$$E_0^{i,j} = \alpha M_i + \beta e_j \quad \text{for} \quad i, j = 1, \cdots, 70, \tag{2.28}$$

where α, β are arbitrary real valued scalars to be determined experimentally for best convergence/performance.

A large range of the set (α, β) has been investigated for each algorithm, by plotting the iteration number N as a function of initial starting guess $E_0^{i,j}$. The best combination of (α, β) is then used to compare the different methods. In order to demonstrate the dependence of the number of iteration on α, β, a selection of surface plots for Newton's and the improved Halley's method are shown in Fig.2.3 and 2.4. Within these plots the range of M has been extended to 3π to demonstrate the 2π periodic nature of the problem. In general, my numerical trials for each iteration algorithm are much more extensive than those shown.

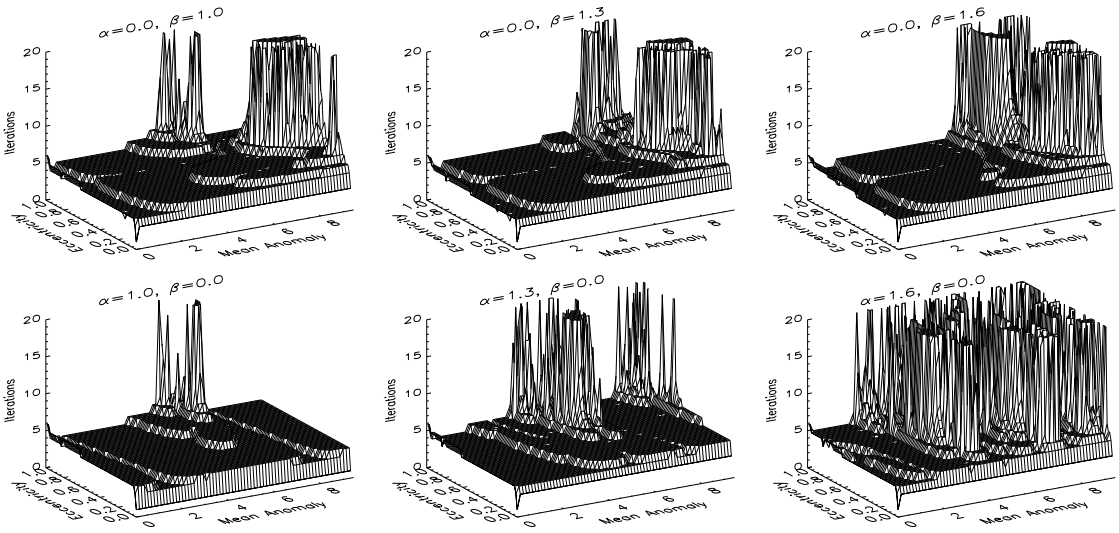

Figure 2.4: Plots showing the number of iterations required by solving Keplers equation, depending on the (M, e) plane for $(\alpha, \beta) = (0.0, 1.0); (0.0, 1.3); (0.0; 1.6)$ using the improved Halley's iteration algorithm (upper panel) and for $(\alpha, \beta) = (1.0, 0.0); (1.3, 0.0); (1.6, 0.0)$ (lower panel).

Considering Newton's algorithm for $\alpha = 0$, from Fig.2.3 it is seen that a larger area of the (M, e) plane begins to converge for increasing values of β. Conversely, for $\beta = 0$ and increasing α, we observe the effect of increasing the number of iterations around the "large-e, large-M" region. On average the Newton-Raphson method reaches convergence within 12 iterations. For the improved Halley's algorithm, convergence is also observed to be dependent on the initial choice of (α, β). For $\alpha = 0$ and increasing β, Fig.2.4 (upper panel) shows a dissapearing of a divergent area within

$(M = 2\pi, \text{high} - e)$. Conversely, for $\beta = 0$ and increasing α, we observe a clear decrease in the number of converging iterations (lower panel). On average this method reaches convergence within 5 iterations. This is explained by the fact, that higher order terms from the Taylor series approximation have been included into the algorithm. For both algorithms, diverging sequences have been observed for large values of the eccentricity and mean anomaly ($M = 0$ or $M = 2\pi$).

Since the improved Halley's method is clearly outperforming Newton's method, we focused on the determination of a best choice of the (α, β) parameters for the Halley's method. Several trials have found $\alpha = 1.0, \beta = 1.0$ to be the best combination for the initial starting value of the eccentric anomaly, in order to ensure a fast convergence for the $\texttt{ABS}f < \texttt{eps}$ criterion. Fig.2.5 shows the corresponding surface- and iso-iteration contour plot. Convergence within 5 iterations is established almost all over the (M, e) space. For some large-e, small-M, no convergence is established and divergent iterations are possible leading to no solution of Kepler's equation at all.

We conclude this section by stating that Halley's method is our method of choice for solving Kepler's equation. It is the fastest method and almost applicable for most of the (M, e) parameter region for a determination of a solution. A limitation of the algorithm is observed only for the high eccentric, low-M parameter region. Since we are only considering low eccentric ($e < 0.5$) orbits, this will have no effect and convergence is guaranteed within this range.

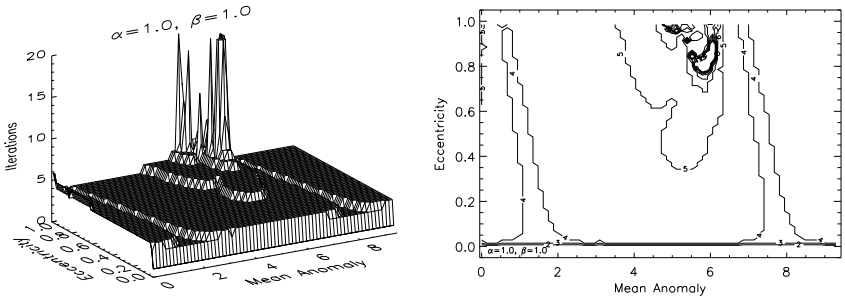

Figure 2.5: Left: iteration surface plot. Right: "iso-iteration" contour plot. Total number of gridpoints is $70 \times 70 = 1400$, where $M \in [0.0, 3\pi]$ and $e \in [0.0, 1.0]$. The maximum number of iterations has been set to 20 and the accuracy parameter has been chosen to be $\texttt{eps} = 10^{-12}$.

2.4 Delaunay variables

Modern aspects of celestial mechanics uses the Hamiltonian formulation (Goldstein, 1980) for the motion of a point mass within a gravitational potential. Within this

formulation the independent variables of the problem are canonical variables. A special class of canonical variables for an integrable problem are action-angle variables. For the two-body problem such a set of canonical action-angle variables are the so-called *Delaunay variables*. Expressed in terms of the classic elements they are (Morbidelli, 2002a) given by

$$\begin{array}{lcllcl} L & = & \sqrt{\mu a} & l & = & M \\ G & = & L\sqrt{1-e^2} & g & = & \omega \\ H & = & G\cos i & h & = & \Omega \ . \end{array} \tag{2.29}$$

The physical information within the action variables are: orbital energy ($L \leftrightarrow a$), magnitude of orbital angular momentum ($G \leftrightarrow a, e$) and magnitude of the z-component of orbital ang. momentum ($H \leftrightarrow a, e, \cos i$).

Using Delaunay's variables the two-body Hamiltonian is then only a function of the action variables and given by

$$\mathcal{H} = -\frac{k^2(m_0+m_1)^2}{2L^2}. \tag{2.30}$$

The corresponding Hamiltonian two-body equation of motion are then given by

$$\frac{dL}{dt} = -\frac{\partial \mathcal{H}}{\partial l}; \qquad \frac{dG}{dt} = -\frac{\partial \mathcal{H}}{\partial g}; \qquad \frac{dH}{dt} = -\frac{\partial \mathcal{H}}{\partial h} \tag{2.31a}$$

$$\frac{dl}{dt} = \frac{\partial \mathcal{H}}{\partial L}; \qquad \frac{dg}{dt} = \frac{\partial \mathcal{H}}{\partial G}; \qquad \frac{dh}{dt} = \frac{\partial \mathcal{H}}{\partial H}. \tag{2.31b}$$

Since $\mathcal{H} = \mathcal{H}(L)$, the only quantity changing linearly in time is the mean anomaly $\dot{l} = n = \sqrt{\mu/a^3}$. The remaining angle and action variables for the two-body problem are constants of motion.

2.5 Summary

In this chapter, we have introduced basic concepts of the two-body Kepler model. Different types of possible orbits have been reviewed and some aspects regarding their kinematics considered. The osculating classic elements are introduced reflecting fundamental geometric properties of the motion in space. Numerical methods for a solution of Keplers equation have been discussed and analysed with the result that only high eccentric orbits could lead to numerical instabilities. The solution of Keplers equation enables the calculation of an analytic solution of the two-body problem using the closed-form f- and g-functions.

Chapter 3

Aspects of Planetary Perturbation Theory

3.1 Introduction

Historically, celestial mechanics is one of the oldest fields within the physical sciences and has originally emerged from a pure mathematical community. The quest to understand the motion of the planets and their future evolution within the Solar System, was initiated by the formulation of the $1/r^2$-force law introduced by Newton in 1766. Since then, famous mathematician like Laplace, Lagrange, Gauss and Poincaré[1] contributed to the development of celestial mechanics and in particular to the theory of planetary perturbation. Consequently, much of the present day litterature on celestial mechanics is formulated in an extensive mathematical language hard to penetrate for a less mathematical oriented physicist, who frequently finds himself in a *Definition - Proposition - Lemma - Theorem - Proof* enviroment, when performing a litterature survey. Today, the equations of motion appearing within celestial mechanics problems, are generally treated within the field of non-linear dynamical systems leading to the ultimate consequence of chaotic motion.

In modern times planetary perturbation theory has developed into two distinct branches: *classic perturbation theory* and *canonical perturbation theory*. Both formulations aims to find approximate analytic solutions (future phase state) of the planetary problem. According to perturbation techniques, the solution is represented by the first few terms of an *asymptotic expansion*. In general, the expansion

[1]To my opinion, Poincaré marks the transition of one school to another by his publication of *Les Méthodes nouvelles de la Mécanique céleste* at the turn of the 19th century. While Laplace, Lagrange, Gauss were the dominating figures in the 19th century shool of celestial mechanics, famous modern contributers like Birkhoff, Smale, Hénon and Kolmogorov marked the first half of the 20th cenury. The monograph by (Barrow-Green, 1996) is interesting reading for an illustration of the work contributed by Poincaré who revolutionized the science within non-linear dynamics.

is carried out in terms of a small parameter which appears natural for the problem at hand. For example, planetary problems involving small masses on circular orbits, the expansion parameters are usually taken to be μ or e. Thus, perturbation methods are series solutions in a small parameter. A major difficulty in both formulations, is the problem of convergence of the series involved. Following Poincaré and his expansion theorem, these series solutions do not converge for $t \to \infty$. This non-uniform convergent nature of the series solutions limits the predictive ability of the analytic theory. *Series solutions are only valid within a limited range of time.* At this point modern celestial mechanics applies numerical methods in order to explore the long-term behavior of a given planetary problem. However, for a complete understanding of a given dynamical system analytic and numerical methods should follow each other hand in hand on a complementary basis. Long term numerical simulations opens the phenomenological questions and analytic theory attempts to give answers based on the underlying dynamics of the problem.

Although the emphasis within this thesis is on the numerical exploration of the equation of motion of the three-body problem, I outline some basic aspects of the analytic theory of planetary perturbations. No attempts will be made to develop an analytic or semi-analytic theory of planetary motion. This would involve a laborious work, which could form the basis of a distinct thesis of its own. Instead, we consider the perturbed two-body problem, which forms the basic step in developing a perturbation theory and introducing fundamental concepts. Perturbed two-body motion is formulated using the three-body model using Jacobi coordinates. The mutual gravitational interactions are described by the perturbation function $\mathcal{R}_{ij}$, and we will consider some of its properties. The time evolution of the classic Kepler elements of a given planet are introduced by the Lagrange equations using Delaunay's canonical elements. Finally, we discuss the time variation of the Kepler elements by applying a disturbing force.

3.2 The three-body problem

3.2.1 Formulation of the problem

The basic model is the three-body problem. Within the classic formulation of Newtonian mechanics, we consider $N = 3$ point masses P_i, where $1 \leq i \leq N$ with masses m_i at position $\boldsymbol{\rho}_i = (x_i, y_i, z_i) \in \mathbb{R}^3$ in an inertial (barycentric) reference frame with origin O.

The gravitational force of attraction of body P_i acting upon body P_j ($1 \leq j \leq N : i \neq j$) is given by

$$\boldsymbol{F}_j \;=\; -k^2 \frac{m_i m_j}{|\boldsymbol{\rho}_j - \boldsymbol{\rho}_i|^3} \, (\boldsymbol{\rho}_j - \boldsymbol{\rho}_i). \tag{3.1}$$

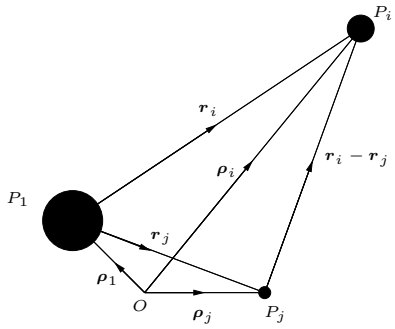

Figure 3.1: Inertial ($\boldsymbol{\rho}$) and heliocentric ($\boldsymbol{r}$) coordinates of the three-body problem. For our purpose P_1 is identified as the central host star.

In general, the total force acting upon P_j by the $N-1$ other masses is

$$\boldsymbol{F}_j \;=\; -k^2 \sum_{\substack{i=1 \\ i\neq j}}^{N} \frac{m_i m_j}{|\boldsymbol{\rho}_j - \boldsymbol{\rho}_i|^3}\,(\boldsymbol{\rho}_j - \boldsymbol{\rho}_i) \tag{3.2}$$

If no other forces are present the *barycentric equation of motion* of P_j can be written in vector form

$$\frac{d^2\boldsymbol{\rho}_j}{dt^2} \;=\; -k^2 \sum_{\substack{i=1 \\ i\neq j}}^{N} \frac{m_i}{|\boldsymbol{\rho}_j - \boldsymbol{\rho}_i|^3}(\boldsymbol{\rho}_j - \boldsymbol{\rho}_i), \tag{3.3}$$

which forms a set of 9 non-linear second order differential equations defining the three-body dynamical system (within the classical Hamiltonian formulation, the system is said to be of order 18). To determine the future evolution of P_j is equivalent to finding a solution $\boldsymbol{\rho}_j$ for a given set of initial conditions. The behavior of a given solution of equation 3.3 constitutes the main problem within this thesis which is to study the dynamical structure for a given range of initial conditions. Any attempt to solve this equation requires a method of numerical integration: the equation of motion must be discretized, that is, continuous variables are replaced by those calculated at discrete intervals in time and with finite time steps as opposed to the infinitesimal limit. For now, we postpone this discussion to chapter 4, and proceed our basic treatment of the three-body problem.

3.2.2 Integrals of motion and integrability

Historically, any attempt to find a solution to equation 3.3 were commonly approached by obtaining a sufficient rich set of first integrals, which are real-valued functions constant along any solutions in $(\boldsymbol{\rho}_j, \dot{\boldsymbol{\rho}}_j)$-phase space. The formulation of a

closed analytic solution for a $3N$-degree of freedom system requires the existence of $6N$-integrals of motion. First integrals imposes algebraic constraints on the motion of the system. Each constant of motion eliminates a phase-space coordinate and reduces the dimension of the problem by one. From a geometric point of view, a first integral foliates phase space into a $(3N-1)$ hyperplane. For any initial condition at time $t = t_0$, the motion is restricted to stay on the hyperplane for all times $t > t_0$. In the case of the existence of multiple first integrals the motion takes place on the locus of points defined by the intersections of the hyperplanes embedded in phase space.

In the previous section, it was shown that the (reduced) two body problem is a completely integrable dynamical system, for which we could find a complete analytical solution of the orbit in time. The non-existence of a closed analytic solution (or the non-integrability) of the three body problem has been shown by Poincaré and others[2] using reduction techniques based on canonical transformations. They showed that only 10 first integrals (algebraic independent of each other or sometimes called 10 involutive integrals) exist (Danby, 1988). Further studies within dynamical systems theory (involving the Ziglin theorem) showed that nonintegrability is intimately related to the appearance of chaotic dynamics (Morbidelli, 2002a, p.88) - a property to be discussed later.

Center of mass integral: For a $N = 3$-body system the center of mass can be written as

$$\sum_{i=1}^{N} m_i \boldsymbol{\rho}_i = \boldsymbol{a}t + \boldsymbol{b}, \tag{3.4}$$

where $\boldsymbol{a}, \boldsymbol{b}$ are constants of motion. Thus, the center of mass of the three-body system either remains at rest or moves uniformly within inertial space.

Integral of areas: By Kepler's 2nd law of planetary motion the conservation of angular momentum can be written as

$$\sum_{i=1}^{N} m_i \boldsymbol{\rho}_i \times \dot{\boldsymbol{\rho}}_i = \boldsymbol{h}, \tag{3.5}$$

where $\boldsymbol{h}$ is the total angular momentum and the quantity $(\boldsymbol{\rho}_i \times \dot{\boldsymbol{\rho}}_i)$ is the projection of the areal velocity of the ith body on the orbit planes.

Energy integral: The final and 10th constant of motion is the total energy of the three-body problem (conservative system) given by

[2]sometimes the credit is given to H. Bruns, (Whittaker, 1999, chap.XIV)

$$E = \frac{1}{2}\sum_{i=1}^{N} m_i \dot{\boldsymbol{\rho}}_i^2 - k^2 \sum_{i<j}^{N} \frac{m_i m_j}{\rho_{ij}}, \tag{3.6}$$

where k^2 is the Gaussian gravitational constant. Both the angular momentum and energy integral are important diagnostic parameters, to test the numerical accuracy/validity of a given numerical solution.

3.2.3 Jacobi coordinates

When considering an hierarchical few-body problem like the three-body problem or a general n-body planetary problem, the most natural coordinates to use are the Jacobian coordinates. This set of coordinates is especially useful for the construction of numerical solution algorithms of the planetary problem. In chapter 6, we consider numerical integration algorithms mainly formulated on the basis of Jacobi coordinates.

The Jacobian coordinates are defined recursively with respect to the center of mass of the hierarchical subsystem. Considering the general case, the Jacobian position of the *ith* planet is defined relative to the center of mass of the remaining $i-1$ subsystem. Fig. 3.2 shows the Jacobian coordinates of a four-planet hierarichal planetary configuration.

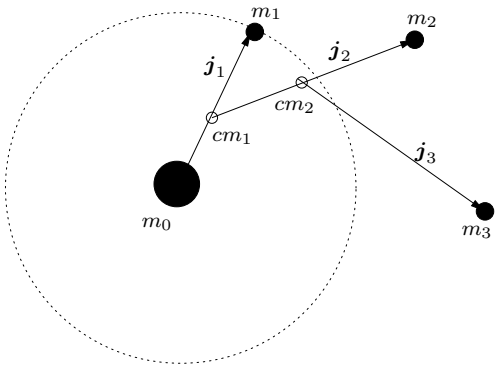

Figure 3.2: Jacobi coordinates (j_1, j_2, j_3) for the four-body planetary problem. A given Jacobi position (velocity) is measured with respect to the center of mass of the subsystem. cm_1 and cm_2 denotes the position of the center of mass of m_0, m_1 and m_0, m_1, m_2, respectively. The figure is partially reproduced from Murray and Dermott (1999, p.442).

Murray and Dermott (1999) gives relations between the Jacobian and heliocentric coordinates and velocities of a given n-body planetary system. Denoting the heliocentric coordinates as $(\boldsymbol{r}, \boldsymbol{v})$, we have the following transformation equations for the ith planet

$$\boldsymbol{r}_i = \Big(\frac{\eta_{i-1}}{\eta_i}\Big)\boldsymbol{j}_i - \sum_{j=i+1}^{n-1}\Big(\frac{m_j}{\eta_j}\Big)\boldsymbol{j}_j \quad (0 < i < n-1), \tag{3.7}$$

$$\boldsymbol{v}_i m_i = \boldsymbol{j}_i m_i - \sum_{j=i+1}^{n-1}\Big(\frac{m_i}{\eta_{j-1}}\Big)\boldsymbol{j}_j \qquad (0 < i < n-1), \tag{3.8}$$

where $\eta_i = \sum m_i$ is the total mass of the system. A special case in which the two sets of coordinates are identical is the two-body motion. The reason to denote Jacobi coordinates as a more natural set of independent variables, is based on the fact that the natural motion is the common motion about the center of mass within an intertial reference system. In Fig. 3.2, m_2 is not orbiting the star with mass m_0, but the center of mass of the combined masses m_0+m_1. In that respect, perturbation theory expressed in Jacobian variables approximates the real planetary motion better than heliocentric coordinates.

3.3 Planetary perturbations

3.3.1 $\mathcal{R}_{ij}$ - the perturbation function

Although no closed form analytic solution for the three-body problem exist, we can approach the problem by using the techniques of perturbation theory. The main idea is the treatment of the three-body problem as a perturbed two-body problem. By changing coordinates $(\boldsymbol{\rho}, \dot{\boldsymbol{\rho}}) \rightarrow (\boldsymbol{r}, \boldsymbol{v})$ to heliocentric coordinates the *relative equation of motion* of P_j is (Murray and Dermott, 1999, p.227)

$$\frac{d^2\boldsymbol{r}_j}{dt^2} = \nabla_j\big(U_j + \mathcal{R}_{ij}\big), \tag{3.9}$$

where

$$U_j = k^2\frac{(m_0+m_j)}{|\boldsymbol{r}_j|} \qquad \text{and} \qquad \mathcal{R}_{ij} = \frac{k^2 m_i}{|\boldsymbol{r}_i - \boldsymbol{r}_j|} - k^2 m_i\frac{\boldsymbol{r}_i\cdot\boldsymbol{r}_j}{|\boldsymbol{r}_i^3|}. \tag{3.10}$$

Here, U_j denotes the two-body Kepler potential and $\mathcal{R}_{ij} = \mathcal{R}_{ij}(m_i)$ denotes the perturbation potential or *perturbation function*. The first term in $\mathcal{R}_{ij}$ measures the direct perturbation potential of m_j due to the presence of m_i. The second indirect term, measures the back-reaction of the point masses on the central mass. It takes into account the motion of m_0 around the center of mass of the system due to the presence of the other masses within the non-inertial heliocentric reference system.

Following Murray and Dermott (1999, p.232), $\mathcal{R}_{ij}$ is periodic in the non-singular variables $(\varpi_i, \Omega_i, \lambda_i, \varpi_j, \Omega_j, \lambda_j)$ and can be expanded in a six-dimensional Fourier

series involving only cosine terms reflecting the periodic nature of planetary perturbations. Formally, this is written as

$$\mathcal{R}_{ij} = \mu_i \sum_{k,l,m}^{\infty} C_{klm} \cos(k_i\lambda_i + k_j\lambda_j + l_i\varpi_i + l_j\varpi_j + m_i\Omega_i + m_j\Omega_j), \tag{3.11}$$

where the summation[3] extends over all integer values of the indices $(k, l, m) = (k_i, \ldots, m_j)$ and μ_i denotes the mass parameter of the outer planet. The expansion is known as the Kaula-type development involving the ratio $\alpha = a_j/a_i$ as the small parameter to describe the perturbation by an outer planet on an inner one. The $C_{klm} = C_{klm}(\alpha, e_i, e_j, i_i, i_j)$-coefficients are evaluated in terms of power series of the eccentricity, semi-major axis and inclinations. If several point mass perturbations are necessary to be included, $\mathcal{R}_{ij}$ is replaced by a sum over all pairs of point masses. In practical problems the power series development of $\mathcal{R}_{ij}$ is complicated and best solved using symbolic computer algebra systems (*Maple* or *Mathematica*) in order to evaluate the C_{klm}-coefficients to any desired order.

Equation (3.10) allows an estimate of $\mathcal{R}_{ij}/U_j$ for our problem at hand. Considering the case of an Earth mass planet within HD70642 (at a mean distance 3 AU) the ratio of the perturbing potential to the two-body point mass potential is

$$\frac{\mathcal{R}_{ij}}{U_j} \sim \frac{7}{18}\frac{m_i}{1+m_j} \sim 4 \cdot 10^{-4}, \tag{3.12}$$

and thus, the two-body orbital elements are expected to be slowly periodic varying quantities.

3.3.2 Lagrange planetary equations

The time variation of the orbital elements of the perturbed body are formulated within *Lagrange planetary equations*. Together with a series expansion of $\mathcal{R}_{ij}$, they form the basic foundation of developing analytic theories within planetary dynamics. Recalling the canonical element of Delaunay $G = L\sqrt{(1-e^2)}$, and omitting any subscripts they are given by (Taff, 1985, p.308)

[3] m_i, m_j are not to be confused with mass parameters

$$\dot{a} = -\frac{2a^2}{\mu}\frac{\partial \mathcal{R}}{\partial M} \tag{3.13}$$

$$\dot{e} = -\frac{G^2}{\mu^2 e}\frac{\partial \mathcal{R}}{\partial M} - \frac{(1-e^2)}{eG}\frac{\partial \mathcal{R}}{\partial \omega} \tag{3.14}$$

$$\dot{i} = \frac{\csc i}{G}\Big(\cos i\frac{\partial \mathcal{R}}{\partial \omega} - \frac{\partial \mathcal{R}}{\partial \Omega}\Big) \tag{3.15}$$

$$\dot{\omega} = \frac{(1-e^2)}{eG}\Big(\frac{\partial \mathcal{R}}{\partial e} - \frac{e\cot i}{(1-e^2)}\frac{\partial \mathcal{R}}{\partial i}\Big) \tag{3.16}$$

$$\dot{\Omega} = \frac{\csc i}{G}\frac{\partial \mathcal{R}}{\partial i} \tag{3.17}$$

$$\dot{M} = \frac{2a^2}{\mu}\frac{\partial \mathcal{R}}{\partial a} + \frac{G^2}{\mu^2 e}\frac{\partial \mathcal{R}}{\partial e}. \tag{3.18}$$

A careful examination of these equation reveals a certain symmetry and allows a division of the equations into two groups. While the first three equations $(\dot{a}, \dot{e}, \dot{i})$ contain derivatives of the remaining elements (ω, Ω, M), the last equations $(\dot{\omega}, \dot{\Omega}, \dot{M})$ contain derivatives only of the first elements (a, e, i). This symmetry property is even more transparent within the canonical formulation of Hamiltonian dynamics.

3.3.3 Classes of perturbations

The solution of Lagrange equations requires an integration of the right hand side of eq. (3.13-3.18). Let η_j denote any orbital element, then the integration process produces an infinte series solution containing terms of the form

$$\eta_j(t) = \eta_j^0 + \sum \Big(A_{ij}t + \frac{B_{ij}}{(k_i n_i + k_j n_j)}\sin\big((k_i n_i + k_j n_j)t + C_{ij}\big)\Big), \tag{3.19}$$

where η_j^0 is determined by the initial conditions, A_{ij}, B_{ij}, C_{ij} are constants and n_i, n_j are the mean motions. The survival of the constants A_{ij}, B_{ij} depends on the order of the truncation of the series solution, which again depends on the required accuracy needed for a given problem. In general, high order corrections of the perturbed two-body orbit are reflected in large values of the summation indices. For the amplitude, we have $B_{ij} \to 0$ as $(k, l, m) \to \infty$.

Several classes of perturbation are generally distinguished and associated to a particular term within eq. (3.19). The action of each class of perturbation manifest itself in the time evolution of a given orbital element by modulating the initial η_j.Terms containing the sine-function are called *periodic*, where $\kappa_{ij} = k_i n_i + k_j n_j$ measures the frequency of the perturbation and $2\pi/\kappa$ is the corresponding perturbation period. If $2\pi/\kappa \gg 2\pi/n$ perturbations are called *long-periodic*, and if

$2\pi/\kappa \sim 2\pi/n$ the perturbations are called *short-periodic* for a given planet with mean motion n. Terms linear in time are called *secular* perturbations lineary modulating the time evolution of η_j causing the element to change without limit[4]. A special class of long-periodic perturbations are *resonant perturbations*. In the case when the mean motions of two planets are nearly commensurable with a ratio n_i/n_j expressible in small integers, then the corresponding frequency $\kappa_{ij} = 0$ and the period of the corresponding term becomes very large.

The designation of a specific class of perturbation does not imply the existence of several physical sources of perturbation potentials, rather it is a way to break down the total perturbation according to their variability in time (cf. Fig. 3.3). Only terms within the series solution of a Kepler element are attributed names according to a specific oscillatory property.

Considering the case of a near mean motion resonance two problems lead to difficulties. If $\kappa \sim 0$, then firstly the corresponding perturbation period term becomes large. Following the time evolution of η_j over a finite time, these super-long perturbation terms can hardly be distinguished from secular perturbations. Secondly, the amplitude B_{ij}/κ becomes undefined resulting in a small divisors problem for the convergence of the series solution in eq. (3.19), leading to difficulties for the development of analytic theories.

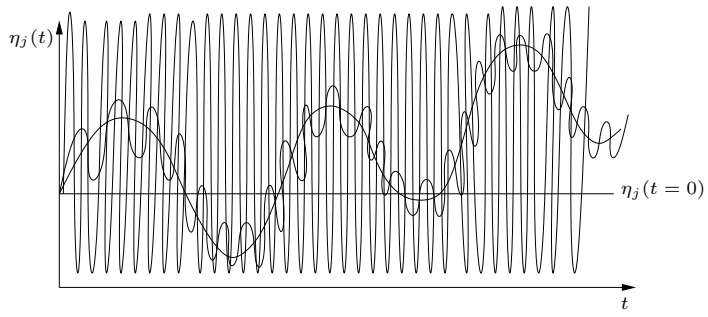

Figure 3.3: Illustration of the effects of the different types of perturbation terms. Three different periodic variations are shown: 1) a short-period, 2) a long-period and an intermediate periodic oscillatory variation, modulating the unperturbed η_j at time $t = 0$. The timescale of the short-periodic oscillation, is comparable to the orbital period. A secular effect is also added. Whether this is a *true secular effect* or a part originating from a long-period term within the expansion series is not decisive, and one needs to prolong the time interval for a further analysis.

[4]the presence or absence of a secular term lead Laplace to the first definition of stability and the stability of the Solar System in general.

3.3.4 Averaging principle

By introducing a perturbation into the two-body potential, i.e $U \rightarrow U + \mathcal{R}$, the Kepler elements are no longer constants of motion. They start to change with time at different frequencies according to the class of perturbation terms occuring in the series expansion of a given Kepler element. Very often and in particular within this thesis, we are mainly interested in long-periodic and secular features within the long-term solutions of a perturbed planet. Any contribution from short-periodic perturbations (or equivalently high-frequency perturbations) involving the mean anomaly M (or the mean longitudes λ) contains no information about the qualitative long-term dynamics. A common used technique (Wisdom, 1982, sec.II, for a historical review) to eliminate the unimportant short-period perturbations (associated to the fast angles) is to average the perturbation function over the mean anomaly. Using non-singular Kepler elements, this is formally written as (Murray and Dermott, 1999)

$$\langle \mathcal{R} \rangle (a, e, i, \varpi, \Omega) = \frac{1}{2\pi} \int_0^{2\pi} \mathcal{R}(a, e, i, \varpi, \Omega, \lambda)\ d\lambda, \tag{3.20}$$

and is known as the *averaging principle* in which $\langle \mathcal{R} \rangle$ only depends on the slow elements $(a, e, i, \varpi, \Omega)$. This principle assumes that perturbation effects of short-period terms will average to zero over long periods of time. Perturbations with periods longer than the *characteristic* orbital period of the system (longest orbital period) remain and forms the major dynamical features to investigate.

The averaging principle forms the starting point in developing analytic and semi-analytic theories of planetary motion. An important property of the averaging principle is the following (Gurzadyan, 2002, p.32): Averaging the the original equations (Lagrange planetary equations) of motion is equivalent to averaging the perturbation function. This leads to the historically important Laplace-Lagrange stability theorem, to be discussed in chap.5. However, within this thesis we consider solutions obtained by numercial integration of the full equations of motion. Necessarily, such a solution includes all the infinite number of short-period terms in the expansion of the perturbation function. Any secular trends within the solutions (displayed by a frequently sampled timeseries of Kepler elements) are likely to 'hide' within the short periods (cf. Fig. 3.3) and a Fourier analysis of the timeseries enables one to filter out the short-period contributions in order to detect secular variations.

3.3.5 Gauss's form of perturbations

The time variation of the elements $(a(t), e(t), i(t), \omega(t), \Omega(t), M(t))$ of a perturbed Kepler orbit are also obtained by considering the effect caused by the action of a small disturbing force

$$d\boldsymbol{F} = R\boldsymbol{e}_R + T\boldsymbol{e}_T + N\boldsymbol{e}_N, \tag{3.21}$$

where R, T, N are the radial, transverse and normal components of the applied perturbation force and R, T are embedded within the orbital plane and N normal to the orbital plane. The set $(\boldsymbol{e}_R, \boldsymbol{e}_T, \boldsymbol{e}_N)$ represents unit vectors centered within the orbit plane reference system. The applied force is assumed to be arbitrary (but small) and by definition includes more complex sources of perturbations. This formulation, known as Gauss form, is more general comparing to the Lagrange equations, which are valid only for perturbation forces derived from a conservative $\mathcal{R}_{ij}$. The decomposition of the action allows the identification of force components responsible for the change in a given orbital element. The resulting time variational equations are derived from first principles (Murray and Dermott, 1999, p.54 and references therein) and are given by

$$\dot{a} = \frac{2\ a^{3/2}}{\sqrt{\mu(1-e^2)}}\big(Re\sin(f) + T(1+e\cos(f)\big) \tag{3.22}$$

$$\dot{e} = \sqrt{a\mu^{-1}(1-e^2)}\big(R\sin(f) + T(\cos(f)+\cos(E))\big) \tag{3.23}$$

$$\dot{i} = \frac{rN\cos(\omega+f)}{h} \tag{3.24}$$

$$\dot{\omega} = \frac{1}{e}\sqrt{a\mu^{-1}(1-e^2)}\Big(-R\cos(f) + T\big(\frac{2+e\cos(f)}{1+e\cos(f)}\big)\sin(f)\Big) \tag{3.25}$$

$$\dot{\Omega} = \frac{rN\sin(\omega+f)}{h} \tag{3.26}$$

$$\dot{M} = \frac{\sqrt{a}(1-e^2)}{e\mu(1+e\cos f)}\Big(R(2e-\cos f - e\cos^2 f) + T\sin f(2+e\cos f)\Big). \tag{3.27}$$

Only forces embedded within the orbit plane can change a, e, ω, M and forces normal to the orbit plane can change i, Ω.

3.4 Summary

We have introduced the three-body problem and some of its properties regarding integrability and the exsistence of constants of motion. Fundamental concepts of perturbation theory were discussed leading to the construction of a solution of the perturbed two-body problem by series approximations. The corresponding time evolution equations are determined by Lagrange planetary equations. A formal integration of these equations enabled the identification of perturbation terms, naturally leading to the formulation of the averaging principle. Finally, we introduced a general small perturbation force and considered the effects of the force components on the time variation of the Kepler elements.

Chapter 4

Symplectic integration and numerical aspects

4.1 Introduction

In order to determine the time evolution of the planetary three-body system the equations of motion are solved using a numerical integration algorithm or a numerical map. The basic principle is to discretice time and advance the system state $(\boldsymbol{r}_i, \boldsymbol{v}_i)$ at some time t_i, to a future state $(\boldsymbol{r}_{i+1}, \boldsymbol{v}_{i+1})$ at time t_{i+1} using some solution operator Φ, representing the integration algorithm

$$(\boldsymbol{r}_{i+1}, \boldsymbol{v}_{i+1}) = \Phi_\tau(\boldsymbol{r}_i, \boldsymbol{v}_i), \tag{4.1}$$

with $\tau = t_{i+1} - t_i$ measuring the discretisation step size.

Early numerical simulations of Solar System dynamics (roughly before 1990) used classical integration techniques such as the Bulirsch-Stoer or Runge-Kutta algorithms (Press et al., 1996; Hiroshi and Hiroshi, 1989) characterised by their high accuracy performance but slow simulation speeds, since they require a small step size (and hence more iterations) to capture the relevant dynamics. Thus, the total integration time, using traditional techniques for the long-term integration of the Solar System, were constrained to a few percent of the total Solar System age.

Since then, research in numerical analysis and planetary dynamics has taken great advantage of increasing computer efficiency and of recent development of new integration techniques known as symplectic integration algorithms (SIAs) (see Morbidelli (2002b) for a historical review). These algorithms have the important property of global stability, by preserving fundamental geometric structures of Hamiltonian dynamical systems. In particular, SIAs have usually only oscillatory and not secular errors in the constants of motion. This allows the choice of a larger step size (reducing the number of iterations), enabling the extension of the total integra-

tion timespan and minimizing the long-term qualitative errors within the dynamical evolution.

Historically, the most famous results employing symplectic algorithms were obtained within Solar System dynamics at the beginning of the 1990s. An example is the study of the motion of the outer planets over a time period of 10^9 years performed by Sussman and Wisdom (1992), demonstrating the chaotic motion of Pluto. In addition, symplectic algorithms are widely used within stability analysis of multiple planet extrasolar planetary systems (Jones and Sleep, 2002).

Within this thesis two symplectic algorithms have been used for dynamical simulations of test particle stability. The first code, `MERCURY6`, is a user friendly multipurpose orbital integration software package. The code contains several integration algorithms, symplectic as well as non-symplectic (or hybrids) to perform n-body integrations to simulate planetary dynamics. Within the package the main symplectic integration algorithm is based on the Wisdom-Holman map (or Dirac δ-formulation). The code is well documented and contact (by mail) has been established to the author during the thesis period.

In addition, a second symplectic algorithm have been applied for long term numerical simulations of planetary dynamics. This code has been made kindly available to me by Seppo Mikkola[1] at the Turku University Observatory, Finland. The algorithm belongs to a class known as composit methods and special properties of this algorithm is the adaptive time-step ability and the fast execution speed at a high degree of accuracy. Although the details of the algorithm implemented within the code are considered as being 'within a black box', some elements on the theory of symplectic integration are discussed. The construction of the algorithm is based on a general Lie series formulation, and we will consider some of its aspects.

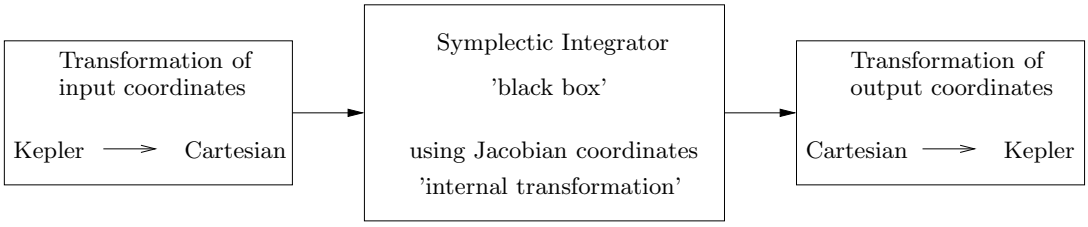

Figure 4.1: Flowchart of data during a single integration.

In addition, I have extended the code by developing and implementing routines for the transformation of coordinates (Kepler $\leftrightarrow$ Cartesian) as outlined in Fig. 4.1.

[1]Upon an initial request by e-mail in december 2004, Seppo Mikkola provided me the algorithm named `g3.f` written within the `Fortran77` programming language, together with the relevant literature reference and lecture notes on numerical celestial mechanics.

These routines represents an interface for the dataflow into and from the integration algorithm and are presented at the end of this chapter. The integrator itself uses internal Jacobian coordinates only. The necessary transformation from Cartesian to Jacobian (and the inverse transformation) are internal within the integrator environment using roughly the transformation equations within section 3.2.3.

4.2 Numerical symplectic integration

4.2.1 Phase space properties and symplecticity

The time evolution operator Φ_τ, or solution flow within phase space of a three body Hamiltonian system, is characterised by certain geometric properties forming the foundation for the construction of symplectic algorithms. In its basic formulation, the phase space solution flow is a canonical transformation constrained by conservation laws associated to certain symmetry principles. Like conservation of angular momentum is associated to a rotation symmetry, conservation of *oriented* differential area is associated to symplecticness (or symplecticity) symmetry. Traditional non-symplectic algorithms have the disadvantage of having no knowledge of these geometric constraints or symmetry properties with the effect of computing inaccurate numerical solutions. This effect is often recognized as numerical dissipation introducing non-physical phenomena. Therefore, it is desirable that a numerical method preserves as much of a systems underlying geometric principles. In the following, we list some basic properties of which the conservation of symplectic differential area is the most important one.

1. *Liouvilles Volume Theorem.* The most well known phase space property is the conservation of volume elements along the solution flow (Goldstein, 1980) within phase space, and forms the content of Liouvilles theorem. Formally, for a small differential volume element δV_n within a phase space region Ω of an n degree of freedom system, this is written as

$$\frac{d\delta V_n}{dt} = \frac{d}{dt}\int_\Omega d\boldsymbol{q} \cdot d\boldsymbol{p} = 0, \tag{4.2}$$

   where $(\boldsymbol{q}, \boldsymbol{p})$ are the canonical phase space coordinates of the system. A formal interpretation of Liuovilles result is, that conservation of phase space volume for a region enclosed by Ω. Along any solution curve this volume is a constant of motion for Hamiltons equation of motion. We call a volume preserving system as conservative system. An important property of conservative dynamical systems is, that no dissipation of energy occurs (determined by volume contraction or expansion) where the solution curve asymptotically evolves

to bounded regions of *limit cycles* known as attractors. Such dynamical regions are non-existent within the phase space of a conservative Hamiltonian dynamical system.

2. *Conservation of Energy.* The total energy of a time independent Hamiltonian system is conserved. This is a reformulation of the energy integral as discussed in section 3.2.2. Consider the Hamiltonian function $H = H(\boldsymbol{q}(t), \boldsymbol{p}(t))$, then the total time derivative of H is

$$\frac{dH}{dt} = \frac{\partial H}{\partial \boldsymbol{q}}\dot{\boldsymbol{q}} + \frac{\partial H}{\partial \boldsymbol{p}}\dot{\boldsymbol{p}} = \frac{\partial H}{\partial \boldsymbol{q}}\Big(-\frac{\partial H}{\partial \boldsymbol{p}}\Big) + \frac{\partial H}{\partial \boldsymbol{p}}\Big(\frac{\partial H}{\partial \boldsymbol{q}}\Big) = 0. \tag{4.3}$$

Thus, the Hamiltonian itself is a constant of motion and measures the total energy of the system. Considering the motion of a system in phase space the conservation of energy constrains the exact trajectory to a hypersurface due to the time translational symmetry of the Hamiltonian itself. The energy of a numerically computed trajectory will deviate from the initial Hamiltonian and the difference can be used as a measure of numerical accuracy.

3. *Conservation of the Symplectic Differential Area.* A more general result than Liouvilles theorem is the conservation of oriented differential area (Sanz-Serna and Calvo, 1994; Ott, 1993)

$$\frac{d}{dt}\big(\delta\boldsymbol{p}\ \delta\boldsymbol{q}' - \delta\boldsymbol{q}\ \delta\boldsymbol{p}'\big) = 0, \tag{4.4}$$

where $(\delta\boldsymbol{q}, \delta\boldsymbol{p})$ and $(\delta\boldsymbol{q}', \delta\boldsymbol{p}')$ are infinitesimal displacements from $(\boldsymbol{q}, \boldsymbol{p})$ forming an n-parallelogram within phase space. Symplectic symmetry is a measure of an *oriented* phase space volume element, projected onto the n coordinate planes (q_i, p_i).

4.2.2 A short review on composit methods

Following Goldstein (1980) the solution operator can be expressed using a Taylor series expansion about the initial conditions. This representation is known as the Lie series form for the exact time evolution of the three body Hamiltons equations of motion (canonical form of Lagrange equations), and is given by

$$\boldsymbol{\eta}(t_0 + \tau) = e^{\tau\tilde{\mathcal{H}}}\Big|_{t=t_0} \boldsymbol{\eta}(t_0) \tag{4.5}$$

where $\boldsymbol{\eta} = (\boldsymbol{q}, \boldsymbol{p})$ are the phase space coordinates (or the solution flow), τ the integration time step and $\tilde{\mathcal{H}} = \mathcal{H}_{Kepler} + \mathcal{H}_{int}$ is the system Hamiltonian separated

into a Keplerian part and an interaction part. From the discussion within chapter 3, the interaction Hamiltonian is identified with the perturbation function. In general, the series representation of $e^{\tau(\mathcal{H}_{Kepler}+\mathcal{H}_{int})}$ leads to practical difficulties and one needs to find an approximation for the computation of the solution operator.

Using the technique of operator splitting (Sanz-Serna and Calvo, 1994) the integration from t_0 to τ is given by the approximate operator

$$e^{\tau(\mathcal{H}_{Kepler}+\mathcal{H}_{int})} \approx \prod_{i=1}^{k} e^{c_i \tau \mathcal{H}_{int}} e^{d_i \tau \mathcal{H}_{Kepler}}, \tag{4.6}$$

where the numerical coefficients (c_i, d_i) are determined by some strategy using the Baker-Campbell-Hausdorff[2] identity. This approximation for a numerical solution is known as a composit method of order $\mathcal{O}(\tau^{k+1})$. The total solution flow is determined by the composition of different solution flows concatenated to one another. The numerical calculated solution flow differs from the true solution by an error introduced from the truncation of the BCH identity. This error is quantified by an error Hamiltonian $\mathcal{H}_{err}$ expressed by a formal power series in τ (Mikkola, 2004). It will be important when discussing error analysis and symplectic corrections.

Composit methods are also called general leapfrog methods and have some additional advantages beside being symplectic: 1) Small number of force evaluations per step. This considerably reduces the amount of CPU load, if the total number of planets (N) is large, as CPU time $\sim N^2$. 2) They are explicit methods, i.e no "warm-up" methods are needed. 3) No use of mixed variables, this reduces roundoff errors. 4) No intermediate variables needs to be stored, leading to a minimization of hardware memory.

A serious limitations of most composit methods is, that they are only valid for a constant timestep. This problem can be overcome by introducing a technique known as time regularisation involving the concept of extending phase space (Goldstein, 1980).

4.2.3 Mikkola's variable step Leap-Frog method

The integrator implementet within the `g3.f` code is a generalized leapfrog method of second order (Mikkola, 1997) with numerical coefficients $(c_1 = 0, d_1 = 1/2)$ and $(c_2 = 1, d_2 = 1/2)$ and given by the following concatenated solution operator

$$e^{\tau(\mathcal{H}_{Kepler}+\mathcal{H}_{int})} \approx e^{\tau/2\mathcal{H}_{Kepler}} e^{\tau\mathcal{H}_{int}} e^{\tau/2\mathcal{H}_{Kepler}}. \tag{4.7}$$

The leapfrog algorithm over a single step of length τ, consists of three substeps representing the numerical solution flow. Using the index notation to indicate the

[2]Considering two operators A, B the BCH identity says that $e^A e^B = e^{A+B+\frac{1}{2}\{A,B\}+\cdots}$ where $\{,\}$ are Poisson brackets.

time τ-change of the phase space coordinates, the solution operator stated in eq. (4.7) is interpreted as the following sequence of steps (Mikkola, 1997; Preto and Tremaine, 1999)

$$
\begin{aligned}
e^{\tau/2\mathcal{H}_{Kepler}}: \quad & (\boldsymbol{q}_i, \boldsymbol{p}_i, t_0) \rightarrow \left(\boldsymbol{q}_i + \frac{\tau}{2} \frac{\partial \mathcal{H}_{Kepler}}{\partial \boldsymbol{p}} \bigg|_{\boldsymbol{p}_i}, \boldsymbol{p}_i, t_0 + \frac{\tau}{2} \right) \\
e^{\tau \mathcal{H}_{int}}: \quad & (\boldsymbol{q}_{i+\tau/2}, \boldsymbol{p}_i, t_0) \rightarrow \left(\boldsymbol{q}_{i+\tau/2}, \boldsymbol{p}_i - \tau \frac{\partial \mathcal{H}_{int}}{\partial \boldsymbol{q}} \bigg|_{\boldsymbol{q}_{i+\tau/2}}, t_0 + \tau \right) \\
e^{\tau/2\mathcal{H}_{Kepler}}: \quad & (\boldsymbol{q}_{i+\tau/2}, \boldsymbol{p}_{i+\tau}, t_0 + \frac{\tau}{2}) \rightarrow \left(\boldsymbol{q}_{i+\tau/2} + \frac{\tau}{2} \frac{\partial \mathcal{H}_{Kepler}}{\partial \boldsymbol{p}} \bigg|_{\boldsymbol{p}_{i+\tau}}, \boldsymbol{p}_{i+h}, t_0 + \tau \right),
\end{aligned}
$$

where the $(\boldsymbol{q}, \boldsymbol{p})-$variables are considered to be Jacobi coordinates. The upper equation is referred to as step 1, the middle as step 2 and the lower equation as step 3. A graphical outline of the algorithm is shown in Fig. 4.2, where the stipulated line indicates the use of endpoints calculated from the preceeding subflow, as initial conditions to the following subflow.

First, the algorithm starts by moving the system along the osculating Keplerian ellipse under the action of the Kepler Hamiltonian $\mathcal{H}_{Kepler}$, over a half time step using the initial conditions at time $t = t_0$ (step1). Then, followed by a whole time step, the system is propagated under the action of the perturbation Hamiltonian $\mathcal{H}_{int}$ (step 2), proceeded by another half step along the Kepler ellipse (step3), ending at time $t = \tau$, with updated positions and velocities.

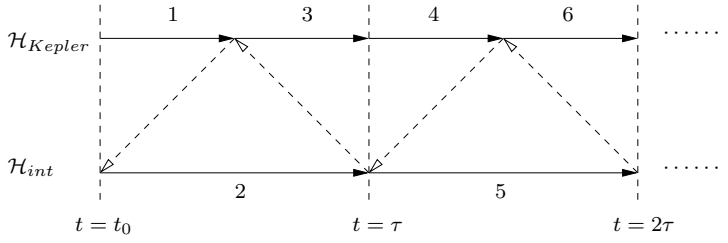

Figure 4.2: Graphical representation of the Leapfrog algorithm over two time steps. The numerical solution or the osculating variables of the Kepler ellipse are available at the indicated times separated at time step τ.

In practice, the future coordinates along the Keplerian ellipse (step1 $\rightarrow 3 \rightarrow 4 \rightarrow 6$) generated under the action of $\mathcal{H}_{Kepler}$, are calculated using the universal formulation (Mikkola, 2004, p.26) of Gauss' $f-$ and $g-$functions involving Stumpff's $c-$functions for the solution of Kepler's equation.

The error of the method introduced at each step is of order $\mathcal{O}(\tau^3)$ and given by (Mikkola, 2004)

$$\mathcal{H}_{err} = \frac{\tau^2}{12}\{\{\mathcal{H}_{Kepler}, \mathcal{H}_{int}\}, \mathcal{H}_{int} + \frac{1}{2}\mathcal{H}_{Kepler}\} + \mathcal{O}(\tau^4), \tag{4.9}$$

where $\{,\}$ are Poisson brackets. This error gives rise to the approximate solution operator represented in eq. (4.7) and the leapfrog algorithm calculates a numerical solution generated by a 'near-by' Hamiltonian given by $\mathcal{H} = \mathcal{H}_{Kepler} + \mathcal{H}_{int} + \mathcal{H}_{err}$. In particular, the leapfrog method conserves the near-by Hamiltonian exactly (upto computer roundoff errors). The accuracy of our symplectic leapfrog method is improved by using the technique of symplectic correctors introduced by Wisdom, Holman and Touma (Mikkola, 1997, and references therein). A symplectic corrector is a mapping (actually a canonical transformation) between the numerically computed solution orbit (including the error) and the true 'zero-error' corrected orbit. Within the algorithm the true orbit is only corrected for the $\mathcal{O}(\tau^2)$ term given in eq. (4.9). The extend of error effect on the accuracy of the corrected orbit, depends on the nature of close encounters between pairs of planets. During close encounters higher order terms within the error Hamiltonian will become dominant and contribute significantly to the total error budget. This will be demonstrated in sec. 4.2.5.

In order to capture the correct physics of the problem, the ability of a numerical integrator to allow an adaptive time step during the integration is in some situations indispensable if close encounters or eccentric orbits are encountered. Although composit general leapfrog methods require the use of a constant integration stepsize to maintain the symplectic properties, Mikkola (1997) circumvented this problem by applying a Poincaré transformation and considering the system within extended phase space denoted by the 'transformed system'. Following (Mikkola, 1997), the physical independent time $t-$variable is transformed to a new ficticious independent coordinate like $s-$variable by introducing a time transformation function $g(\boldsymbol{q}, t)$ given by

$$ds = g(\boldsymbol{q}, t)dt = \left(\frac{A_1}{q_1} + \frac{A_2}{q_2}\right)dt, \tag{4.10}$$

where A_1, A_2 are adjustable constants determined by numerical experiments and q_1, q_2 denote the generalized coordinates. The number of degrees of freedom of the system has consequently increased by one. The corresponding transformed Hamiltonian generating the orbit within extended phase space (or the conjugate momenta to s) is given by

$$\Gamma = g(\boldsymbol{q}, t)\Big(\mathcal{H}(\boldsymbol{q}, \boldsymbol{p}, t) + p_0\Big), \tag{4.11}$$

where p_0 is the initial conjugate momentum with numerical value given by $p_0 = -\mathcal{H}(t_0)$ and, by analogy to eq. (4.3), $\Gamma = 0$ and is constant along the orbit. In order to apply the generalized leapfrog method to the 'transformed problem', the new Hamiltonian is separated into two individually integrable components $\Gamma = \Gamma_0 + \Gamma_1$ and the algorithm proceeds by attempting $\Gamma = 0$ along the orbit. The neccesary

constant stepsize is transformed to a constant $s-$step within the 'transformed problem' maintaining the symplectic conservation properties. The variable time adaptive character is then given by eq. (4.10) for a suitable choice of the adjustable constants. In practice, the initial stepsize is measured in terms of the initial number of steps per inner planet orbital period (`ns` $= P_{inner}/\tau$ within the code). In the case of close encounters the `ns`-parameter is adjusted in order to maintain the $\Gamma = 0$ condition.

4.2.4 Tests and demonstrations

In order to establish the validity of the algorithm, we need to perform some numerical tests. Following a standard procedure, the numerical obtained solution is compared to an analytic problem for which exact solutions exist. The most obvious testcase to use is the 2-dimensional Kepler problem. However, the `g3.f` integrator is designed and implemented to numerically calculate the orbits of a three-body system. Considering only two bodies (i.e a Sun and a planet) is not possible. This excludes the use of the 2D Kepler problem as a test case.
A second method to establish the validity of the algorithm, is to reproduce published data within the literature. Testing by data reproduction assures the validity of the numerical method at least as accurate as the published data.

Assuming the published data are accurate enough, I decided to reproduce the time evolution of orbital parameters of the planets within the 47UMa extrasolar planetary system published within Jones and Sleep (2002, Fig.3) using the symplectic method and the high-accurate Bulirsch-Stoer[3] extrapolation method (Press et al., 1996) for a comparison. The Bulirsch-Stoer extrapolation method takes an ϵ-accuracy parameter as an input variable to estimate the maximum size of the local truncation error at each integration step. This error estimate is then used to adjust the current stepsize to accomplish the required ϵ-accuracy. Adopting equivalent initial conditions specified by Jones and Sleep the reproduced orbital time evolutions of the eccentricities and semi-major axis are shown in Fig. 4.3, using the the symplectic and non-symplectic (BS) method.

By comparison, no exact quantitative reproduction is obtained. However, since we are not interested in accurate ephemeris data, our numerical method matches the right order of magnitude for the time evolution of the orbital elements of the two planets considered within 47UMa. We conclude that our numerical method reproduces *qualitative* characteristics of the 47 UMa dynamical planetary system, confirming the validity of the symplectic numerical method. This conclusion is based on a series of questions, which will be outlined and discussed in the following.

[3]This method is commonly trusted and widely used within the literature for a variaty of celestial dynamics problems (Laughlin and Adams, 1999; Rivera, 2000). A working version is implemented within the `mercury6` integration package (Chambers and Migliorini, 1997; Chambers, 1999) available at http://www.arm.ac.uk/∼jec/home.html

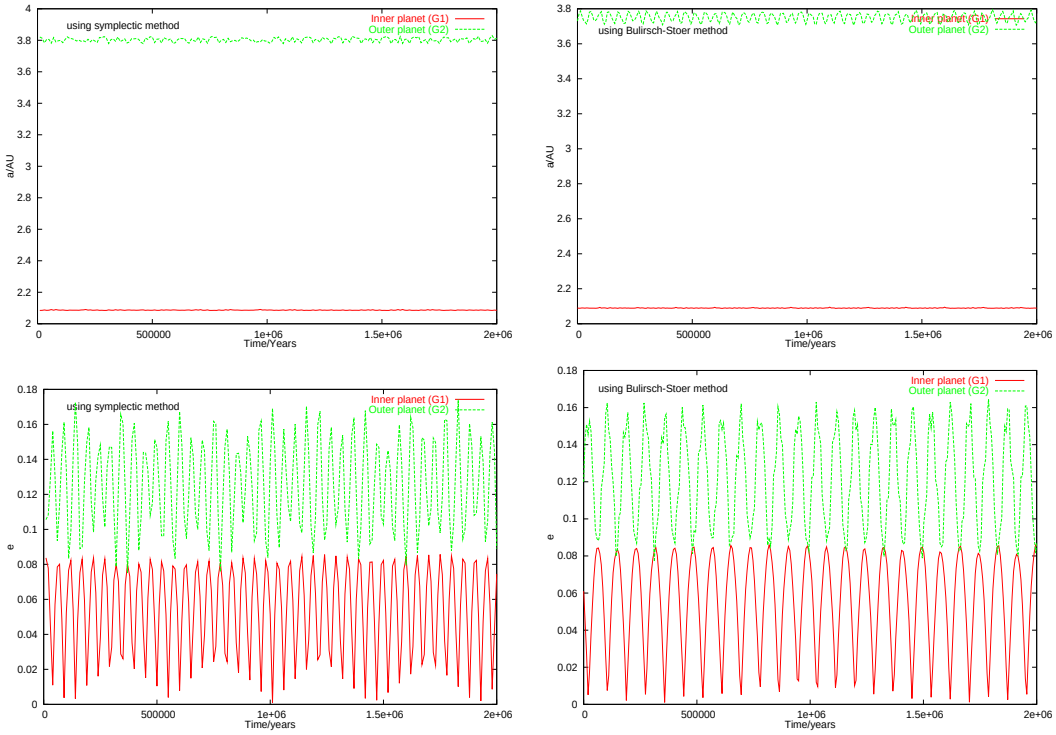

Figure 4.3: Time evolution of orbital parameters (a, e) for the two planets (G1 and G2) within 47 Ursae Majoris during a simulation time of 2×10^6 years. The sampling rate is $\sim 10^4$ years. Both the Bulirsch-Stoer (right panel) and symplectic method (left panel) have been used to reproduce data using initial conditions from Jones and Sleep (2002). For the BS-runs the $\epsilon = 10^{-14}$ have been chosen and the maximum relative energy error for the symplectic method was $\sim 10^{-10}$. Considering the e-evolution using the symplectic method, an apparent periodicity for the inner planet is observed with period $\sim 5 \times 10^5$ years. Whether this periodicity is a true dynamical phenomenon or originating due to the numerical approximation is not clear. Note the anti-correlation in the eccentricity, which is explained by the angular momentum conservation.

Another measure to test the validity of a numerical result, is the ability of the numerical method to conserve energy and angular momentum. We will use the concept of relative error and define the relative energy error as $\Delta E/E = \frac{E(t)-E(t_0)}{E(t_0)}$. Here, $E(t)$ is the systems energy at time t and $E(t_0)$ is the initial energy of the system. Equivalently, the relative error in angular momentum is defined as $\Delta L/L$. Using double precision arithmetics within our computations this concept limits the measurement to machine precision of order 10^{-15}. In the ideal case, the relative energy (or angular momentum) error should be 0 and constant. To demonstrate the property of symplecticity and its effect on the long-term conservation of energy, I have compared the relative energy error for the symplectic and the extrapolation

method for the 47 UMa simulation.

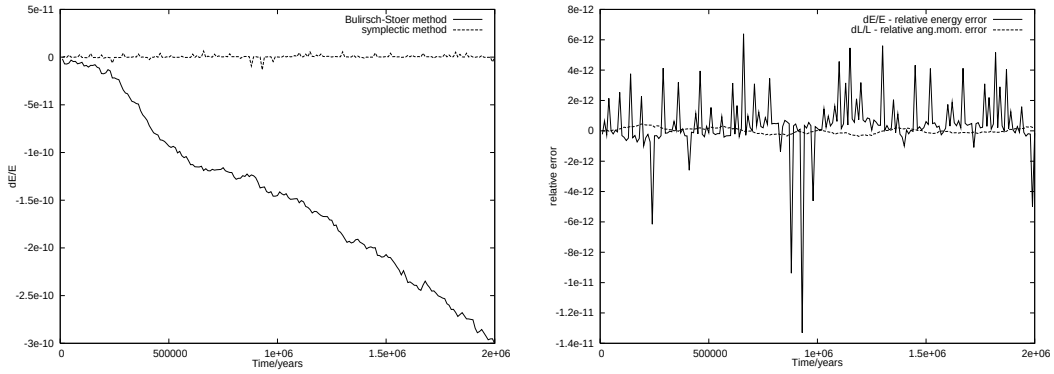

Figure 4.4: Left panel: Plot of the time evolution of relative energy error for the symplectic (dashed line) and non-symplectic (solid line) method. Right panel: Comparing the sensitivity of conserved quantities ($\Delta E/E$ and $\Delta L/L$). The time evolution of the energy error is the same as shown in the left panel figure. In general, the total integration time is 2×10^6 years.

The result is shown in Fig. 4.4 (left panel) and reveals the superior advance of the symplectic method for long-term simulations. The symplectic method shows a steady random walk of the relative error which is mainly explained by round-off errors (Gladman et al., 1991). Using the non-symplectic Bulirsch-Stoer method the relative energy error shows a secular trend over time, indicating a numerically induced pumping of energy into the system. Assuming a consistent linear accumulation rate growth the relative energy error after 2×10^9 years is estimated to be $\sim 10^{-7}$.

During the test period of Mikkola's symplectic numerical method the following question became apparent: which of the conserved quantities $\Delta E/E$, $\Delta L/L$, should I use for benchmark testings? Should both be used, or is there any preference? Comparing the relative energy and angular momentum errors by considering different numerical experiments, revealed that the energy error is the most sensitive quantity. Fig. 4.4 (right panel) shows angular momentum and energy measurements during a numerical integration of the 47 UMa system. A comparison suggests the use of the relative energy error to quantify accuracy for a given numerical experiment. The improved conservation of the angular momentum within machine precision is unclear and in the following no attempts will be made to find an explanation.

A final but important question is to ask: how much precision is needed in the conservation of energy in order to calculate a correct orbit? Is 10^{-3} accurate enough or minimum 10^{-7} or should it be no more less than 10^{-10} in terms of relative error measurements? At this point a second question needs to be considered: does the conservation of energy to a given degree of accuracy imply the correct calculation

of *all* planetary orbits within the system?

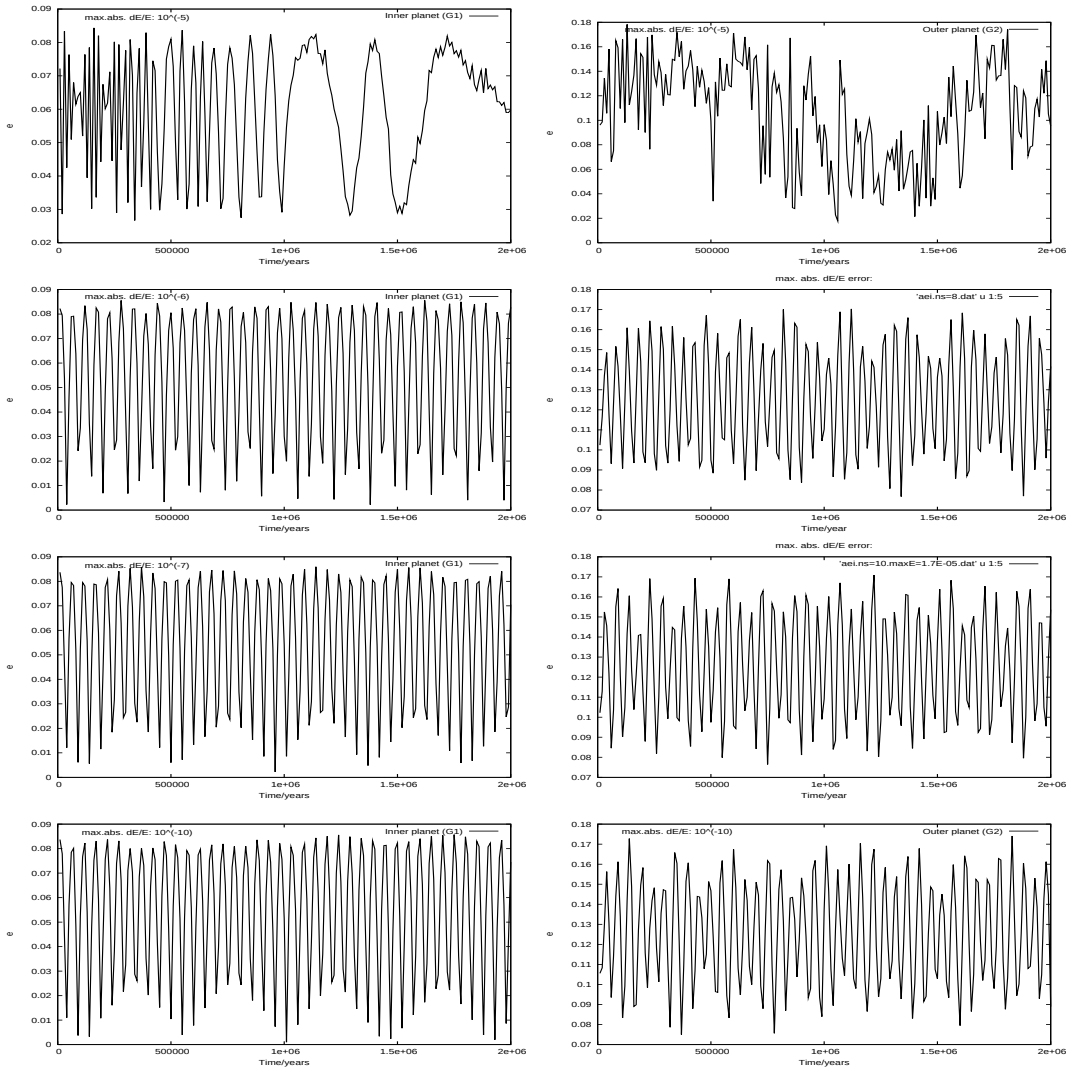

Figure 4.5: Demonstrating the process of converging solution for increased conservation of relative energy. In increasing order from top the stepsize is decreased. This corresponds to a decrease in the maximum relative energy error are $max\{dE/E\} : 10^{-5}, 10^{-6}, 10^{-7}, 10^{-10}$. Left panel plots represents the inner (G1) and right panel figures the outer (G2) planets eccentricity evolution.

The use of the relative energy error as an indicator for the quality of a numerical experiment is only a nessecary condition, but not sufficient. As an example, we consider a planetary three-body system containing a massive and a much smaller planet (think of the Sun-Earth-Jupiter system). The contribution of the smaller planet to the total energy is much smaller than for the massive planet. Hence, the conservation of energy to a given accuracy would indicate the correct calculation

of the massive planets orbit. The correctness of the smaller planets orbit is left uncertain, since its contribution to the total energy is much smaller. This problem of accuracy test has allready been pointed out by (Mikkola and Innanen, 2002, and references therein), who suggest a solution by means of individual accuracy checks to test the computations of correct orbits of low-mass bodies. The numerical use and implementation of the individual accuracy check is beyond the scope of this project, and only stated here for the purpose of future aspects within planet dynamics simulations indicating the existence of tools for further improvements of numerical results. It should be mentioned that this kind of accuracy check is of importance in the case of frequent close encounters, an issue we will discuss within the next section.

In order to return to the precision question the principle of convergence of a true solution is followed. Intuitively, the following aspect is clear. The higher the resolution of the innermost orbit, that is the smaller the stepsize, the more accurate is the numerical solution compared to the true solution. Equivalently, the maximum relative energy error should decrease for $\tau \to 0$. Following the principle of convergence, I examined and studied the eccentricity time evolution over a 2×10^6 year period for the two planets within 47 UMa. Different stepsizes according to a given accuracy in energy have been chosen. The result is shown in Fig. 4.5. This test shows a convergence of the qualitative time evolution as the accuracy of energy conservation increases. From the e-plots, we observe a change-over at $dE/E \sim 10^{-7}$, suggesting an initial stepsize of > 18 steps per inner orbit. A similar conclusion is obtained by examining the time evolution of the planets semi-major axis.

4.2.5 Close encounters

The event of a close encounter or close approach between two celestial objects will almost always result in a catastrophic disruption of the system by either an ejection (of the less heavier body) or a collision. Although our numerical method is able to capture the correct physics during a close approach by reducing the current stepsize, it is almost always worthless to follow the subsequent time evolution of the system. The reason for this is twofold. First, the energy integral of the system may not be well conserved during a close approach passage introducing an artificial source or sink of energy. Secondly, the chance for a second close approach in the remote future is high with the consequence of a possible ejection.

Initial conditions leading to artificial close encounters have been extensively studied by numerical experiments, in order to learn about the subsequent dynamical evolution. To be as realistic as possible, we considered close encounters between an Earth mass object and HD70642b. Fig. 4.6 demonstrates the resulting outcome of two encounter events at apoastron position for the terrestrial planet. We classify the encounter events as 'soft' and 'hard' for the initial condition within the upper and

lower panel, respectively. Both planets orbit a central star of one Solar mass and the time evolution of the orbits are counterclockwise. The initial mean anomaly for HD70642b have been experimentally determined in order to realise a close encounter event to take place at the terrestrial planets apocenter distance. The two encounter event differs only in the mass parameter of HD70642b. For the soft-encounter event, we consider a 3 Jupiter-mass planet and for the hard-encounter event a 5 Jupiter-mass planet on a circular orbit.

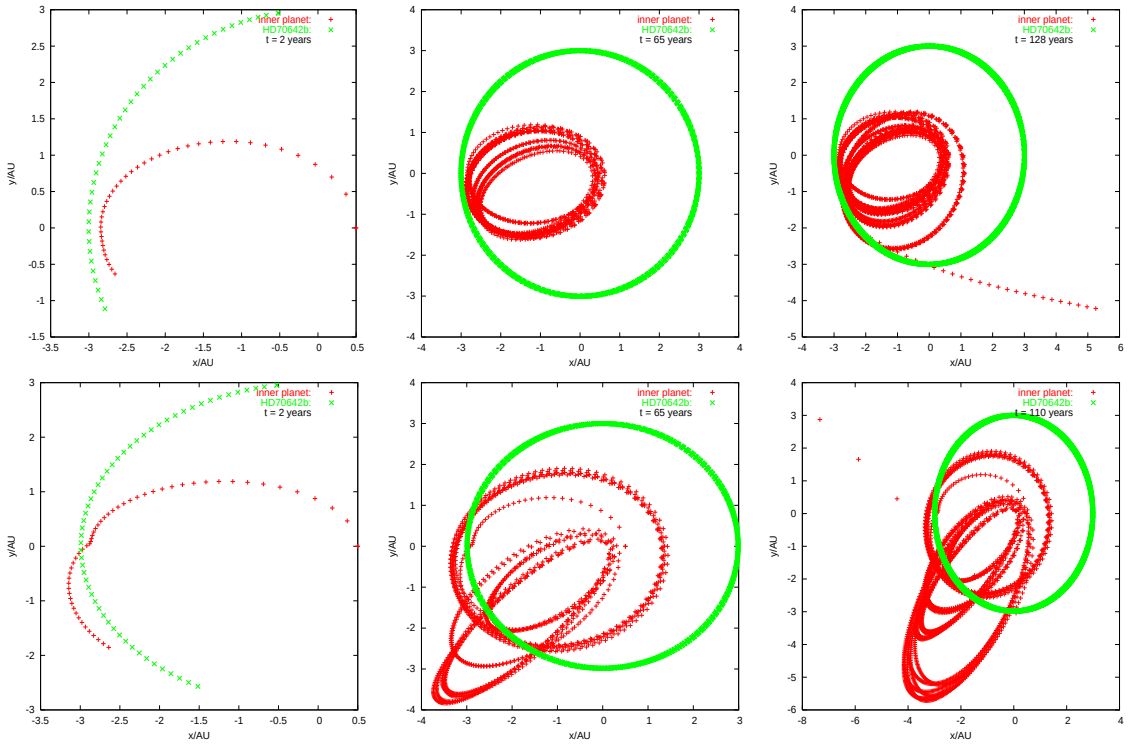

Figure 4.6: Snapshots of the time evolution after a close encounter event for two different initial conditions of the terrestrial inner planet (red orbit, with start point at $(x, y) = (0.5, 0)$). The orbit of HD70642b (green orbit, with start point $(x, y) = (-0.5, 3)$) is circular with $a = 3.0$ AU and the terrestrial planet is initially placed on a high-eccentric orbit with $(a, e, M) = (1.66 \text{ AU}, 0.7, 0.0°)$. The apparent elliptic shape of HD70642b in some plots is due to different scales on the axis. Note the automatic decrease in step size during a close approach.

For both encounter events at $t = 2$ years, the symplectic method reduces the time step of the terrestrial inner planet in order to capture the physically correct dynamics under the close approach. The subsequent evolution is then dramatically changed from the initial elliptic orbit and characterised by several close aproaches. The orbit of HD70642b is only slightly changed as a result of the close encounters. For the soft-encounter event at $t = 65$ years, the inner planet orbit starts to precess coun-

terclockwise due to several close approaches. The dynamics for the hard-encounter event are much more 'active'. At time $t = 65$ years the orbit first circularise then changing to a high eccentric orbit nearly grazing the host star. The ultimate fate of both encounter is the ejection of the terrestrial planet into interstellar space after some 100 years. Fig. 4.7 represents a record of the mutual planetary distance for the soft-encounter scenario and the corresponding change in the total relative energy during the numerical integration time. For close encounters less than 0.5 AU the terrestrial planets experiences a total number of 5 close approaches during 100 years and the time evolution of the mutual distance is behaving erratic reflecting the overall chaotic nature of the post-encounter dynamics. In addition, 'energy-jumps' with increasing levels are observed. These jumps correlates exactly with close encounter events. The smaller the mutual distance the larger the jump in relative energy error. This kind of behavior reflects the failure of the symplectic corrector (Mikkola, 1997).

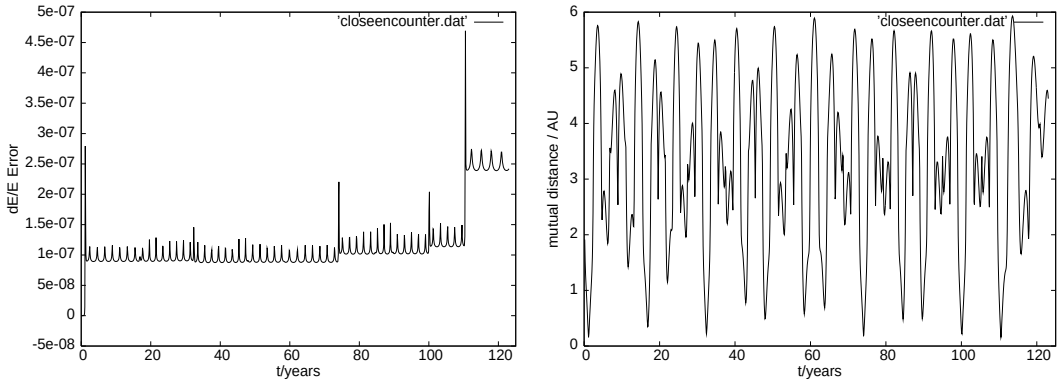

Figure 4.7: Left panel: Change in total relative energy, $\Delta E/E$. Right panel: Time monitoring of the mutual distance between planets during the 120 year integration time. Cf. text for details.

The event of a close approach can be quantified by the *sphere of influence* or *sphere of activity* (Roy, 1988, p.168). It is the region around a planet within which the motion of a second planet (or a testparticle) should be considered as planetocentric disturbed by the central host star. If m, M measures the mass of the planet and the host star with $m < M$, then the radius of the sphere of influence centered on the massive planet is

$$r_{soi} = \left(\frac{m}{M}\right)^{2/5} r_p, \tag{4.12}$$

where r_p is the massive planets heliocentric distance. Experience obtained by numerical experiments, suggests that a close encounter should be defined whenever 2 objects are within $3-4\ r_{soi}$. Another measure for the detection of a close approach is quantified in terms of the *Hill's radius* (Murray and Dermott, 1999, p.116) and

is roughly equivalent (in magnitude) to the activity sphere. The Hill's stability approach is usually adopted within the literature to detect close encounter.

Within this work the mass ratio will be of order $m/M \sim 10^{-3}$ and $r_p \sim 3$ AU. Thus the sphere of influence of HD70642b will be of order ~ 0.1 AU. For an Earth-mass planet at $r_p = 1$ AU, we have $r_{soi} = 0.01$ AU. From Fig. 4.7 the strongest encounters have mutual distance comparable to the radius of the sphere of influence. We will use the concept of the sphere of influence in order to detect a possible close approach between the two planets. Since the evaluation of r_{soi} is computational cheap, we test for a possible close encounter at each timestep during a numerical simulation. In the case of a close encounter event, we decide to terminate the integration process and classify the corresponding initial condition of the terresial planet as unstable.

4.3 Coordinate transformation algorithms

Numerical computations within planetary dynamics are in general done using Cartesian or Jacobi coordinates. Since these coordinates are counterintuitive for the geometric representation of a particular orbit, we need to find a relationship between Keplerian[4] and Cartesian coordinates in order to transform from one set to the other.In the following discussion, we consider two algorithms for the conversion between Keplerian elements and Cartesian coordinates

$$(a, e, i, \omega, \Omega, M(t)) \longleftrightarrow (x, y, z, v_x, v_y, v_z), \tag{4.13}$$

at some given time t. Several methods for constructing transformation algorithms exists within the literature and the following outline is based on Roy (1988) and Boulet (1991). Both algorithms are tested against computed ephemeris data for the major planets and some asteroids, obtained from the JPL Horizons ephemeris generator. Fig. 4.8 represents the geometric concepts involved for the following discussion. Both algorithms (`car2kep.f90` and `kep2car.f90`) are implemented within `Fortran90` and listed in appendix A.2 and A.3, respectively.

4.3.1 Cartesian to Kepler coordinate transformation

Considering a general inertial rectangular coordinate system $\mathcal{O}(x, y, z)$ with origin at m_1 and basis vectors $(\boldsymbol{u}_1, \boldsymbol{u}_2, \boldsymbol{u}_3)$, the procedure for transforming rectangular coordinates to Kepler elements is:

[4] the Cartesian $\rightleftarrows$ Jacobi transformations are done within the `g3.f` code, as indicated within Fig. 4.1

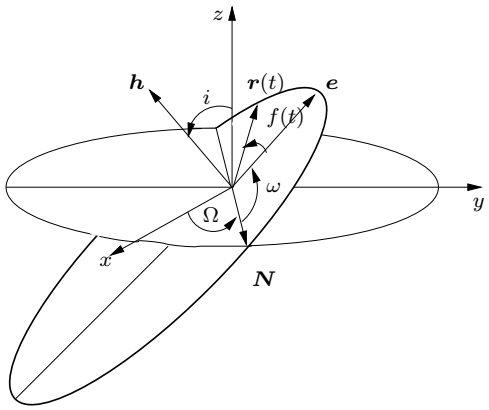

Figure 4.8: The orbit in space. $\boldsymbol{e}$ denotes the eccentricity vector pointing from the origin to the pericenter and $\boldsymbol{h}$ is the orbital angular momentum. The ascending node vector $\boldsymbol{N}$, is constructed from $\boldsymbol{h}$ and the unit vector $\boldsymbol{u}_3$ along the z-axis. The inclination is also given by the angle between $\boldsymbol{h}$ and the z-axis.

1. At time t, calculate the quantities $v^2 = \boldsymbol{v}\cdot\boldsymbol{v}$, $rv = \boldsymbol{r}\cdot\boldsymbol{v}$, $r = \sqrt{\boldsymbol{r}\cdot\boldsymbol{r}}$, $h = \sqrt{\boldsymbol{h}\cdot\boldsymbol{h}}$ from $\boldsymbol{r} = (x, y, z)$, $\boldsymbol{v} = (v_x, v_y, v_z)$.

2. Calculate the eccentricity e, from the *Laplace vector* $\boldsymbol{P}$ (see Goldstein (1980) for a derivation and a historical discussion)

$$\boldsymbol{P} = \mu\boldsymbol{e} = \boldsymbol{v}\times\boldsymbol{h} - \mu\frac{\boldsymbol{r}}{r}, \tag{4.14}$$

where $\boldsymbol{e}$ is the *eccentricity vector* (Boulet, 1991), $e = |\boldsymbol{e}|$ and μ is the reduced mass. The Laplace vector is a constant of motion for the two-body problem and points from the dynamical center to the pericenter with magnitude μe. The eccentricity is used to test the type of the orbit. An orbit with $|1.0 - e| < 10^{-8}$ is defined as an unbound orbit (parabolic case). Circular orbits are defined with eccentricities $e < 10^{-5}$.

3. Calculate the inclination angle i, and the longitude of the ascending node Ω, from

$$\cos(i) = \frac{h_z}{h} \quad \text{and} \quad \cos(\Omega) = \frac{N_x}{N}, \tag{4.15}$$

where N is the magnitude of the *ascending node vector* defined as $\boldsymbol{N} = \boldsymbol{u}_3 \times \boldsymbol{h}$. Since (inverse) trigonometric functions are not single valued, some care must be denoted for the determination of the proper quadrant. Here we have no quadrant ambiguities for the calculation of the inclination, since the principle values of the cosine function matches the angular range for which i is defined and no special test

should be performed here. Difficulties are encountered for the determination of Ω, since $0 \leq \Omega < 2\pi$ and $\cos(\Omega)$ only returns values within its principle range. However, it can be shown that if $h_x < 0$, then the range $\pi \leq \Omega < 2\pi$ is covered, and if $h_x > 0$ then $0 \leq \Omega < \pi$. A singularity in Ω is encountered for zero inclinations. In the case $i = 0$, we have that Ω is not defined, and we set $\Omega = 0$ for $i = 0$.

4. Calculate the true longitude θ. We recall that $\theta = \omega + f$. In the case of an inclined orbit $i \neq 0$, we have the following rotation relations (Roy, 1988)

$$\tan(\omega + f) = \frac{z}{\sin(i)} \frac{1}{x\cos(\Omega) + y\sin(\Omega)}, \tag{4.16}$$

and for the coplanar case $i = 0$, we have

$$\tan(\omega + f) = \frac{y\cos(\Omega) - x\sin(\Omega)}{x\cos(\Omega) - y\sin(\Omega)} = \frac{y}{x}. \tag{4.17}$$

Using the intrinsic `Fortran90` function `ATAN2(arg1,arg2)` the proper angular quadrant for the true longitude is determined without any ambiguities.

5. Calculate the semimajor axis a, using table 2.1 for the eliptic case.

6. Calculate the true anomaly f, from $\boldsymbol{e}$ and $\boldsymbol{r}$ by

$$\cos(f) = \frac{er}{\boldsymbol{e} \cdot \boldsymbol{r}}. \tag{4.18}$$

In order to determine the proper quadrant, it can be shown that if $rv < 0$, then $\pi < f < 2\pi$ for the evaluation of the true anomaly.

7. Calculate the argument of pericenter ω, from 6. and 4. as $\omega = \theta - f$.

8. Calculate the eccentric anomaly from eq. 2.8. This relation is particular useful since the `ATAN2` function can be used in order to determine the proper quadrant, and it is numerically stable for small values of e, an important property as we will see later.

9. Calculate the mean anomaly M, by using Kepler's equation 2.10.

4.3.2 Kepler to Cartesian coordinate transformation

We now consider the reverse problem: the derivation of Cartesian coordinates from a given set of Kepler elements at a given time. Boulet (1991) discusses the general

case for all possible orbits. In the following, we restrict ourself by discussing the most important case of elliptic motion. Considering Fig. 2.1, if $\bar{\mathcal{O}}(\bar{x}, \bar{y}, \bar{z})$ represents the orbit plane reference system with unit basis vectors $(\bar{\boldsymbol{u}}_1, \bar{\boldsymbol{u}}_2, \bar{\boldsymbol{u}}_3)$, then the position and velocity of the point mass can be written as

$$\begin{aligned} \bar{\boldsymbol{r}}(t) &= \bar{x}(t)\bar{\boldsymbol{u}}_1 + \bar{y}(t)\bar{\boldsymbol{u}}_2 + \bar{z}(t)\bar{\boldsymbol{u}}_3 && (4.19)\\ \bar{\boldsymbol{v}}(t) &= \dot{\bar{x}}(t)\bar{\boldsymbol{u}}_1 + \dot{\bar{y}}(t)\bar{\boldsymbol{u}}_2 + \dot{\bar{z}}(t)\bar{\boldsymbol{u}}_3, && (4.20) \end{aligned}$$

where the scalar and vector components can be written in terms of (a, e, M) and (i, ω, Ω), respectively. We have the following two steps.

1. From Fig. 2.1 the scalar components (with $\dot{\bar{z}} = \bar{z} = 0$) are given by

$$\begin{aligned} \bar{x}(t) &= a(\cos(E(t)) - e) && (4.21)\\ \bar{y}(t) &= b\sin(E(t)) && (4.22)\\ \dot{\bar{x}}(t) &= -a\dot{E}(t)\sin(E(t)) && (4.23)\\ \dot{\bar{y}}(t) &= b\dot{E}(t)\cos(E(t)), && (4.24) \end{aligned}$$

where $b = a\sqrt{1-e^2}$, is the semi-minor axis and $\dot{E} = \sqrt{\mu/ar^2}$ is the time derivation of the eccentric anomaly. E is determined by Kepler's equation from M and e. For now, we have determined the orbit and position of the point mass, and what remains is a determination of its spatial orientation.

2. The angular quantities (i, ω, Ω) are measured with respect to the general coordinate system $\mathcal{O}(x, y, z)$. We need the following series of rotations in order to map $\bar{\mathcal{O}}(\bar{x}, \bar{y}, \bar{z}) \rightarrow \mathcal{O}(x, y, z)$:

$$\boldsymbol{r}(t) = \boldsymbol{R}_3(\omega)\boldsymbol{R}_2(i)\boldsymbol{R}_1(\Omega)\bar{\boldsymbol{r}}(t), \tag{4.25}$$

where $\boldsymbol{R}_1, \boldsymbol{R}_2, \boldsymbol{R}_3$ are standard rotation matrices. The vector component in equations 4.19-4.20 are then given by (with $\dot{\bar{z}} = \bar{z} = 0$)

$$\begin{aligned} \bar{\boldsymbol{u}}_1 &= \begin{pmatrix} \cos(\omega)\cos(\Omega) - \sin(\omega)\sin(\Omega)\cos(i) \\ \cos(\omega)\sin(\Omega) + \sin(\omega)\cos(\Omega)\cos(i) \\ \sin(\omega)\sin(i) \end{pmatrix} && (4.26)\\ \bar{\boldsymbol{u}}_2 &= \begin{pmatrix} -\sin(\omega)\cos(\Omega) - \cos(\omega)\sin(\Omega)\cos(i) \\ -\sin(\omega)\sin(\Omega) + \cos(\omega)\cos(\Omega)\cos(i) \\ \cos(\omega)\sin(i) \end{pmatrix} && (4.27) \end{aligned}$$

4.3.3 Tests

Several tests have been performed for the algorithms as outlined within the previous sections using double precision arithmetic. A set of ephemerides expressing the classic and vector elements have been retrieved from the JPL Horizons ephemeris generator[5] for the major planets within the Solar System, and the minor planets Pallas and Ceres at epoch JD2453295.0 (corresponding to the civil date 2004-Oct-16 12:00). These coordinate elements are referred to the mean ecliptic and mean equinox at epoch J2000.0.

For both algorithms the converted output quantities have been compared with the exact JPL ephemeris data, inferring a measure of absolute error for the accuracy of the transformation algorithms. Transforming from classic to vector elements introduces a maximum absolute error of 10^{-13}AU in the positions and 10^{-15}AU/day in the velocities. Transforming from vector to classic elements introduces a maximum absolute error of 10^{-14} in semimajor axis, 10^{-14} in eccentricities, 10^{-9} in inclination, 10^{-6} in the argument of pericenter, 10^{-13} in the longitude of ascending node and 10^{-11} in the mean anomaly. The variation of the error is probably explained by numerical round-off error inherent in the finite precision arithmetics. Since observational errors for the orbital parameters are several magnitudes larger, we can safely trust the outlined algorithms for transforming from one set to the other.

4.4 The MERCURY6 orbit integration package

Short term numerical simulations considering multi-particle dynamics have been done using the MERCURY6 integration package. This package is available at *http://star-.arm.ac.uk/∼jec/home* and implemented in FORTRAN77. The code contains some 8000 lines. The package is well documented and developed by Chambers and Migliorini (1997); Chambers (1999). An online manual is available at *http://aitken.math.-auckland.ac.nz/∼ sharp/n-body_integrators/mercury/mercury6_man.html*. The code compiles on any UNIX/Linux platform (Intel, AMD or SUN architectures). Compilation of the source code is done using a machine dependent compiler (ifc, g77 or Compaq's f90 compiler). Depending on hardware architecture different options in compiler flags may be chosen to enhance computational performance. From experience, it is not recommended to start simulations over a NFS network connection since MERCURY6 needs frequent disk access for file writings and maintainance. MERCURY6 has been installed and compiled on the DCSC[6] supercomputer facility

[5]The JPL Horizon's system is the source for authoritative Solar System information and ephemeris data. Its online service provides access to key Solar System data with a flexible production of highly accurate ephemerides for Solar System objects. The Horizons On-Line computation service is accessible via `telnet ssd.jpl.nasa.gov 6775`

[6]Danish Center for Scientific Computing, University of Copenhagen.(www.dcsc.ku.dk)

and on the local AMD Linux cluster at the Astronomical Observatory, Copenhagen. All numerical simulations presented in this thesis are done using these computer facilities.

The package contains several input files necessary for execution (see Fig. 4.9 displaying a principle data flowchart). Parameters (initial conditions, names) for mass-less testparticles and planetary objects are stored within the `small.in` and `big.in` data files, respectively. General integration parameters (algorithm, integration start and end dates, stepsize, accuracy tolerance, data output frequency etc.) are stored within the `param.in` file. The status of integration process (mainly accuracy information) is frequently displayed and at optional intervals dumpfiles are generated for practical reasons (`*.dmp`) in case of possible hardware failure. Orbital data are progressively stored into a (binary format) data file (`xv.out`) and each integration is summarized in a `info.out` file.

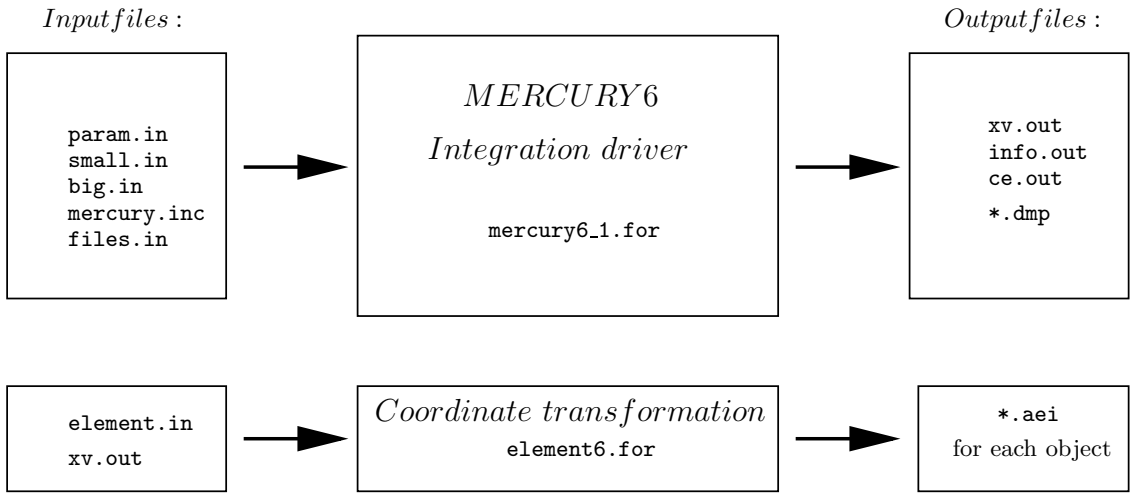

Figure 4.9: Data flowchart of `MERCURY6`. The additional binary compressed data file `ce.out` contains information on possible close enounter events between any two bodies specified within the `small.in` and `big.in` files.

In order to convert the binary orbital data file into a ready-to-read format (ASCII text) for data visualisation the package provides the `element6.for` conversion program (`FORTRAN77`). This programme produces single ASCII data files (`*.aei`) for each object containing orbital elements. The type of output elements (Cartesian, Kepler or barycentric) and sampling frequency of the time series are specified within the `element.in` file.

4.5 Summary

In this chapter, we have outlined the basic theory of symplectic integration and demonstrated the adaptive variable step property of the leap-frog method. For conservative Hamiltonian systems (i.e the three-body problem) symplectic integration algorithms are the choice of method for exploring long-term dynamical characteristics of a given planetary system. The accumulation of energy error shows no secular growth in time. In general, the symplectic method outperformes traditional numerical methods in both accuracy and CPU speed. We have performed several tests to highlight these aspects and confirming the general validity of the `g3.f` integrator. Using the 47 UMa planetary system helped to gain a great understanding of some key questions, improving the intuition of some of its dynamical characteristics. In addition, two algorithms for coordinate transformation have been outlined and succesfully tested.

Chapter 5

Dynamics Analysis: The MEGNO Indicator

5.1 Introduction

A fundamental property of the dynamics of a three-body dynamical system, is the appearance of chaotic motion. Although the three-body equations of motion are determinstic, the future evolution of the system is not always predictable and well determined. In that case, we speak of *deterministic chaos* within a dynamical system.

Historically, at the end of the 1900 century, Poincaré[1] discovered the possibility of unpredictable (chaotic) motion within his studies of solving the differential equations of the restricted three-body problem. A major issue of scientific interest at this time, was the question of the stability of the Solar System. His results changed the deterministic view of the motion of the planets as a predictable clock-work orrery and proved existing stability theorems to be false. Since then, with Poincaré as the initial founder, sophisticated mathematical techniques have been developed to gain a qualitative understanding of the dynamical behavior of chaotic dynamical systems.

A formal definition (and as a common manifestation) of the appearance of chaotic dynamics is *sensitive dependence of initial conditions and/or system parameters*. In a quasi-periodic (regular) deterministic dynamical system, almost identical initial conditions correspond to almost identical solutions for all times. This behavior is completely different in a chaotic system: A small δ-change in the initial conditions causes a system response to evolve exponentially away from the original solution. The emergence of chaotic evolution is not always at the beginning of a given time series and cases exists in which the onset of chaotic dynamics appears after some time (Murray and Dermott, 1999, p.412). As a consequence, a chaotic dynamical

[1] Les Méthodes Nouvelles de la Mécanique Céleste

system will evolve unpredicatable in time and naturally leads to the question of stability of a given solution.

Poincaré himself developed a method to test chaotic behavior within the restricted three body problem. This method is known as the Poincaré surface of section or Poincaré map, but is only applicable to three-dimensional dynamical systems (i.e restricted three-body problem (Murray and Dermott, 1999, p.414)). For higher dimensional systems (i.e full three-body problem) more sophisticated methods are needed.

In this chapter, we discuss the Lyapunov definition of stable motion and introduce the *Lyapunov characteristic exponent* (LCE), as a measure of chaotic time evolution. From the Lyapunov exponent, we define a more powerful measure of chaoticity known as the MEGNO (Mean Exponential Growth of Nearby Orbits) indicator, which is closely related to the LCE.

5.2 Measures of chaotic dynamics

5.3 Stability concepts

The concept of stability within Celestial Mechanics and planetary dynamics finds its origin in the ancient quest of the stability of the Solar System. A straightforward definition of stable motion within within a planetary system is a state wherein orbits of bodies remain well separated, and the planets will remain bound to the central host star for infinite time. However, Szebehely (1984) gives a review of various stability concepts used within the literature. The first idea in defining a stability criterion is based on secular perturbation theory (or Lagrange-Laplace theory) involving the averaging principle for the series expansion of the perturbation function in Lagrange planetary equations. The idea is the following. The absence of secular terms within the semi-major axis (cf. Fig.3.3) indicate bounded motion, i.e as long as no secular trend appears the orbital motion of a given planet would be confined. This idea is ascribed to Laplace and Lagrange and developed in the late 1770 century (Diacu and Holmes, 1996, chap.4). Formally, considering only the time evolution of the semi-major axis, the lowest order of the Lagrange planetary equation for the semi-major axis (from eq. 3.13) can be written (Murray and Dermott, 1999, p.254)

$$\dot{a} = -\frac{2a^2}{\mu}\frac{\partial\langle\mathcal{R}\rangle}{\partial\lambda}, \tag{5.1}$$

where $\langle R\rangle$ is the averaged perturbation function. Since $\langle R\rangle$ is not a function of the mean longitudes λ (i.e $\langle\mathcal{R}\rangle = \langle\mathcal{R}\rangle(a, e, i, \varpi, \Omega)$ by virtue of equation 3.20), we have that the time rate of change of the planetary semi-major axis is $\dot{a} = 0$, and hence a is constant in time. Historically, Poisson proofed this statement to be true even

for the case of a second-order expansion. However, as long as no knowledge of the presence of secular terms in higher order perturbations within the semi-major axis of planetary orbits exists, nothing can be said on the stability of the Solar System. The statements of Laplace-Lagrange and Poisson seems to be inadequate to demonstrate Solar System stability (Gurzadyan, 2002, p.290-291).

In an attemp to settle the question of the stability of the Solar System, King Oscar II of Sweden announced (in honor of his 60th birthday in 1889) a prize contest[2]. The winner to be rewarded was Poincaré in 1890. In his prize winning paper Poincaré outlines fundamental new ideas to the field of celestial mechanics and founded a new branch of science today known as dynamical systems theory. Although he was unable to give a proof of the stability of the Solar System, he introduced the idea of qualitatively studying the behavior of solutions to the three-body problem. As a measure of stability he considered solutions (with different initial conditions) to be stable, if their orbits, not necessarily the motions themselves, remain close to each other at later times. This geometrical picture of stability of solutions is originally ascribed to Poisson (Barrow-Green, 1996, p.179), (Szebehely, 1998, p.243) and generally known as orbital stability. As such Poisson stability only requires occasional returns of solutions and does not preclude wild excursions.

Recently, the stability of the Solar System has been investigated using long-term numerical integrations. Ito and Tanikawa (2002) presents results of the orbital motions of the planets over $4 \times 10^9-$year time-spans. Their results indicate that the Solar System is stable over this time period with Mercury exhibiting chaotic variations in its eccentricity. Nowadays, chaotic motion within the Solar System is quantified and measured in terms of Lyapunov times and current research uses a modern and more general concept of stability known as Lyapunov stability.

5.3.1 Concept of Lyapunov stability

Following the idea of Lyapunov's notion of stability an equilibrium solution $\mathcal{C}_1(t, \alpha)$ of a system is considered Lyapunov stable, if other δ-near-by solutions $\mathcal{C}_2(t, \alpha + \delta)$ remain close to the reference solution at later times. Here, α denotes the systems phase space state vector at some time t. In a more formal notation: Given $\epsilon > 0$ and $\delta > 0$ at initial time $t_0 = 0$ such that

$$\text{if} \quad |\mathcal{C}_1(t_0, \alpha_1) - \mathcal{C}_2(t_0, \alpha_2)| < \delta \quad \text{then} \quad |\mathcal{C}_1(t, \beta_1) - \mathcal{C}_2(t, \beta_2)| < \epsilon, \tag{5.2}$$

for all $t > 0$ (Barrow-Green, 1996). A geometrical interpretation of Lyapunov's concept of stable motion is given in Fig. 5.1. In contrast to Poisson's definition of

[2]See the books by J.Barrow-Green and Peterson (1993) for interesting technical and historical details. Especially the book by Peterson is highly recommended for details in the development of celestial mechanics from the time of Newton to the discovery of chaotic motion of asteroids and planets.

stability, Lyapunov's concept is more general and stricter demanding nearby solution to remain bounded for all times. Within Fig. 5.1 the $\mathcal{C}_2-$solution illustrates an example of Lyapunov instability. The solution diverges from the equilibrium solution at some time in the future. Small changes in the initial conditions can lead to major divergence at later times.

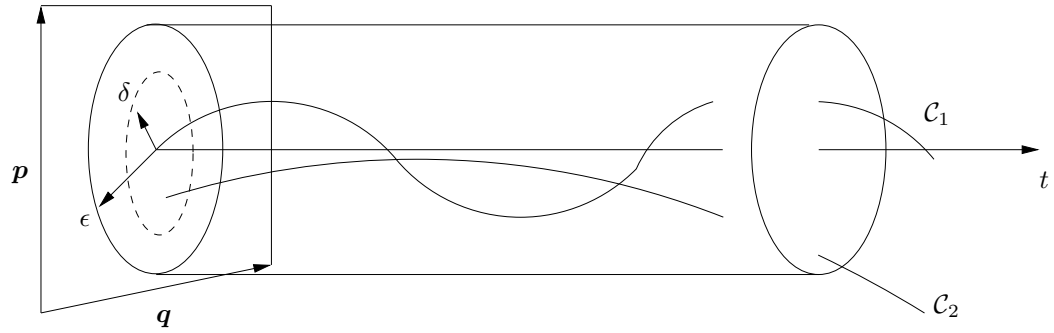

Figure 5.1: Graphical illustration of Lyapunov's concept of stability of solutions with time, showing the variation of two solution on phase space $(\boldsymbol{q}, \boldsymbol{p})$. The solution curve $\mathcal{C}_1$ is called Lyapunov stable if nearby solutions stay within a distance δ to it and $\mathcal{C}_2$ demonstrates exponential divergence (Lyapunov instability).

5.3.2 Variational equations

In order to measure exponential divergence from an equilibrium solution the equations of motion are linearized. Linearization explores the dynamics of the solution flow locally around a given initial condition. The linearized equations are obtained by Taylor expanding the equations of motion around a $\delta-$nearby initial condition. In the following, let $\dot{\eta}_i = f_i(\eta_1, \ldots, \eta_n)$ with $i = 1, \ldots, n$ represent Hamiltons equations of motion with $\boldsymbol{\eta} = (\eta_1, \ldots, \eta_n)$ denoting the phase space variables for a given planetary problem. A Taylor expansion around the point $(\xi_1, \ldots, \xi_n)$ results in the variational equations (Contopoulos, 2002; Boccaletti and Puccaco, 1998). The variational equations represents the equation of motion for the separation of two nearby orbits with initial condition $\delta_i(t_0) = \delta_{i,0}$ and, in component form, are given by

$$\dot{\delta}_i = \sum_{k=1}^{n} \frac{\partial f_i}{\partial \eta_k}\bigg|_{(\xi_1,\ldots,\xi_n)} \delta_k \equiv A_{ik}\delta_k, \tag{5.3}$$

with $\delta_i \equiv \eta_i - \xi_i$ measuring the initial small deviation and terms of order $\mathcal{O}(\delta_i^2)$ are omitted. The matrix $\partial f_i/\partial \eta_k$ is the Jacobian matrix and describes the possible exponential propagation of a small change in the initial condition along a given direction (basically, it is the growth-rate). Formally, a complete solution for the ith

component of the separation within the variational equations (eq. 5.3) is given by $\delta_i(t) = \delta_{k,0} \exp^{A_{ik}(t-t_0)}$. In practice, the Jacobian matrix is unknown and its components must be computed by numerical methods. However, the Jacobian matrix suitably quantifies exponential divergence and its components are known as Lyapunov characteristic exponents. For a $n-$dimensional dynamical system (n degrees of freedom) there exists at most a total of n distinct Lyapunov exponents, measuring the rate of change along a given direction in phase space. Details of the theory of Lyapunov exponents within linear stability theory will be omitted and in the following we just state, that there exists a unique maximum Lyapunov exponent, $\gamma = max(A_{ik})$, characterising the overall rate of change of arbitrary nearby initial conditions (Murray and Dermott, 1999; Contopoulos et al., 1978).

5.3.3 The maximum Lyapunov exponent

Within the literature the maximum Lyapunov exponent (MLE) is introduced and defined (Morbidelli, 2002a) as

$$\gamma = \lim_{t \to \infty} \frac{1}{t - t_0} \ln \Big(\frac{\parallel \boldsymbol{\delta}(t) \parallel}{\parallel \boldsymbol{\delta}(t_0) \parallel} \Big), \tag{5.4}$$

where $\parallel \boldsymbol{\delta}(t) \parallel$ denotes the norm or phase space distance of two nearby trajectories. The sign of γ determines the dynamical behavior of trajectories within phase space. For $\gamma > 0$, initial deviations grows exponentially away from each other (indicating chaotic dynamics) and decays if $\gamma < 0$. Moreover, the time rate of change of the separation vanishes, $\dot{\delta}_i = 0$, for the case $\gamma = 0$. Since the three-body problem is a conservative Hamiltonian system the case $\gamma < 0$ is never encountered in practical calculations and would indicate the presence of dissipative forces (asymptotic spiral orbits).

From the Lyapunov exponent (MLE) the characteristic time scale for exponential divergence of trajectories is defined as

$$t_L = \frac{1}{\gamma}, \tag{5.5}$$

and known as the Lyapunov time. It is basically the timescale after which nearby orbits have separated a distance $e \sim 2.72$. It reflects the limit of predictability and is therefore also known as the e-folding time scale measuring the length of time for a dynamical system to indicate chaotic behavior.

The numerical computation of γ implies a number of practical difficulties in real calculations. 1) Computing γ rigorously requires the limit $t \to \infty$, which involves numerical integration for infinite time. Clearly, this is unfeasible in the real world. 2) A solution to the variational equations is only valid within the ($\delta_i \ll$

1) linearized regime (i.e solutions are only correct locally around the equilibrium solution and exponential divergence is a measure of local divergence). 3) Because of the limited representation of floating-point numbers, exponential divergence could cause an numerical overflow within the storage architecture during the progress of computation. These difficulties urgently needs attention in order to avoid unstable (false conclusive) results, while at the same time exploring any kind of limitations within the numerical method.

To overcome these problems the concept of renormalisation (or rescaling) is introduced and the following idealized outline for the practical calculation of γ, is taken from Morbidelli (2002a) (see additional reference therein). In general, this method is not the exact procedure as implemented within the MEGNO code, which we will mainly deal with and use in our study of chaotic planetary dynamics. However, the renormalisation part is an recurrent element in calculating either the LCN or the MEGNO indicator. In a later section, results of practical numerical tests of the applied code (`cs.f`), capable of calculating MEGNO (and from it the derived LCN), are presented.

The renormalisation procedure is based on a periodical application of normalising the separation vector $\boldsymbol{\delta}$ between any two trajectories (cf. Fig. 9.9 (Murray and Dermott, 1999, p.419) for a geometric interpretation). Starting at time $t = 0$ with initial conditions $\boldsymbol{\delta}_0$ the system is followed up to a fixed time τ, called the *renormalisation time*. The choice of length of τ depends on the onset of exponential divergence and its subsequent character. A too large renormalisation time step, could possibly lead to numerical overflow and unreliable results due to the $\mathcal{O}(\delta_i^2)$ truncation in the Taylor expansion around the nearby initial condition. How to find a proper choice of the renormalisation time step, using a quasi-analytic solution, will be demonstrated by numerical experiments in a later section. However, after a time τ, the following quantity is computed, $s_1 = \| \boldsymbol{\delta}(\tau) \| / \| \boldsymbol{\delta}_0 \|$ and a "new" set of initial conditions are constructed by $\boldsymbol{\delta}_1 = \boldsymbol{\delta}(\tau)/s_1$ from which the system is restarted and followed upto the next renormalisation time step 2τ. Iterating this procedure generates a series of renormalisation factors $s_1, s_2, \ldots, s_l$. The maximum Lyapunov exponent can then be determined by

$$\gamma = \lim_{l \to \infty} \frac{\sum_{j=1}^{l} \ln s_j}{l\tau}, \tag{5.6}$$

where $l\tau$ is the total integration time. The renormalisation factors $s_j = \delta_j/\delta_0$, can be regarded as the rate of divergence of two neighboring trajectories in the j'th integration interval of length τ. To overcome the "$t \to \infty$" problem for real calculations the quantity $\sum_{j=1}^{l} \ln s_j/l\tau$ is plotted against $l\tau$ in a log-log graph up to "some suitable time" corresponding to the integration time. The length of this time interval depends on the chaotic nature of the dynamical system. By a combination

of experience and guess work the future evolution (Morbidelli calles this evolution - asymptotic behavior) of this curve is determined.

In Fig. 5.2, two examples for the calculation of γ, are shown from the literature. The left panel figure shows the asymptotic behavior of the MLE for Pluto within the Solar System and is adapted from Sussman and Wisdom (1988). From Fig. 5.2, it is seen that the motion of Pluto is chaotic with a maximum Lyapunov exponent $\gamma \simeq 10^{-7.2}$ after $\simeq 10^{8.5}$ years. Correspondingly, the Lyapunov time of Pluto is $t_L \simeq 10^7$ years. The linear dashed line (with slope -1) would indicate regular or quasi-periodic[3] behavior for given initial conditions of Pluto. This kind of evolution makes it reasonable to expect, that the limit of γ for $t \to \infty$ is 0.

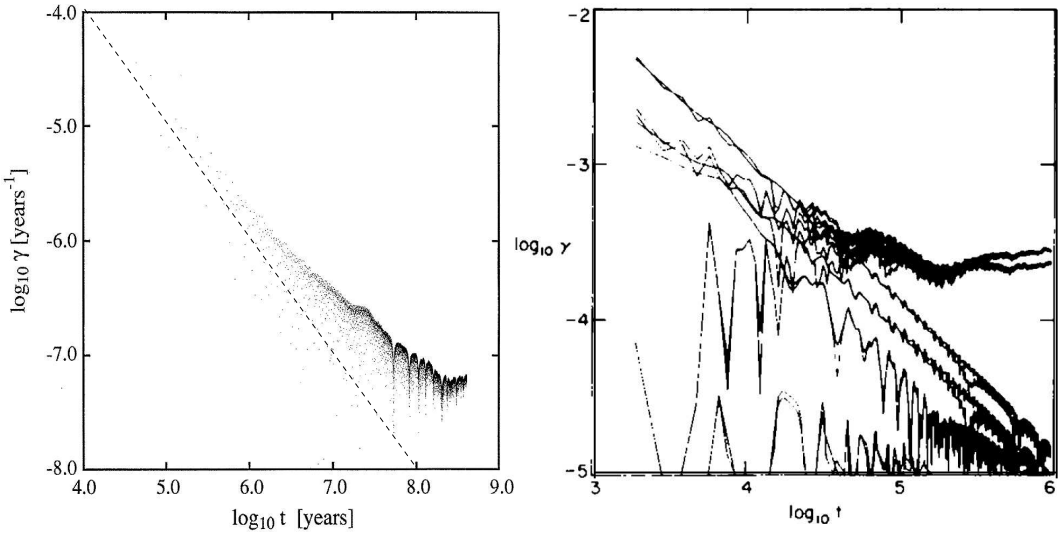

Figure 5.2: Log-log plot of the maximum Lyapunov exponent γ, as a function of time for the orbital motion of Pluto (left panel) and an asteroid within the 3:1 mean motion resonance with Jupiter (right panel). See text for additional information. Left panel: the maximum Lyapunov exponent levels off at $\gamma \approx 10^{-7.2}$ after a $10^{8.5}$ year integration. The dashed line represents a regular orbit with $\gamma \to 0$ and would indicate quasiperiodic motion of Pluto for given initial conditions. Right panel: again, the maximum Lyapunov exponent levels off at $\gamma \approx 10^{-3.5}$ for initial conditions resulting in chaotic motion. The figures are reproduced from (Sussman and Wisdom, 1988) (left panel) and (Wisdom, 1983) (right panel).

The right panel within Fig. 5.2 shows the MLE as a function of time for an asteroid (here modelled as a test-particle) located within the 3:1 mean-motion resonance with Jupiter. This resonance is located at approximately $a \approx 2.5$ AU within the asteroid belt and the total integration time spans 10^6 years. The figure is from Wisdom (1983) who, as the first, demonstrated the dynamical effect of mean-motion

[3]Quasi-periodic behavior is generally characterised by a linear growth of $\boldsymbol{\delta}$, in contrast to exponential growth for initial conditions leading to chaotic dynamics.

resonances producing large eccentricity excursions of asteroid orbits providing a mechanism for explaining the Kirkwood gaps. Within this paper, Wisdom thoroughly studied the effect of numerical precision on the accuracy of the MLE by both calculating the MLE in single- and double-precision arithmetics for different initial conditions chosen within and outside the nominal 3:1 mean-motion resonance. Additional MLE-graphs within Fig. 5.2 are due to several other numerical testings. Of particular interest are initial conditions resulting in the flattening of MLE at $\gamma \approx 10^{-3.5}$ at the simulation end after 10^6 years. Converting to Lyapunov times corresponds to $t_L \approx 3000$ years for the 3:1-asteroid. Comparing Lyapunov times, asteroids (at least those whithin the 3:1 mean-motion resonance) exhibit chaotic motion on a shorter time scale than Pluto. We will use data presented in the (Wisdom, 1983) paper, to test against numerical results of the code used in this thesis. Finally, Fig. 5.2 gives numerical examples of initial conditions resulting in quasi-periodic dynamics of the test-particle. The imposed oscillations of γ with time, is explained by the presence of a nearby resonance "acting" on the particle occasionally within phase space (Morbidelli, 2002a, p.96).

5.3.4 MEGNO indicator and its properties

The expression for the MLE in eq. 5.4 can be rewritten in integral form (Goździewski, 2001; Morbidelli, 2002a) as

$$\gamma = \lim_{t\to\infty} \frac{1}{t} \int_0^t \frac{\dot{\delta}(t')}{\delta(t')} dt', \tag{5.7}$$

where δ is the length of $\boldsymbol{\delta}$ and $\dot{\delta}/\delta$ is the relative rate of change of the separation. The main problem in a proper determination of the MLE, or γ, is the question of convergence and the choice of the total integration time. For how long should a numerical integration follow the system in order to compute a γ with sufficient certainty? It is clear, that if the method to compute γ (applying the classic way, as outlined previously) is rapidly converging to a limiting value for initial conditions leading to chaotic dynamics, the integration time over which the system is followed, can be greatly shortened. This would paramountly benefit practical applications, as it would lower the overall CPU load for numerical simulations in higher dimensional problems. Unfortunately, classic methods have poor converging properties and are by nature "slow" numerical tools to explore the phase space structure of a dynamical system. In general, γ converges as $\ln t/t$ (Goździewski, 2001).

However, a fast method to study global dynamics has been introduced, with application to problems in galactic stellar dynamics, by Cincotta and Simó (2000) and is known as the MEGNO indicator. Subsequently, this technique has been successfully applied to problems within the field of Celestial Mechanics and stability

analysis of multiplanet extrasolar planetary systems (Goździewski, 2001, 2002, 2003, 2004).

This MEGNO technique is based on a modified version of the integral form of the maximum Lyapunov exponent given in eq. 5.7. Instead of following the evolution of the MLE over time, Cincotta et al. introduced and defined the MEGNO indicator Y, together with its time-average $\langle Y \rangle$, as

$$Y(t) = \frac{2}{t} \int_0^t \frac{\dot{\delta}(t')}{\delta(t')} t' dt' \qquad \text{and} \qquad \langle Y \rangle(t) = \frac{1}{t} \int_0^t Y(t') dt'. \tag{5.8}$$

The evolution of $Y(t)$ allows the determination of the dynamical character of the separation vector δ in time. In the case of quasi-periodic behavior, $Y(t)$ oscillates about $Y(t) = 2$, for which δ grows linearly with time. For chaotic behavior, δ diverges exponentially, and $Y(t)$ oscillates around a linearly divergent line $y = \gamma t$.

In general, Cincotta and Simó (2000) showed that the limit for $t \to \infty$ of $\langle Y \rangle(t)$ is 2, for the case of quasi-periodic (regular) dynamics. In addition, for chaotic dynamics, we have for $t \to \infty$, $\langle Y \rangle(t) = \gamma t/2$, relating the time-average MEGNO with MLE. The MLE is recovered from the MEGNO by a linear fit to $\langle Y \rangle(t)$ within the chaotic regime. Determining the slope would yield γ, instantly. Alternatively, Goździewski (2001) demonstrated that the MLE can be directly expressed by the time-running evolution law ($\gamma =$) $2\langle Y \rangle / t$.

The main advantage of applying the MEGNO technique, is it's great converging properties. By construction, MEGNO amplifies any effect originating from chaotic evolution by introducing the time as a weightfactor in eq. 5.8. As a consequence MEGNO converges faster compared to standard computations for the calculation of the MLE. This allows a more rapid exploration of the dynamical structure in phase space. Following (Goździewski, 2001) this computational efficiency is cherished within higher dimensional dynamical problems dealing with a large number of initial conditions for simulations.

5.4 Program outline and test runs

The program calculating the MEGNO indicator have been made available to me by Dr. K. Goździewski, affiliated at the Torun Center for Astronomy, Poland upon an initial request. Elements of the program (and some details of it) are presented and described in (Goździewski, 2001). The program source code is written within the `FORTRAN 77` programming language. It is developed and build in modular form and makes extensively use of libraries[4] and routines known from the SWIFT orbital integration and the linear algebra (Netlib) software package. In its current version

[4]publically available from www.boulder.swri.edu/∼hal and www.netlib.org

the MEGNO indicator can be calculated for a planetary system containing 2 planets. The extension of the program to include more than two planets is a straightforward implementation process. Two input files exists, necessary for running and execution, holding planetary parameters together with initial conditions and general integration and accuracy parameters. The program enables the option to perform a single orbit integration or an integration scan survey, using initial conditions within a phase space region of dynamical interest. The scanning option will associate to each initial condition a calculated $\langle Y \rangle$ producing a scanning map of the underlying dynamics. During execution notification of the integration process is displayed on-screen progressively and numerical data are stored in an ASCII-formatted datafile. For a particular epoch the output data holds information on the MEGNO and its time average, semimajor axis, eccentricity and orbit inclination of the planets and values for the relative energy and angular momentum of the system. All numerical quantities are computed using double-precision arithmetics.

The method of calculating the MEGNO indicator and its time average is based on the solution of two coupled first-order differential equations, supplemented to the equations of motion for the planetary problem. The differential form of eq. 5.8 are given (Goździewski, 2001) by

$$\frac{dz}{dt} = \frac{\dot{\delta}}{\delta} t \qquad \text{and} \qquad \frac{dw}{dt} = 2\frac{z}{t}, \tag{5.9}$$

respectively, with initial conditions $\dot{\delta}(t = 0) = \dot{\delta}_0$ and $\delta(t = 0) = \delta_0$. In order to determine $\dot{\delta}$ and δ the variational equations are solved by a method introduced and outlined by Mikkola and Innanen (1999). The MEGNO and its time-average are recovered from the solutions and given by $Y(t) = 2z(t)/t$ and $\langle Y \rangle(t) = w(t)/t$. The differential equations are, together with the equations of motion, solved using the Bulirsch-Stoer-Gragg interpolation method implementet within the ODEX integrator[5].The numerical error on energy and angular momentum are controlled by accuracy parameters adjusting, if necessary according to a tolerance requirement, via the step-size during integration.

Tests of the code have been performed and presented thoroughly by Goździewski (2001) considering numerical stability and accuracy checks on various computer architectures. For obvious reasons, I conducted additional tests to check on the reliability of the MEGNO code. Since no analytic solutions exists, to which results obtained from MEGNO runs can be compared, I decided to use the "method of reproducability" of allready published data within the literature. If successfull, numerical results obtained by the MEGNO code would then be, at least, as correct

[5]E. Hairer provides several numerical algorithms suitable for work within Solar System dynamics including symplectic and geometric algorithms for solving first-order diff. equations. See www.unige.ch/math/folks/hairer for more details.

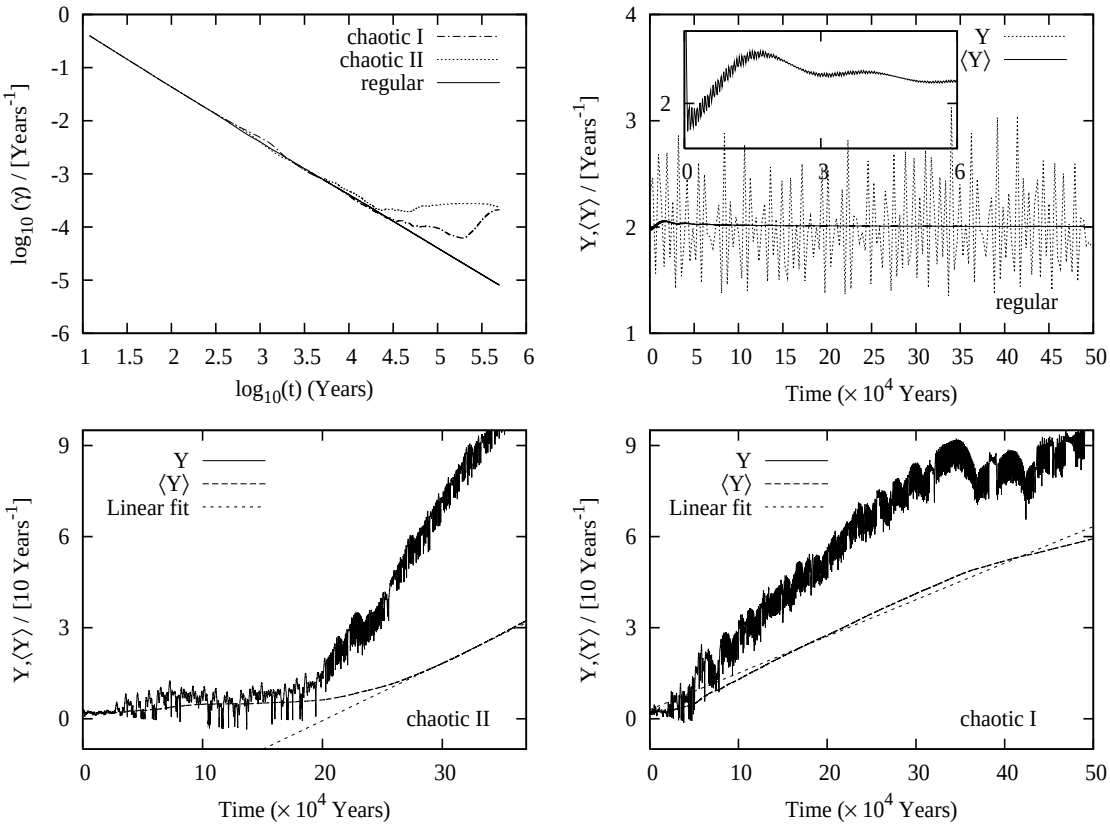

Figure 5.3: Numerical results and demonstration of testruns for the calculation of MLE (γ) in addition to MEGNO and its time average. Results are compared against published data (Wisdom, 1983) for the choice of two chaotic and one regular trajectory of a test particle (asteroid) within the 3:1 mean-motion resonance with Jupiter (cf. right panel in Fig. 5.2). The maximum integration time were at most 10^6 years. Upper left panel: The MLE as a function of time within a log-log graph for three different initial conditions of the test particle. The MLE is derived from the MEGNO using the evolution law $2\langle Y\rangle/t$. Top right panel: Plot of Y and $\langle Y\rangle$ for a quasi-periodic trajectory. The small inlet figure shows the asymptotic functional behavior of $\langle Y\rangle$ for the first 60000 years. Lower panels: Plot of Y and $\langle Y\rangle$ for two initial conditions (denoted by chaotic I+II) leading to chaotic dynamics of the test particle. From the linear fits the MLE can be determined. See text for more information.

(or false) as the published data. However, at this time published data, to which tests are being compared, are known to be well established knowledge within the astrodynamical community.

The idea is to reproduce results in the field of asteroid dynamics. Two test cases have been chosen both reflecting qualitative and quantitative aspects of results obtained by the MEGNO technique. 1) Dynamics of asteroids in mean-motion resonance and 2) dynamical structure of the asteroid belt within the Solar System.

The model involves Jupiter and a test particle in quasi-Keplerian orbit around the Sun.

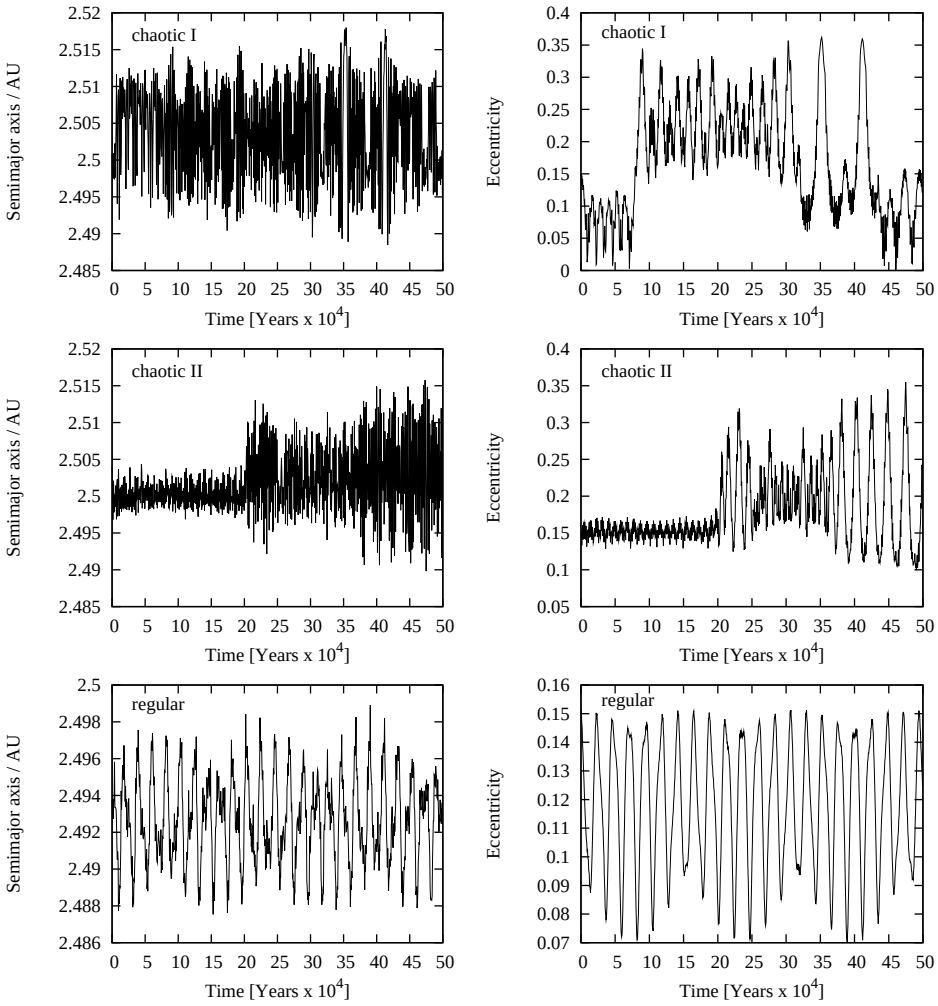

Figure 5.4: Time evolution of main orbital elements (a, e) for a test particle initially placed around the 3:1 mean-motion resonance with Jupiter. Initial conditions have been chosen in order to reproduce two chaotic (chaotic I+II) and one regular trajectory. The figures should be compared to Fig. 5.3 for any correlations with the MEGNO factor. Top panel: sudden, eccentricity excursions are observed with large amplitude variations over short time scales. Middel panel: chaotic time evolution of a, e for a second initial condition nearby the 3:1 mean-motion resonance. Lower panel: initial conditions leading to quasi-periodic or regular behavior in a, e.

Numerical test I: Resonant test-particle dynamics

First, and in particular, I consider the dynamical perturbation of a test particle initially located within the 3:1 mean-motion resonance with Jupiter. This kind of study have been allready performed by J. Wisdom in the early 1980 (Wisdom, 1983) and my goal is to reproduce some of his results. Basically, I will reproduce the Lyapunov time for asteroids within the 3:1 mean-motion resonance, which is well established and confirmed by other means. Adopting initial conditions for the test particle and Jupiter from (Wisdom, 1983, p.58), I performed numerical integrations over a similar period of time using the MEGNO code. In his paper, Wisdom mainly considers the dynamics for two initial conditions leading to quasi-periodic and chaotic dynamics (denoted by "regular" and "chaotic II" within Fig. 5.4 and 5.3). In addition, for reasons of robustness of obtained results, I changed the initial semimajor axis within the "chaotic II"-run considering the dynamics nearby the 3:1 mean-motinon resonance. This run is denoted by "chaotic I" within the figures. The nominal location of the 3:1 mean-motion resonance within the asteroid belt is $a \sim 2.5$ AU and orbit eccentricity for the particles is set to $e = 0.15$. Orbital parameters for Jupiter are kept constant during each testrun and numerical values are adopted from within the Wisdom-paper. In all simulations, the relative energy were conserved to within the acceptable level of $dE/E \sim 10^{-12}$.

Results are shown in Fig. 5.3 and 5.4. The former figure displays properties of the MLE, as derived from the MEGNO and details of the MEGNO indicator and its time-average for three different initial conditions (chaotic I+II and regular). The latter shows the corresponding time evolution of the (a, e) orbital elements. Comparing the top left panel in Fig. 5.3, displaying the MLE as calculated by the evolution law $2\langle Y\rangle/t$, with the right panel figure in Fig. 5.2, it is evident that results obtained by the MEGNO code excellently matches the stated Lyapunov times given by Wisdom (1983) using initial conditions within and around the 3:1 mean-motion resonance. From the MEGNO runs, I obtain $\log\gamma \sim 10^{-3.7}$ yrs^{-1}, which is quantitatively in agreement and comparable with Wisdom's announced $\log\gamma \sim 10^{-3.5}$ yrs^{-1}. In addition, the time evolution of $\langle Y\rangle$ and Y (lower panel in Fig. 5.3) displays the characteristics as described in Cincotta and Simó (2000); Goździewski (2001) and this behavior is expected from theory. For large times the t'-weight factor in eq.5.8 for the expression of $Y(t)$, becomes dominating having the effect of enhancing chaotic properties at later times. In Fig. 5.3, determining the MLE from the slope of $\langle Y\rangle$ yields comparable results and are also in excellent agreement with Wisdom's calculated Lyapunov times. In particular, determining a linear fit for the "chaotic II" testrun in Fig. 5.3, I use datapoints within the time interval $26 \times 10^4 \leq T \leq 39 \times 10^4$ years. Comparing the time evolution of $Y(t)$ for both chaotic testruns, we observe a difference in the onset of divergence of $Y(t)$. For the "chaotic II" run, an initial quasi-periodic transient is visible; while for the other

run ("chaotic I") the onset of divergence is almost immediately apparent.

By visual inspection, the maximum Lyapunov exponent for the "regular" testrun is expected to asymptotically approach 0, for $t \to \infty$ (top-left panel in Fig. 5.3). An additional testrun, extending the integration baseline, confirms this assumption. The corresponding functional behavior for $\langle Y \rangle$ and Y, are shown in the top-right panel in Fig. 5.3. It is observed that $\langle Y \rangle \to 2$ for $t \to \infty$ and $\langle Y \rangle$ reflects the running time-average of $Y(t)$ with the latter oscillating around 2.

In Fig.5.4, I display the corresponding time evolution of the orbital elements for the testruns. It is remarkable to see an exact correlation between the onset of chaos in one or two Kepler elements with $\langle Y \rangle$ or $Y(t)$. For the case of the "chaotic II" testrun the initial quasi-periodic transient is clearly reflected in a steady and calm variation in both the eccentricity and semimajor axis. In a way to speak, MEGNO registers any sudden change in one of the orbital elements and quantfies the sum of these changes in $\langle Y \rangle$ and Y. Of particular interest is the change in eccentricity, over short time scales, of the test particle within the "chaotic I" testrun (top-right panel within Fig. 5.4). This figure should be compared with Fig. 4 in Wisdom (1983) as shown in Fig. 5.5.

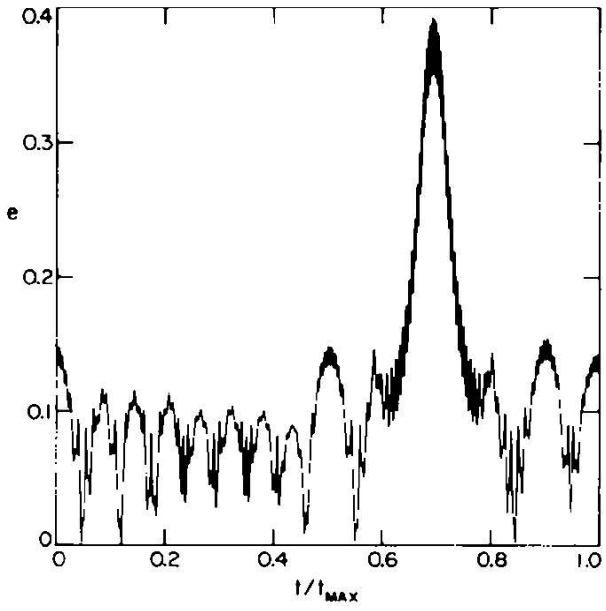

Figure 5.5: Reproduction of Fig. 4 from Wisdom (1983) showing the eccentricity as a function of time for a test particle initially placed within the 3:1 mean-motion resonance with Jupiter. The maximum integration time $t_{max} = 2 \times 10^5$ years.

Although not exact, they share qualitatively similarities to one another. This confirms the proper calculation and conversion of orbital elements within the MEGNO

code. The difference may be explained by the use of different algorithms where Wisdom's results are based on a symplectic mapping algorithm. In the case of the time evolution of orbital elements for the "regular" testrun, we observe quasi-periodic variation in a, e. In particular, the existence of different classes of perturbations are present with long-period perturbation modulated by several short-periodic perturbations. The origin and nature of the long-periodic perturbation is probably due to resonance perturbations due to the closeness of the initial conditions to the 3:1 mean-motion resonance (see chapter 3, for my discussion of different classes of perturbations). In addition, the change in orbital elements are observed to be different. As an example, we consider the "chaotic II" testrun. The percentage change in semimajor axis is $\delta a_{\%} \sim 0.6$ and for the eccentricity $\delta e_{\%} \sim 60$. This leaves us with the question, why it is easier to change the orbital eccentricity (i.e exchange of angular momentum) by gravitational perturbations, than it is to change the semimajor axis (i.e orbital energy).

Numerical test II: Dynamical structure of the asteroid belt

In a second test we consider the dynamics of a test particle within the asteroid belt of the Solar System. The dynamical structure of the asteroid belt is well constrained by observations. I conducted a parameter survey using the scanning option available within the MEGNO code. The region of interest for initial conditions is the (a, e)-space for a test particle. The range in semimajor axis roughly covers the region for which the asteroid belt is currently defined (cf. Fig.1.9) and given by the interval $a \in [1.8; 3.7]$ AU. The range in orbital eccentricity is chosen to be within the interval $e \in [0; 0.2]$. The MEGNO computations are done on a $(150, 100)$-grid, corresponding to 15×10^3 single simulations. Each initial condition is integrated for 30×10^4 years and at the end of each run $\langle Y \rangle$ were computed and assigned to the (a_i, e_i)-grid point (actually, $\langle Y \rangle$ is computed during integration).

Comparing Fig. 5.6 with the histogram distribution of asteroids within Fig.1.9, we observe a remarkable high correlation between the locations of Kirkwood gaps and mean-motion resonances. Here, we can directly assign a cause-and-effect mechanism for the depletion of asteroid at certain locations within the asteroid belt. The effect of mean-motion resonances are eccentricity excitations resulting in orbit-crossers and eventually in close encounters with planets. Although, mean-motion resonances have an important dynamical effect, the presence of secular resonances contribute to Kepler element excitations as well. However, it must be stressed that this result has been known for long time. In addition, quasi-periodic MEGNO values are computed at Kirkwood anti-gaps for test particles initially on circular orbits (7:2 and 8:3). The main conclusion regarding this testrun, must be that the MEGNO technique is reliable in detecting or discriminating regular as well as chaotic dynamics, for given initial conditions.

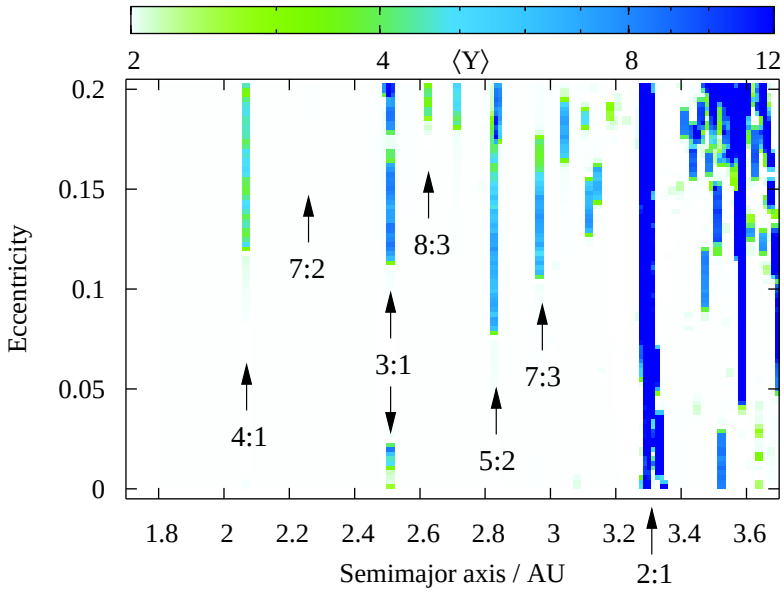

Figure 5.6: Dynamical map of a MEGNO scan within the asteroid belt region. Numerical values of $\langle Y \rangle$ are color coded. White colors corresponds to $\langle Y \rangle = 2$ (i.e quasi-periodic or regular dynamics) and $\langle Y \rangle > 2$ corresponds to chaotic dynamics. Prominent mean-motion resonances are indicated by small arrows. The absence of any chaotic features at the 7:2 and 8:3 mean-motion resonance, for most eccentricities, is in perfect agreement with observations showing regions populated with asteroids. The most dominating resonance is the 2:1 commensurability, marking the outer edge of the asteroid belt. This resonance is also the only one which is independent of initial eccentricity.

Numerical test III: The renormalisation time step

A final concern on the accuracy/reliability of the MEGNO code, is the question regarding the choice of the renormalisation time step. Should it be chosen at the order of the integration step size? Or larger? This question is quickly answered by considering the dynamics of a test particle located within the 3:1 mean-motion resonance, as discussed previously.

The idea is to repeat the calculation presented in the top-left panel in Fig. 5.3 for different renormalisation time scales, in order to reproduce the particles Lyapunov time as published by Wisdom (1983). Renormalisation time scales resulting in deviations from the nominal $\log \gamma \sim 10^{-3.5}$, are to be considered as producing false conclusions, violating the linearisation requirement underlying the variational equations.

In Fig. 5.7, we plot the MLE given by the evolution law $2\langle Y \rangle / t$, for several choices of the renormalisation time step τ in units of Jupiter periods. For increasing

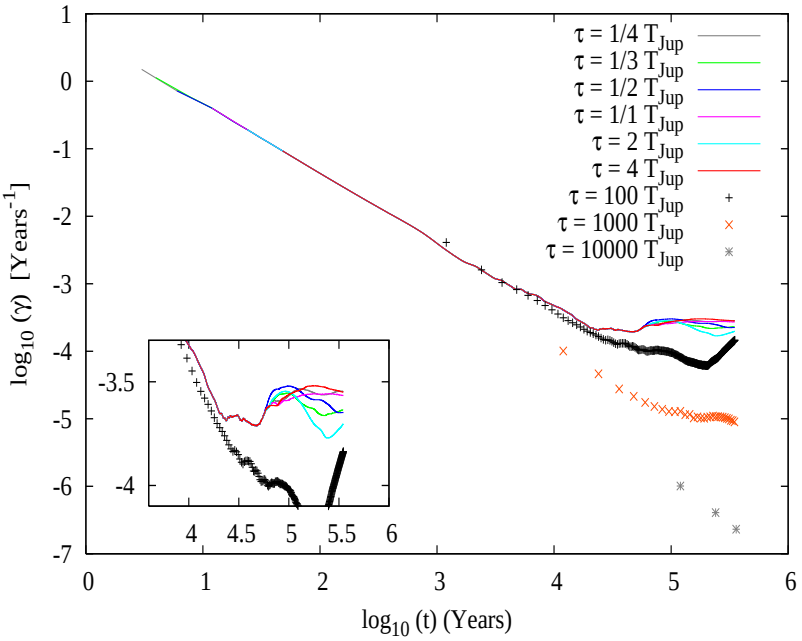

Figure 5.7: Parameter survey of the renormalisation time step τ for reproducing MLE as published by Wisdom (1983) for an asteroid in 3:1 mean-motion resonance. The graphs follow the $2\langle Y\rangle/t$ evolution law. T_{Jup} is the orbital period of Jupiter. The range for the variable renormalisation time step is from $\tau = 0.25\ T_{Jup}$ to $\tau = 10^4\ T_{Jup}$ as indicated in the legend. The plot suggests, that rescaling of the variational equations should be done at the order of $1 - 10\ T_{Jup}$. For $\tau = 10^3 - 10^4\ T_{Jup}$, the algorithm is no longer stable yielding too high Lyapunov times. The small inlet figure gives some details on the MLE for low choices of τ.

τ, we observe a deviation of the final MLE from the nominal value. The onset of the deviation, appears to start for $\tau > 100\ T_{Jup}$. The reason why only three values of the MLE are available for $\tau = 10^4\ T_{Jup}$ (gray crosses), is due to technical details in the implementation of the MEGNO program. However, we conclude this section by stating that a proper renormalisation time scale is of the order of $\sim\ T_{Jup}$. In the preceeding testruns and all upcoming simulations, we will use $\tau \sim T_{Jup}$ or $\tau \sim T_{pl}$, where T_{pl} is the orbital period of the planet under consideration.

5.5 Summary

We have introduced and described the maximum Lyapunov exponent (MLE) and the concept of mean exponential divergence factor of nearby orbits (MEGNO). The numerical computation of the latter have been thoroughly tested against observed

and published data. The MEGNO indicator will be used to study the dynamical structure of (a, e)-space within the terrestrial region of observed extrasolar planetary systems. Results suggests that MEGNO is adequate to detect the presence (or non-existence) of mean-motion resonances.

Chapter 6

Observations and the habitable zone

6.1 Introduction

In the following, we present the orbital parameters for the systems HD4208 and HD70642 as determined from observations using the radial velocity technique. A brief outline is given describing the procedure of Keplerian fitting to obtain orbital parameters for planet companions in extrasolar planetary systems. A discussion on the techniques of processing and reduction of spectral data is omitted and the outline starts after radial velocities have been retrieved from observations.

In addition, we consider simple aspects of the habitable zone for both system. In particular, we will derive the boundaries of the habitable zone within the (a, e)-orbital parameter space and special attention will be given to the Kasting et al.(1991) model for their determinations.

6.2 Observations and Kepler elements

6.2.1 Outline of orbit fitting method

Orbital parameters for observed extrasolar planets are determined from spectroscopic observations, by measuring a Doppler spectral line shift for the reflex-motion of the host star. Let $(v_m(t_i), t_i)$ represent a series of measured radial velocities, each corresponding to a measured spectral line shift at times t_i (observation times are generally measured in Julian date (JD) and velocities in ms^{-1}) with $i = 1, \ldots, N$; and N denoting the total number of observations during the survey program period.

A first indication for the presence of a single- or multiplanet system is obtained by determining the spectral power of periods within the radial velocity data set.

This determination is normally done using the *Lomb-Scargle periodogram* analysis (Fischer et al., 2002; Press et al., 1996) in the case of irregular spaced data sets. If the periodogram exhibits the presence of a single period (indicated by a maximum power peak associated with a given false-alarm probability), then a single planet Kepler model is used for a synthetic fit of the observed radial velocity curve (otherwise a 2-planet Kepler model, accounting for short-term perturbations, is used). Since the radial velocity technique is unable to determine the orbital inclination i, the single-planet Kepler model is subject to 5 adjustable parameters, related to properties of the planet's orbit. The expression for the synthetic (or analytic) radial velocity is given by (Hilditch, 2001, p.42),

$$v_s = K\big(\cos\theta(t) + e\cos\omega\big) + v_{s,0} \quad , \tag{6.1}$$

where $K = (2\pi a \sin i)/[P(1-e^2)^{1/2}]$ is the semiamplitude of the velocity curve and $v_{s,0}$ is the center of mass velocity or systemic velocity. The angle θ (true longitude) is related to time by Kepler's equation, from which the mean anomaly and hence the periastron date τ, is determined.

Since the Kepler model depends nonlinearly on the adjustable parameters (P, τ, e, ω, K), a multidimension nonlinear minimization fitting procedure is used, known as the *Levenberg-Marquardt* method (Press et al., 1996). In short, this method attempts to minimize the χ^2-function, accounting for the quality of a given parameter fit, and is given by

$$\chi^2(P,\tau,e,\omega,K) = \sum_{i=1}^{N} \Big(\frac{v_m(t_i) - v_s(t_i,P,\tau,e,\omega,K)}{\sigma_{t_i}}\Big)^2, \tag{6.2}$$

where $1/\sigma_{t_i}^2$ is the weight or standard deviation of the radial velocity measurements at time t_i. The iteration procedure follows the principle of steepest descent, in order to determine a best fit set of orbit parameters and the speed of convergence depends on the complexity of the parameter space topology. The weight $1/\sigma^2$, used within the Marquardt iteration procedure, is assembled from two contributions reflecting two main sources of radial velocity errors. 1) actual measurement (instrumental) errors, and 2) astrophysical effects. The effects account for stellar phenomena contributing to spectral line shifts in addition to the induced reflex-motion of a planet, and could be due to star-spot activity and/or stellar pulsations. Actual measurement errors are inferred from internal telescope/instrument uncertainties.

Uncertainties within the derived (fitted) orbital parameters (P, τ, e, ω, K) are modelled and inferred by using a Monte Carlo approach (Marcy, 2005). At each observation time t_i, the residual function is formed, using the observed and best-fit computed radial velocities, given by $(O-C)(t_i) = v_m(t_i) - v_s(t_i)$. Each $(O-C)(t_i)$ represents and simulates the magnitude of a measurement uncertainty in

an individual radial velocity measurement. The range of uncertainty is then given by the maximum and minimum velocity residuals. The "variation" of the best-fit Kepler velocity curve is then realised by adding a random residual velocity to the best-fit synthetic Kepler velocity at a given time. The resulting "distorted" set of radial velocities is then used to determine a "new" Kepler-fit with corresponding orbit parameters. This process is repeated, each time producing a new possible set of orbital parameters. By this method, a total of 100 variated Kepler fits have been determined. The resulting uncertainty in a given orbit parameter, is then simply determined by calculating the 1-σ standard deviation of the accumulated parameter.

The two remaining parameters to be derived from the set of fitted orbital parameters are the orbital semi-major axis a, and the projected minimum mass $M_{pl} \sin i$, of the planet companion. If the stellar mass is known, the semi-major axis is determined from Kepler's third law of planetary motion. The derivation of the minimum mass of the planet, starts by considering the *mass-function* (Perryman, 2000; Hilditch, 2001) valid for single-lined spectroscopic binaries

$$f(M_{pl}, M_\star) = \frac{(M_{pl} \sin i)^3}{(M_\star + M_{pl})^2} = \frac{1}{2\pi G}(1 - e^2)^{3/2} K^3 P, \tag{6.3}$$

where $M_\star$ is the mass of the host star, G the gravitational constant and e is the eccentricity of the planet. The equation for the mass-function is transcendental in the minimum mass and no analytic expression is obtained without assuming something on the mass ratio $M_{pl}/M_\star$. In practice, the minimum mass of the planet is determined using a root-finding iteration procedure (Marcy, 2000 - private communication). Both parameters $(a, M_{pl} \sin i)$, are derived using numerical quantities and are stated without any formal uncertainty. In a later section, we will use Eq. 6.3 for a proper determination of planet-mass range within our parameter survey.

6.2.2 HD70642

As allready mentioned within the thesis introduction, Carter et al. (2003) announced the existence of a planet within HD70642 using the Anglo-Australian Telescope facility. As a result of the long observation baseline and constant precision measurements, HD70642b marks the onset of emergence of planets in orbits characterised by long-periods and low eccentricities. HD70642 is frequently monitored within the Anglo-Australian Planet Search Program and data aquisition has been ongoing during a time period of 5 years. A total of 21 radial velocity measurements have been obtained using an ECHELLE spectrograph with a radial velocity measurement precision of 3 ms^{-1} during observations. Further details concerning this search program are located under the following URL: http://www.aao.gov.au/local/www/-cgt/planet/aat.html.

All 21 spectroscopic measurements for the reflex motion of the host star, are shown in Fig. 6.1 over the observation period. The sinusoidal line represents the best 2-body Kepler fit, according to the induced velocity signature within the center-of-mass frame of the system.

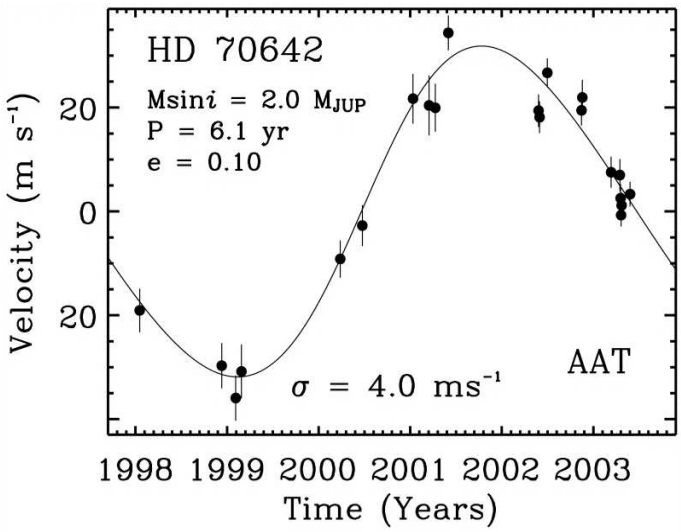

Figure 6.1: Radial velocity curve for HD70642 spanning a time period of 5 years. Here, P measures the orbital period, e orbit eccentricity and $M \sin i$ is the projected minimum mass of the observed planet companion. The root mean square of the observations is $\sigma = 4.0\ ms^{-1}$. The velocity amplitude of the reflex motion is $K = 32\ ms^{-1}$. The figure is reproduced from Carter et al. (2003).

Orbital parameters for this system, including observational uncertainty ranges, are listed within table 6.1. Physical properties of the host star are obtained by either photometric or spectroscopic observations (Carter et al., 2003, and references therein). HD70642 is a Solar-like star of spectral type G5 with a surface temperature $T_{\text{eff}} = 5670 \pm 20$ K. The mass of HD70642 is $1.0 \pm 0.05\ M_{\odot}$ and its age is estimated to be 4×10^9 years. The metallicity of HD70642 is consistent with the majority of observed host stars harboring planets and is metal rich relative to the Sun with [Fe/H] = 0.16. For comparison, the Sun is of spectral type G2 with a surface temperature $T_{\text{eff}} = 5770\ K$ and age 4.5×10^9 years.

6.2.3 HD4208

The presence of a single Jupiter-like planet within HD4208 was announced by Vogt et al. (2001), based on observations obtained within the Keck precision Doppler survey under the Keck Planet Search Program (http://planetquest.jpl.nasa.gov/-

Keck/keck_index.html). A total of 35 radial velocity measurements have been obtained for this system over a time period of 4.9 years, covering 2 orbital periods for the observed planet. Using the HIRES echelle spectrometer, a radial velocity measurement precision of 3 ms^{-1} is obtained for the observations.

Fig. 6.2 shows the radial velocity measurements as a function of time during the survey program. The sinusoidal line represents a best 2-body Kepler fit. The minimum mass for this system is nearly a factor of 2 smaller compared to HD70642. Additional orbital parameters derived from the synthetic Kepler fit, are listed within table 6.1.

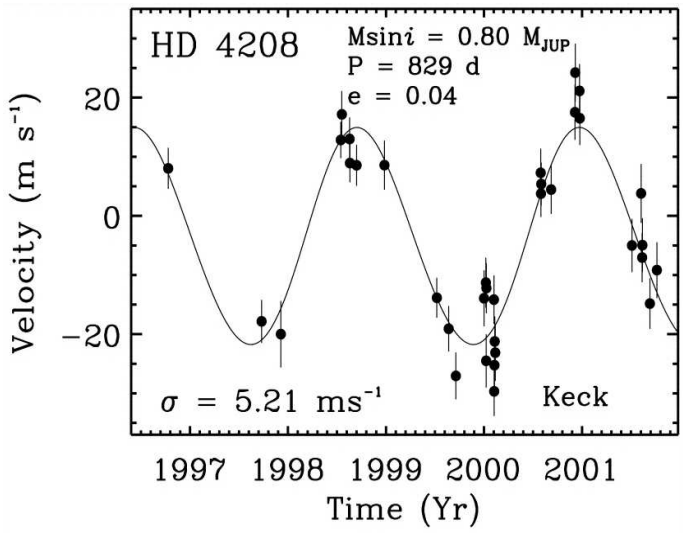

Figure 6.2: Radial velocity curve for HD4208. The sinosodial line represents a 2-body Kepler fit with orbital period of 829 days, eccentricity $e = 0.04$ and velocity amplitude $K = 18.3ms^{-1}$. The goodness of fit is $\sigma = 5.21ms^{-1}$. The figure is reproduced from Vogt et al. (2001).

Information on properties of the host star is based on Strömgren photometry, *Hipparcos* astrometric measurements and Keck-HIRES spectral observations (Vogt et al., 2001, and references therein). The star HD4208 is a Sun-like star of spectral type G5V with an estimated mass of 0.93 $M_{\odot}$ and metallicity [Fe/H] = −0.21. In addition, HD4208 is included within the Geneva-Copenhagen star survey program (Nordström et al., 2004). Based on observed parameters, Nordström et al. derive a stellar mass within the range $0.82-0.95M_{\odot}$ with effective temperature $T_{eff} = 5572$K in close agreement with the results of Vogt et al.. However, no estimate on stellar age is published within the literature. Preliminary calculations using stellar evolution models indicate an age of 4.5 ± 0.5 Gyrs (Southworth, 2005). Unfortunatly, the process of age determination, using isochrone fitting, is not reliable for certain stars including HD4208. Following Nordström (Private communication, September 2005.

Astronomical Observatory, Copenhagen) the isochrone evolutionary tracks are too dense and observed parameters too uncertain in order to reliably determine the age of HD4208. A formal uncertainty range for the age of HD4208 is $0 - 9 \times 10^9$ years.

Parameters	HD70642b	HD4208b
a (AU)	3.3 ± 0.4	1.68 ± 0.05
e	0.1 ± 0.06	0.04 ± 0.12
ω ($^\circ$)	277 ± 75	301 ± 84
$M_{pl} \sin i$ (M_{Jup})	2.0	0.80
P (days)	2231 ± 400	829 ± 36
K (ms^{-1})	32 ± 5	18.3 ± 2
τ (JD)	2451749 ± 300	2451774 ± 197

Table 6.1: Derived orbital parameters from synthetic Kepler fits for the observed planets HD70642 and HD4208 (Vogt et al., 2001; Carter et al., 2003). From Kepler's law of planetary motion, the uncertainties in the semi-major axis have been obtained from the corresponding uncertainties in the orbital period, using the stated value of the minimum masses in each system. Minimum masses of order $M_{pl} \sin i \sim 10 M_{jup}$, have an effect on the semi-major axis of order $\Delta a \sim 10^{-2}$ AU. Within the litterature, the time of periastron date (introduced in chapter 2) is often denoted by T_0. For consistency with previous notation, we will use τ to denote the periastron date. A final remark concerns the uncertainty range in eccentricity for the system HD4208. Formally, the lower bound in eccentricity assumes a negative value, which is clearly unphysical. This is probably explained by details within the fitting method applied to derive orbital parameters.

6.3 Determination of the habitable zone

6.3.1 A simple model

In order for liquid water to exist on a planet (with surface pressure $p \sim 1$ atm) the average surface temperature must be within the range 273 K $\leq T_{pl} \leq$ 373 K. Assuming a simple energy budget model for thermal properties of the planet, we can estimate the habitable zone (HZ: $r_{min} = r(T_{pl} = 273 \text{ K})$ and $r_{max} = r(T_{pl} = 373 \text{ K})$), in terms of planetary and stellar parameters. The following discussion is taken from Clark (1998). If A measures the albedo and f denotes the absorbed heat circulation factor for a planet at radial distance r, then

$$r = \frac{R_\star T_\star^2}{2\, T_{pl}^2} \sqrt{f(1-A)}, \tag{6.4}$$

where $R_\star$, $T_\star$ denotes the stellar radius and effective temperature respectively. Following Clark, the albedo (ratio of absorbed and reflected radiation) of an Earth

like planet is extrapolated from measurements of terrestial planets within the Solar System and the circulation factor accounts for a temperature gradient between the day/night hemispheres for a rotating planet. The habitable annulus within the Solar System can be calculated from Eq. 6.4, using stellar parameters $R_\star = R_\odot$, $T_\star = T_\odot$, and $A \sim 0.5$, $f \sim 1$ for the terrestrial planet (numerical values adopted from Clark (1998)). The inner and outer radius (or equivalently, the minimum and maximum radius) are calculated to be $r_{in} = 0.39$ AU and $r_{out} = 0.73$ AU. The model clearly underestimates the range of habitability, since the only habitable planet within the Solar System is Earth at ~ 1 AU. Within the next sections we will determine more accurate boundaries of the habitable zone based on a more detailed atmospheric model of the habitable planet.

6.3.2 Habitable stable orbit constrains

The confinement of a planet's orbit to within a given annulus (see Fig. 1.7), imposes some constraints on the orbital parameters (a, e) for that planet. At some osculating time, the orbit has a well defined periastron and apoastron distance (which are equal to each other for circular orbits). It follows from the conservation of angular momentum, that for increasing eccentricity (at constant semi-major axis) the pericenter distance $a(1-e)$ becomes smaller while the apocenter distance $a(1+e)$ becomes larger. Therefore, we must have some *upper limit in eccentricity, for a given semi-major axis*, in order to confine the orbit into a predefined concentric region defining the habitable zone. The corresponding conditional constrain equations are given by

$$r_{in} \leq a(1-e) \leq r_{out} \quad \text{and} \quad r_{in} \leq a(1+e) \leq r_{out}. \tag{6.5}$$

Fig. 6.3 represents the habitable zone within (a, e)- space for the two planetary systems under study and reflects a graphical representation of the constrain equations Eq. 6.5. Numerical values for the inner and outer radius of the habitable annulus are calculated from the simple energy budget model. Although this model is incorrect for the determination of the habitable zone boundaries, I will use it to outline the interpretation of the habitable zone boundaries expressed within (a, e)-space. In Fig. 6.3, contourlines represents the inner and outer boundary of the habitable annulus. The lower triangle marks the region of habitability. Planetary orbits restricted within this (a, e)-triangular region are defined to be within the habitable zone. All orbits confined to within this region are defined to be *habitably stable*. Within this thesis, we will use this criterion to ascertain wether orbits are habitable or not during a given time interval.
Considering the left panel within Fig. 6.3, e_{max} is the maximum allowed eccentricity for an orbit with indicated semi-major axis $a = 0.55$ in order to remain within the

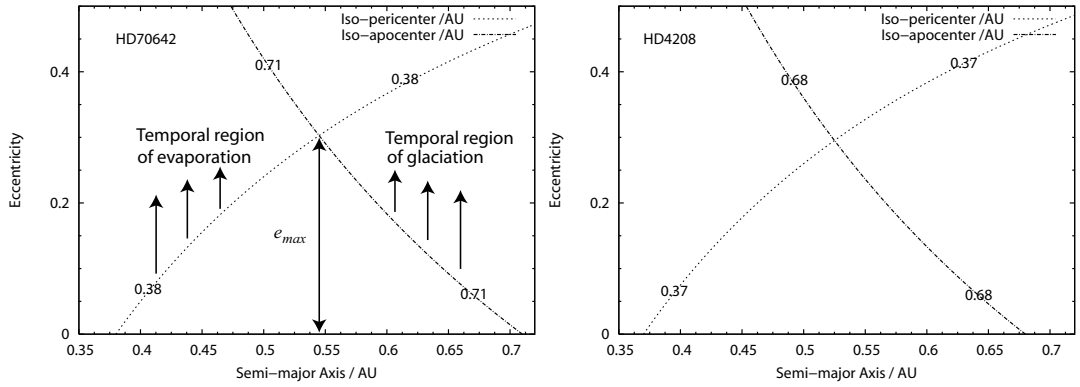

Figure 6.3: Graphical representation of the habitable zone annulus within (a, e)-space for HD4208 (left) and HD70642 (right). The extend of the habitable zone is almost similar for both systems (and the Solar System) and are valid for current age and surface temperature of the host stars. Inner and outer radius are calculated using the simple energy budget model. The iso-pericenter contour line (dashed line) marks the inner edge of the habitable zone and the iso-apocenter contour line (dashed-dotted) marks the outer edge. e_{max} denotes the maximum eccentricity allowed for a planetary orbit in order to be confined to within the habitable annulus at $a = 0.55$ AU. From the figure, $e_{max} \sim 0.3$. For further information see thesis text.

habitable zone. Orbits with $a < 0.55$ and eccentricities exceeding the inner boundary (iso-pericenter contour line) have their pericenter distance located closer to the host star than the inner edge of the habitable zone. A similar geometric picture is obtained for the region $a > 0.55$. Orbits with eccentricities exceeding the outer boundary (iso-apocenter contour line) have their apocenter distance located beyond the outer edge of the habitable zone. For the case $a = 0.55$ with eccentricity greater than e_{max}, we have both the pericenter and apocenter distance exceeding the inner and outer boundary of the habitable zone, respectively. As a consequence a planet not confined to within the habitable zone will experience temperature changes of temporary character. Depending on the orbital semi-major axis, a planet can experience either periods of warm or cold climate (or both, if $a = 0.55$) because of the variation of stellar energy flux outside the habitable zone region. The discussion of the energetic effects on planet climate is complicated further, since the duration of the periastron passage is smaller than the duration at apoastron distance. Considering the case with $a = 0.55$ and $e > e_{max}$ cold periods (of longer duration) marked by extensive glaciation (ice age periods) are alternated with short periods of relative warmth.

6.3.3 Aspects of the Kasting et al. climate model

In their one-dimensional radiative-equilibrium climate atmospheric model, Kasting et al. (1993) calculated the boundaries of the HZ for the Sun and some main sequence stars, assuming water rich Earth-like planets with $CO_2/H_2O/N_2$ atmospheres. Kasting et al. apply several theoretical criteria to define the inner and outer boundary of the habitable zone. The general strategy to find the criteria is to state enviromental conditions for a terrestial like planet, which keeps surface water in its liquid form. A planet located too close to the star will result in evaporation and too far away will result in glaciation of all surface water.

The *inner edge* of the HZ were defined by the onset of the formation of a moisty atmosphere. In order of decreasing radial distance these criteria are: 1) *Water loss limit.* By photodissociation or photolysis, water is gradually lost by hydrogen escape into space. This occurs in an atmosphere warm enough to have a wet stratosphere. 2) *Runaway greenhouse limit.* Water vapour enhances the greenhouse effect and therefore promotes surface warming. This increases the atmospheric vapour content, increasing the surface temperature. At the critical point of water (647 K), all surface water starts to evaporate into the atmosphere. Subsequently, all water is then (in a runaway manner) lost from the upper atmosphere by hydrogen escape.

The *outer edge* of the HZ were defined by the distance of a planet at which CO_2 and other greenhouse gases no longer can compensate the lower solar flux, resulting in a glaciation of all surface water. In general the role played by carbon dioxide concentration in Earth's atmosphere is important in controlling the surface temperature and thus the extent of the HZ. For example, decreasing the atmospheric carbon dioxide level, decreases the absorption of surface reflected infrared radiation, resulting in a surface cooling of the planet. The amount of atmospheric carbon dioxide on a life-less planet is controlled by the carbonate-silicate cycle. Two reaction mechanisms are important to operate the cycle: decarbonation and silicate weathering. Decarbonation releases carbon dioxide into the atmosphere by thermally decomposing carbon-containing rocks in crustal subduction zones at high temperatures and pressure or by volcanic outgassing. The reverse direction (silicate weathering) removes carbon from the atmosphere by dissolving carbon dioxide in atmospheric water to produce carbonic acid (also known as acid rain), which reacts with silicates in surface rocks by weathering.

The existence of the carbon-silicate cycle (on planet Earth) greatly extends the width of the HZ acting as a natural thermostat: at greater radial distance the silicate weathering reaction mechanism ceases because of loss of atmospheric water vapour in form of glaciation (water ice). This reduction of atmospheric water results in the accumulation of carbon dioxide within the atmosphere. In particular, the decarbonation mechanism maintain operation due to plate tectonics and vulcanism, continously enriching the atmosphere with carbon dioxide. This results in a global

planetary warming (greenhouse effect) maintaining habitability at greater stellar distances.

In order of increasing radial distance the outer edge criteria are: 3) *first* CO_2 *condensation limit*. For a surface temperature of 273 the distance at which carbon dioxide clouds first begin to form and 4) *maximum greenhouse limit*. This is the maximum distance at which a surface temperature of 273 K can be maintained by a cloud-free carbon dioxide atmosphere, i.e the point where there would be enough carbon dioxide and water in a planet's atmosphere to raise surface temperatures to 273 K.

Within the climate model, Kasting et al. allows the possibility of planetary thawning and is denoted by "planetary cold starts". Model calculations including the allowance of "cold starts" means that planets initially formed beyond the outer region of the habitable zone, will start to warm up for a critical high stellar luminosity. Fig. 6.4 describes the time evolution of the habitable zone without allowing cold starts. Kasting et al. argues that a model calculation assuming the allowance for possible planetary cold starts are to some extend questionable (cf. discussion within section 5v in Kasting et al. (1993)). Accordingly, we will consider model calculation without considering the possibility of planetary cold starts. In Fig. 6.4 (left panel) the width of the habitable zone within the Solar System is decreasing with time for a $1M_{\odot}$ Solar like star. For the most conservative estimate of the boundaries (dashed line) the habitable zone is ceased after 7 Gyrs. At the end of the main sequence period the habitability width for the most optimistic boundary estimate (dotted line) is 0.21 AU and centered at 1.39 AU.

The current width of the Solar System habitable zone can be estimated using the intermediate boundary criteria (solid line). At time 4.5 Gyrs the inner and outer edge are located at $r_{in} \sim 0.84$ AU and $r_{out} \sim 1.41$ AU, respectively. Compared to values for the range of habitability adopted from the simple energy budget model, it is apparent that the simple model underestimates the zonal habitability range for main sequence stars.

6.3.4 The habitable zones of HD70642 and HD4208

As demonstrated the simple energy budget model underestimates the range of the habitable zone. Within this thesis we adopt numerical estimates for the habitable zone from model calculations within the Kasting et al. paper. Kasting et al. provides estimates of the time evolution of the habitable zone for different stellar masses shown in the right panel in Fig. 6.4. In general, we use the intermediate estimates for the habitable zone boundaries (runaway greenhouse and maximum greenhouse limits).

For the case of HD4208 the zonal range of habitability is determined by linear interpolation between the 0.75 $M_{\odot}$ and 1.0 $M_{\odot}$ boundary evolution lines in Fig. 6.4

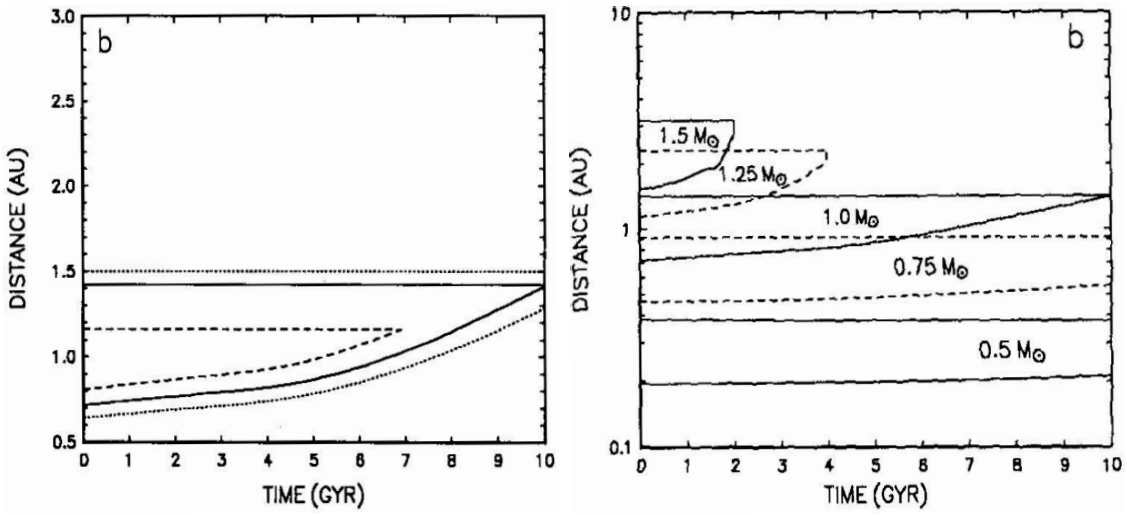

Figure 6.4: Left panel: Time evolution of the width of the habitable zone for a 1 $M_{\odot}$ star using a Iben's solar evolution model (see ref. within Kasting et al. (1993)). Three different criteria for the region of habitability are shown. a) *Water loss* and *1st CO_2 condensation* limit (most conservative estimate, dashed lines), b) *runaway greenhouse* and *maximum greenhouse* limit (intermediate estimate, solid lines) and c) *recent Venus* and *early Mars* (most optimistic estimate, dotted lines). The last habitability estimate (c) is not discussed within this thesis and details can be found in (Kasting et al., 1993, section 3). Right panel: Evolution of the habitable zone (using the intermediate estimates for the habitable boundaries) for main sequence stars of various masses. Note that the 1 $M_{\odot}$ evolution matches the intermediate boundaries (solide line) within the left panel figure. The figures are reproduced from Kasting et al. (1993).

(right panel). From this the initial ZAMS[1] and current boundaries of the habitable zones are determined, assuming a 0.9 $M_{\odot}$ stellar mass and current age of 5.0 Gyrs. For the case of HD70642 the boundaries are adopted directly from the Fig. 6.4 using the 1 $M_{\odot}$ zonal evolution model. The current width of the habitable zone is determined by adopting a stellar age of 4 Gyrs.

Fig. 6.5 represents boundaries for the current and ZAMS habitable zone for HD4208 and HD70642 as determined from Kasting et al.. The current inner and ZAMS outer boundary marks the (a, e)-parameter space for the continuouse habitable zone (CHZ). The zonal radius of habitability increases because of an increase in stellar luminosity during the main sequence evolution period. A planet initially formed and subsequently dynamically confined within the CHZ region, is habitable throughout the lifetime of the host star.

[1]ZAMS = zero-age main sequence, i.e $t = 0$yrs

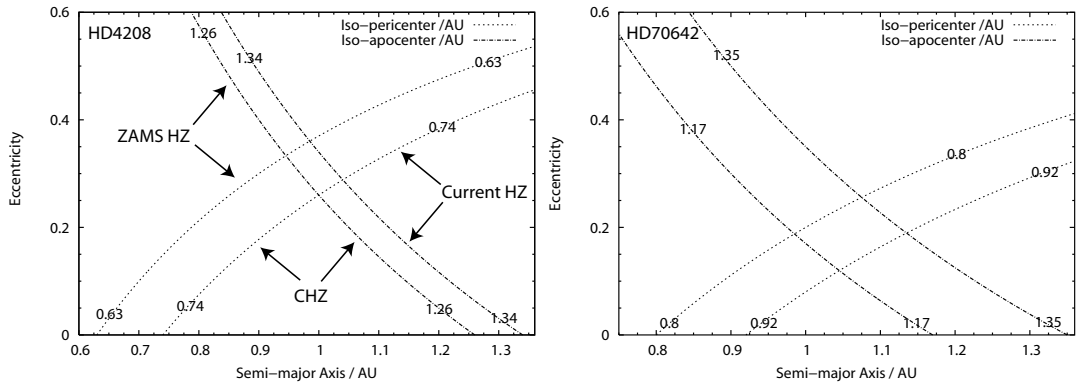

Figure 6.5: Zonal boundaries for the habitable zone for HD4208 (left) and HD70642 (right) within (a, e)-parameter space. Boundary radii are determined from Kasting et al. (see text for details). ZAMS HZ refers to zero-age main sequence boundaries (initial boundaries) and CHZ refers to the continuouse habitable zone. The current HZ are determined from the current estimated age of the host star. Planets with orbital (a, e)-parameters within the inner triangle are habitable during the lifetime of the host star. Comparing the CHZ for HD4208 and HD70642 it is seen that the CHZ for HD70642 is much smaller than the CHZ for HD4208.

6.4 Summary

In this section, we have introduced and discussed technical aspects of Kepler orbit fitting method to radial velocities obtained from spectroscopic observations. From measured radial velocities the orbital parameters for HD4208 and HD70642 have been presented. Fundamental physical properties of the host stars were mentioned and necessary parameters for the determination of the habitable zone discussed. The habitable zone(s) for both systems were introduced in more detail and the corresponding boundaries in (a, e)-space were derived and explained. We have adopted the conservative Kasting et al. (1991) model for the determination of the extend of the habitable zonal boundaries. For the star HD4208, we assumed an current age of 4 Gyrs. Also, we have discussed problems in the determination of the current age for HD4208.

Chapter 7

Parameter survey, simulations and results

7.1 Introduction

Up to this time we have introduced, described and tested various numerical methods for studying dynamical aspects of the three-body problem. Within this chapter, we will use and apply these methods for studying stability properties of test particles within the habitable zone of two selected extrasolar planetary systems. Results from numerical experiments are presented considering giant planets observed around the stars HD70642 and HD4208. For clarity, we consider and study the subsequent time evolution of Earth sized planets after the late stage of planet formation and assume that Earth like planets have been formed within the terrestrial region of extrasolar planetary systems. Test particles are used to model terrestrial planets and are characterised by being mass less. This assumption is justified because the perturbation of an Earth mass planet on the orbital elements of a giant planet is small. Within numerical experiments, I will use the MEGNO indicator to study chaotic dynamics of the three-body problem and infer direct numerical integration of test particles to follow the dynamical evolution of the orbit.

Our leading question will be: "within a given system (HD70642 or HD4208) and under the gravitational perturbation of a giant planet, is it possible that terrestrial planets (test particles) follow dynamically stable orbits within the continuous habitable zone?". Orbital elements of the giant planets have been introduced. My strategy will be a systematic parameter survey of giant planet orbital elements using simplifying assumptions. The subject is to study the effect of giant planet orbital parameters on the dynamical behavior of test particles within the habitable zone. This approach seems obvious, since orbital elements derived from one-planet Kepler fits to radial velocity observations are characterised by a large uncertainty range.

Especially, the radial velocity method is unable to determine the true mass of the detected planet and the derived orbital eccentricity is not well constrained. The general approach for numerical experiments, is to consider the time evolution of orbital elements of a large number of particles (2×10^3) on a small time scale (10^6 years). Additional numerical integrations of single (selected) particles are then performed over time scales of $10^8 - 10^9$ years in order to gain some understanding of the long-term dynamics of terrestrial planets within the systems. At the end of this section, a comparative discussion of the systems HD70642 and HD4208 will be presented. Final concluding remarks of the thesis will be given in the next chapter.

7.2 A final test: The Solar System

A final test to infer the reliability of the `Mercury6` integration code is the reproduction of the time evolution of the orbital elements of planets within the Solar System.
The long-term dynamical behavior of the Solar System has been extensively studied since mid 1980. In the following, I will compare the outcome of numerical simulations with the results obtained by Ito and Tanikawa (2002) and Brasser (2003) using identical initial conditions. Perturbations of *all* planets within the Solar System are considered and initial conditions have been obtained from the JPL Horizons Ephemeris Generator. The hybrid mixed-variable symplectic integrator is used to integrate the equations of motion. The total time span of numerical integration is 2×10^6 years. This choice is convenient for a direct comparison, in order to match the presented results within Brasser (2003). During integration the maximum change in relative energy was $dE/E \simeq 10^{-8}$ indicating an acceptable limit for reliable numerical results. Fig.7.1 represents the obtained results showing the time evolution of the orbital eccentricity and inclination for all terrestrial planets and Jupiter. Comparing the time evolution of the planets eccentricity with (Brasser, 2003, fig.1.3), we find a close agreement in both the qualitative and quantitative behavior. However, comparing the time evolution of orbital inclinations reveals a mismatch in magnitude and qualitative behavior. This difference is *not* due to failure in the numercial method and is explained by the different use of coordinate systems within which the orbital elements are represented (Brasser, 2005) (private communication). The coordinate system used by Brasser (2003), to express the time evolution of orbital elements, is the so-called fundamental plane, which uses the location of the total angular momentum as the origin. The elements within Fig. 7.1 are expressed with respect to the heliocentric frame of reference, which explains the difference.

Within Fig.7.1 the oscillatory variations of the eccentricity and inclination are shown for the inner planets and Jupiter. From the figure, it is noted that there exist a strong dynamical coupling between Earth and Venus. Both the eccentricities

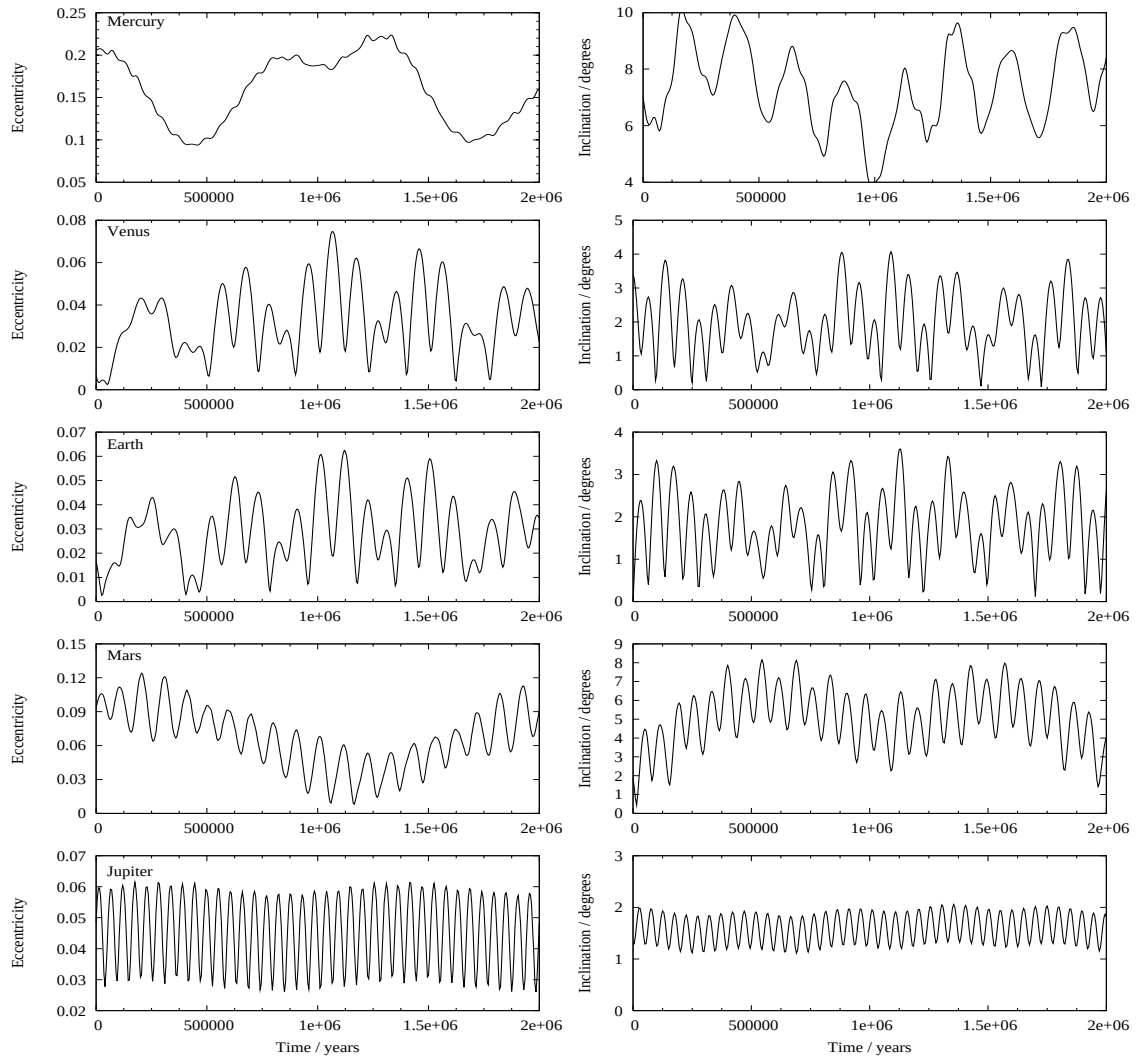

Figure 7.1: Plot of orbital elements (e, i) for some planets within the Solar System. The time evolution of the eccentricity and inclination for all terrestrial planets (Mercury-Mars) and Jupiter are shown. The total integration time span is 2×10^6 years.

and the inclinations are correlated. Peak values in both quantities occur at same times. According to Brasser (2003) the secular (long-period) oscillations in e and i for Mercury and Mars are caused due to perturbations from Venus and Earth, respectively. Also, the short-period oscillations for Jupiters orbital eccentricity and inclination can be attributed to perturbations by Saturn (Saturn's time evolution of orbital elements are not shown within Fig. 7.1). However, the secular variations of Jupiter's elements are due to the presence of Uranus (Brasser, 2003).

In order to study the dynamical behavior of mass less particles within the Solar Systems habitable zone, a multi-particle simulation have been performed over 2×10^6 years, considering perturbations of all 9 planets. The corresponding change in orbital elements of selected planets have allready been presented within Fig. 7.1. The current habitable zone boundaries are determined from Kasting et al. (1993). Particles are initially distributed with random mean anomaly ($M \in [0°; 360°]$) within the habitable zone boundaries ($d_{in} = 0.84$ AU, $d_{out} = 1.41$ AU) on circular ($e = 0$) orbits. Plots of simulation snapshots are shown in Fig. 7.2 for 4 different evolution times. Particular snapshot times are chosen to enhance the current and subsequent dynamical evolution in the (a, e)-parameter space for the particles. The dynamical behavior is shown for 10^6 years, since the dynamical picture of the evolution is not changing much beyond this time.

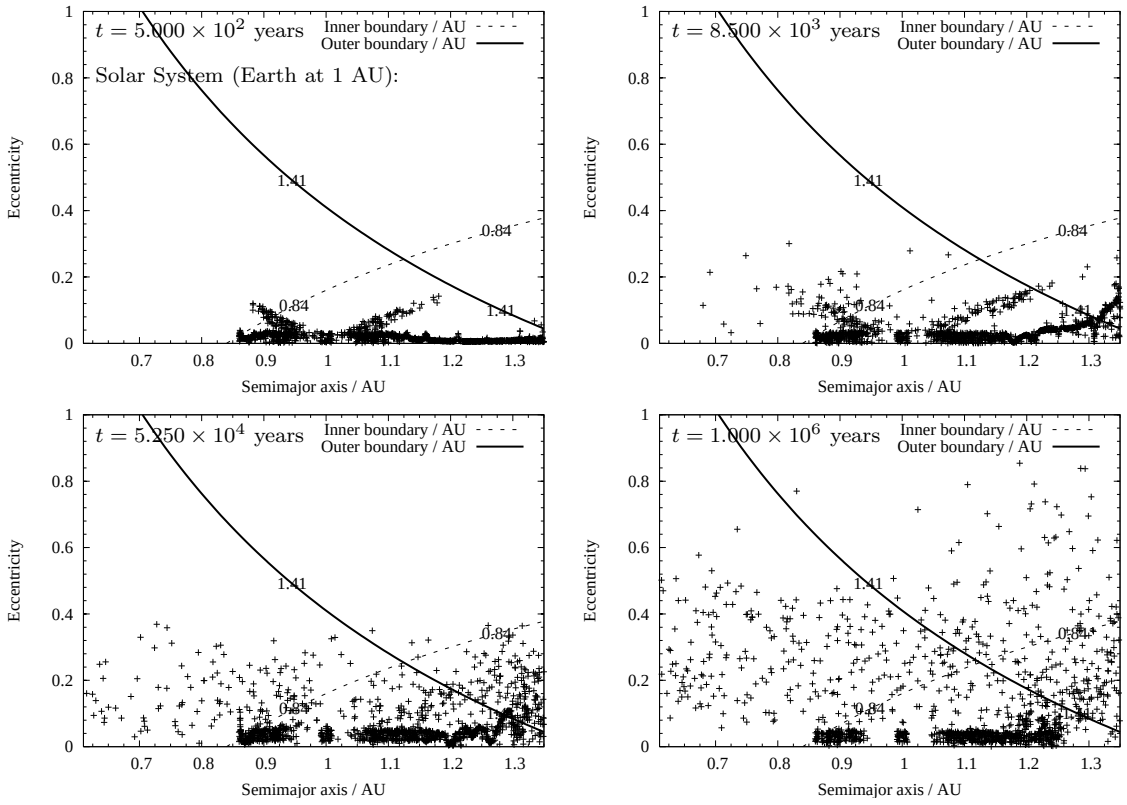

Figure 7.2: Simulation snapshots of a multi-particle simulation with 10^3 particles distributed with random mean anomalies throughout the Solar System habitable zone. The contour lines in each plot represents the inner (dashed) and outer (solid) boundaries of the current habitable zone as determined from Kasting et al. (1993). The Earth is initially located at $a = 1$ AU with $e = 0.017$.

Within figure 7.2, at time $t = 500$ years, it is seen that particles are initially ejected away from a region near $a = 1$ AU. At $t = 8.5 \times 10^3$ years the dynamical picture is characterised by orbital excitation ($a = 1.35$ AU) and radial mixing ($a < 0.9$ AU) of particles initially located around $a = 1$ AU. At time $t = 8.5 \times 10^3$ years the formation of a gap clearing is easily identified and located within and beyond the orbit of Earth. The process of radial mixing and eccentricity excitation of particle orbits continues to operate. Within the final snapshot at $t = 10^6$ years the gap clearing at $a = 1$ AU is now prominently evident. Most particles on high eccentricity orbits were initially located within this region. Particles initially located near $a = 1.35$ AU are excited possibly due to perturbations by Mars ($a \simeq 1.52$ AU). Remaining particles at $a = 1$ AU are possibly trapped near the Lagrange L_4 or L_5 stable region. This coorbital configuration resembles the same configuration as the Greek- and Trojan asteroid families observed in the 1:1 mean-motion orbital resonance state with Jupiter. At current time, no observations suggest the existence of a large population of Trojan-like objects within or near Earth's Langragian L_4 or L_5 points (Whiteley and Tholen, 1998; Veillet et al., 2001). This suggests that the integration time for the simulation is too short (even after 2×10^6 years particles remain in a coorbital state with Earth within Fig. 7.2) in order to remove the remaining particles from Earth's vicinity by the accumulation of subsequent planetary perturbations. The question on the general dynamical behavior and survival times of Lagrangian coorbital objects with Earth (or other terrestrial planets) is interesting and could form a thesis of its own. The width of the gaps located around $a = 1$ AU is approximately 0.03 AU wide. This corresponds to $3 - 4\ r_{soi}$ or $\simeq 3$ Hill's radii as introduced in chapter 4. Particles initially located near $a = 1.1$ AU remain in low-eccentric orbits ($e < 0.08$) throughout the integration time. The confinement of Earth to within the Solar Systems habitable zone is no proof of stability/habitability, since the integration time corresponds to 0.04% of the total age of the Solar System. However, long-term simulations by Ito and Tanikawa (2002) and the fact that Earth is observed to be within the habitable zone suggests the numerical reliability of the hybrid symplectic integration code within the `MERCURY6` integration package.

7.3 Parameter space and initial conditions

The total number of degrees of freedom for the general three-body problem is 9 and the system follows a trajectory in an 18 dimensional phase space. Taking into account the mass of each body, we are confronted with an 21-parameter problem. Clearly, we need some simplifying assumptions which reduces the number of free parameters of the system.

First, we consider the problem within a star-centered heliocentric frame of reference. This introduces an additional term within the equations of motion (see

discussion in section 3.3.1 and in particular eq.3.10) accounting for the motion of the star around the center of mass due to the presence of planetary perturbations. Generally, the mass of the central star will be kept constant in each numerical experiment and its numerical value is adopted from the literature.

Secondly, we consider co-planar orbits. This reduces the problem to be two-dimensional and removes 4 parameters for the orbit of each planet. In particular, co-planar orbits are characterised to have no inclination (i), and thus the nodal longitude (Ω) is undefined. This assumption is justified by the "angular-momentum" argument: for an interstellar collapsing initially rotating cloud, gas and dust material will start to form a two dimensional disk-like structure. This is a natural consequence of the conservation of angular momentum. The subsequent evolution of the disk then starts to form planets in nearly the same plane. This formation scenario is conform with observation of planets within the Solar System and with the geometric structure of observed protoplanetary disks.

Consequently, we are left with orbital parameters $(a_i, e_i, \omega_i, M_i)$ for each planet in a two dimensional three-body system (giant and Earth like planet). It is noted that the argument of pericenter ω, is only defined if $e \neq 0$. At this stage the parameter space is still large (in addition, we have the giant planet mass as a free parameter) and additional bounds on initial orbital elements seems necessary.

For the Earth mass planet we consider initial circular orbits ($e = 0$) with random mean anomalies $M \in [0°; 360°]$ within the terrestrial region $a \in [a_{min}, a_{max}]$. The exact bounds in semi-major axis for the Earth like (particle) planet depends on the extend of the habitable zone. Since we consider initial circular orbits the bounds in semi-major axis represents a constant radial distance from the central star defining an annulus for the habitable zone(s).

For the giant planet, I adopt published nominal numerical (cf. table 6.1) values for the mean anomaly M, semi-major axis a and argument of pericenter ω in all numerical experiments. Only the orbit eccentricity e and mass M_{pl} of the giant planet are considered to be free variables within a parameter survey.

The final parameter to be discussed is the mass of the giant planet. The derived mass of observed (using radial velocity measurements) giant planets is only the minimum mass (cf. table 6.1). The true planetary mass depends on the $\sin i$ projection factor. Only if the orbital plane of an extrasolar planet is parallel to the observers line of sight. That is, only if $i = \pi/2$, the true planet companion mass is known and enables the possible observation of a transit occultation. However, observational evidence of photometric transits are currently not available for HD70642 and HD4208 and therefore the line-of-sight inclination is assumed to be less than $\pi/2$. This raises the question of the choice in the upper limit of giant planet mass to consider in a parameter survey within numerical experiments.

The functional dependence of a planets real mass on the line-of-sight inclination i, is obtained by considering the mass-function eq. 6.3. Assuming the case $M_{pl} \ll M_\star$,

we have the following (analytic) expression for the minimum mass of the planet companion

$$M_{pl} \sin i = \Big(\frac{M_\star^2}{2\pi G} \big(1 - e^2\big)^{3/2} K^3 P \Big)^{1/3}, \tag{7.1}$$

where $M_\star$ and M_{pl} is the mass of the host star and the planet respectively. K denotes the semi amplitude of radial velocity measurements and P measures the orbital period of the observed planet (in fact, it is the orbital period of the host star due to the reflex motion). e denotes the eccentricity of the planetary orbit.

Fig.7.3 represents the graphical relationship between M_{pl} and the line-of-sight inclination i for different orbit eccentricities e for the observed planets within HD70642 and HD4208. The remaining observed parameters (K, P) are taken from table 6.1. For decreasing line of sight inclinations the planetary mass is increasing.

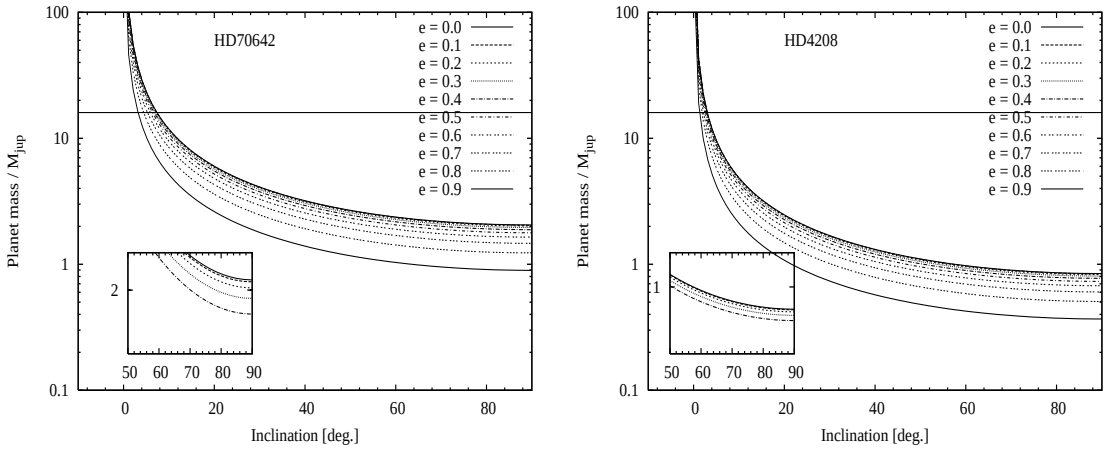

Figure 7.3: Graphical representation of eq. 7.1 showing plots of planet mass dependence on (the unknown) line-of-sight inclination for different orbital eccentricities for the giant planets within HD70642 (left panel) and HD4208 (right panel). The horizontal line indicates the $16 M_{Jup}$-mass limit for planets. Radial velocity obervations suggests an upper limit on orbit eccentricity to be $e \simeq 0.2$. Larger values in eccentricity are shown to demonstrate any effect on the mass-inclination dependency. The small in-let figures in each plot represents (i, M_{pl}) dependencies for $e = 0.0, 0.1, 0.2, 0.3, 0.4$ with $i \in [50°, 90°]$.

Within Fig.7.3 the effect of eccentric orbits on the (i, M_{pl}) dependency is illustrated for both systems under study. The range in orbital eccentricities $e = [0.0, 0.9]$ is considered. The maximum eccentricity for both planets is $e = 0.16$ as derived from observations. From the inlet figures the qualitative change in the graphs for $e = 0.0, 0.1$ and $e = 0.2$ are nearly indistinguishable. For $i = \pi/2$, the difference in mass between circular and high-eccentric orbits corresponds to a factor of two for HD70642 and HD4208. In order for the planet within HD4208 to become larger

than 1 M_{jup} (or 2 M_{Jup}) the line of sight inclination needs to be smaller than $\simeq 56°$ (or $\simeq 22°$). A similar discussion applies to the planet within HD70642.

Based on a statistical analysis on observed minimum masses of extrasolar planets Zucker and Mazeh (2001) argues that the mass distribution declines for planetary masses larger than $10 - 16\ M_{Jup}$. This result suggests an upper bound for planetary masses in extrasolar planetary systems. Within the parameter survey, we will consider giant planet masses in the range $1 - 16\ M_{Jup}$.

The following list represents an overview of initial conditions used within the numerical simulations. Two type of simulations are differentiated. 1) Simulations calculating the MEGNO indicator producing stability maps to study chaotic aspects of the three-body systems and 2) direct numerical integration of a swarm of particles under the perturbation of a giant planet.

Initial conditions - MEGNO scan simulations:

1. Host star:

   - $M_\star = 1.0\ M_\odot$ (HD70642) and $M_\star = 0.93\ M_\odot$ (HD4208).

2. Inner Earth-like planet:

   - $m_{pl} = 3 \times 10^{-3}\ M_{Jup}$.
   - $a \in [0.76; 1.43]$ AU (HD70642) and $a \in [0.57; 1.34]$ AU (HD4208)
   - $e = 0.0$ (fixed).
   - $\omega =$ undefined, (fixed to $\omega = 0.0$).
   - $M = 180°$ (fixed).

3. Outer giant planet:

   - $M_{pl} = [2.0, 8.0, 12.0, 14.0, 16.0]\ M_{Jup}$ (HD70642b) and
     $M_{pl} = [1.0, 4.0, 6.0, 8.0, 12.0, 16.0]\ M_{Jup}$ (HD4208b)
   - $a = 3.3$ AU (fixed, HD70642b) and $a = 1.68$ AU (fixed, HD4208b).
   - $e \in [0; 0.16]$ (HD70642b) and $e \in [0; 0.20]$ (HD4208b).
   - $\omega = 277°$ (fixed, HD70642b) and $\omega = 301°$ (fixed, HD4208b).
   - $M = 0.0°$ (fixed for HD70642b and HD4208b).

Initial conditions - direct particle simulations:

1. Host star:

   - $M_\star = 1.0\ M_\odot$ (HD70642) and $M_\star = 0.93\ M_\odot$ (HD4208).

2. Inner Earth-like planet:

   - 2×10^3 mass less test particles in all numerical experiments. Particles are distributed randomly within the habitable zones.
   - $a \in [0.76; 1.35]$ AU (HD70642) and $a \in [0.60; 1.34]$ AU (HD4208).
   - $e = 0.0$ (fixed), "dynamically cold", (for HD70642 and HD4208).
   - ω = undefined, since $e = 0$ initially. We set $\omega = 0$ (for HD70642 and HD4208).
   - $M \in [0°; 360°]$ distributed randomly within the terrestrial habitable region.

3. Outer giant planet:

   - $M_{pl} \in [2.0, 4.0, 12.0, 16.0] M_{Jup}$ (HD70642b)
     and $M_{pl} \in [1.0, 3.0, 12.0, 16.0] M_{Jup}$ (HD4208b).
   - $a = 3.3$ AU (fixed, HD70642b) and 1.68 AU (fixed, HD4208b).
   - $e \in [0.0, 0.16]$ (HD70642b) and $e \in [0.0; 0.16]$ (HD4208b).
   - $\omega = 277°$ (HD70642b) and $\omega = 301°$ (HD4208b).
   - $M = 0.0°$ (for HD70642b and HD4208b).

7.4 General remarks on numerical computations

In this section some remarks and practical details concerning numerical experiments are given. It is intended to explain how results have been obtained by use of different numerical integration algorithms. The general approach is first to study the chaotic properties of Earth like planets within the terrestrial region. This is done by calculating the MEGNO indicator for different initial conditions in Kepler elements. This analysis is complemented with direct numerical integration of particles over 10^6 years, for which we study the time evolution of the orbit eccentricity and semi-major axis. Finally, we study the long-term dynamics of single Earth like planets on time scales corresponding to $10^8 - 10^9$ years.

Numerical calculation of MEGNO stability maps

The MEGNO indicator is calculated using the `cs.f` program for the integration of the three-body problem. The program reads input data from two files: 1) `csi.input` and 2) `csi.elements`. The former input file holds information regarding accuracy, configuration and renormalisation parameters for the numerical integrator. Furthermore, `csi.input` hold information regarding names of data files for data output storage and scanning parameters defining the scanning range and resolution of selected orbital elements. The latter input file holds the mass of the central star and planet companions and initial Kepler elements for each planet.

Within the MEGNO computation a Gragg-Bulirsch-Stoer algorithm is used. This algorithm requires two accuracy parameters for the local error tolerance in order to determine the integration step size for a given accuracy requirement: 1) Absolut (δ) and 2) relative (ϵ) error tolerance parameter needs to be specified. Since the code uses double precision arithmetics, I adopt numerical values similar to Goździewski (2001) with numerical values given by $\delta, \epsilon = 10^{-14}$. This choice leads to relative energy errors on the order of $dE/E \simeq 10^{-12}$ during a given integration. Generally, the time evolution of energy error is characterised by a random walk. This is explained by stochastic numerical rounding errors.

The MEGNO scans explores the dynamics of Earth-like planets within the (a_{Earth},-$e_{Giantplanet}$) parameter phase space using a typical scan grid of $(N_x, N_y) = (120, 100)$. This corresponds to a typical spacing of $(\Delta a, \Delta e) = (0.0056 \text{ AU}, 0.0016)$ for each MEGNO scan. Thus, a total of 12000 initial conditions are necessary to generate a single MEGNO map. At each grid point (a_i, e_j) the MEGNO indicator $\langle Y \rangle$ is calculated. For a given range in eccentricity and semi-major axis the grid of initial conditions is given by

$$a_i = a_{min} + i\Delta a = a_{min} + \frac{a_{max} - a_{min}}{N_x} i \tag{7.2}$$

and

$$e_j = e_{min} + j\Delta e = e_{min} + \frac{e_{max} - e_{min}}{N_y} j \tag{7.3}$$

where $i = 0, \ldots, N_x$ and $j = 0, \ldots, N_y$. The calculation of MEGNO is performed row-by-row within the program. For a given giant planet eccentricity e_j the terrestrial habitable region $a_0, \ldots, a_{N_x}$ is scanned. The total integration time for each initial condition is chosen within the range $10^3 - 10^4$ P_{orb}. Here, P_{orb} is the orbital period of the giant planet and reflects the characteristic period of the system. The renormalisation time is set to 1 P_{orb} within all MEGNO calculations, as suggested by numerical experiments presented in chapter 5. On average (depending on the total number of initial conditions) the calculation of a single MEGNO stability map uses 2-3 days of dedicated CPU time on an AMD 2800+ PC. All MEGNO maps

presented in this work were calculated using the PC's within the local linux cluster. Visualisation of data and the generation of stability maps makes use of Gnuplot 4.1.

Direct numerical particle simulations

To follow the dynamical time evolution of particles under the perturbation of a giant planet the MERCURY6 orbit integrator is used. MERCURY6 reads input data from several files as described in section 4.4. Initial Kepler elements for mass less test particles are specified within the `small.in` parameter file. It is noted that no self gravitation is considered. Each particle only "feels" the gravitational potential of the giant planet. Inter-particle potentials are not evaluated within numerical integrations.

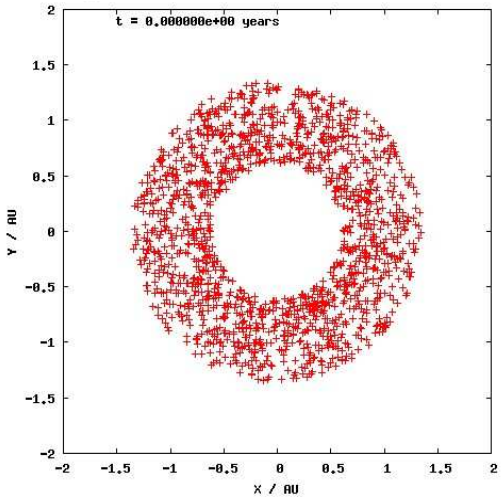

Figure 7.4: Plot of initial distribution of particles within the terrestrial habitable region of HD4208. A total of 2×10^3 particles are randomly distributed within an annulus defined by a_{min} and a_{max} on initial circular orbits.

A total of 2×10^3 particles are used. To generate the `small.in` parameter file for 2000 particles, a small `FORTRAN` program (`randomkep.f90`) have been developed to automate this process. Individual particles (Earth planets) are labelled using the format "tp0001-tp2000". All particles are initially started on circular orbits. The mean anomaly is determined at random adopting the Park-Miller random number generator (i.e adopting the `ran0(iseed)` subroutine) within Press et al. (1996). Random numbers[1] are initialized by an iseed integer parameter determined from

[1]Numerical problems have been enountered using the intrensic `FORTRAN90` random number generator!

the internal system clock. Each particle orbit is constrained to an annulus corresponding to the region of habitability. The current version of `randomkep.f90` only generates initial conditions for co-planar orbits, but the extension to the general three dimensional case is easily implemented.

Fig.7.4 represents a typical initial distribution of particles within the terrestrial habitable region. Initial conditions for the giant planet are adopted from the literature. A parameter survey considers the different giant planet eccentricity and mass. The system is then integrated for 10^6 years. Dumpfiles of integration parameters and initial conditions are generated for every 10^5 years for reasons of restarting a given integration in case of system power failure. For the hybrid mixed-variable symplectic integrator the changeover distance for detecting close approaches is set to 3 R_{Hill} radii.

During each numerical integration the corresponding relative change in energy and angular momentum have been frequently monitored and stored within a data file. In general, relative energy were always conserved to better than $dE/E \simeq 10^{-8}$. Within some simulations, in particular using the fixed step-size hybrid symplectic algorithm, some accuracy issues were encountered for high orbit eccentricities. In some cases a systematic linear decrease were observed for the relative energy. Accordingly, particular experiments were repeated by decreasing the step size in order to suffice the corresponding accuracy requirement. Within all integrations using the `MERCURY6` mixed variable symplectic algorithm a Bulirsh-Stoer accuracy parameter of $\epsilon = 10^{-12}$ were adopted for the upper bound of the local integration error.

The 2000 particle simulations were calculated using multiple CPU super computer facilities at the Danish Center for Scientific Computing and the local linux cluster. UNIX shell scripts were developed to distribute simulations automatically. Regarding computations on the linux cluster best computing performance during numerical simulations is obtained by executing the program on local machines. This is due to reasons of reducing I/O network traffic representing the bottleneck effect.

In the following, results obtained from numerical simulations will be presented. It turns out to be useful to compare the dynamical behavior of test particles for two different systems. The dynamics of terrestrial planets (modelled as test particles) are studied within HD4208 and HD70642 under the perturbation of a giant planet.

7.5 MEGNO scans: Numerical simulations and results

In order to study the chaotic nature and dynamical effect of giant planet perturbations on an Earth-mass planet, the MEGNO indicator is calculated for a range of initial conditions. The MEGNO indicator is calculated for 12×10^3 initial conditions

considering the giant planet eccentricity and the semi-major axis of an Earth-like planet as variable parameters. Within this parameter space, we will consider different mass-parameters for the observed giant planet in HD70642 and HD4208. Within the figures, to be discussed shortly, the MEGNO indicator is color coded. From the theory outlined in chapter 5, we found that initial conditions with $\langle Y \rangle \rightarrow 2$ for $t \rightarrow \infty$, corresponds to quasi-periodic motion of the Earth-like planet. For $\langle Y \rangle \neq 2$ indicated diverging or chaotic motion. Within the MEGNO stability maps quasi-periodic motion is color coded using the white color; any colors different from white indicate chaotic (erratic) dynamical behavior of the Earth-like planet at the specified initial condition. The different panels in Fig.7.5 are examples for the time evolution

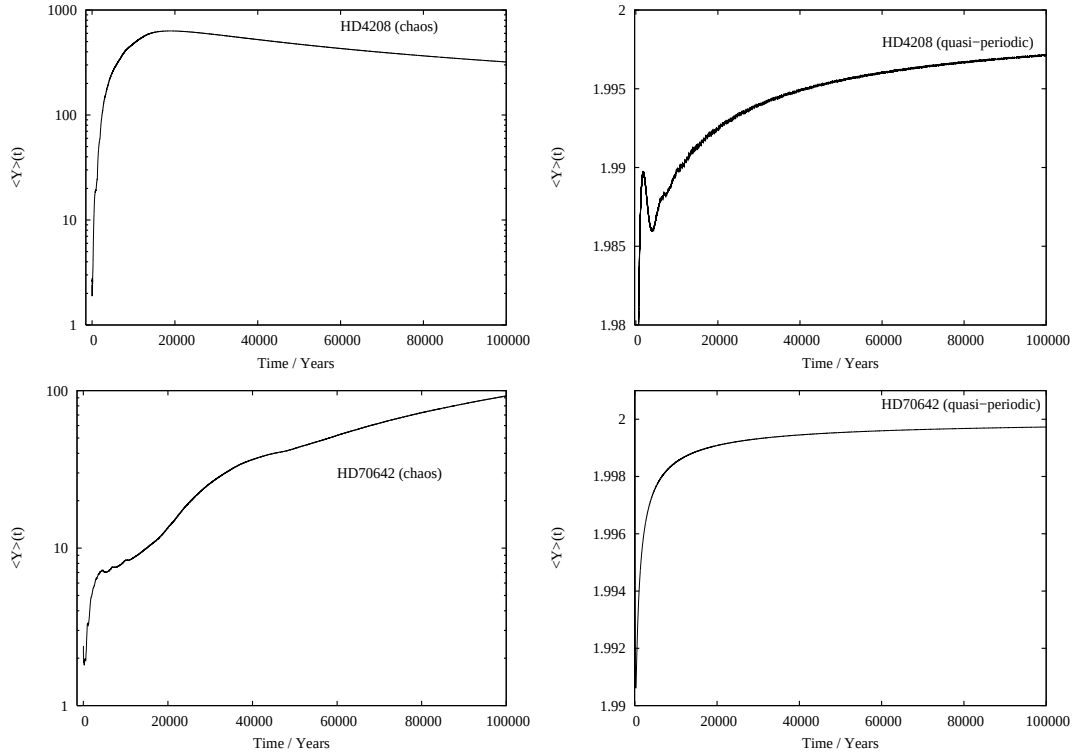

Figure 7.5: Plots of the time evolution of $\langle Y \rangle$ considering chaotic and quasi-periodic initial conditions for HD70642 and HD4208. From the theory, we have for quasi-periodic dynamics: $\langle Y \rangle \rightarrow 2$ and for chaotic dynamic: $\langle Y \rangle \rightarrow \gamma t/2$ for $t \rightarrow \infty$. Here, γ is the maximum Lyapunov exponent. The total integration time for the calculation of $\langle Y \rangle$ is 10^6 years. Initial conditions leading to chaotic dynamics are taken within mean-motion resonances. The typical integration time scale for computing $\langle Y \rangle$ within MEGNO scans for HD70642 is $t_{max} \simeq 3 \times 10^4$ years. Considering HD4208 the maximum integration time for the calculation of $\langle Y \rangle$ is $t_{max} \simeq 12 \times 10^3$ years.

of $\langle Y \rangle$ for HD70642 and HD4208. For initial conditions leading to quasi-periodic motion, it is observed that $\langle Y \rangle$ is asymptotically approaching the numerical value

of two. For chaotic dynamics $\langle Y \rangle$ is quickly diverging. The typical integration time scale for computing $\langle Y \rangle$ within MEGNO scans for HD70642 is $t_{max} \simeq 3 \times 10^4$ years. Considering HD4208 the maximum integration time for the calculation of $\langle Y \rangle$ is $t_{max} \simeq 12 \times 10^3$ years.

For the MEGNO stability maps the habitable zone(s) are superimposed within each figure. This enables a quick visualisation of the dynamics within this region. Formally the boundaries of the habitable zone(s), within the MEGNO stability maps, should be ascribed using the orbital eccentricity of the Earth-like planet as outlined in chapter 6, and should not be confused with the giant planet eccentricity.

7.5.1 MEGNO stability maps - HD70642

A total of eight scans for the computation of the MEGNO indicator have been performed for masses of the giant planet in the range $m_{pl} = 2, 4, 6, 8, 10, 12, 14$,-16 M_{Jup}. Fig. 7.6 presents the results of a MEGNO scan for four selected masses ($m_{pl} = 2, 8, 14, 16\ M_{Jup}$) of the observed giant planet within HD70642. This range in mass corresponds to a line of sight inclination within the range $i \in [10°; 90°]$ ($i = 0°$ corresponds to a pole-on (or face-on) observation of the system, in which case no doppler measurements should be detected). The MEGNO scans within Fig. 7.6 are representative and the presentation of the remaining scans have been omitted within the thesis, since the qualitative dynamical information of these is more or less equivalent to the scans shown in Fig. 7.6. As an example, plots of MEGNO scans considering giant planet masses $m_{pl} = 4, 6\ M_{Jup}$ (not shown) corresponds qualitatively to $m_{pl} = 2\ M_{Jup}$ scan within Fig.7.6 (upper left panel).

The upper left panel in Fig.7.6, considering the $m_{pl} = 2\ M_{Jup}$ MEGNO scan map, shows the initial faint appearance of discrete vertical lines located at $a \simeq 1.0$ AU, $a = 1.13$ AU and $a = 1.31$ AU. It turns out that the location of these "chaotic stripes" is not random and corresponds to orbit configurations (with specific particle semi-major axis) in which the Earth-like planet is in mean-motion resonance with the giant planet. In each MEGNO map the location of resonances are indicated and labelled by an arrow. From Kepler's law of planetary motion the location of different mean motion resonances can be calculated. If a_1 and a_2 denotes the semi-major axis of the giant and Earth like planet respectively, then

$$\left(\frac{n_1}{n_2}\right)^2 = \left(\frac{a_2}{a_1}\right)^3, \tag{7.4}$$

where n_2 and n_1 are integers and measures the mean motion of the Earth and giant planet. For example, calculating the (nominal) location of the 4:1 resonance ($n_1 = 4, n_2 = 1$), we find $a_1 = a_2/(4/1)^{2/3}$. For $a_2 = 3.3$ AU we have $a_1 \simeq 1.31$ AU. Increasing the mass of the giant planet mainly results in a strengthening of the effect of mean-motion resonances over a larger range in giant planet orbit eccentricity. This

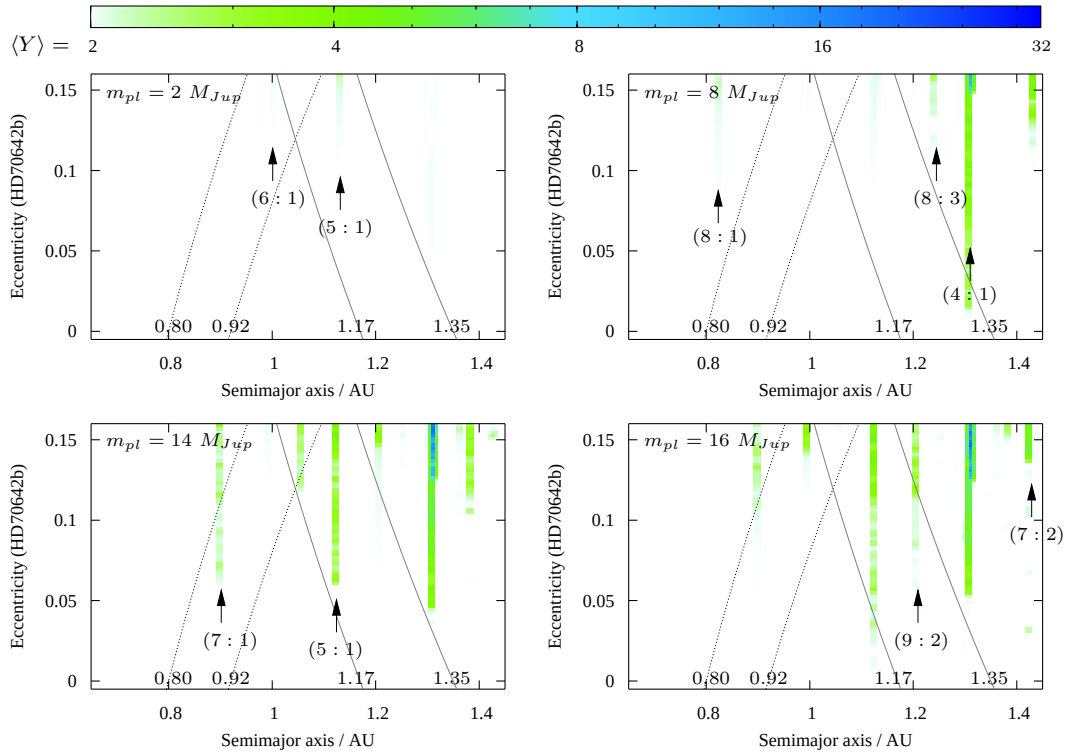

Figure 7.6: Plots representing MEGNO stability maps of an Earth-like planet initially within the terrestrial region of HD70642. Four different masses of the giant planet are considered: 2 M_{Jup} (upper left panel), 8 M_{Jup} (upper right panel), 14 M_{Jup} (lower left panel) and 16 M_{Jup} (lower right panel). The MEGNO ($\langle Y \rangle$) is color coded with "white" representing initial conditions leading to quasi-periodic motion and with any color different from white representing chaotic motion. The boundaries of the habitable zone for HD70642 are superimposed. A total of 12×10^3 initial conditions are considered using a grid of $(N_x, N_y) = (120, 100)$.

is in particular the case for the 4:1 mean-motion resonance as observed within the upper right panel in Fig.7.6. In this case the 4:1 mean-motion resonance starts to appear for almost circular orbits of the giant planet perturber. In addition, the increase of giant planet mass have the effect to give rise of the emergence of previously unseen mean-motion resonances. This is the case for the 7:1, 9:2 and 7:2 resonances within the lower left and right panel in Fig.7.6. For giant planet mass $m_{pl} = 16\ M_{Jup}$ the 5:1 resonance appears in the outer edge of the continuous habitable zone.

In general, mean-motion resonances start to appear at higher giant planet eccentricity. Initial conditions for the Earth-like planet within the continuous habitable zone of HD70642 are characterised to indicate quasi-periodic dynamics. However, it must be noted that the MEGNO stability maps only represents a portion of the

systems phase space. No information on the time evolution of the terrestrial planet's eccentricity is obtained from these scan maps. Other means need to be addressed in order to study the time variation of eccentricity for the Earth-like planet as a result of giant planet perturbations.

7.5.2 MEGNO stability maps - HD4208

Fig.7.7 shows the results of MEGNO scans within the HD4208 parameter space. Four selective scans corresponding to giant planet masses $m_{pl} = 1, 4, 6, 16\ M_{Jup}$ are presented. In all figures the habitable zone(s) are superimposed. The inner

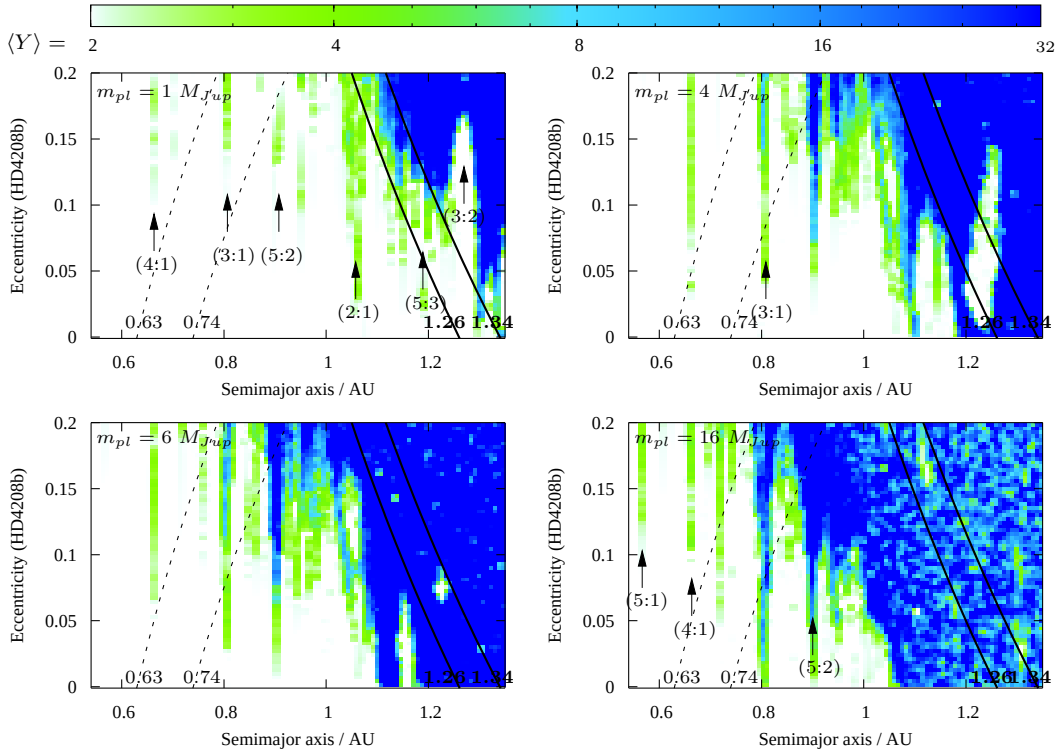

Figure 7.7: Plots representing MEGNO stability maps of an Earth-like planet initially within the terrestrial region of HD4208. Four different masses of the giant planet (m_{pl}) are considered: 1 M_{Jup} (upper left panel), 4 M_{Jup} (upper right panel), 6 M_{Jup} (lower left panel) and 16 M_{Jup} (lower right panel). The MEGNO indicator ($\langle Y \rangle$) is color coded with "white" representing initial conditions leading to quasi-periodic motion and any color different from white representing chaotic motion. The boundaries of the habitable zone for HD4208 are superimposed (and measured in AU) and a total of 12000 initial conditions are considered within the terrestrial region using a grid of $(N_x, N_y) = (120, 100)$. Locations of important mean-motion resonances are indicated by arrows.

triangular region represents the continuous habitable zone. The dynamical effect of

increasing the outer giant planet's mass is apparently observed. For $m_{pl} = 1\ M_{Jup}$ within the upper left panel in Fig.7.7, a general instability region occurs for semi-major axis greater than $a > 1.30$ AU. This instability region starts to move inward towards the center of the continuous habitable zone for larger masses of the observed giant planet. An interesting feature to note is the reduction, with increasing giant planet mass, of the stability island at $a = 1.26$ AU extending over a giant planet eccentricity range $e \in [0.0; 0.15]$.

The presence of mean-motion resonances are observed and indicated with an arrow in each MEGNO map wihin the figure panels. Of particular interest is the 2:1 mean-motion resonance located at $a = 1.05$ AU for $m_{pl} = 1\ M_{Jup}$ (upper left panel). The 2:1 resonance is "active" for almost all eccentricities of the outer giant planet. With increasing giant planet mass the continuous habitable zone becomes dominated by the 3:1, 5:2 and 2:1 mean-motion resonances. This is clearly visible for $m_{pl} = 16\ M_{Jup}$ (lower right panel) in Fig.7.7.

7.5.3 Resonance finestructure

An interesting question to follow up after studying MEGNO stability maps concerns the finestructure of the observed mean-motion resonances. What is the appearance of mean-motion resonances within a high resolution scan? In Fig.7.7 (upper left panel) the low resolved shape of the 2:1 mean motion resonance resembles a wing V-form. The width of the wing appears to be a function of giant planet eccentricity: the width increases with increasing orbit eccentricity. Furthermore, we observe several mean-motion resonances ("resonance fingers") located near and around the 5:3 resonance ($a \simeq 1.18$ AU). The exact number of resonances are not clear from the figure. A high resolution scan within this region should enhance any details of the resonance structure in this particular phase space region. In the following, we will focus on these two regions and present results from a zoomed high resolved MEGNO scan revealing the resonant fine structure for the case of giant planet mass $m_{pl} = 1\ M_{Jup}$.

Fig.7.8 shows the fine structure of the 2:1 mean motion resonance for a giant planet mass $m_{pl} = 1\ M_{Jup}$. Compared with the upper left panel in Fig.7.7, this result confirms that the 2:1 commensurability is wing-like structured with a well defined transition region from chaotic to quasi-periodic motions. An explanation for the peculiar V-shape structure is based on analytic resonance perturbation theory (Murray and Dermott, 1999). The width of the resonance at a given eccentricity is called the libration width. The semi-major axis of a planet captured within the 2:1 mean motion resonance will exhibit librations (oscillations). The extend (amplitude) of the libration depends on orbit eccentricity of the external perturber and the specific mean-motion resonance considered (cf. Fig. 8.7 in (Murray and Dermott, 1999, p.341)).

Fig.7.9 shows the fine structure of (a, e)-space in the region $a \in [1.1; 1.25]$ AU. The high resolution MEGNO scan indicates the presence of three prominent mean-motion resonances. In particular they correspond to the 9:5 ($a \simeq 1.145$ AU), 5:3 ($a \simeq 1.183$ AU) and 8:5 ($a \simeq 1.22$ AU) commensurabilities. Each resonance is located at the outer edge of the continuous habitable zone and dynamically active for near-circular orbits of the giant perturber. Again, we observe the characteristic

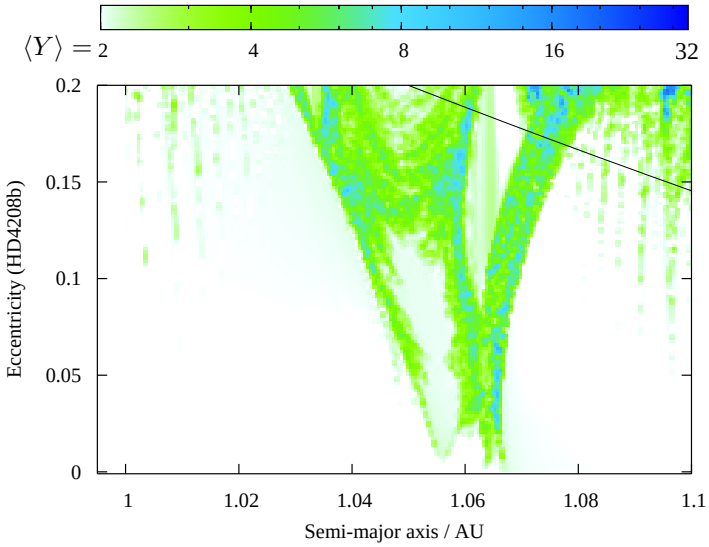

Figure 7.8: High resolution MEGNO map considering the fine structure of the 2:1 mean motion resonance. The terrestrial region is scanned within the interval $a \in [1.0; 1.1]$ AU. The mass of HD4208b is $m_{pl} = 1\ M_{Jup}$. The resolution of the scan is $(N_x, N_y) = (200, 100)$. The line represents the outer boundary ($a \sim 1.26$ AU) of the initial (ZAMS) habitable zone. In addition to the wing-like structure of the 2:1 resonance several high order mean motion resonances are identified predominantly at high giant planet eccentricities.

V-shape geometry of each resonance. Of particular interest is the 5:3 resonance line exhibiting a large O-shaped splitted region, indicating initial conditions resulting in quasi-periodic (regular) motion. In its simplest interpretation this result suggests that for certain giant planet eccentricities regular quasi-periodic motion is possible for a planet initially started with semi-major axis near $a \simeq 1.185$ AU corresponding to the 5:3 mean-motion resonance. From the figure, it is observed that chaotic motion is dominating the dynamics for giant planet orbit eccentricities $e \geq 0.14$. An explanation for this phenonmenon is not readily derivable from simple Newtonian mechanics and must be found within analytic resonance perturbation theory. Apparently this "hole-in-a-resonance" feature is not the norm. This is the case for the 9:5 commensurability exhibiting chaotic dynamics within the full range of giant

planet eccentricity.

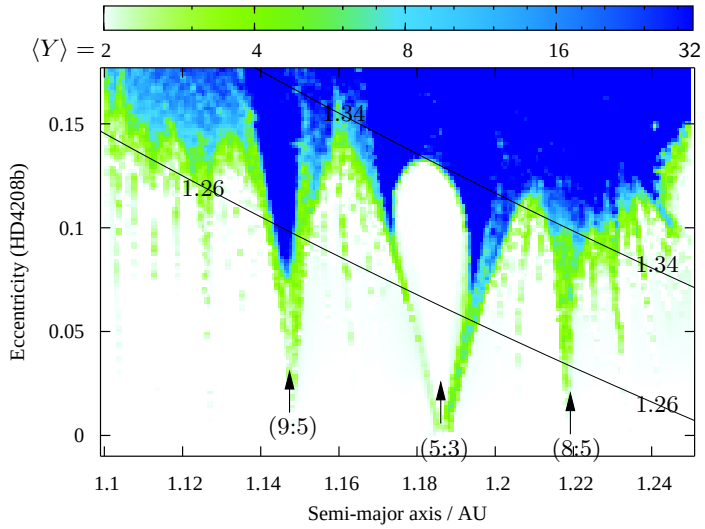

Figure 7.9: High resolution MEGNO scan considering the finestructure of the 9:5, 5:3 and 8:5 mean-motion resonance. The terrestrial region covers the range $a \in [1.1; 1.25]$ AU. The mass of HD4208b is $m_{pl} = 1\ M_{Jup}$. The resolution of the scan is $(N_x, N_y) = (200, 100)$. The two (parallel) lines corresponds to the outer boundaries of the initial (1.26 AU) and current (1.34 AU) habitable zone (cf. Fig. 7.7). The main characteristic feature is the wing V-shape of resonances with increasing giant planet eccentricity.

7.6 Numerical particle simulations

Up to this point we considered the chaotic dynamics of a particle within the terrestrial region. By studying the time evolution of $\langle Y \rangle$, we identified the presence of mean-motion resonances. However, the effect of mean-motion resonances on particle orbital elements is not clear. What is the dynamical consequence of these resonances? From the MEGNO maps, it is not possible to extract any information on the time variation of a and e for the particle orbit. It is remembered that MEGNO is a measure of exponential divergence of initially close orbits. Hence, we need to follow the dynamics of a particle initially started within the terrestrial habitable region by numerical integration. Instead of considering a single particle initially started on a circular orbit with different semi-major axis, we consider several particles and study their time evolution in (a, e) space. This approach should give

some insight on the effect of mean-motion resonances on terrestrial planet orbital elements.

In order to study the effect of giant planet perturbations on test particles as a function of giant planet parameters, direct numerical simulations have been performed using the `MERCURY6` integration package. In Fig.7.10 - Fig.7.17 and Fig.7.18-Fig.7.25 dynamical planet-particle simulation snapshots of test particles for different choices of giant planet parameters are presented. Snapshots are taken for the (a, e)-parameter space of test particles within the habitable zone representing the time evolution of test particle semi-major axis and orbit eccentricity. Each figure shows four simulation snapshots representing a total simulation time of 10^6 years. Different parameters for the giant planet are varied within a parameter survey. Parameters used in each simulation are indicated within the upper left panel in each snapshot figure. Both the giant planet's mass and eccentricity are considered as variable parameters. Four different masses for the giant planet in each system are considered. Simulations for every mass parameter are paired with two choices in eccentricities of the giant planet orbit. This produces eight simulation snapshots for each system; resulting in 16 snapshots in total for both HD70642 and HD4208. At the beginning of each simulation all particles have circular (dynamically cold) orbits and are distributed within the habitable zone with a random mean anomaly within the range $M \in [0°; 360°]$. In all simulations, a total of 2×10^3 particles are considered. The inner and outer boundaries of the habitable zone for each system, is shown in each simulation snapshot. In particular, we will focus our discussion on the continuous habitable zone. Each particle is regarded and assumed to model an Earth-like planet initially formed within the habitable zone. This assumption is justified by considering the time evolution of giant planet orbit parameters due to perturbations of an Earth-like planet. Different Earth masses have been considered in an increasing order within numerical experiments. Changes in the giant planet orbital elements have been observed only for sub-Saturn masses, indicating that Earth-mass planets can be modelled as mass less test particles. In physical terms, by considering mass less test particles only means the neglection of the perturbative back-reaction of the massive Earth planet on the giant observed planet. However, an Earth mass planet is to small to have any perturbative gravitational effect on giant planet orbital parameters.

In the following, we first consider the dynamics of particles under the perturbation of HD70642b. The results are then compared with similar simulations considering HD4208b.

7.6.1 HD70642: Numerical simulations and results

Numerical planet-particle simulations within HD70642 considers the following mass range for the observed giant planet: $m_{pl} = [2, 4, 12, 16]\ M_{Jup}$. For each mass the

eccentricity of the giant planet is varied for each numerical value in eccentricity: $e \in [0.0, 0.1, 0.16]$. Within the figures, I only present simulation snapshots for the lower and upper range in giant planet eccentricity (i.e $e = 0.0$ and $e = 0.16$). All figures representing simulation snapshots for the HD70642 system are appended at the end of this section.

In order to study the dynamical effect on particle orbital parameters for variable giant planet mass at constant giant planet eccentricity (i.e e = 0.0), we need to discuss and compare snapshot Fig. 7.10, 7.12, 7.14 and 7.16.

In order to study the effect of giant planet mass for an eccentric giant planet orbit (upper observed limit, $e = 0.16$), we need to discuss and compare Fig. 7.11, 7.13, 7.15 and 7.17.

Discussion - the case of circular giant planet eccentricity ($e = 0.0$)

In Fig.7.16, it is noted that the scale in eccentricity is changed. In general, within all snapshots we observe a periodic variation for the eccentricity of particles. This is explained by general giant planet perturbations. For increasing mass of the giant planet, we observe a higher eccentricity excitation of particles initially placed near the giant planet (i.e outer edge of the current habitable zone). The general trend at the end of each simulation, is the emergence of an "eccentricity gradient" throughout the terrestrial habitable zone.

In Fig. 7.14 and 7.16, we observe an additional (snapshots at $t = 7.0 \times 10^3$ years and $t = 7.75 \times 10^4$ years, respectively) excitation in eccentricity of some particles near $a \simeq 1.30$ AU. An explanation to this phenomenon is obtained from our MEGNO analysis (cf. Fig.7.6). At this location within the terrestrial habitable zone, we identify the presence of the 4:1 mean-motion resonance clearly visible over a large range of giant planet eccentricity. However, the MEGNO indicator does not fully exhibit the 4:1 mean-motion resonance for e(HD70642b) $\simeq 0.0$. This is an excellent example of demonstrating the limitation of a MEGNO stability analysis in general. The MEGNO indicator is capable of quickly indicating strong chaotic (unstable) dynamics. In order to detect weak chaotic motion it is necessary to prolong the time span of numerical integrations. The results suggests that dynamical weak chaos manifest itself by exponential divergence on longer time scales. It is important to note, that a MEGNO analysis is *not* capable of *proving* stable quasi-periodic motion! The indication of a quasi-periodic orbit is only quasi-periodic within the considered time period. A possible onset of chaotic behavior at later times can not be ruled out! The dynamical behavior of a particle, might show irregular (chaotic) dynamics at some later time.

Furthermore, it is observed (in particular in Fig.7.16) that the eccentricity of the particles is characterised by an transient excitation wave in eccentricity. The wave length is quickly decreasing with time. It should be noted that there is no on-

going mass-transport. The main particle dynamics is characterised by an oscillatory vertical motion at constant semi-major axis. Finally we note, that for each giant planet mass, particles are confined to within the continuous habitable zone for a circular giant planet orbit. That this is the case, even for a giant planet mass of $m_{pl} = 16\ M_{Jup}$ should be considered as a surprise. My general conception, at the beginning of the thesis period, suggested that such a giant Jupiter mass planet with $a \simeq 2 - 3$ AU and $e = 0$, would definitely render the orbit of an Earth mass planet to become inhabitable resulting in some form of orbital instability. This is not the case as simulations indicate.

Discussion - the case of eccentric giant planet orbits ($e = 0.16$)

Independent of giant planet mass, it is quickly observed that particles are rapidly excited in eccentricity up to $e = 0.16$. Comparing simulation snapshots for $m_{pl} = 2\ M_{Jup}$ and $m_{pl} = 4\ M_{Jup}$ (Fig. 7.11 and Fig.7.13), we observe no difference in the qualitative behavior of particle dynamics. In addition, we observe an initial transient excitation wave in particle eccentricity within all four simulations in Fig.7.11, 7.13, 7.15 and 7.17. The presence of mean-motion resonances are clearly visible within the snapshots, and it is observe that they cause additional particle eccentricity excitation. Comparing the upper left panel in Fig.7.13 with Fig.7.6, we can identify the following mean-motion resonances (and their locations): 7:1 ($a \simeq 0.9$ AU), 6:1 ($a \simeq 1.0$ AU), 5:1 ($a \simeq 1.13$ AU) and 4:1 ($a \simeq 1.31$ AU). Finally we note, that for a high eccentricity ($e \geq 0.16$) giant planet the orbits of particles are *not* confined to within the continuous habitable zone. This would indicate that high eccentric extrasolar planet would render the orbits of terrestrial planets, possibly formed within the terrestrial habitable region, to become inhabitable due to periodic excursions to regions outside the continuous habitable zone. In the following simulation snapshots are presented.

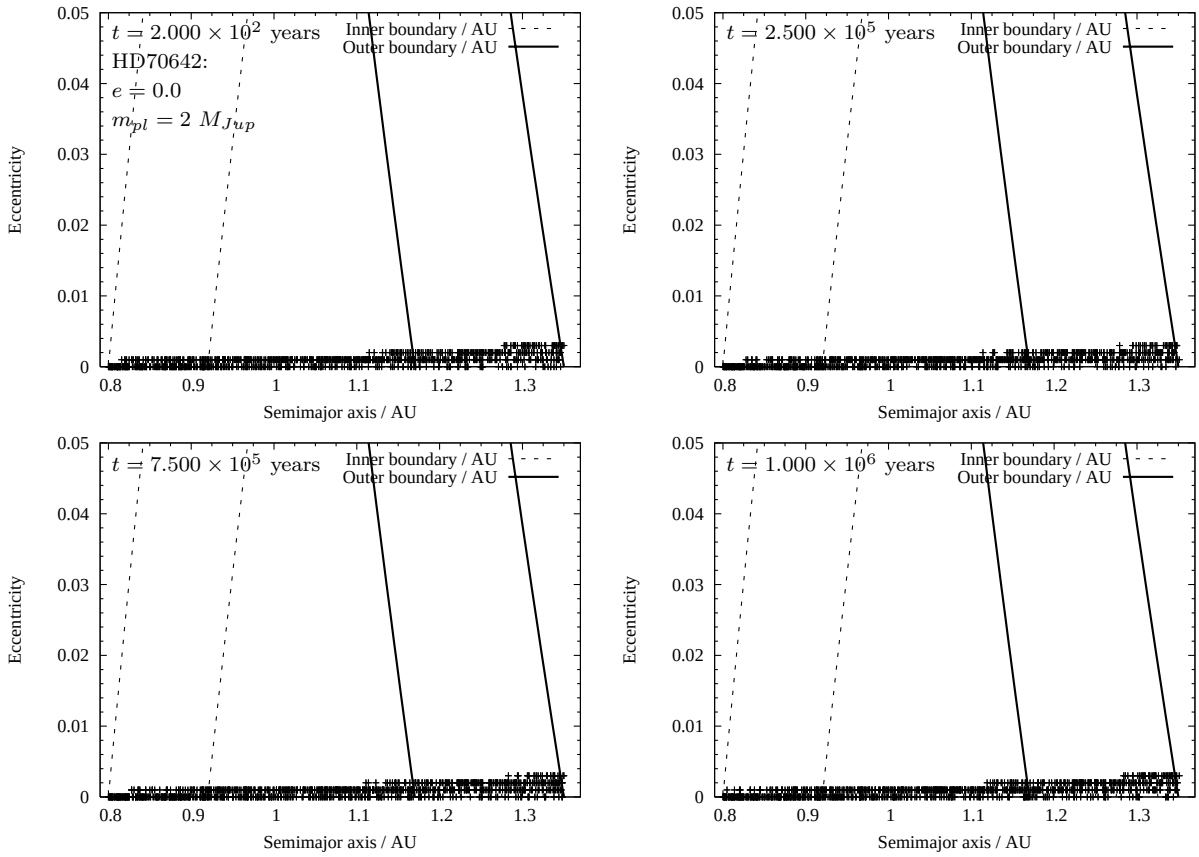

Figure 7.10: Simulation snapshots for particles in HD70642 with giant planet parameters: $m_{pl} = 2\ M_{Jup}$ and $e = 0.0$. A total of 2×10^3 particles are randomly distributed within the habitable zone. Boundaries of the habitable zone are superimposed. The continuous habitable zone is marked by the inner boundary at 0.92 AU and outer boundary 1.17 AU. The two outermost boundaries are located at 0.80 AU (inner) and 1.35 AU (outer). The total integration time is 10^6 years.

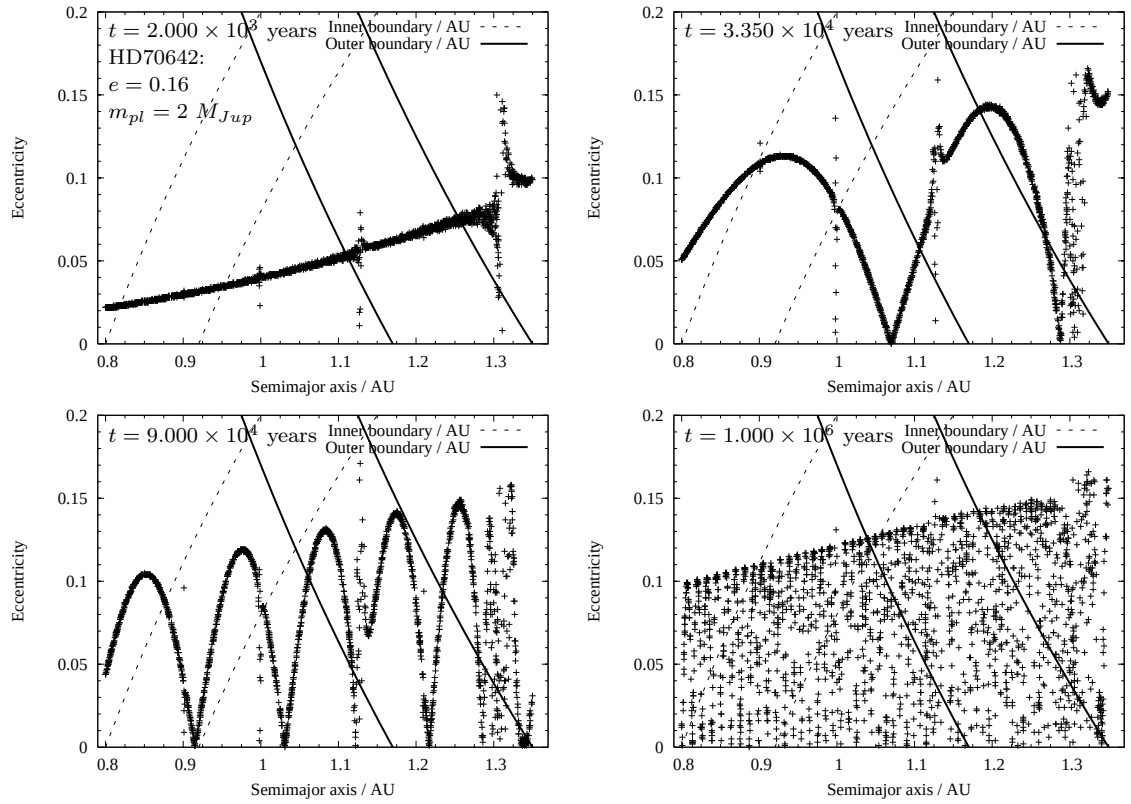

Figure 7.11: Simulation snapshots for particles in HD70642 with giant planet parameters: $m_{pl} = 2\ M_{Jup}$ and $e = 0.16$. A total of 2×10^3 particles are randomly distributed within the habitable zone. Boundaries of the habitable zone are superimposed. The continuous habitable zone is marked by the inner boundary at 0.92 AU and outer boundary 1.17 AU. The two outermost boundaries are located at 0.80 AU (inner) and 1.35 AU (outer). The total integration time is 10^6 years.

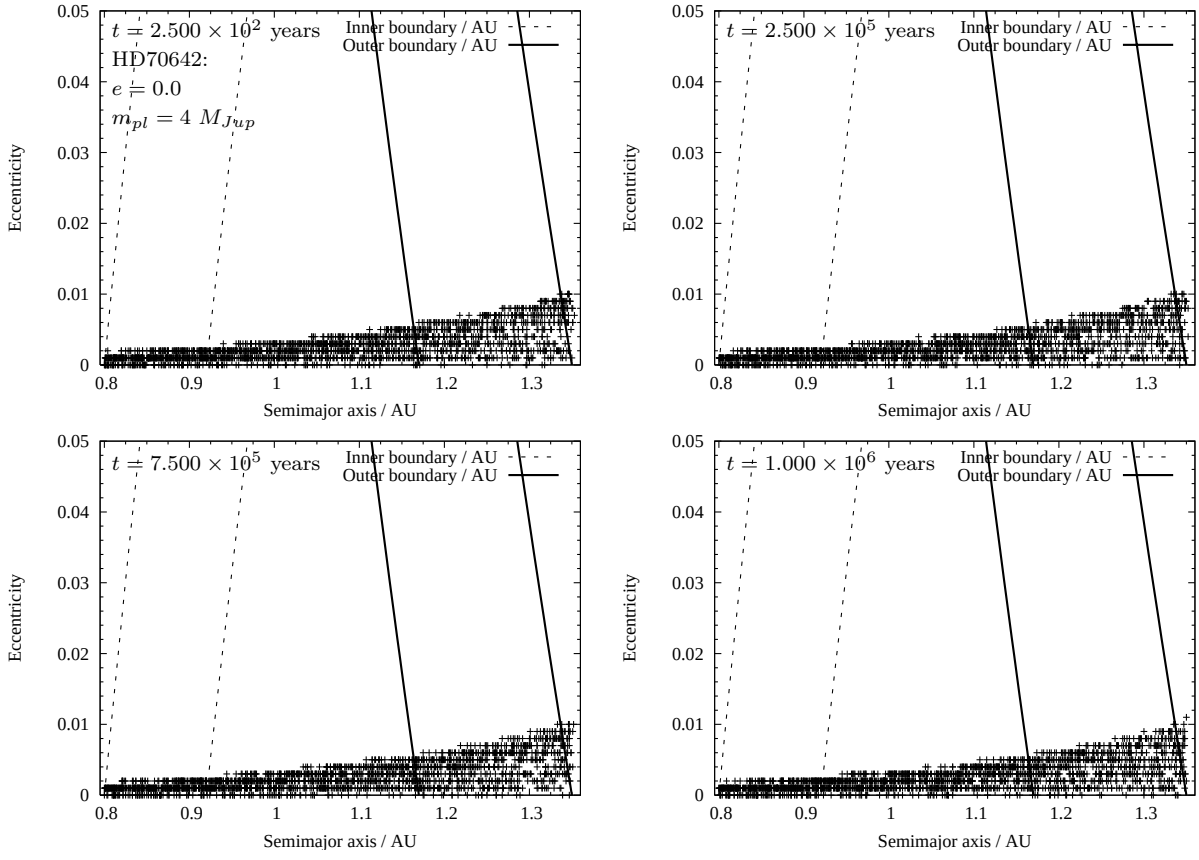

Figure 7.12: Simulation snapshots for particles in HD70642 with giant planet parameters: $m_{pl} = 4\ M_{Jup}$ and $e = 0.0$. A total of 2×10^3 particles are randomly distributed within the habitable zone. Boundaries of the habitable zone are superimposed. The continuous habitable zone is marked by the inner boundary at 0.92 AU and outer boundary 1.17 AU. The two outermost boundaries are located at 0.80 AU (inner) and 1.35 AU (outer). The total integration time is 10^6 years.

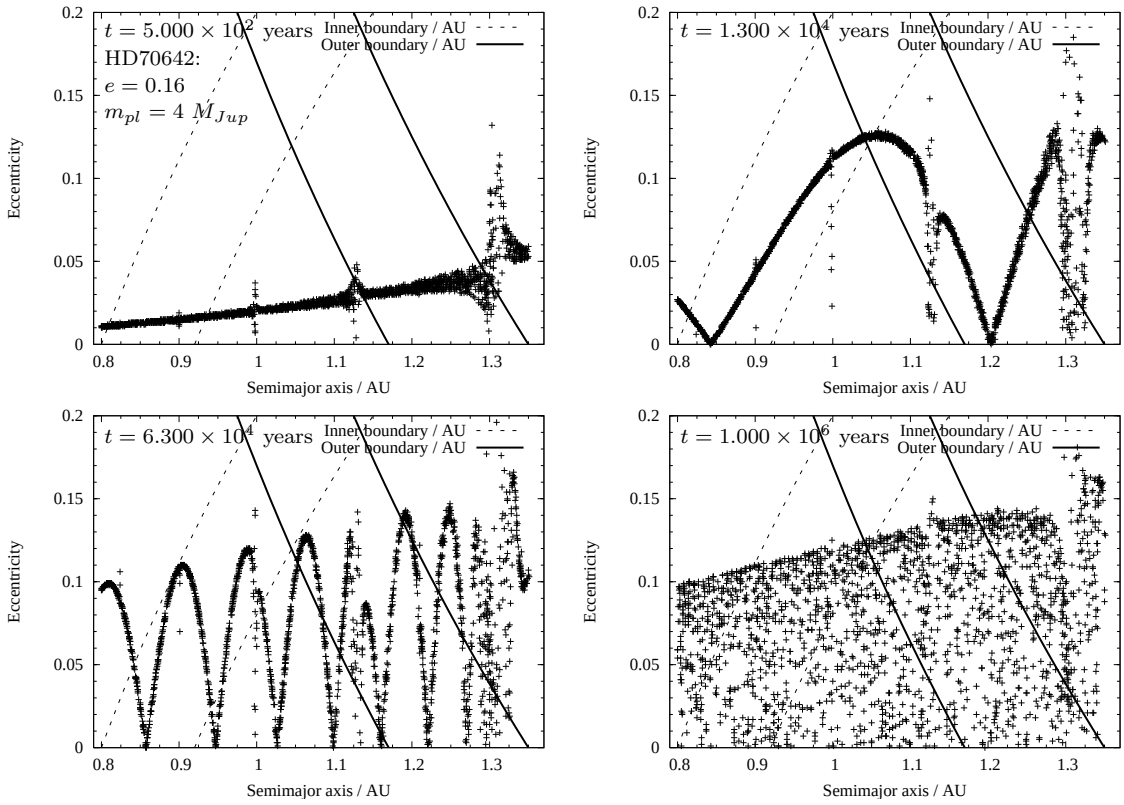

Figure 7.13: Simulation snapshots for particles in HD70642 with giant planet parameters: $m_{pl} = 4\ M_{Jup}$ and $e = 0.16$. A total of 2×10^3 particles are randomly distributed within the habitable zone. Boundaries of the habitable zone are superimposed. The continuous habitable zone is marked by the inner boundary at 0.92 AU and outer boundary 1.17 AU. The two outermost boundaries are located at 0.80 AU (inner) and 1.35 AU (outer). The total integration time is 10^6 years.

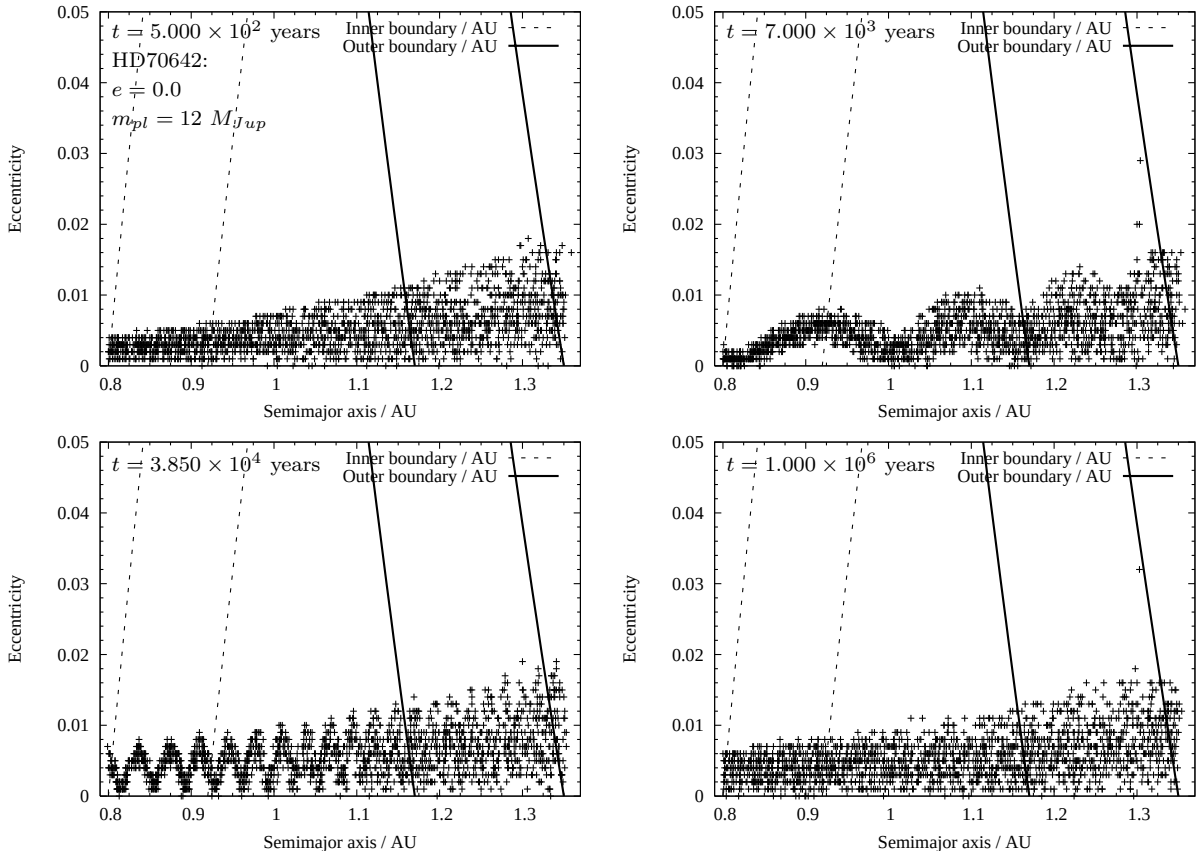

Figure 7.14: Simulation snapshots for particles in HD70642 with giant planet parameters: $m_{pl} = 12\ M_{Jup}$ and $e = 0.0$. A total of 2×10^3 particles are randomly distributed within the habitable zone. Boundaries of the habitable zone are superimposed. The continuous habitable zone is marked by the inner boundary at 0.92 AU and outer boundary 1.17 AU. The two outermost boundaries are located at 0.80 AU (inner) and 1.35 AU (outer). The total integration time is 10^6 years.

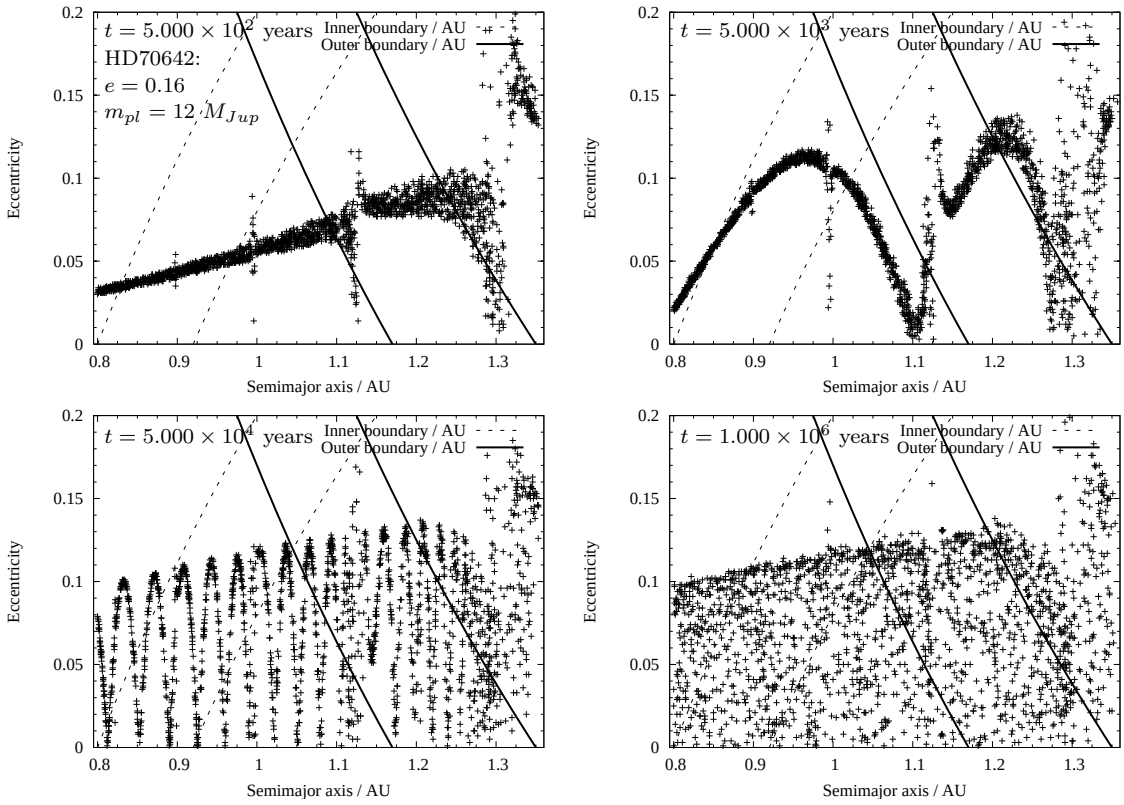

Figure 7.15: Simulation snapshots for particles in HD70642 with giant planet parameters: $m_{pl} = 12\ M_{Jup}$ and $e = 0.16$. A total of 2×10^3 particles are randomly distributed within the habitable zone. Boundaries of the habitable zone are superimposed. The continuous habitable zone is marked by the inner boundary at 0.92 AU and outer boundary 1.17 AU. The two outermost boundaries are located at 0.80 AU (inner) and 1.35 AU (outer). The total integration time is 10^6 years.

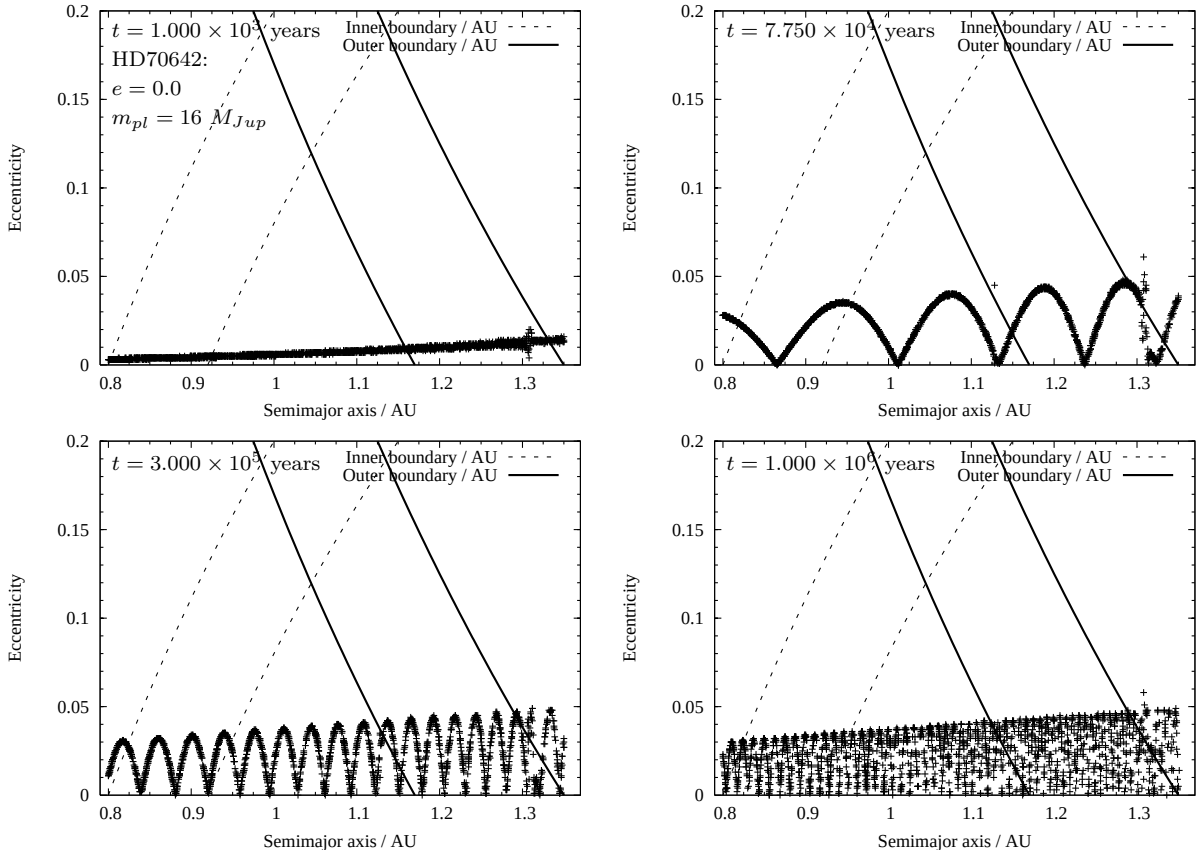

Figure 7.16: Simulation snapshots for particles in HD70642 with giant planet parameters: $m_{pl} = 16\ M_{Jup}$ and $e = 0.0$. A total of 2×10^3 particles are randomly distributed within the habitable zone. Boundaries of the habitable zone are superimposed. The continuous habitable zone is marked by the inner boundary at 0.92 AU and outer boundary 1.17 AU. The two outermost boundaries are located at 0.80 AU (inner) and 1.35 AU (outer). The total integration time is 10^6 years.

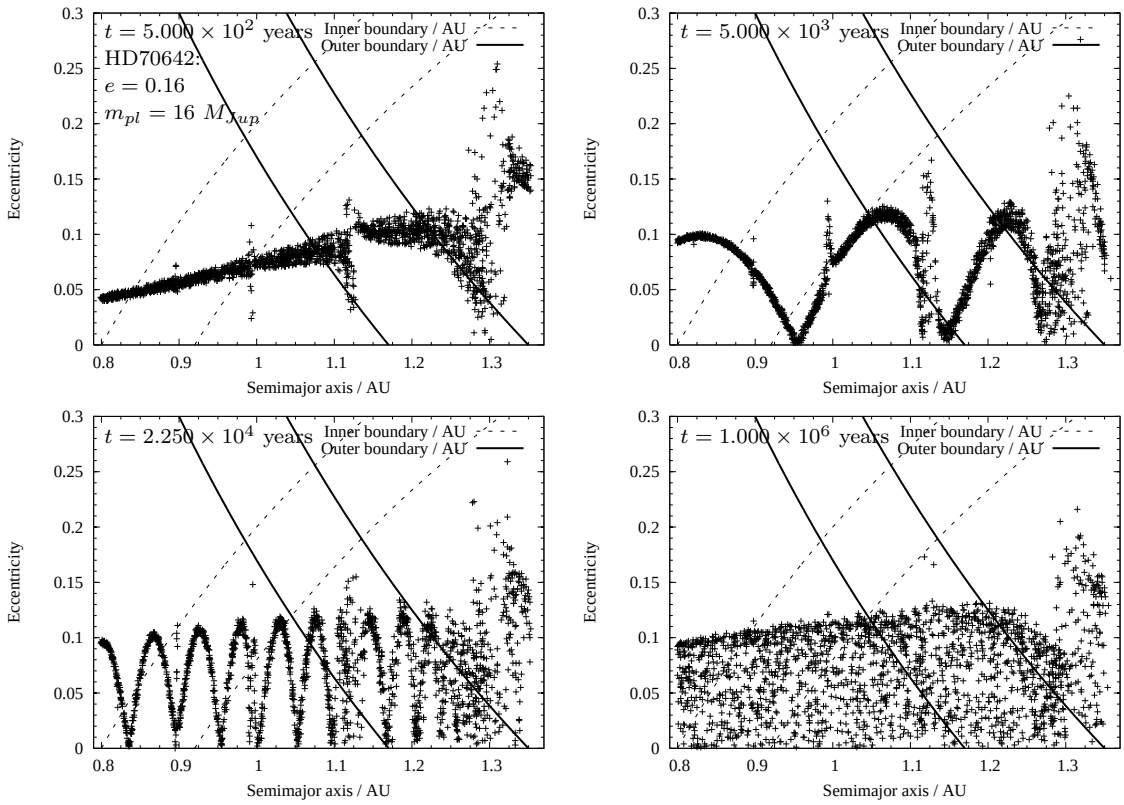

Figure 7.17: Simulation snapshots for particles in HD70642 with giant planet parameters: $m_{pl} = 16\ M_{Jup}$ and $e = 0.16$. A total of 2×10^3 particles are randomly distributed within the habitable zone. Boundaries of the habitable zone are superimposed. The continuous habitable zone is marked by the inner boundary at 0.92 AU and outer boundary 1.17 AU. The two outermost boundaries are located at 0.80 AU (inner) and 1.35 AU (outer). The total integration time is 10^6 years.

7.6.2 HD4208: Numerical simulations and results

Planet-particle simulations within HD4208 considers the following mass range for the observed giant planet: $m_{pl} = [1, 3, 12, 16]\ M_{Jup}$. For each mass the eccentricity of the giant planet is varied within the range $e \in [0.0, 0.1, 0.16]$. Numerical values for the remaining orbital parameters are given within the initial condition section. Within the figures, I only present simulation snapshots for the lower and upper range in giant planet eccentricity (i.e $e = 0.0$ and $e = 0.16$). All figures are shown at the end of this section and in the following, a discussion on the results will be given.

In order to study the dynamical effect on particle orbital parameters for variable giant planet mass at constant giant planet eccentricity (i.e e = 0.0), we need to discuss and compare snapshot Fig. 7.18, 7.20, 7.22 and 7.24.

In order to study the effect of giant planet mass for an eccentric giant planet orbit (upper observed limit, $e = 0.16$), we need to discuss and compare Fig. 7.19, 7.21, 7.23 and 7.25.

Discussion - the case of circular giant planet eccentricity ($e = 0.0$)

In Fig.7.18, we observe eccentricity excitations at $a \simeq 1.06$ AU and $a \simeq 1.2$ AU. These locations correspond to the 2:1 and 4:3 mean-motion resonance configuration. Particles within the 2:1 resonance are observed to be excited in eccentricity up to $e \simeq 0.18$ within the continuous habitable zone. Within the simulation snapshots the motion is mainly oscillatory in eccentricty at nearly constant semi-major axis (i.e for example, for particles initially within the 2:1 commensurability the eccentricity is oscillating between $e_{max} \simeq 0.2$ and $e_{min} \simeq 0$ at $a \simeq 1.06$ AU). However, all planets (except at the very outer boundary of the continuous habitable zone at $a \simeq 1.23$ AU) have orbital parameters well constrained within the continuous habitable zone exhibiting only small eccentricity variations (excepts at the 2:1 and 4:3 commensurability). Furthermore, the case of particle removal is observed. Particles initially located at $a \simeq 1.33$ AU are ejected (or accreted onto the giant planet) from the system. This decadence of particles is faintly indicated by the formation of a void region in the (a, e)-space at $a \simeq 1.33$ AU.

In Fig.7.20 (considering $m_{pl} = 3\ M_{Jup}$) the gravitational effect of the 3:1 mean-motion resonance (located at $a \simeq 0.8$ AU) is observed (the presence of this resonance

was allready visible within Fig. 7.18). For an increased mass, we observe the 2:1 resonance increasing in strength resulting in a further excitation of particle eccentricities beyond the boundaries of the continuous habitable zone ($e \simeq 0.3$). Terrestrial planets with $a \simeq 1.05$ AU and $e \simeq 0.3$ have their orbital pericenter distance located at $q \simeq 0.74$ AU and apocenter distance located at $Q \simeq 1.37$ AU. This means that those planets occasionally will experience periods of glaciation (mainly because of a decrease in stellar radiation flux), since the outer boundary of the continuous habitable zone is priodically crossed. However, we observe stable habitable terrestrial planets (particles) located within the interval 0.85 AU $< a <$ 1.0 AU. Those planets experience eccentricity oscillations of $e < 0.04$ caused by giant planet perturbations . In addition, a narrow region around $a \simeq 0.77$ AU indicate habitable orbits of terrestrial planets. Whether particles are removed from this region, is not clear from the simulation snapshots. However, particles are definitely removed from the terrestrial region around $a \simeq 1.3$ AU and larger.

In Fig.7.22, we observe a further increase of particle eccentricity within the 3:1 mean-motion resonance, suggesting that those planets have their pericenter distance crossing the inner boundary of the continuous habitable zone. The majority of particles initially located beyond $a \simeq 1.1$ AU have been ejected from the system or accreted on either the central star (because of large eccentricity excitations leading to stargrazers) or the giant planet. Particles with $a \simeq 0.99$ AU have large eccentricities and are crossing the outer and inner boundary of the continuous habitable zone.

A similar discussion applies for the simulation snapshots in Fig.7.24, and it is emphasized that for giant planet mass $m_{pl} > 12\ M_{Jup}$ for a planet with semi-major axis $a = 1.68$ AU would render the terrestrial habitable region beyond $a = 0.97$ AU to become unstable for Earth-mass terrestrial planetary (particle) orbits. However, it is again noted that the semi-major axis is almost constant and only the orbital eccentricity is changing in time. This dynamical behavior is, for example, observed for particles located at $a = 0.9$ AU in Fig.7.20 and 7.22.

Discussion - the case of eccentric giant planet orbits ($e = 0.16$)

In Fig.7.19 we observe a general eccentricity excitation of particles within the first snapshot at $t = 10^3$ years - resembling a Planckian-like continuum curve. This increase in eccentricity is explained by general gravitational giant planet perturbations. Increasing the giant planet orbit eccentricity results in the shift of the pericenter distance closer to the terrestrial region. Additional eccentricity excitations are observed at regions corresponding to mean-motion resonances. Particles initially located within a narrow band ($\Delta a \simeq 0.06$ AU) centered on $a \simeq 1.0$ AU have orbital eccentricities well defined within the continuous habitable zone exhibiting oscillations in eccentricity between $e_{min} = 0.0$ and $e_{max} \simeq 0.23$ (this region corresponds to $\simeq 12\%$ of the total range of the continuous habitable zone). At the

end of the 10^6 year integration, the formation of a gap is observed with a cleared region within $a_{min} = 1.1$ AU and $a_{max} = 1.28$ AU. From the MEGNO stability maps this region is dominated by chaotic particle motion resulting in radial mixing and subsequent accretion or ejection from the system. The survival of particles at $a \simeq 1.3$ AU is explained by regular (oscillatory in eccentricity) motion. Comparing with the corresponding MEGNO map in Fig.7.7 (upper left panel) this region is characterised by quasi-periodic motion. The location of the particles corresponds to the 3:2 mean-motion resonance and it seems that this resonance has the ability to act as a protective mechanism for particle ejection or accretion. At this point the details of protective mean-motion resonances are not further discussed, but is clearly an interesting dynamical feature to be investigated in future studies.

In Fig.7.21 the range in eccentricity is changed in order to stress and demonstrate the existence of high eccentricity excitations of particles. In particular, the orbits of particles initially located within the 5:2 mean-motion resonance ($a \simeq 0.9$ AU) are quickly (within 500 years, or equivalently, corresponding to 220 orbital periods of HD4208b) excited in eccentricity and consequently removed from the system. In the subsequent snapshots the ejection of these particles are indicated by the formation of a gap in semi-major axis near $a \simeq 0.9$ AU. Particle dynamics is generally characterised to be erratic with the formation of a void region within $a_{min} \simeq 1.1$ AU and $a_{max} \simeq 1.28$ AU. Because of this erratic dynamical behavior, it seems not plausible that Earth-like planets can survive on dynamically stable orbits during the lifetime of the host star. However, particles with initial semi-major axis near $a \simeq 1.0$ AU are confined to within the continuous habitable zone.

In Fig.7.23 and 7.25 the dynamical information within the simulation snapshots is nearly equivalent within both figures. Hence, a discussion is only given for Fig. 7.25. For the considered extreme planetary and orbital parameters, we observe a nearly complete removal of particles throughout the continuous habitable zone. The formation of a gap is observed at $a \simeq 0.82$ AU and characterised by a gradual depletion of particles during the simulation. Comparing the simulation snapshots with the results obtained from the MEGNO calculation in Fig.7.7 (lower right panel, for e(HD4208b) = 0.16), we identify that the gap clearing is caused by the action of the 3:1 mean-motion resonance. The chance for observing a terrestrial Earth-like planet within the continuous habitable zone, is likely to be minimal. In the following simulation snapshots are presented.

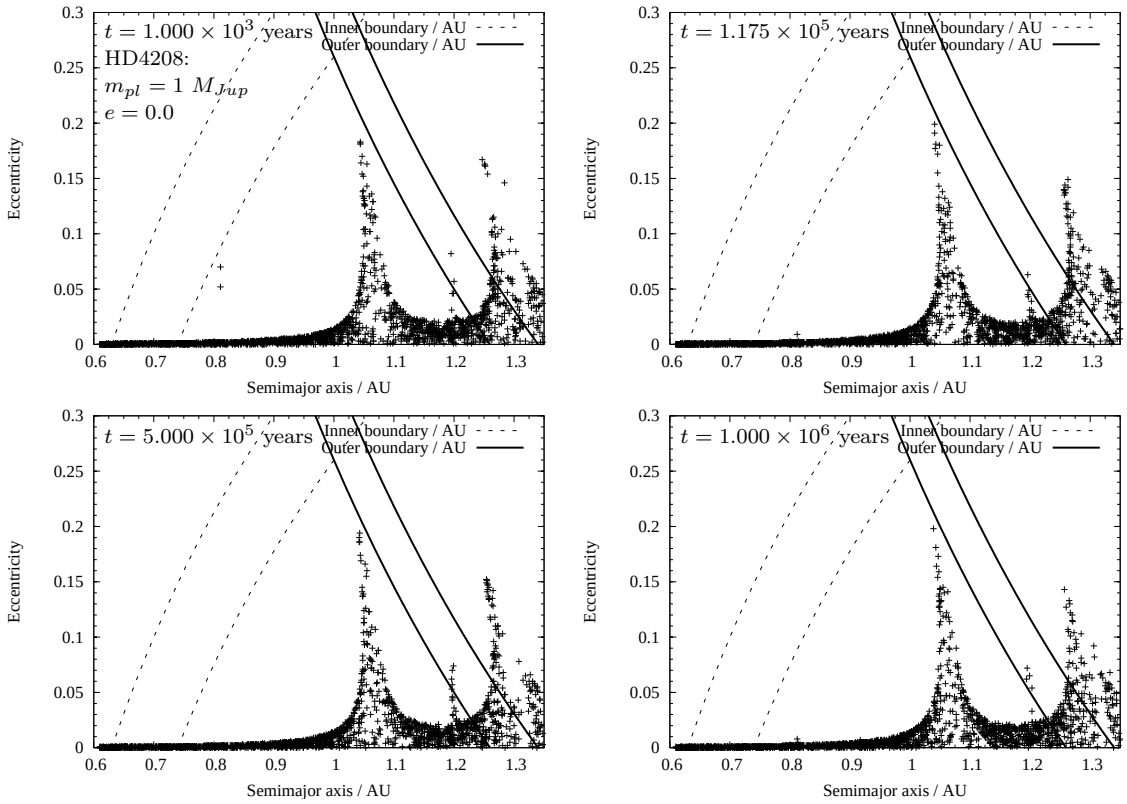

Figure 7.18: Simulation snapshots for particles in HD4208 with giant planet parameters: $m_{pl} = 1\ M_{Jup}$ and $e = 0.0$. A total of 2×10^3 particles are randomly distributed within the habitable zone. Boundaries of the habitable zone are superimposed. The continuous habitable zone is marked by the inner boundary at 0.74 AU and outer boundary 1.26 AU. The two outermost boundaries are located at 0.63 AU (inner) and 1.34 AU (outer). The total integration time is 10^6 years.

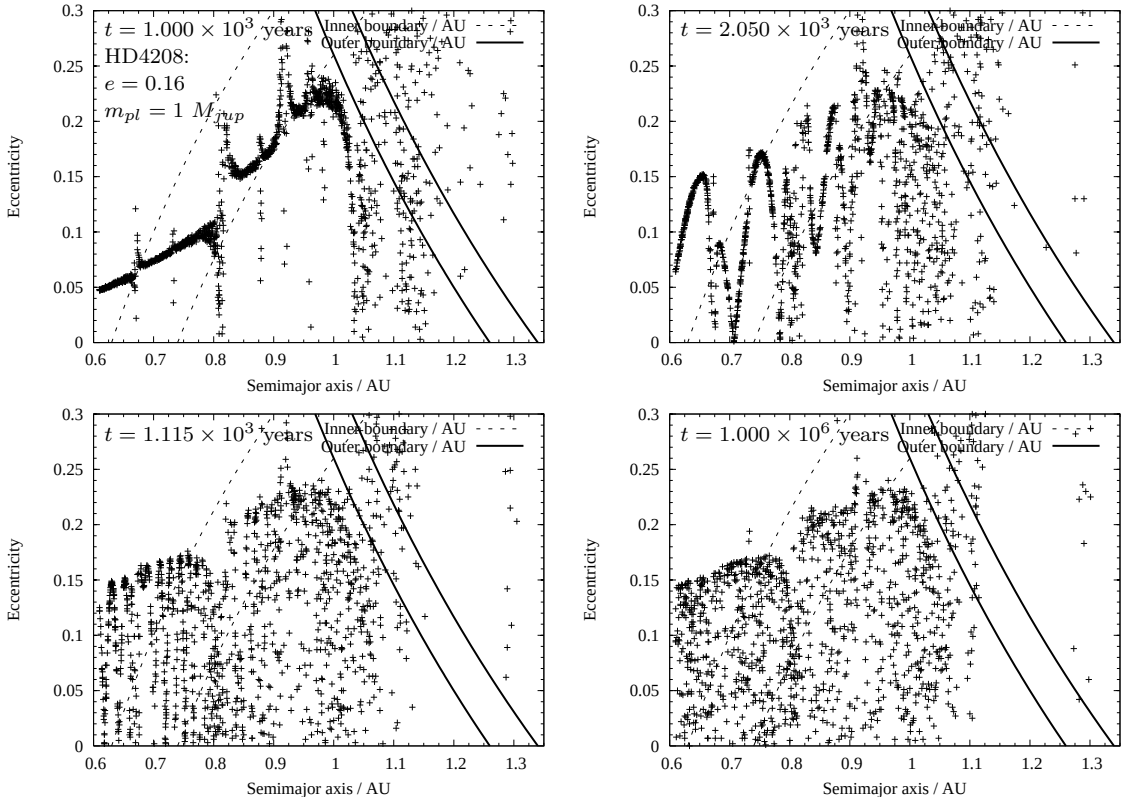

Figure 7.19: Simulation snapshots for particles in HD4208 with giant planet parameters: $m_{pl} = 1\ M_{Jup}$ and $e = 0.16$. A total of 2×10^3 particles are randomly distributed within the habitable zone. Boundaries of the habitable zone are superimposed. The continuous habitable zone is marked by the inner boundary at 0.74 AU and outer boundary 1.26 AU. The two outermost boundaries are located at 0.63 AU (inner) and 1.34 AU (outer). The total integration time is 10^6 years.

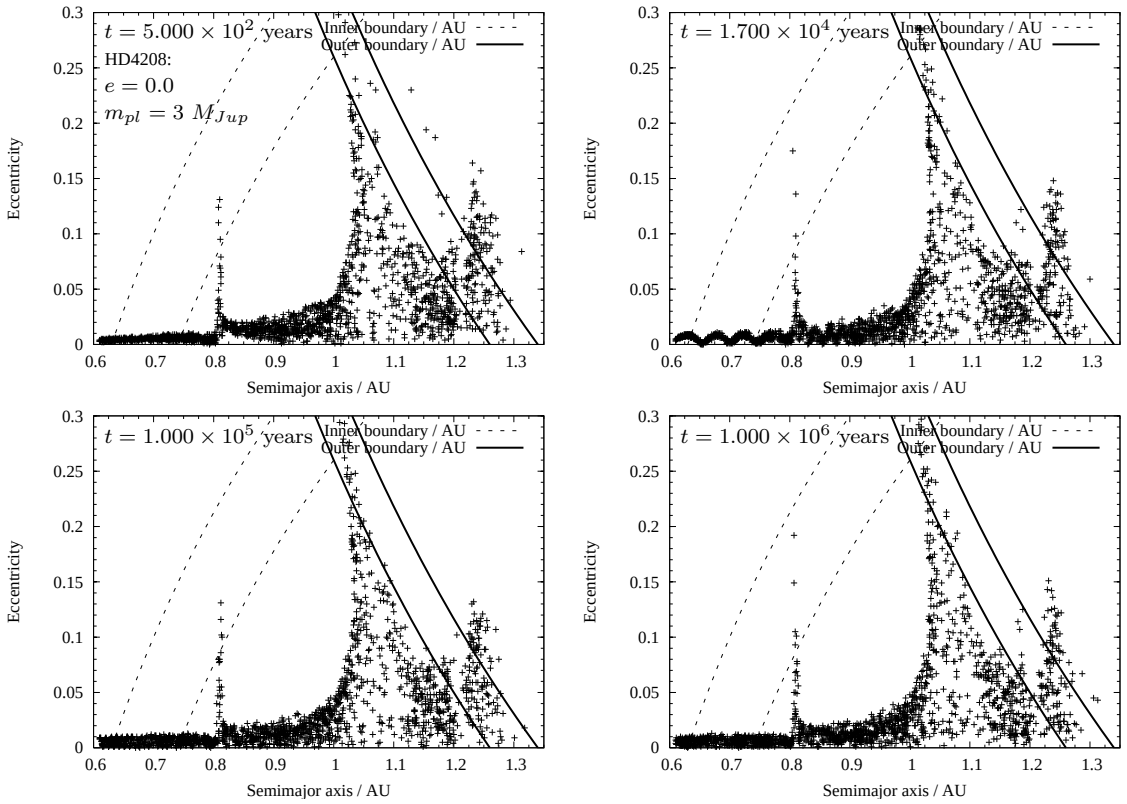

Figure 7.20: Simulation snapshots for particles in HD4208 with giant planet parameters: $m_{pl} = 3\ M_{Jup}$ and $e = 0.0$. A total of 2×10^3 particles are randomly distributed within the habitable zone. Boundaries of the habitable zone are superimposed. The continuous habitable zone is marked by the inner boundary at 0.74 AU and outer boundary 1.26 AU. The two outermost boundaries are located at 0.63 AU (inner) and 1.34 AU (outer). The total integration time is 10^6 years.

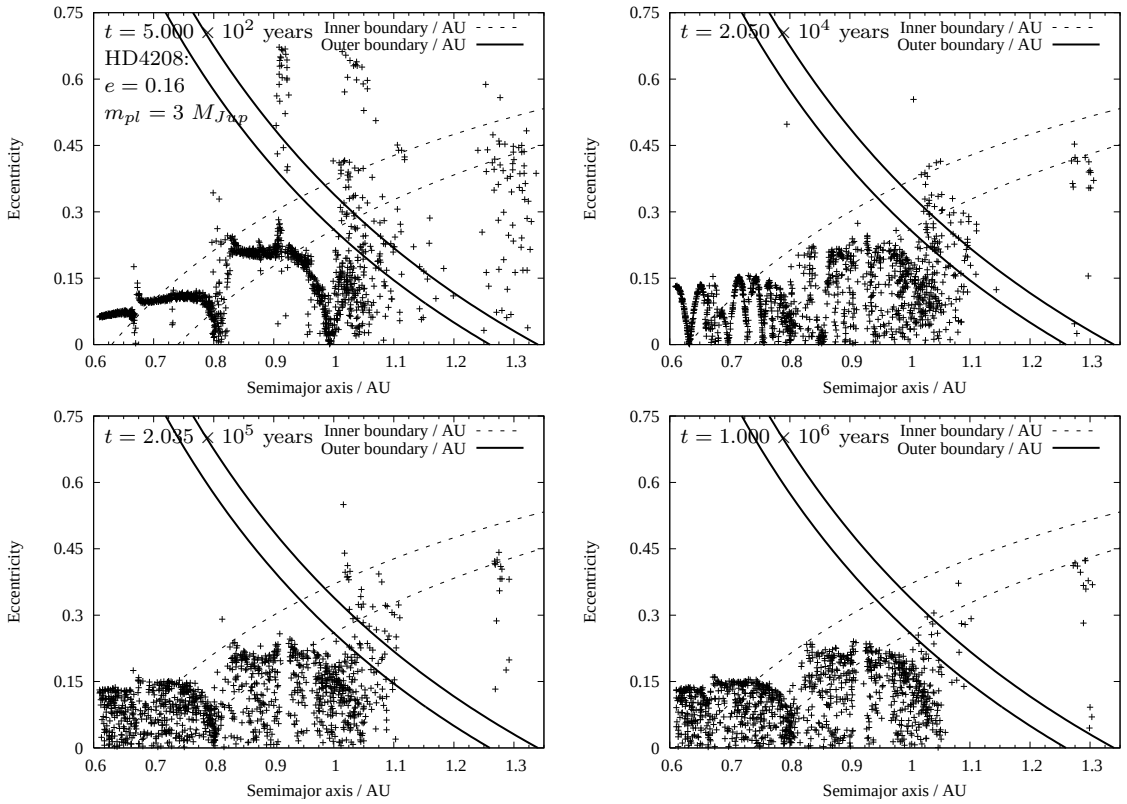

Figure 7.21: Simulation snapshots for particles in HD4208 with giant planet parameters: $m_{pl} = 3\ M_{Jup}$ and $e = 0.16$. A total of 2×10^3 particles are randomly distributed within the habitable zone. Boundaries of the habitable zone are superimposed. The continuous habitable zone is marked by the inner boundary at 0.74 AU and outer boundary 1.26 AU. The two outermost boundaries are located at 0.63 AU (inner) and 1.34 AU (outer). The total integration time is 10^6 years.

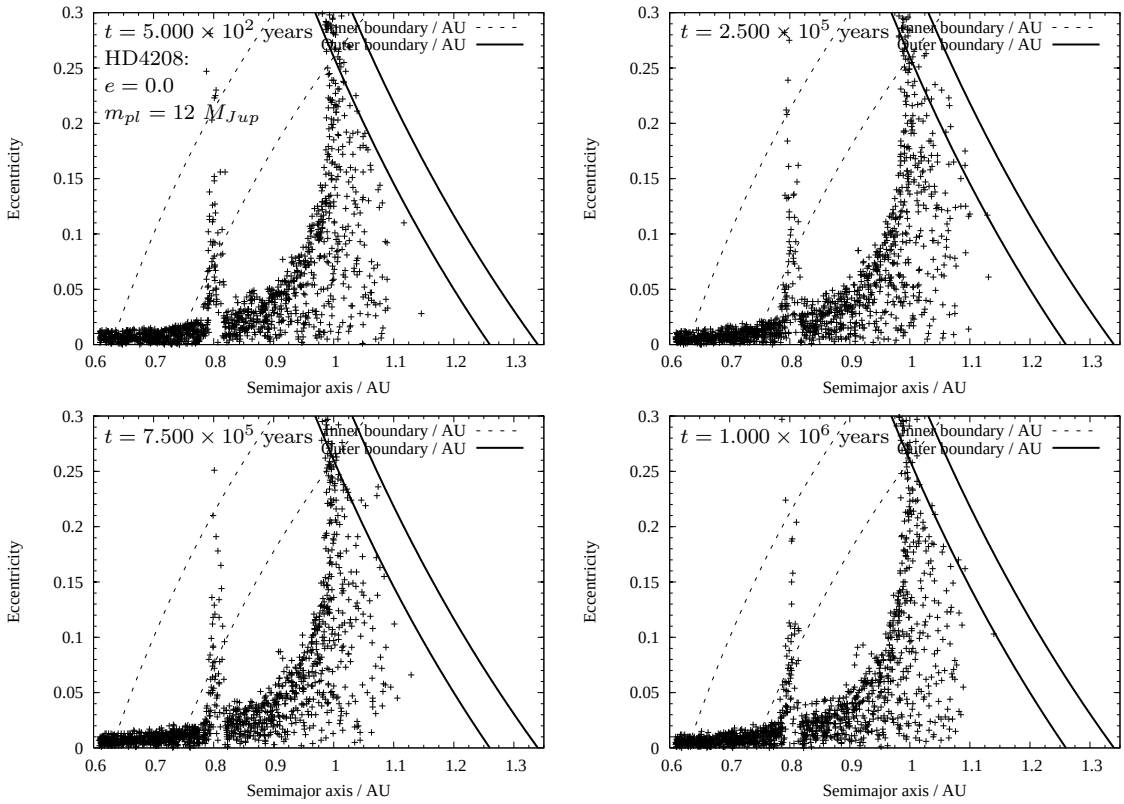

Figure 7.22: Simulation snapshots for particles in HD4208 with giant planet parameters: $m_{pl} = 12\ M_{Jup}$ and $e = 0.0$. A total of 2×10^3 particles are randomly distributed within the habitable zone. Boundaries of the habitable zone are superimposed. The continuous habitable zone is marked by the inner boundary at 0.74 AU and outer boundary 1.26 AU. The two outermost boundaries are located at 0.63 AU (inner) and 1.34 AU (outer). The total integration time is 10^6 years.

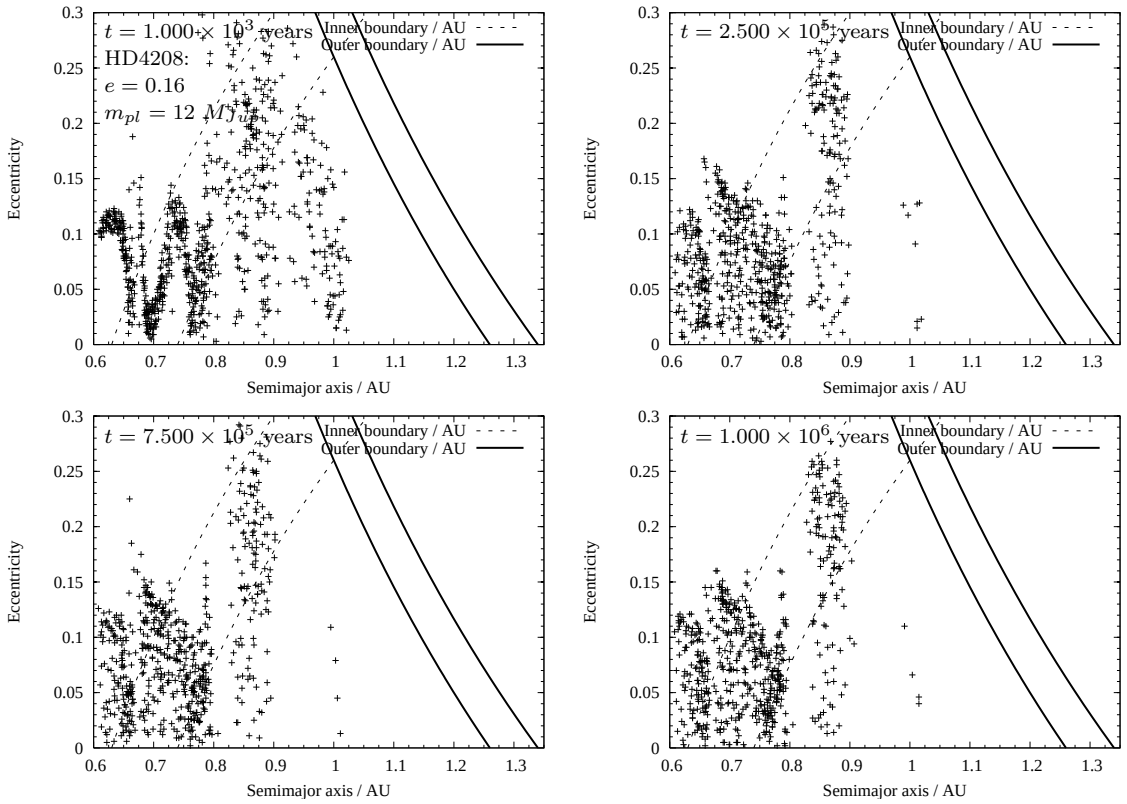

Figure 7.23: Simulation snapshots for particles in HD4208 with giant planet parameters: $m_{pl} = 12\ M_{Jup}$ and $e = 0.16$. A total of 2×10^3 particles are randomly distributed within the habitable zone. Boundaries of the habitable zone are superimposed. The continuous habitable zone is marked by the inner boundary at 0.74 AU and outer boundary 1.26 AU. The two outermost boundaries are located at 0.63 AU (inner) and 1.34 AU (outer). The total integration time is 10^6 years.

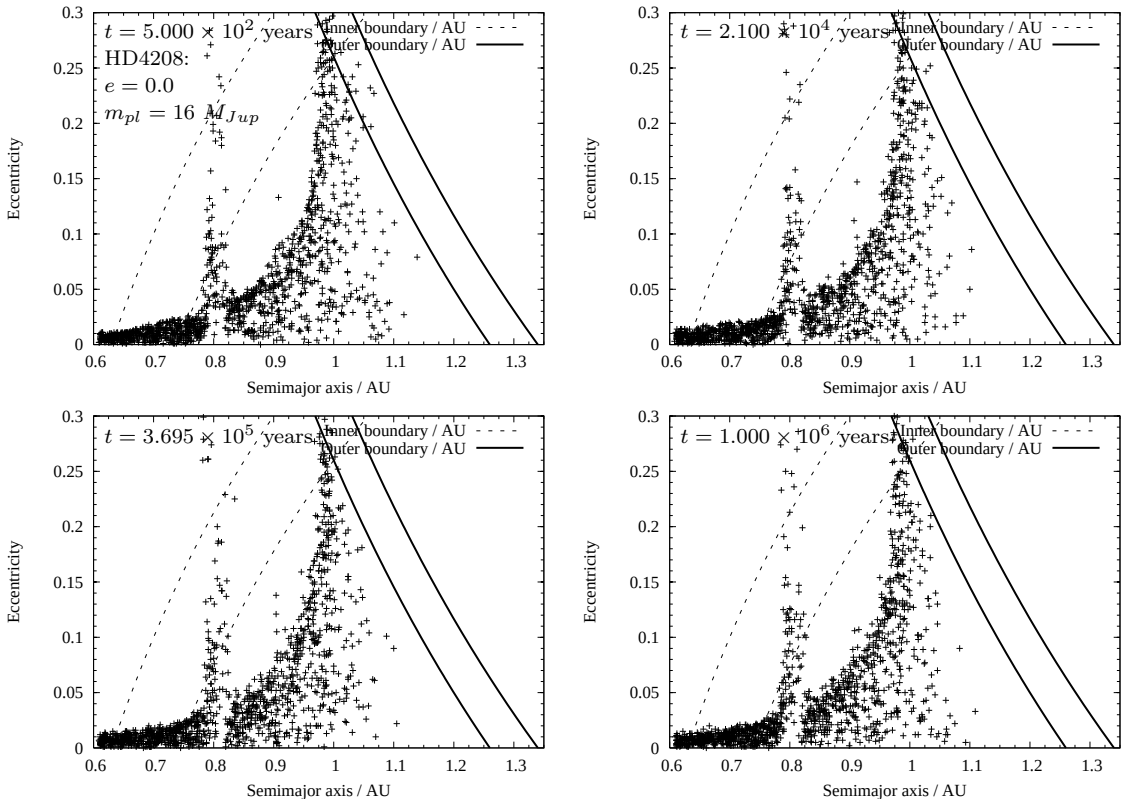

Figure 7.24: Simulation snapshots for particles in HD4208 with giant planet parameters: $m_{pl} = 16\ M_{Jup}$ and $e = 0.0$. A total of 2×10^3 particles are randomly distributed within the habitable zone. Boundaries of the habitable zone are superimposed. The continuous habitable zone is marked by the inner boundary at 0.74 AU and outer boundary 1.26 AU. The two outermost boundaries are located at 0.63 AU (inner) and 1.34 AU (outer). The total integration time is 10^6 years.

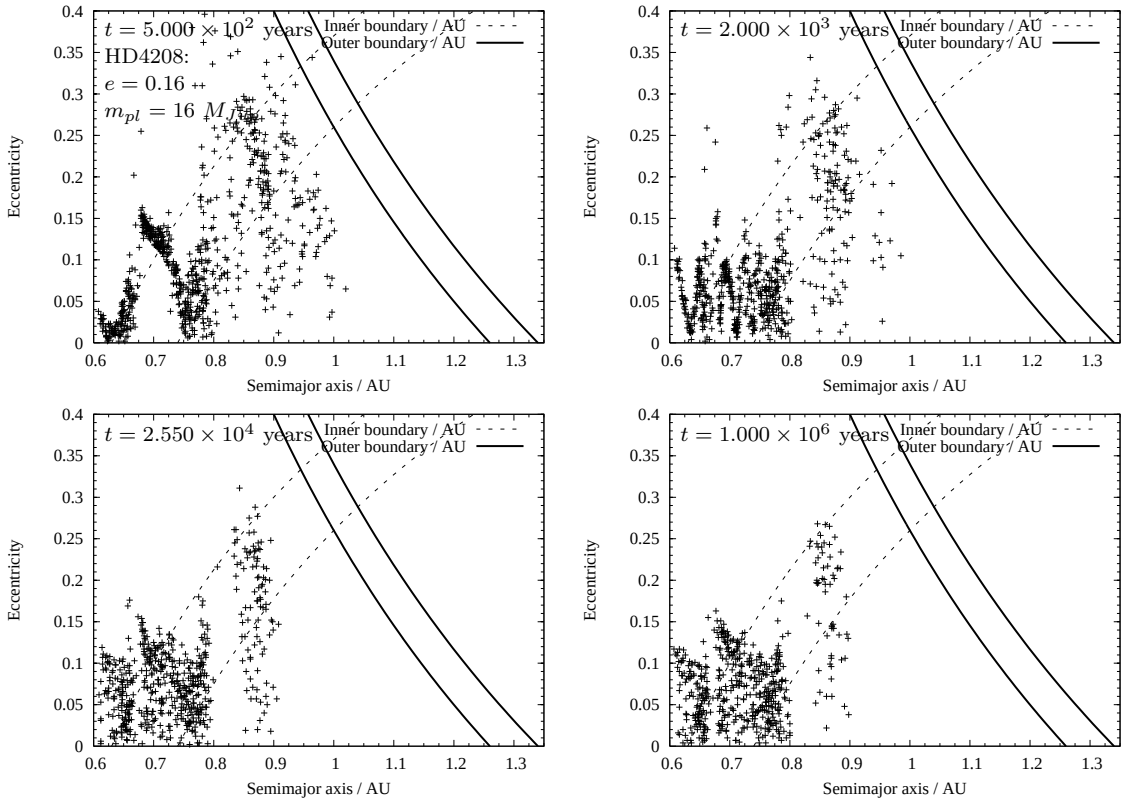

Figure 7.25: Simulation snapshots for particles in HD4208 with giant planet parameters: $m_{pl} = 16\ M_{Jup}$ and $e = 0.16$. A total of 2×10^3 particles are randomly distributed within the habitable zone. Boundaries of the habitable zone are superimposed. The continuous habitable zone is marked by the inner boundary at 0.74 AU and outer boundary 1.26 AU. The two outermost boundaries are located at 0.63 AU (inner) and 1.34 AU (outer). The total integration time is 10^6 years.

7.7 Single particle dynamics

Within the presented particle simulations, we only considered a total integration time of 10^6 years in order to study the time evolution of particle orbits. Strictly, nothing can be concluded on the subsequent evolution of orbital elements. It might be possible that particles exhibiting quasi-periodic regular motion within the first 10^6 years, suddenly undergoes dynamical changes with large excursions in orbital elements. However, short period integrations allowed us to perform a large parameter survey of different initial conditions. Obviously, we ask: What is the long-term dynamical behavior of single particles? The most promising extrasolar planetary system to possibly harbor a terrestrial Earth-like planet is HD70642. Hence, we will consider long-term integrations of single particles within this system.

7.7.1 Longterm dynamics - HD70642

In order to study the long-time dynamics of single particles, I have performed long-time integrations of the orbits of single particles using Mikkola's symplectic variable-step leap-frog algorithm (`g3.f`).

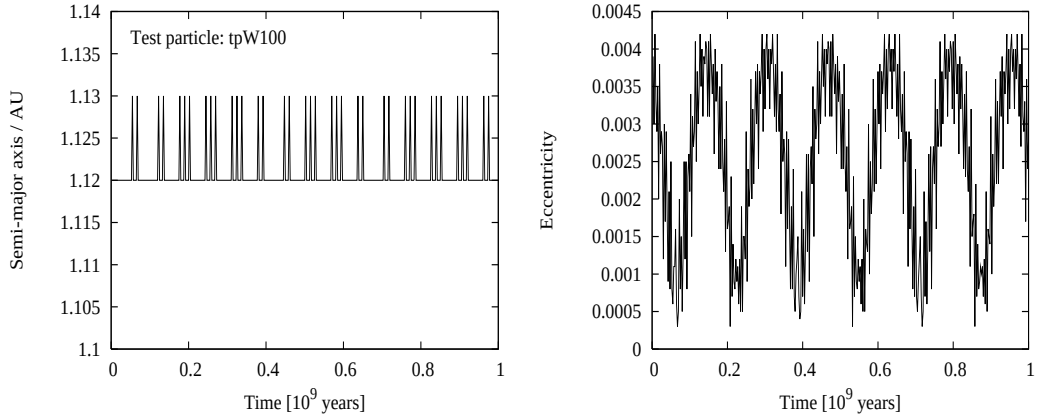

Figure 7.26: Long-term integration of test particle tpW100 under the perturbation of a giant planet in HD70642. The mass of the giant planet is $m_{pl} = 12\ M_{Jup}$ with orbit eccentricity $e = 0.0$. The total integration time is 10^9 years. Test particle "tpW100" is initially located within the continuous habitable zone.

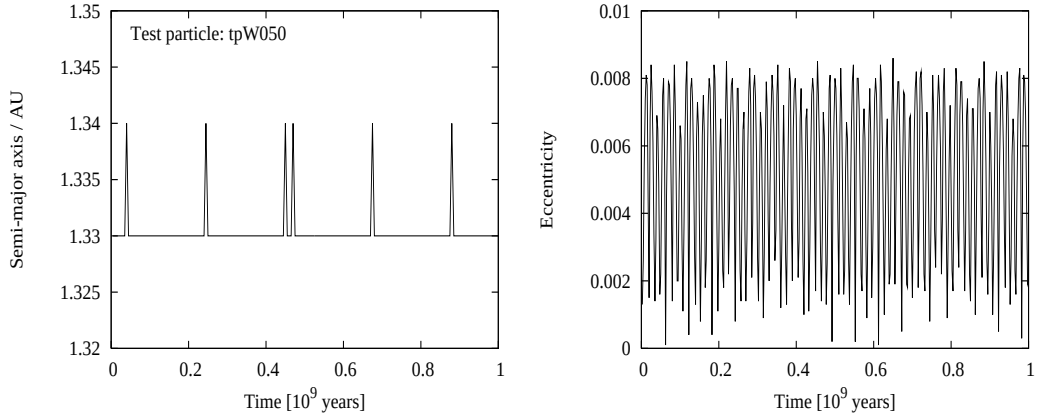

Figure 7.27: Long-term integration of test particle tpW050 under the perturbation of a giant planet in HD70642. The mass of the giant planet is $m_{pl} = 12\ M_{Jup}$ with orbit eccentricity $e = 0.0$. The total integration time is 10^9 years. Test particle "tpW050" is initially located outside the continuous habitable zone.

The time variation of orbital semi-major axis and eccentricity of particles are monitored for $\simeq 2 \times 10^8$ years and 1×10^9 years. In the following, we consider perturbations on particle orbital parameters of the observed giant planet within the system HD70642.

The integration time spans corresponds to 5% and 25% of the current age of the host star. The integrations follow the dynamics of single particles initially located inside and outside the continuous habitable zone. The mass of the giant planet is fixed to $m_{pl} = 12\ M_{Jup}$ and two eccentricities of the giant planet orbit are considered.

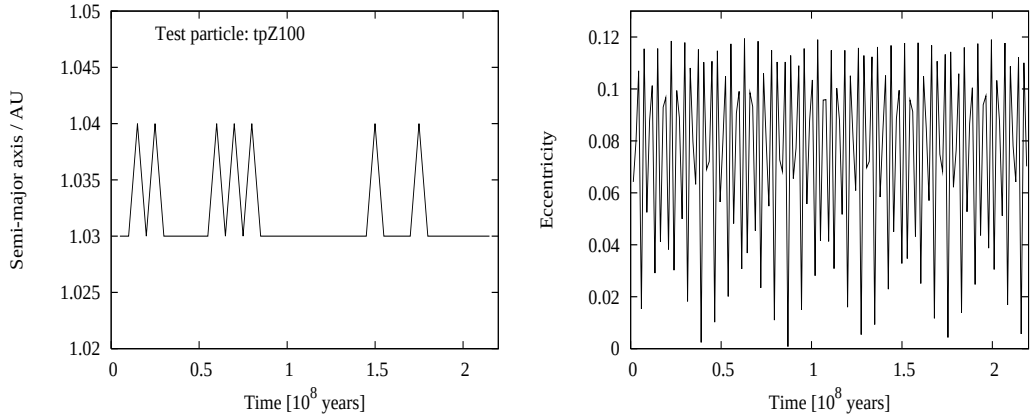

Figure 7.28: Long-term integration of test particle tpZ100 under the perturbation of a giant planet in HD70642. The mass of the giant planet is $m_{pl} = 12\ M_{Jup}$ with orbit eccentricity $e = 0.16$. The total integration time is 2.2×10^8 years. Test particle "tpZ100" is initially located inside the continuous habitable zone.

Fig.7.26 - 7.29 represents the time variation of semi-major axis (left panel) and eccentricities (right panel) of single particles. From the figures, it is noted that the particle semi-major axis is nearly constant during the integration time. This is a typical behavior and is also observed and noted within the section discussing multi-particle simulation snapshots. Long-term perturbations originating from the giant planet are mainly transferred in the variation of particle orbital eccentricities. For the time evolution of particle eccentricities, both long-term and short-term perturbations are identified and best observed in Fig.7.28. A detailed frequency analysis of the time series of orbital elements (mainly the eccentricity) would require the application of a Fourier analysis.

7.7.2 Orbital $(e_{max} - \Delta\omega)$ correlations

Lecar et al. (2001) notes the existence of a correlation between eccentricity excita-

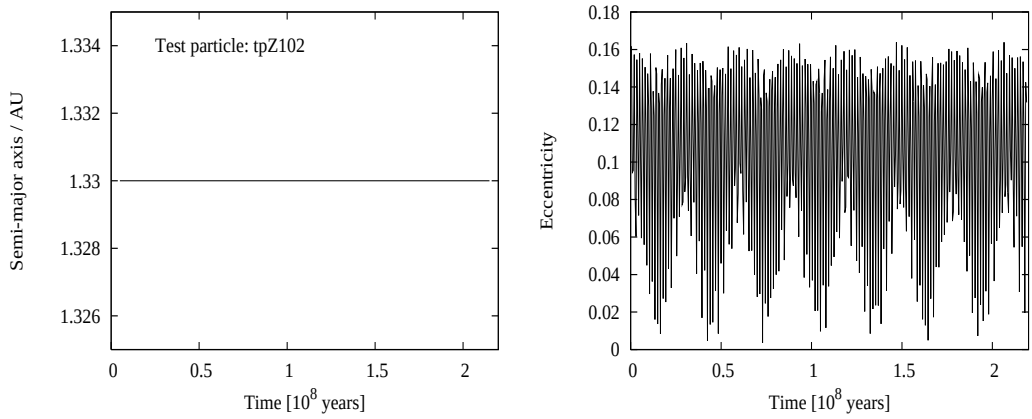

Figure 7.29: Long-term integration of test particle tpZ102 under the perturbation of a giant planet in HD70642. The mass of the giant planet is $m_{pl} = 12\ M_{Jup}$ with orbit eccentricity $e = 0.16$. The total integration time is 2.2×10^8 years. Test particle "tpZ102" is initially located outside the continuous habitable zone.

tions (Δe) and the difference in apsidal arguments for the giant planet and the test particle ($\omega_{tp} - \omega_{pl}$). In particular Lecar et al. notes that two different behaviors for the time evolution of the apsidal argument can be observed. 1) Circulation and 2) libration. Both domains induces different dynamical behavior in the dynamics of a particle. Inspired from this, I investigated the possibility of any similar correlation between orbital elements within the numerical integrations.

In Fig.7.30 a correlation is found between the particles eccentricity (upper left panel) and the difference in apsidal argument for the giant planet and test particle. It is seen, that whenever $\omega_{tp} - \omega_{pl} \simeq 0$ in the lower left panel of Fig.7.30, we observe a maximum in particle eccentricity (upper left panel). This is an example of a so-called secular resonance. Secular resonances occur if there exists an integer relationship between the apsidal arguments of any two bodies. Secular resonances are characterised to induce or cause long-term dynamical behavior in the system. In particular the time evolution of the particles eccentricity is of secular nature. From the upper right panel in Fig.7.30, it is noted that the particle's apsidal argument is librating (or oscillating) around $\omega_{tp} \simeq 280°$.

Sometimes the apsidal argument is observed to circulate. This is the case shown in Fig.7.31 (upper right panel), and it is noted that ω_{tp} traverses the range $[0°; 360°]$ with a positive slope. Occasionally, ω_{tp} librates for a small period of time followed by a circulation in the subsequent evolution. Searching for any correlations, we observe that repeated periods of the circulation in ω_{tp}, is correlated with the presence of eccentricity beats. To enhance this relationship vertical lines are superimposed onto

the figure.

A final note to remark concerns the perihelion shift of the giant planet. Since the performed simulations takes full account of and evaluates all forces involved within the three-body problem, we observe a perturbating effect in form of the advancement of the perihelion angle for the giant planet. This effect is caused by the gravitational potential of the Earth-mass planet. From the bottom left panel in the figures, it is observed that this shift is minimal an amounts to 15 - 20 degress at most.

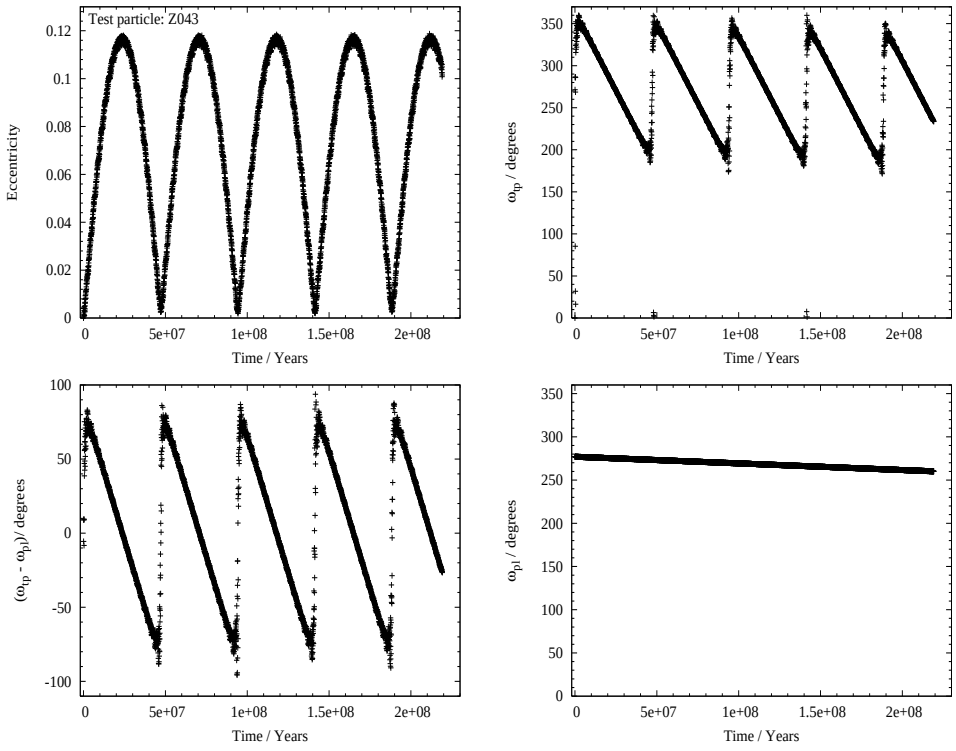

Figure 7.30: Plot of time evolution of orbital elements demonstrating ω-libration. Upper left panel: Time evolution of the eccentricity of a particle. Upper right panel: Time evolution of the apsidal argument of the particle. Lower right panel: Time evolution of apsidal argument (ω_{pl}) of the giant planet in HD70642. Lower left panel: Difference in apsidal argument for the particle and the giant planet.

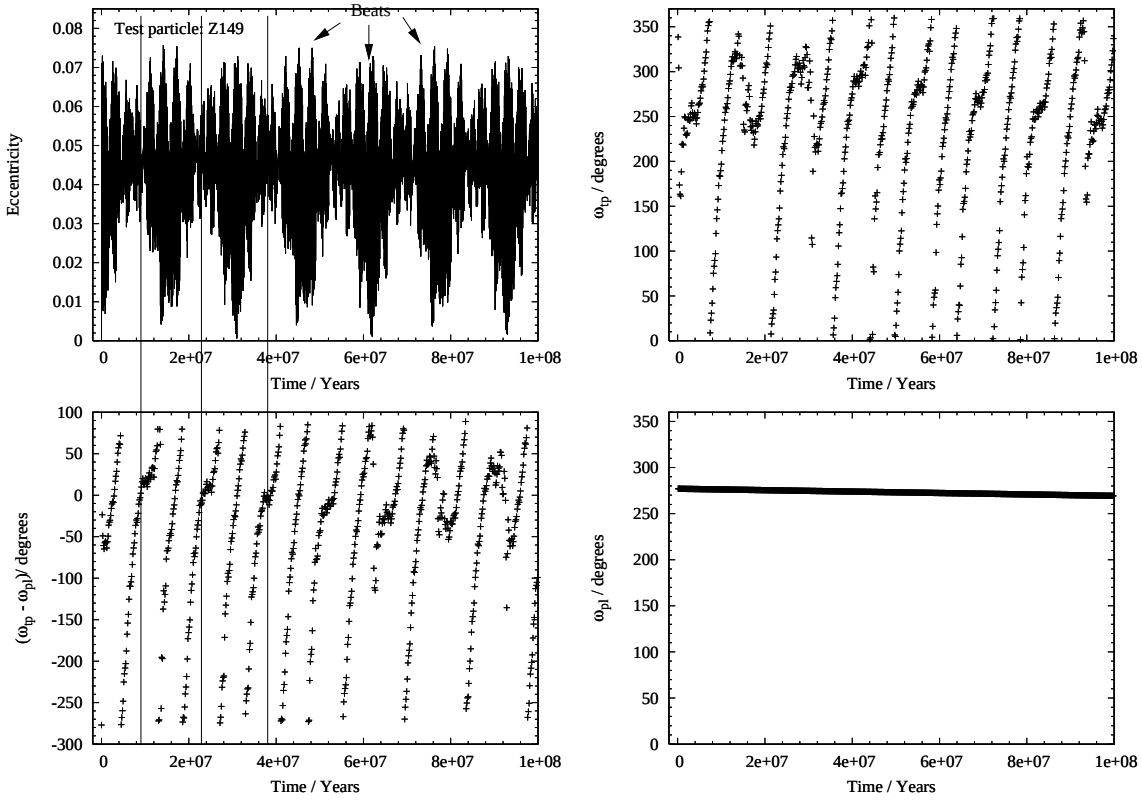

Figure 7.31: Plot of time evolution of orbital elements demonstrating ω-circulations. Upper left panel: Time evolution of the eccentricity of a particle. Upper right panel: Time evolution of the apsidal argument of the particle. Lower right panel: Time evolution of apsidal argument (ω_{pl}) of the giant planet in HD70642. Lower left panel: Difference in apsidal argument ($\Delta\omega = \omega_{tp} - \omega_{pl}$) for the particle and the giant planet.

7.8 Conclusion and discussion of results - what has been learned?

Regarding general comments on particle dynamics:

Combining the calculation of the MEGNO indicator with direct particle simulations, enables us to correlate chaotic regions in phase space (MEGNO maps) with eccentricity excitations. Most of these chaotic regions are identified to correspond to orbital mean-motion resonances. The effect of chaotic commensurabilities causes pumping of orbital eccentricities. Objects (planets, asteroids, etc.) on (high) eccentric orbits are generally unstable. The reason for this is because of radial mixing: objects on eccentric orbits become crossing orbits, implying an increase probability

of close encounters or even direct collisions with other objects. This enables us to designate and characterise chaotic regions within a given MEGNO map to be unstable. The use of the word "unstable" needs some remarks and should be treated with caution. The identification of chaotic regions within a MEGNO map implies not necessarely unstable orbits for given initial conditions. In our simulations for example, it has been demonstrated that planets with large eccentricity excursions ($e_{max} \simeq 0.65$) remained on stable orbits, despite of that the corresponding MEGNO map indicated chaotic motion. If we included additional planets in our simulations, particles on high eccentric orbits (possibly driving by a resonancs mechanism) would probably be removed from the system by the event of a close encounter or collision. Whether there exists a correlation between the maximal excited orbital eccentricity and the corresponding MEGNO indicator is not clear at this point. This question has not been addressed within the thesis. However, Goździewski (2002) reports on correlations between $\langle Y \rangle$ and e_{max}. Hence, we conclude that MEGNO maps always needs to be accompained with information on the time variation of a planets orbital eccentricity.

It is interesting to note the underlying dynamical effect of mean-motion resonances on orbital elements. In all simulations, we observed that repeated giant planet resonant perturbations are preferably affecting the eccentricity of particles. While the eccentricity undergoes large excursions the semi-major axis almost remains constant (cf. Fig. 7.27, 7.28, 7.29). In section 3.3.5, following Gauss's form of perturbation theory, we identified force components of the applied perturbation force responsible for changes in orbital elements. Only forces embedded within the plane (the transverse, T and radial, R force components) have the effect to change the orbital eccentricity (shape) and semi-major axis (size) of a Keplerian orbit. The question then is: If the cause for their time variation is the same, why is the eccentricity changing more rapidly compared to the semi-major axis? Murray and Dermott (1999) presents an explanation only discussing the change in semi-major axis. This question is left for future clarification.

All simulations indicates that giant planet perturbations have a general impact on orbital eccentricity. Particles are observed to be quickly excited with a final eccentricity gradient throughout the habitable terrestrial region. In general, the driving of eccentricity is larger for particles located near the giant planet.

Regarding stability of Earth-like planets within HD70642:

Using the MEGNO stability analysis, we identified several mean-motion resonances. The strength (measured in terms of $\langle Y \rangle$) of various resonances is observed to be an increasing function for increasing giant planet eccentricity and mass. From the stability maps no global chaos is observed and only initial conditions located within mean-motion resonances indicate chaotic dynamics. For a circular giant planet orbit

and nearly independent of giant planet mass, the simulations suggest that all Earth-like planets (particles) initially within the continuous habitable zone remain confined to this region within a 10^6 year time scale. Furthermore, based on the results obtained from long-term simulation of single particles, we conclude the existence of confined orbits on 10^9 years time scales. However, non-confinement of terrestrial orbits are observed for giant planet eccentricity exceeding $e_{max} = 0.16$. Eccentric orbits have their perihelion distance closer to the host star compared to circular orbits. This leads to orbit crossings and an increased potential of the event of close encounters. Assuming that no additional planets exists and if the giant planet eccentricity is less than $e = 0.16$, this system is a promising candidate to harbor habitable Earth-like planets (assuming a terrestrial planet has been initially formed within the habitable zone).

Regarding stability of Earth-like planets within HD4208:

Ashgari et al. (2004) presents a stability map analysis of terrestrial orbits within HD4208 using the Kolmogorov entropy as a measure to detect chaotic dynamics. Comparing their results with the MEGNO stability maps presented in this thesis reveals a qualitative conformity of the obtained dynamical results. Nearly every feature from global (general) chaos to the presence of mean-motion resonances are reproduced. However, Ashgari et al. did not undertake a mass parameter survey for the giant planet. The results presented here in the form of MEGNO stability maps considered various masses of the giant planet. For increasing mass, we observe most of the continuous habitable zone to become chaotic for nearly the whole range in giant planet eccentricity. For giant planet eccentricity $e \simeq 0.16$, we observed only a narrow band in semi-major axis exhibiting confined habitable orbits. For this eccentric orbit, we estimated that 98% of the total range within the continuous habitable zone would render terrestrial orbits inhabitable by either having their pericenter or apocenter distance crossing the inner and outer boundaries of the continuous habitable zone. Increasing the giant planet mass would result in even more dramatic dynamical events. For masses larger than 3 M_{Jup} our simulations indicated a depletion of particles mainly from $a > 1$ AU. Because of short-range perturbations particles are removed as a consequence of strong two-body gravitational interactions and close-encounters. In some cases the formation of gaps and void regions are observed. However, an exception is the case for which the giant planet have a circular ($e = 0$) orbit. In this case nearly the whole range for particles within the continuous habitable zone, have small eccentricity variations (except at the 2:1 and 4:3 resonance). For a low mass ($m_{pl} \simeq 1 - 3\ M_{Jup}$) giant planet with $e \simeq 0.0$, we observe (cf. Fig.7.19) that terrestrial planets with initial semi-major axis in the range 0.85 AU $< a <$ 1.0 AU of the continuous habitable zone are confined during the 10^6 integration period. We conclude, that a Jupiter-mass giant planet

with a circular orbit at $a \sim 1.68$ AU, could render Earth-like planetary orbits to be confined within the continuous habitable zone. However, an interesting question, not addressed in this thesis is, how likely is the formation of a terrestrial planet in the proximity of a giant planet perturber? A partial answer exist and has been given within the stability discussion of the 47 UMa planetary system. We will take up this discussion in the final conclusion section.

Comparison of results - what has been learned?:

Comparing the results for the two systems, we conclude the following. In general, giant planets (HD4208b, $a \simeq 1.68$ AU) with orbital parameters in the vicinity of the habitable region excert strong gravitational mean-motion perturbations on terrestrial Earth-like orbits. The dynamical effect of giant planet mean-motion resonances increases for increasing giant planet eccentricity, resulting in a resonance replenishing within the terrestrial habitable zone. The effect of mean-motion resonance perturbations is dynamically manifested in eccentricity excitations. This result suggests that the presence of mean-motion resonances are best avoided within the terrestrial region, in order to circumvent strong resonance effects. However, for giant planets close to the terrestrial region, confinement of terrestrial planetary orbits to within the continuous habitable zone is guaranteed only for a low-mass ($m_{pl} < 3\ M_{Jup}$) and circular orbit giant planet. Although, the 2:1 and 4:3 mean-motion resonances dominates the dynamics for these parameters. One could speculate that mean-motion resonances could have a counteracting effect on terrestrial planet accretion in the late stage of planet formation. Moderate high eccentricities of planetesimals within the terrestrial region would represent a stirring in the late evolved planetesimal disk, represent a higher velocity dispersion relative to circular planetary orbits. A higher mean velocity would automatically mean a higher relative impact velocity within the event of two-body collisions. This mechanism could imply a higher fragmentation frequency of planetesimals, counteracting the proces of planet accretion in order to form Moon to Mars sized protoplanets. However, the presence of mean-motion resonances in the outskirts of the terrestrial region within the Solar System are important in order to provide a transport mechanism of hydrated planetesimals from the asteroid belt toward the inner terrestrial region (i.e Earth - cf. Fig. 1.5, Chapter 1, Raymond et al. (2004)).

In order to bypass the dynamical effect of mean-motion resonances, results from our numerical simulations suggests a larger separation between the terrestrial and the perturbing planet. The optimal configuration would be represented by a giant planet in a wide orbit (HD70642, $a \geq 3.3$ AU). Simulations considering the giant planet HD70642b indicate a decrease in the number of mean-motion resonances in the continuous habitable zone. However, for eccentric giant planet orbit a general eccentricity excitation is observed. This excitation is attributed to the inforced giant

planet perturbations, due to the decrease of the orbital pericenter distance. From simulation snapshots, a maximum allowed eccentricity ($e_{max} = 0.16$) for the orbit is determined in order for terrestrial Earth-like planets to remain confined to within the continuous habitable zone at $a \simeq 1.0$ AU. This upper limit should be regarded very restrictive, since only 12% of the continuous habitable zone were populated with confined orbits (namely those particles with initial semi-major axis $a \simeq 1$ AU).

Application to giant planet data, general conclusion:

The results obtained from our simulations can be used to gain some information on the general possibility of the existence of habitable Earth-like planets within the current population of observed giant planets. Fig. 7.32 shows the (a, e)-space for the total population of giant planets observed in extrasolar planetary systems. Within each figure panel, the semi-major axis and the upper bound in eccentricity (as determined for HD70642b) are indicated by stipulated lines.

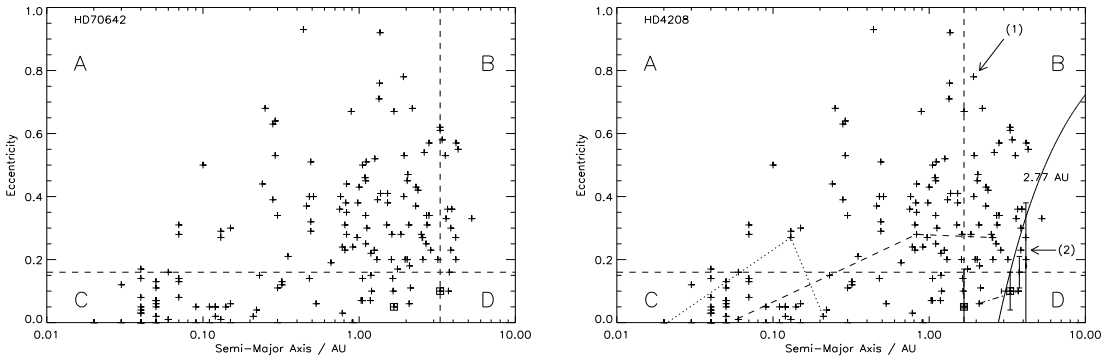

Figure 7.32: Plots of the current population of observed giant extrasolar planets in (a, e)-space. In both panels orbital parameters (nominal) for HD70642b and HD4208b are indicated by (□). Stipulated lines represent the current observed semi-major axis (vertical line) and upper bound in eccentricity (horizontal line). Left panel: HD70642, $a = 3.3$ AU and $e = 0.16$. Right panel: HD4208, $a = 1.68$ AU and $e = 0.16$. Giant planets being members in multiplanet systems are indicated by lines. Dashed line: Ups And. Dotted line: Gliese 876. Dashed-dot line: 47 Uma. The solid curve is the contour line for a pericenter distance of $a = 2.77$ AU. Giant planet candidates located below this line, will have a pericenter distance greater than 2.77 AU. Giant planet candidates located above this line, will have a pericenter distance smaller than 2.77 AU. Results from numerical simulations, suggests that $q < 2.77$ AU marks the onset of global unconfinement of terrestrial orbits. For both systems error bars indicate the uncertainty range in orbital parameters. For HD4208 the error in semi-major axis is smaller than the indicated box. In addition, the error range in eccentricity for two selected giant planets are shown.

From Fig.7.32, we conclude the following. For each panel the stipulated lines marks the nominal semi-major axis (vertical line for each giant planet) and the maximum

eccentricity (horizontal). The lines divide the (a, e)-parameter space into 4 regions (A,B,C,D). Considering first the case for HD70642 (left panel), it is clear that giant planets populating the A-region would introduce large gravitational perturbations on planets within the terrestrial region. The reason for this is, because extrasolar giant planets located within this region are characterised by (moderate/high) eccentric orbits (eccentric orbits have their pericenter distance shifted closer to the central star, resulting in terrestrial orbit crossings). Hence, results from numerical simulations suggest a destabilisation and non-confinement of terrestrial orbits within the continuous habitable zone for $e \geq 0.16$ and $a \leq 3.3$ AU.

The survival of terrestrial Earth-like planets within planetary systems with giant planet orbital parameters attributed to the C-region in Fig.7.32 ($a \leq 3.3$ AU and $e \leq 0.16$) seems intuitively unlikely. According to standard (Solar System) planet formation theory, it is believed that giant planets are formed in the outer region ($a > 5$ AU) of the initial protoplanetary disk. For a sufficient massive disk, it has been shown that disk-planet interactions induces the process of planet migration (Murray et al., 1998; Kley, 2000; Nelson and Papaloizou, 2004). Hence, during the migration process, strong perturbation interactions are expected to exist between the giant and terrestrial planet. The ultimate fate of an Earth-like planet would either be an ejection or collision event, while the giant planet traverses inwards through the terrestrial region. However, Mandell and Sigurdsson (2003) reports on the possible survival of terrestrial planets in the presence of giant planet migration. Further studies of this kind needs to be considered in order to confirm the published results. For now, we will regard this region to be very suspicious regarding the possibility of the existence of an Earth like planet within these systems. Detailed investigation needs to be performed in order to clarify this question.

This leaves us with the final two regions to be discussed. The most obvious parameter space for which terrestrial planets are on stable and confined orbits is represented by the D-parameter space ($a > 3.3$ AU and $e \leq 0.16$). From our studies considering the system HD4208 (with giant planet semi-major axis $a = 1.68$ AU), we concluded that terrestrial planets could remain on stable orbits confined to within the continuous habitable zone for circular giant planet orbits (having in mind the effect of the 2:1 resonance). For the case of HD4208 had an eccentric orbit ($e \simeq 0.16$), we observed dramatic dynamical effects rendering nearly the complete continuous habitbale zone to be unstable for confined particle dynamics.

The final region of interest is represented by the B-parameter space within Fig. 7.32 (right panel). High eccentric giant planet candidates are orbit crossing within the terrestrial region. For example, the planet with orbital parameters $a \simeq 2$ AU and $e \simeq 0.78$ (see arrow (1) within the figure panel), have a pericenter distance ($q \simeq 0.44$ AU) well located within the terrestrial region. The chance for a close encounter event with a terrestrial planet on a circular orbit at $a \simeq 1$ AU is most likely imaginable.

However, orbits with a larger semi-major axis allows for a larger eccentricity before the pericenter distance reaches some predescribed inner boundary. Obviously, some borderline must exist for the combined region (B+D) in order to divide the population into two regions: From our study considering HD70642, we determined a maximum eccentricity of $e_{max} = 0.16$. For a semi-major axis given by $a = 3.3$ AU the pericenter distance is given by $q = 3.3$ AU$(1.0 - 0.16) \simeq 2.77$ AU. If we adopt this distance to be the closest distance of a giant planet to allow visit the terrestrial region, then we can determine the allowed region within (a, e)-parameter space for which giant planet perturbations render terrestrial planets to be on confined habitable orbits. This constraint on orbital parameters inroduces the restriction of orbital pericenter distance to be $q > 2.77$ AU. Within Fig.7.32 (right panel), the solid contour line represents the ($q = 2.77$ AU) limiting pericenter distance, constraining and dividing the (a, e) parameter space.

Giant planets with orbital parameters located below this line represent giant planet candidates with $q > 2.77$ AU. Again, as an example we consider a planet with semi-major axis $a = 4.16$ AU and eccentricity $e = 0.18$ (marked by an arrow (2) within the right panel of Fig. 7.32). The pericenter of the orbit is located at $q \sim 3.41$ AU. The class of candidates belonging to within this parameter space are suggested to be dynamically "quiet" enough and "well spaced", to allow terrestrial planets on stable confined habitable orbits.

This result is in agreement with dynamical stability studies of terrestrial planets within the 47 Ursae Majoris extrasolar planetary system. Within Fig. 7.32 the two planets observed within 47 UMa are connected with a dashed-dotted line. Ashgari et al. (2004) determines stable orbits within the terrestrial region (with semi-major axis in the range 1.05 AU $< a <$ 1.3 AU and 0.65 AU $< a <$ 0.8 AU). However, Goździewski (2002) points out that several mean-motion and secular resonances are detected to be present within the habitable zone of 47 UMa, resulting in large orbit instabilities of possible terrestrial planets. In addition, (Laughlin et al., 2002) performed accretion simulations of terrestrial planets considering a ring of initial planetesimal within 47 UMa, addressing the question of how likely terrestrial planets could be formed. Laughlin et al. (2002) concluded that final Earth-like planets could only form within $a < 0.7$ AU by considering the perturbative effects of both giant planets. The removal of planetesimals within the habitable zone, were dominated by the presence of secular resonances causing large eccentricity excitations of planetesimal orbits.

Up to this point, we have identified possible orbital parameters of giant planets favouring the existence of terrestrial Earth-like planets on stable habitable orbits. This results are only valid for the case of single planet extrasolar planetary systems. From numerical simulation presented within the literature, the existence of terrestrial like planets were questionable for two-giant planetary systems in close proximity to the terrestrial region. This was discussed for the case of 47 UMa and

the dynamical effects of mean-motion and secular resonances were identified to be disruptive and counter acting the process of planet formation by planetesimal accretion. A similar mechanism is observed within the asteroid belt in the Solar System. This result suggests, that if two giant planets exists within a single planetary system, the inner planet needs to be located in the outskirts of the system in order to avoid the gravitational perturbative effects of mean-motion and secular resonances on planetesimals (and possible planets) within the terrestrial region.

Chapter 8

Conclusion and prospects

The work presented in this thesis concerned aspects of planet dynamics and Celestial Mechanics within the field of dynamical astronomy. We considered and outlined the basic theory for the three-body problem and its application to dynamical studies within extrasolar planetary systems. The main effort during the thesis period has focused on numerical methods for the integration of planetary orbits and the detection of their possible chaotic nature. Results of intensive numerical experiments broadened my physical understanding of planetary dynamics. Realistic and accurate numerical simulations enabled the assessment of necessary conditions on giant planet orbital parameters in order to render stable orbits of terrestrial like planets within extrasolar planetary systems.

The thesis period has been a laborious and time consuming project. However, from an academic point of view, I have acquainted myself in details on fundamental theory within modern celestial mechanics, planet dynamics and related numerical aspects. Numerical tools outlined and presented in this thesis can readily be applied to a large variety of physical problems within Solar System dynamics (i.e satellite dynamics, small-body dynamics, long-term stability), terrestrial planet formation (n-body accretion simulations within the late stage formation regime) and subsequent orbital evolution and orbital stability analysis of multi-planet extrasolar planetary systems.

8.1 Thesis summary

In the following, a summary of thesis highlights will be presented. Technical aspects regarding numerical issues and physical results are listed.

General and numerical aspects

- The three-body problem is identified and introduced. It represents a fundamental model to study the dynamical evolution of an Earth (particle) like body under gravitational perturbations of a giant planet.

- The solution of Kepler's equation has been investigated using different numerical algorithms (as outlined in Danby (1988)) by comparing the convergence speed of iterations within the (M, e)-parameter space. Implementation of numerical algorithms uses `IDL`.

- Modern algorithms for the numerical integration of planetary orbits were retrieved from the dynamical astronomy community. In particular, I have acquainted myself with the public available `MERCURY6` orbit integration package (Chambers and Migliorini, 1997; Chambers, 1999) and Mikkola's symplectic leap-frog code (Mikkola, 1997). The codes have been tested for possible limitations for applications of dynamical simulations within extrasolar planetary systems. Special properties of symplectic methods have been demonstrated and their numerical advantage outlined.

- Routines for coordinate transformation algorithms have been adopted from the literature (Boulet, 1991; Roy, 1988) and implemented within `F90`. The algorithms are outlined and tested and concerns transformation between Cartesian coordinates and Kepler elements. The routines are developed as modular input/output interfaces for coordinate transformation within the symplectic leap-frog integration algorithm.

- A numerical method to compute the MEGNO indicator have been obtained from the astrodynamical community. Theory and properties of the MEGNO indicator are discussed and outlined (Goździewski, 2001). The code have been tested against known results published within the literature. These tests enabled the identification of numerical issues regarding limitations and the proper calculation of MEGNO within a dynamical stability analysis.

- Orbital parameters for the giant planets HD70642b and HD4208b have been introduced and physical properties of the host stars are discussed (Carter et al., 2003; Vogt et al., 2001). For HD4208, we assumed a current stellar age of 5×10^9 years. The boundaries of the continuous habitable zone are inferred within the (a, e)-parameter space of the terrestrial regions for both systems. Boundaries for the continuous habitable zone are obtained from (Kasting et al., 1993). Considering the dynamics of Earth-sized planetary orbits within (a, e)-parameter space is more fruitful regarding the gain of system information in terms of orbital energy and angular momentum.

Physics, dynamical aspects and the effect of giant planet gravitational perturbations

From numerical simulations, we observe:

- The presence of high-order mean-motion resonances for large values of giant planet orbital eccentricity (HD4208 and HD70642) within the terrestrial region.
- Gravitational planet-particle resonance interactions, causing particle eccentricity excitations beyond the continuous habitable zone.
- Chaos dominated dynamics within the continuous habitable zone of HD4208 for large values of giant planet mass. The effect is particle removal (either accretion or ejection) and gap formation at regions corresponding to mean-motion resonances.
- General eccentricity excitation (eccentricity gradient) by giant planet perturbations on particle orbits throughout the considered terrestrial regions and within the continuous habitable zone (HD70642, HD4208).
- Correlation of "resonance strength" with giant planet orbital parameters. Planet-particle resonance interaction within HD70642 are more quiescent as compared to HD4208.
- Secular resonance dynamics. Correlation between particle eccentricity e_{tp}, and difference in apsidal argument $\omega_{tp} - \omega_{pl}$.

8.2 Concluding remarks, application and future work

In this thesis, we addressed the question whether orbits of possible Earth like planets are dynamically confined within the habitable zone of extrasolar planetary systems by considering the long-time effects of giant planet gravitational perturbations.

At the beginning, my motivation to persue this question is inspired by the existence of stable mean-motion resonances as observed within the asteroid belt in the Solar System. The first candidate subject for a numerical dynamical analysis were the extrasolar planetary system HD70642. This star is observed to exhibit spectroscopic signatures indicating the existence of a giant planet. During the thesis period, it proofed useful to compare the results obtained by numerical simulations

with a second exosystem characterised by different orbital parameters. For this purpose, we considered HD4208 for an additional dynamical analysis of the stability of hypothetical Earth like planets.

Numerical studies (Jones et al. (2001), Jones and Sleep (2002), Noble et al. (2002a)) concerning orbital stability simulations of Earth like planets in extrasolar planetary systems, generally considers the long-term dynamical evolution of single Earth sized planetary orbits. The numerical integration of planetary orbits is very CPU intensive. Hence, a parameter survey of giant planet orbital parameters is consequently restricted and limited by the factor of time. The overall strategy to

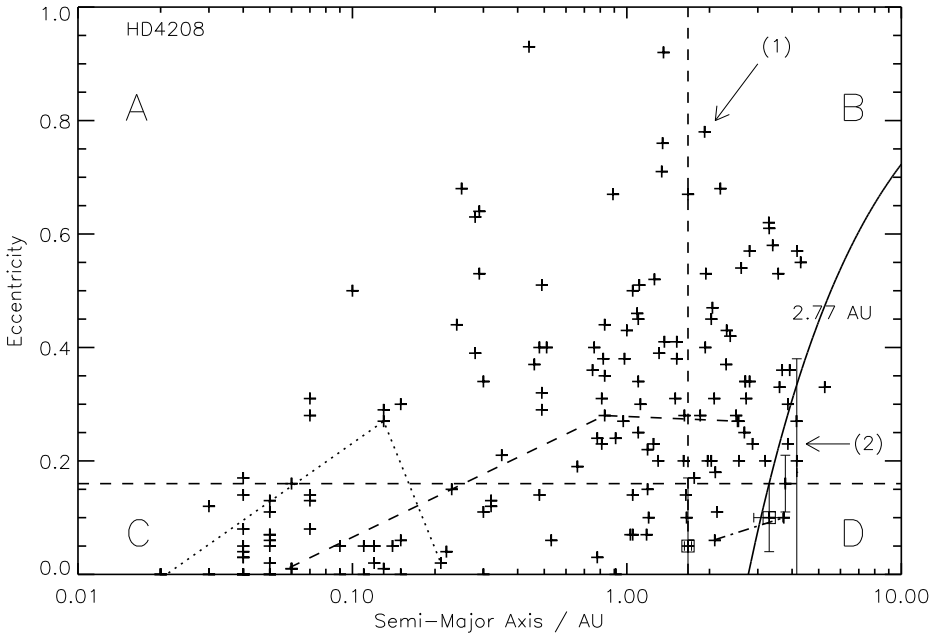

Figure 8.1: Population of observed (184 in total) giant planets within the (a, e)-parameter space. The planets HD70642b and HD4208b are indicated by (□) at their nominal published orbital values. HD4208: semi-major axis, $a = 1.67$ AU. HD70642: semi-major axis, $a = 3.3$ AU. The vertical dashed line indicates the position of the semi-major axis for HD4208 as determined by observations. This line represent the smallest allowed semi-major axis, as suggested from numerical stability simulations. The horizontal dashed line at $e = 0.16$, represents the maximum allowed orbital eccentricity for HD70642 (with $a = 3.3$ AU), as suggested from numerical stability simulations. The region below the solid contour line (representing the $a \simeq 2.77$ AU inner boundary) represents orbital parameters of (single) giant planets in order to render Earth like planets on stable orbits within the terrestrial region. For both systems error bars indicate the uncertainty range in orbital parameters. In addition, uncertainty ranges in eccentricity for two additional giant planets are shown. Data is taken from http://vo.obspm.fr/exoplanetes/encyclo /encycl.html.

accomplish our quest for the possible existence of Earth like planets in stable orbits

within extrasolar planetary systems, considers the short-term dynamics of an particle ensemble under the action of giant planet perturbations. This approach is different compared to work published within the literature and enabled us to perform a large parameter survey on initial conditions.

A comparative analysis of the systems HD70642 and HD4208, enabled us to generally conclude on the possible existence of Earth-like planets within the current population of observed extrasolar planetary systems. As a result, we identified a region within the (a, e)-parameter space for the current population of observed giant planets, for which the existence of an Earth like planet on a stable orbit within the continuous habitable zone is most likely. However, it is noted that the derived conditions of giant planet parameters to render stable Earth like orbits, represents a necessary condition. The gravitational effect from possible undetected (smaller) planets within HD70642 or HD4208 would introduce additional perturbations on the orbit of the considered Earth like planet. Hence, our conclusion is restricted to one-planet systems. Fig.8.1 represents and reflects the overall result obtained from numerical simulations. Single giant planets with orbital parameters located below the contour line corrsponding to $a = 2.77$ AU, are identified to possibly have terrestrial Earth-like planets on confined orbits within the habitable zone. Nevertheless, we did observe confined terrestrial planets for circular orbits of HD4208b. This result remains valid only for $m_{pl} < 3\ M_{Jup}$ considering HD4208b. However, it must be stressed that the presented stability analysis considered giant planets with host stars nearly similiar to the Sun. Strictly, only G-type stars should be considered within the suggested (a, e)-parameter plot.

Application

The results presented in this thesis are of purely theoretical character. Obviously, a direct comparison with observations is not possible at current time. The detection of terrestrial planets is beyond the resolving capabilities of current telescope technology. However, the results could be used to guide future satellite missions in their search for terrestrial planets in extrasolar planetary systems. Planned space missions like TPF (Terrestrial Planet Finder, NASA) or DARWIN (ESA) involves free-flying space telescopes designed to directly detect Earth-like planets orbiting nearby stars. The observation technique is based on nulling interferometry and first light is expected to be within 8 to 15 years.

In order to detect terrestrial planets within future search missions the results presented in this work could be used to compile a mission targeting list of extrasolar planetary systems, with a high confidence (based on a numerical stability analysis) to harbor Earth-like planets on stable orbits within the terrestrial region. In fact, a possible region within (a, e)-parameter space of observed giant planets is readily identified (cf. Fig.8.1) to be considered as allowed orbital parameters for potential

candidates harboring terrestrial planets. A continuation of numerical experiments considering additional giant planet systems, would improve our understanding of general aspects of gravitational planetary interactions.

Future work

Several questions were left unanswered that need detailed investigation. The most obvious question concerns terrestrial planet formation: How is the process of terrestrial planet formation affected by the presence of near giant planet perturbations? What conditions on orbital parameters are mostly favouring the accretion process of terrestrial planets within the late stage of formation history? What is the general formation frequency of terrestrial Earth-mass planets? Some work considering accretion simulations of terrestrial planets have been done within the literature, but needs to be taken much further. The `MERCURY` integration package could be used for future studies considering accretion with possibly including collision induced fragmentation physics.

In addition, we pose the question on the dynamical effect of migrating giant planets on terrestrial planets. What is the survival frequency of terrestrial planets? Within numerical integrations the effect of migration could be modelled by adding a dissipative term to the equation of motion of the giant planet. This would require the use of different numerical techniques, as symplectic algorithms are strictly valid for conservative mechanical systems (although, some symplectic workarounds exists within the literature).

A further aspect of habitability is spin axis dynamics of the terrestrial planet. A planet rotating irregular or chaotic would not favour a stable climate environment. For the case of the Earth-Moon system, the Moon has a stabilizing effect on the Earth's spin axis. The most general question for future investigations is: what is the dynamical evolution of a planets spin axis considering both tidal and gravitational perturbations from various sources?

Appendix A

Fortran 90 and IDL source codes

A.1 analkep.f90

```
program analkep

 ! This program calc. exact position and velocities of a 2D Kepler orbit
 ! with eccentricity e and semi-major axis a. The program uses f and g
 ! functions to calc. the position and vel. at time t_n.
 ! Reference: Boulet, 1991

 use kinds
 use math
 use apc

 implicit none

real(KIND=kind15)  :: &
e,a,x_0,y_0,vx_0,vy_0,t_start,t_stop,n,solve_kep_eq,h,mm,x,y,vx,vy, &
r_0,r,cape_0,cape,t,f_func,g_func,f_dot,g_dot,ma,time

  integer :: &
counter

 ! integration param.:

 t_start = 0.0
 t_stop = 1.0*twopi
 n = 64 ! number of steps
```

```
h = (t_stop - t_start)/n ! step size

! orbit parameters:

e = 0.3
a = 1.0
mm = 1.0

! Initial values: (object starts at pericenter in an orbit with a=1.0 AU and
! the orbital period is

x_0 = a*(1-e)
y_0 = 0.0
vx_0 = 0.0
vy_0 = sqrt((1+e)/(1-e))
r_0= sqrt(x_0*x_0 + y_0*y_0)
cape_0 = 0.0

t = t_start
counter = 1

Open (1, file='analkep.dat', form='formatted', action='write', &
      blank='null')

do while (t .le. t_stop)

  ! first get eccentric anomaly

  ma = mm * t
  if (ma .gt. twopi) ma = mod(ma,twopi)

  ! solve kepler's equation:

  cape = solve_kep_eq(ma, e)

  ! calc. the f-function:

  f_func = a/r_0 * (cos(cape) - 1.0) + 1.0  ! (eq. 2.69)

  ! calc. the g-function:
```

```
   g_func = time + (sin(cape) - cape)/mm ! (eq. 2.69)

   ! calc. the position components and magn. of radius vector:

   x = f_func*x_0 + g_func*vx_0
   y = f_func*y_0 + g_func*vy_0
   r = sqrt(x*x + y*y)

   ! calc. the f_dot-function:

   f_dot = -(a*a*mm*sin(cape))/(r*r_0) ! (eq. 2.71)

   ! calc. the g_dot-function:

   g_dot = a/r * (cos(cape) - 1.0) + 1.0 ! (eq. 2.71)

   ! calc: the velocity components:

   vx = f_dot*x_0 + g_dot*vx_0
   vy = f_dot*y_0 + g_dot*vy_0

   ! read out data:

   write (1,'(f10.3,1X,f10.6,1X,f10.6,1X,f10.6,1X,f10.6)') t,x,y,vx,vy

   t = t + h
   time = time + h
   if (time .gt. twopi) time = mod(time,twopi)
   counter = counter + 1

 enddo

 ! make a final data dump (last data!):

 write (1,'(f10.3,1X,f10.6,1X,f10.6,1X,f10.6,1X,f10.6)') t,x,y,vx,vy

 close(1)

end program analkep
```

A.2 car2kep.f90

```
program car2kep

 !#########################################################################
 !# Program description:                                                  #
 !# This program converts heliocentric cartesian elements (x,y,z,vx,vy,vz) at  #
 !# epoch t0 to osculating keplerian elements (a, e, i, omega, capo, ma) and   #
 !# derived quantities like (piomega, ml, q, bigq, tau, f, tlon, mm, theta)    #
 !# where                                                                 #
 !# a = semimajor axis                                                    #
 !# e = eccentricity                                                      #
 !# i = inclination                                                       #
 !# omega = argument of pericenter                                        #
 !# capo = longitude of ascending node                                    #
 !# ma = mean anomaly                                                     #
 !# piomega = longitude of pericenter                                     #
 !# ml = mean longitude (lambda)                                          #
 !# q = pericenter distance                                               #
 !# bigq = apocenter distance                                             #
 !# tau = time of pericenter passage                                      #
 !# f = true anomaly                                                      #
 !# tlon = true longitude                                                 #
 !# mm = mean motion                                                      #
 !# theta = true longitude                                                #
 !# Note: The velocities must be given in units of vx/k, vy/k, vz/k       #
 !#                                                                       #
 !#########################################################################

 use kinds
 use math
 use apc

 implicit none

 ! external variables (going in):

  real(KIND=kind15)  :: &
x,y,z,vx,vy,vz,t0,m_pl,m_star

 ! external variables (going out):
```

```
real(KIND=kind15)  :: &
a,e,i,q,capo,omega,ma,mm,f,tau,theta,piomega,ml

integer  :: &
conic

 ! internal variables:

real(KIND=kind15)  :: &
v,mu,r,v2,rv,hx,hy,hz,h2,h,ex,ey,ez,e2,tmp1,tmp2,tmp3,capn, &
cosi,coscapo,capne,cosomega,xbar,ybar,b,cape,pocs,bigd,bigh, &
per,sini,coscape,sinf,cosf,er

 ! first compute basic quantities:

 r = sqrt(x*x + y*y + z*z) ! heliocentr. distance from central body (Sun)
 v2 = vx*vx + vy*vy + vz*vz ! "v dot v" heliocentric velocity squared
 rv = x*vx + y*vy + z*vz ! "r dot v" heliocentric

 hx = (y*vz) - (z*vy) ! ang. mom. 1.component, heliocentric
 hy = (z*vx) - (x*vz) ! ang. mom. 2.component, heliocentric
 hz = (x*vy) - (y*vx) ! ang. mom  3.component, heliocentric

 h2 = hx*hx + hy*hy + hz*hz ! square of ang. mom. , heliocentric
 h  = sqrt(h2)
 capn = sqrt(hy*hy + hx*hx) ! Boulets ascending node vector, heliocentric

 ! calc. conic parameters - e, p and Laplace-Runge-Lenz vector:

 mu = m_star + m_pl ! Boulets mu, masses in units of m_star
 pocs = h2/mu ! semi-parameter, param. of conic section
 tmp1 = (v2/mu) - (1.0/r) ! used for the L-R-L vector
 tmp2 = rv/mu ! used for the L-R-L vector

 ex = tmp1*x - tmp2*vx ! Laplace-Runge-Lenz vector, x-comp
 ey = tmp1*y - tmp2*vy ! Laplace-Runge-Lenz vector, y-comp
 ez = tmp1*z - tmp2*vz ! Laplace-Runge-Lenz vector, z-comp

 capne = hx*ey - hy*ex ! vec{N} dot vec{e}
 e2 = ex*ex + ey*ey + ez*ez ! mag. of eccentricity
```

```
! calc. eccentricity from Laplace-Runge-Lenz vector:

if (e2 .lt. 0.0) then
  e = 0.0
else
  e = sqrt(e2)
endif

! calc. the inclination, true longitude and long. of ascending node and
! consider special cases:

! inclination:   will always be within 0 .le. i .le. pi

if (h .ne. 0) then
  cosi = hz/h
  sini = capn/h
  i = acos(hz/h) ! i is in proper quadrant since 0 <= acos <= pi
endif

! watch for the case when inclination is small or 0.0:

if (sini .lt. 1.0e-10) then ! then i is either nearly pi or 0 (no inclination case)
  theta = atan2(y,x) ! true longitude within proper quadrant,see Roy p.104-105
  if (ABS(i - pi) .lt. 1e-10) theta = -theta !change sign for retrograde orbit
  if (cosi .gt. 0.0) then
  i = 0.0 ! brutally set i = 0.0 and have prograde orbits
  capo = 0.0 ! long. of ascending node is not defined, we set capo=0.0
  endif
  if (cosi .lt. 0.0) then
  i = pi ! we have retrograde orbits
  capo = 0.0 ! long. of ascending node is not defined, we set capo=0.0
  endif
else
  capo = acos(-hy/capn) ! asc. node within 0 and pi
  if (hx .lt. 0) capo = twopi - capo ! asc. node within pi and 2pi
  theta = atan2( z/sin(i), x*cos(capo) + y*sin(capo) ), see Roy,p.104-105
endif

! normalize the angles:
```

```
if (capo .lt. 0.0) capo = capo + twopi ! normalize capo
if (capo .gt. twopi) capo = mod(capo,twopi) ! normalize capo
if (theta .gt. twopi) theta = mod(theta, twopi)! normalize theta
if (theta .lt. 0.0) theta = theta + twopi ! normalize theta

! determine type of conic section (using the eccentricity parameter):

if (ABS(1.0 - e) .lt. 1.0e-8) then ! if e > 0.99999999 then
  conic = 0  ! parabola (the e = 1 case)
else
  if (e .lt. 1.0) conic = -1 ! ellipse
  if (e .gt. 1.0) conic = +1 ! hyperbola
endif

! the elliptic and circular case:

if (conic .eq. -1) then
  if (e .gt. 1.0e-5) then ! the elliptic case also if e=1e-5
    print *, 'ellipse'

    ! working within orbit plane coordinate system:

    ! semimajor axis and pericenter distance:

    a = 1.0/(2.0/r - v2/mu) ! semimajor axis
    q = pocs/(1.0 + e) ! pericenter distance
    bigq = a*(1.0 + e) ! apocenter distance

    ! true anomaly:

    er = ex*x + ey*y + ez*z ! e dot r

    if (e .ne. 0) then
      f = acos(er/(e*r)) ! true anom. within 0 and pi
      if (rv .lt. 0) f = twopi - f ! true anom. within pi and 2pi
      if (f .lt. 0) f = f + twopi ! normalizing
      if (f .gt. twopi) f = mod(f,twopi) ! normalizing
    endif

    ! eccentric anomaly, accurate also for small eccentricities (guthmann):
```

```
    cape = acos( (e+cos(f))/(1.0+e*cos(f)) ) ! E within 0 and pi

    if ( (f .lt. twopi) .and. (f .gt. pi) ) cape=twopi-cape ! E w. pi and 2pi
    if (cape .lt. 0) cape = twopi + cape ! normalizing
    if (cape .gt. twopi) cape = mod(cape,twopi)! normalizing
    ma = cape - e*sin(cape) ! mean anomaly from Kepler eq.
    omega = theta - f ! arg. of pericenter
  else          ! the circular case e < 0.00000001
    !print *, 'circular orbit'
    e = 0.0
    f = theta ! true anomaly becomes true longitude
    cape = theta      ! eccentric anomaly becomes true long.
    a = pocs
    omega = 0.0
    ma = theta
  endif

  if (omega .lt. 0) omega = omega + twopi ! normalizing within 0 and 2pi
  if (omega .gt. twopi) omega = mod(omega,twopi)! normalizing within 0and2pi
  mm = sqrt(mtot/(a*a*a))*k ! mean motion rad./day
  tau = t0 - (ma/mm) ! time of pericenter passage
  per = (twopi/k)*sqrt((a*a*a/mtot)) ! orbital period
endif

! the hyperbola (e > 1.0) case:

if (conic .eq. +1) then
  !print *, 'hyperbola'
  ybar = (rv/e)*sqrt(pocs/mu)
  xbar = (pocs - r)/e
  b = -a*sqrt(e*e - 1.0)
  bigh = sinh(ybar/b)
  ma = e*(ybar/b) - bigh
  mm = k*sqrt(mtot/(-a)**3) ! mean motion
  tau = t0 - ma/mm
  per = 0.0
endif

! the parabolic (e = 1.0 = (0.99999999)) case:

if (conic .eq. 0) then
```

```
   !print *, 'parabola'
   a = 0.5*pocs ! here a means pericenter distance
   bigd = rv/sqrt(mtot)
   ma = q*bigd + (bigd*bigd*bigd)/6.0
   mm = k*sqrt(mtot)
   tau = t0 - ma/mm
   per = 0.0
 endif

 if (ma .gt. 0.0) ma = mod(ma, twopi)
 if (ma .lt. 0.0) ma = ma + twopi

 ! calc. weired angles and normalizing:

 piomega = capo + omega
 ml = ma + capo + omega

 if (piomega .lt. 0) piomega = twopi + piomega
 if (piomega .gt. twopi) piomega = mod(piomega,twopi)

 if (ml .lt. 0) ml = twopi + ml
 if (ml .gt. twopi) ml = mod(ml,twopi)

end program car2kep
```

A.3 kep2car.f90

```
program kep2car

!##############################################################################
!# Program description:                                                       #
!# This program converts Kepler elements to Cartesian heliocentric coordinates #
!# or any inertial coordinate system for which Kepler elements are defined.   #
!#                                                                            #
!# input: (a,e,M,i,omega,capo,t0,mu)-Kepler elements                          #
!#                                                                            #
!#output: (x_h,y_h,z_h,vx_h,vy_h,vz_h) ( heliocentric Cartesian coordinates   #
!#        (celestial ecliptic coordinates) and velocities                     #
!#                                                                            #
!# where:                                                                     #
!#        a - semimajor axis, [a] = AU                                        #
!#        e - eccentricity                                                    #
!#        M - mean anomaly                                                    #
!#        i - inclination                                                     #
!#        omega - argument of pericentre                                      #
!#        cap   - long. of ascending node                                     #
!#        t_0   - Initial Epoch                                               #
!#                                                                            #
!#                                                                            #
!# compiling option(s): f90 -O2 kep2car.f90 -o kep2car                        #
!#                                                                            #
!# reference    Boulet, "Methods of Orbit Determination" (1991)               #
!#                                                                            #
!##############################################################################

 use kinds
 use apc
 use math

 implicit none

 ! external variables (going in and going out)

  real(KIND=kind15)  :: &
a,e,i,ma,omega,capo,m_pl,x_h,y_h,z_h,vx_h,vy_h,vz_h,lop &
ta,m_cen,x_e,y_e,z_e,vx_e,vy_e,vz_e,t0,mm,ta,tau
```

```
 ! internal variables:

  real(KIND=kind15)  :: &
z1,z2,z3,z4,d11,d12,d13,d21,d22,d23,x_scalar,y_scalar, &
x_dot_scalar,y_dot_scalar,tmp1,tmp2,tmp3,tmp4,mu,q, &
solve_kep_eq,solve_barkers_eq,lop,solve_hyper_eq

integer  :: &
conic

 mu = k2*(m_cen + m_pl)

 ! converting from degrees to radian measure:

 i     = i*DtoR
 ma    = ma*DtoR
 omega = omega*DtoR
 capo  = capo*DtoR

 ! normalizing angles (i, omega, capo, ma):

 if (i .gt. 0.0) then
   i = mod(i,twopi)
   else
   i = i + twopi
 endif

 if (omega .gt. 0.0) then
   omega = mod(omega, twopi)
   else
   omega = omega + twopi
 endif

 if (capo .gt. 0.0) then
   capo = mod(capo, twopi)
   else
   capo = capo + twopi
 endif
```

```
if (ma .gt. 0.0) then
  ma = mod(ma, twopi)
  else
  ma = ma + twopi
endif

if ( (i .eq. 0.0) .and. (e .eq. 0.0) ) then
  capo  = 0.0
  omega = 0.0
  lop = capo + omega
else
  if (i .eq. 0.0) then
    capo = 0.0
    lop = capo + omega
  else
    if (e .eq. 0.0) then
      omega = 0.0
      lop = capo + omega
    endif
  endif
endif

! Determine type of conic section (using the eccentricity)

if (ABS(1.0 - e) .lt. 1.0e-8) then ! if e > 0.99999999 then
  conic = 0  ! parabola (the e = 1 case)
else
  if (e .lt. 1.0) conic = -1 ! ellipse
  if (e .gt. 1.0) conic = +1 ! hyperbola
endif

! calc. scalar components of orbital motion (using e,a and ma)

! elliptic and circular case:

if (conic .eq. -1) then
  a = q/(1.0 - e)
  tmp1 = sqrt(1.0 - e*e)
  tmp2 = solve_kep_eq(ma,e)
  tmp3 = sqrt(mu/a)/(1.0 - e*cos(tmp2))
  x_scalar     = a*(cos(tmp2) - e) ! From (4.117) (ok)
```

```
  y_scalar     = a*tmp1*sin(tmp2) ! From (4.117) (ok)
  x_dot_scalar = -tmp3*sin(tmp2) ! From (4.117) (ok)
  y_dot_scalar = tmp1*tmp3*cos(tmp2) ! From (4.117) (ok)
endif

! parabolic orbit case:

if (conic .eq. 0) then
  tmp1 = solve_barkers_eq(ma, q) ! Call function (ok)
  tmp2 = q + 0.5*tmp1*tmp1 ! r from eq. (4.126) (ok)
  tmp3 = sqrt(mu) / tmp2 ! D_dot eq. (4.127) (ok)
  x_scalar     = q - 0.5*tmp1*tmp1 ! From eq.(4.129) (ok)
  y_scalar     = sqrt(2.0*q)*tmp1 ! From eq.(4.129) (ok)
  x_dot_scalar = -tmp1*tmp3 ! From eq.(4.129) (ok)
  y_dot_scalar = sqrt(2.0*q)*tmp3 ! From eq.(4.129) (ok)
endif

! hyperbolic orbit case:

if (conic .eq. +1) then
  a = q/(1.0 - e) ! here, "a" is well defined
  tmp1 = solve_hyper_eq(ma, e)         ! Call function
  tmp2 = -a * sqrt(e*e - 1.0)         ! From eq.(4.123) (=b)
  tmp3 = -a * (e * cosh(tmp1) - 1.0)         ! From eq.(4.120) (=r)
  tmp4 = sqrt(-mu/a) / tmp3 ! From eq.(4.122) (hdot)
  x_scalar = a * (cosh(tmp1) - e) ! From eq.(4.123) (ok)
  y_scalar = tmp2 * sinh(tmp1)         ! From eq.(4.123) (ok)
  x_dot_scalar = a * tmp4 * sinh(tmp1)         ! From eq.(4.123) (ok)
  y_dot_scalar = tmp2 * tmp4 * cosh(tmp1) ! From eq.(4.123) (ok)
endif

! rotation from star centeret coordinate system to the orbit-plane
! coordinate system (using capo, i and omega)

! auxiliary quantities:

z1 = cos(omega)*cos(capo)
z2 = cos(omega)*sin(capo)
z3 = sin(omega)*cos(capo)
z4 = sin(omega)*sin(capo)
```

```
 d11 = z1 - z4*cos(i) ! P_x component
 d12 = z2 + z3*cos(i) ! P_y component
 d13 = sin(omega)*sin(i) ! P_z component

 d21 = -z3 - z2*cos(i) ! Q_x component
 d22 = -z4 + z1*cos(i) ! Q_y component
 d23 = cos(omega)*sin(i) ! Q_z component

 ! calc. comp. of pos. and vel. using eq. (4.110, Boulet p.158):

 x_h  = d11*x_scalar + d21*y_scalar
 y_h  = d12*x_scalar + d22*y_scalar
 z_h  = d13*x_scalar + d23*y_scalar
 vx_h = d11*x_dot_scalar + d21*y_dot_scalar
 vy_h = d12*x_dot_scalar + d22*y_dot_scalar
 vz_h = d13*x_dot_scalar + d23*y_dot_scalar

end program kep2car
```

A.4 kepler.pro

```
Pro Kepler

; Goal: Solve elliptic Kepler equation with 3 methods:
; 1) N-R method (quadriatic convergence)
; 2) Hally's method (cubic convergence)
; 3) 3-method (quartic convergence)
; 1), 2) and 3) are compared to each other by plotting either
; (# iterations, x_n+1) and/or (# iterations, delta eps)

; After comparing the 3 methods, begin to investigate the initial
; (ma, e)-parameter space for which each of the three methods converge and plot
; a surface plot of (ma, e, #iterations used).

ma_min = 0.0D
ma_max = 3.0*!DPI

; find increment function for mean anomaly, dma
nma = 70
dma = (ma_max - ma_min)/nma

e_min = 0.0D
e_max = 1.0D

; find increment function for eccentricity, de
necc = 70
de = (e_max - e_min)/necc

; variable parameters
eps = 1.0E-12 ; tolerance for iteration accuracy
maxit = 20 ; maximum number of iterations
alpha = 0.0d0 ; alpha parameter for initial guess
beta =  1.0d0 ; beta parameter for initial guess

iter_array_nr = IntArr(nma, necc)
iter_array_halley = IntArr(nma, necc)
iter_array_quartic = IntArr(nma, necc)

arr_x = DblArr(nma)
arr_y = DblArr(necc)
```

```
; generating mean anomaly array
For i = 0, nma-1 Do Begin
   ma = i*dma + ma_min
   arr_x(i) = ma
Endfor

; generating eccentricity array
for j = 0, necc-1 do begin
   e = j*de+e_min
   arr_y(j) = e
endfor


for i = 0, nma-1 do begin ; mean anomaly loop
   for j = 0, necc-1 do begin ; eccentricity loop
       iter_array_nr(i,j) = Solve_kep_NR(arr_x(i), arr_y(j),eps,maxit,alpha,$
                                         beta)
       iter_array_halley(i,j) = Solve_kep_halley(arr_x(i),arr_y(j),eps,maxit,$
                                                 alpha,beta)
       iter_array_quartic(i,j) = Solve_kep_quartic(arr_x(i), arr_y(j),eps,$
                                                   maxit,alpha,beta)
   endfor
endfor

;************************************************************
; Newton-Raphson - plotting section

Set_plot, 'ps'
!X.Margin = [2,0]
!Y.Margin = [2,2]
;Device, filename='NR_surf_a1.0_b0.0best.eps', /Encapsulated
Device, filename='NR_surf_a1.0_b0.0_new.eps', /Encapsulated
surface, iter_array_nr, arr_x, arr_y, CharSize=3.0, XTITLE='!3Mean Anomaly', $
         ZTITLE='!3Iterations', YTITLE='!3Eccentricity', $
 XRANGE=[ma_min, ma_max], $
 /XSTYLE, TITLE='!3   !4a=!N1.0, !4b=!N0.0!3'
Device, /CLOSE

!X.Margin = [6,1]
!Y.Margin = [3,1]
```

```
Device, filename='NR_cont_a1.0_b0.0best.eps', /Encapsulated

Contour, iter_array_nr, arr_x, arr_y, /Follow, CharSize=1.5, $
         XTITLE='Mean Anomaly', YTITLE='Eccentricity', $
 XRANGE=[0.0, ma_max], YRANGE=[-0.05, 1.05], /YSTYLE, $
 ;Nlevels=20
 ;C_LABELS = [1,0,1,1,1,1,1,1,1,1,1,1], /DOWNHILL, $
 C_LABELS=[1,1,1,1,1,1,1,1,1,1,1,1,1],$
 LEVELS = [1,2,3,4,5,6,7,8,9,10,11,12,13];, /DOWNHILL
XYOUTS, 0.05, -0.03, '!3 !4a=!N1.0, !4b=!N0.0!3'
Device, /CLOSE
;*************************************************************

;*************************************************************
; Halley Area - plotting section

Set_Plot, 'ps'
!X.Margin = [2,0]
!Y.Margin = [2,2]

Device, filename='H_surf_a1.0_b0.0best.eps', /Encapsulated

surface, iter_array_halley, arr_x, arr_y, XTITLE='!3Mean Anomaly', $
         ZTITLE='!3Iterations', CharSize=3.0, XRANGE=[0.0, ma_max], $
 /XSTYLE, YTITLE='!3Eccentricity', $
 TITLE='!3   !4a=!N1.0, !4b=!N0.0!3'

Device, /CLOSE
!X.Margin = [6, 1]
!Y.Margin = [3, 1]

Device, filename='H_cont_a1.0_b0.0best.eps', /Encapsulated

Contour, iter_array_halley, arr_x, arr_y, /Follow, CharSize=1.5, $
         XTITLE='Mean Anomaly', YTITLE='Eccentricity', $
 XRANGE=[0.0, ma_max], YRANGE=[-0.05, 1.05], /YSTYLE, $
 ;Nlevels=20
 ;C_LABELS = [1,0,1,1,1,1,1,1,1,1,1,1], /DOWNHILL, $
 C_LABELS=[1,1,1,1,1,1,1,1,1,1,1,1,1],$
 LEVELS = [1,2,3,4,5,6,7,8,9,10,11,12,13];, /DOWNHILL
```

```
XYOUTS, 0.05, -0.03, '!3 !4a=!N1.0, !4b=!N0.0!3'
Device, /CLOSE
;*************************************************************

;*************************************************************
; Halley's quartic method - plotting section

Set_plot, 'ps'
!X.Margin = [2,0]
!Y.Margin = [2,2]

;Device, filename='Qua_surf_a1.3_b0.0.eps', /Encapsulated
Device, filename='test.eps', /Encapsulated

surface, iter_array_quartic, arr_x, arr_y, XTITLE='!3Mean Anomaly', $
         ZTITLE='!3Iterations', YTITLE='!3Eccentricity', $
 CharSize=3.0, XRANGE=[ma_min, ma_max], /XSTYLE, $
 TITLE='!3   !4a=!N1.0, !4b=!N0.0!3'

Device, /CLOSE

!X.Margin = [6, 1]
!Y.Margin = [3, 1]

Device, filename = 'Qua_cont_a0.0_b1.0.eps', /Encapsulated

Contour, iter_array_quartic, arr_x, arr_y, /Follow, CharSize=1.5, $
         XTITLE='Mean Anomaly', YTITLE='Eccentricity', $
 XRANGE=[-0.05, ma_max], YRANGE=[-0.05, 1.05], /XSTYLE, /YSTYLE, $
 ;Nlevels=20
 ;C_LABELS = [1,0,1,1,1,1,1,1,1,1,1], /DOWNHILL, $
 C_LABELS=[1,1,1,1,1,1,1,1,1,1,1,1,1],$
 LEVELS = [1,2,3,4,5,6,7,8,9,10,11,12,13];, /DOWNHILL
XYOUTS, 0.05, -0.03, '!3 !4a=!N0.0, !4b=!N1.0!3'

Device, /CLOSE
;*************************************************************

end

function Solve_kep_NR, ma,e,eps,maxit,alpha,beta
```

```
 ea = alpha*ma + beta*e
 func1 = ea - (e*sin(ea)) - ma
 iter = 1

 while ( (ABS(func1) GE eps) AND (iter LT maxit) ) do begin
      func1 = ea - (e * sin(ea)) - ma
      df = 1.0D - e*cos(ea)
      ea = ea - (func1/df)
      ;print, FORMAT = '(f17.15)', ea
      iter = iter + 1
 endwhile

 return, iter

end

function Solve_kep_halley, ma,e,eps,maxit,alpha,beta

 ea = alpha*ma + beta*e
 func1 = ea - (e*sin(ea)) - ma
 iter = 1

 while ( (ABS(func1) GE eps) AND (iter LT maxit) ) do begin
      func1 = ea - (e*sin(ea)) - ma
      df = 1.0 - e*cos(ea)
      ddf = e*sin(ea)
      temp = (func1 * ddf) / (0.5*df)
      ea = ea - ( (func1) / (df - temp) )
      iter = iter + 1
 endwhile

 return, iter

end

function Solve_kep_quartic, ma,e,eps,maxit,alpha,beta

 ea = alpha*ma + beta*e
 f = ea - (e*sin(ea)) - ma
 iter = 1
```

```
 while ( (ABS(f) GE eps) AND (iter LT maxit) ) do begin
      f = ea - (e*sin(ea)) - ma
      temp1 = e*sin(ea); second derivative of f
      temp2 = e*cos(ea); third derivative of f
      df = 1.0 - temp2 ; first derivative of f
      eps1 = -f/df
      eps2 = -f/(df + 0.5*eps1*temp1)
      ;ea = ea - f/(df + 0.5*eps2*(temp1 + 0.333333333333333*eps2*temp2) )
      eps3 = -f/( df + 0.5*eps2*temp1 + ((eps2*eps2*temp2)/6.0))
      ea = ea + eps3
      iter = iter + 1
 endwhile

 return, iter

end
```

Appendix B

Poster

Poster (next page) presented at the annual DPS/AAS conference meeting, Cambridge (UK), September 2005. T.C.Hinse, U.G.Jørgensen (BAAS, v.37 p.3).

Chaos and Planet-Particle Dynamics within the Habitable Zone of Extrasolar Planetary Systems

A qualitative numerical stability study of HD4208 and HD70642

Tobias C. Hinse (tobiash@astro.ku.dk), Uffe G. Jørgensen (uffegj@astro.ku.dk)
(Niels Bohr Institute, Astronomical Observatory, Copenhagen, Denmark)

1. Motivation and introduction

One of the most interesting question is the possibility of the existence of Earth-like planets within observed extrasolar planetary systems. We investigate whether extrasolar terrestial planetary orbits dynamically remain confined within the habitable zone (HZ) of selected one-planet extrasolar systems. The habitable zone for each system, is determined from Kasting et al. (1993). We consider orbit constrains on both a- and e-parameters. Using numerical chaos indicators and performing dynamical large-scale test-particle simulations, the parameter phase-space is explored within the region of habitability. We introduce the MEGNO indicator for the study of chaotic dynamics within the habitable zone. It allows a fast determination and identification of orbital mean motion resonances. Direct numerical integration of mass-less test-particles explores the dynamical evolution under the presence of giant planet perturbations.

2. Numerical methods and model

The equations of motion (and variational equations) are solved using classic and symplectic integration algorithms. The model is based on Newtonian point-mass mechanics.

- Symplectic (hybrid) mixed-variable algorithm (Chambers,J. (1999) MNRAS,304, 793.
- Interpolation algorithms (BS, GBS)

3. Observations and Kepler elements

- Orbital parameters are derived from synthetic Kepler fits to observed radial velocity measurements. (Vogt et al. (2001), ApJ, 568, p. 352 and Carter et al. (2003), ApJ, 594, p. L43)

Parameters	HD70642b	HD4208b
a (AU)	3.3 ± 0.4	1.68 ± 0.05
e	0.1 ± 0.06	0.04 ± 0.12
ω (°)	277 ± 75	301 ± 84
$M_{pl} \sin i$ (M_{Jup})	2.0	0.80
P (days)	2231 ± 400	829 ± 36
K (ms^{-1})	32 ± 5	18 ± 2
T (JD)	2451749 ± 300	2451774 ± 197

4. Habitable zone boundaries

- Boundaries (R_{in} and R_{out} at ZAMS and current host star age) are determined by interpolation from Kasting et al. (1993) (Icarus, 101, p.108) using conservative atmosphere model.
- Constrains on orbital parameters: $R_{pl} \leq a\,(1 \pm e) \leq R_{out}$.
- Stellar parameters: HD4208 - m = 0.93 M_{sol}, T_{eff} = 5572 K, G5V, 5 Gyrs.
  HD70642 - m = 1.0 M_{sol}, T_{eff} = 5670 K, G5, 4 Gyrs.

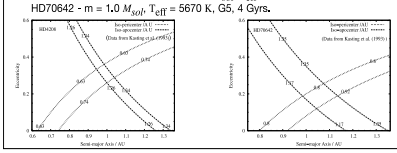

5. Phase space exploration and parameter survey

- Phase space exploration within uncertainty range of observed parameters.
- Real planet mass is undetermined. Only minimum mass is known.
- Co-planar orbits with fixed (a, ω) and $M = 0$ are considered.
- We explore the (M_{pl}, e) parameter space within the HZ corresponding to various line-of-sight inclinations.

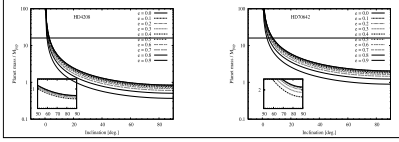

6. Conclusions, applications and future work

- The application of a MEGNO analysis proves useful for obtaining a quick global picture of the dynamics within the habitable zone(s).
- Giant planets on low eccentric, long period orbits have an increased probability in harboring terrestial planets within the HZ. This result is independent of giant planet mass. Giant planet eccentricity is the most dominant parameter.
- Future work aims to assess a statistical measure to quantify habitability as a function of giant planet orbit parameters.
- This kind of dynamical analysis could help future space-based search missions for habitable planets, by providing a mission targeting list of observed extrasolar systems on confined and dynamically stable orbits within the habitable zone(s).

HD4208

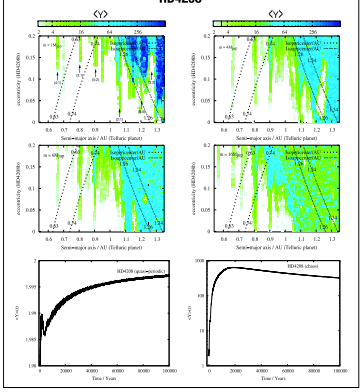

MEGNO analysis and restricted 3-body dynamics

- MEGNO ($\langle Y \rangle$) measures exponential divergence of nearby orbits and distinguish between quasi-periodic (regular) and chaotic dynamics. Megno is fast converging and efficient - allowing the exploration of a large set of initial conditions (K. Goździewski et al. (2001) A&A 378, p.569).
- Quasi-periodic time evolution of a solution: $\langle Y \rangle(t) \to 2$, $t \to \infty$
- Chaotic time evolution (with Lyapunov characteristic exponent λ): $\langle Y \rangle(t) \to \lambda t/2$, $t \to \infty$
- We explore (a, e_{pl}) - phase space on a $(N_X, N_Y) = (110, 80)$ grid with $T_{int} \sim 5 \times 10^4\ P_{orb}$ and a renormalisation time of $\tau \sim P_{orb}$.
- 2000 particles are randomly distributed on circular orbits within the habitable zone boundaries. Total simulation time: 10^6 years. Integration accuracy in relative energy: $dE/E \sim 10^{-9}$.

Main results - We observe ...

- The presence of high-order mean-motion resonances for large values of giant planet eccentricity.
- Gravitational planet-particle resonance interactions, causing particle eccentricity excitations within the habitable zone(s).
- Chaos dominated dynamics within the habitable zone(s) (HD4208) at large values of giant planet mass. This leads to particle removal (either accretion or ejection) and gap formation.
- A final particle eccentricity gradient confined throughout the habitable zone(s) (HD70642) for a low eccentric giant planet orbit.
- Decrease of "resonance strength" for long period orbits (HD70642).

HD70642

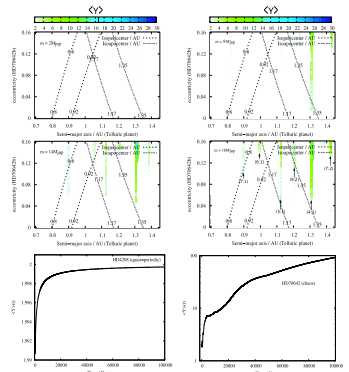

HD4208 - Particle simulation snapshots

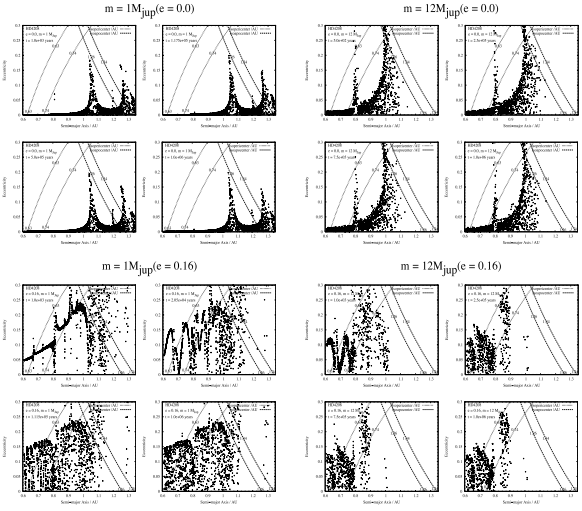

HD70642 - Particle simulation snapshots

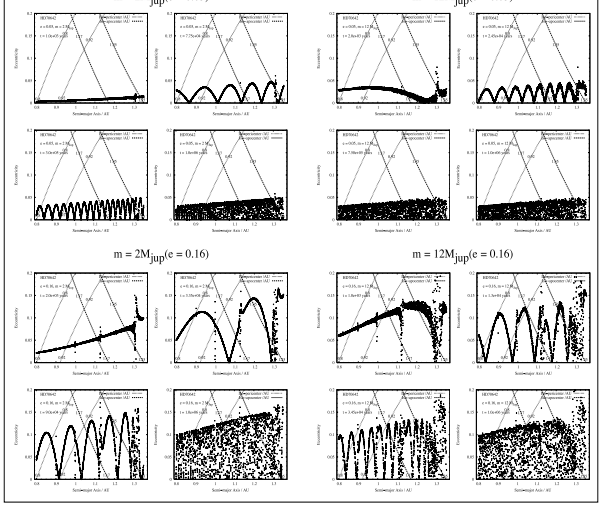

Bibliography

Agnor, C., Canup, R., and Levison, H.: 1999, *On the Character and Consequences of Large Impacts on the Late Stage of Terrestial Planet Formation*, *Icarus* **142**, 219

Ashgari, N., Broeg, C., Carone, L., Casas-Miranda, R., Castro Palacio, J., Csillik, I., Dvorak, R., Freistetter, F., Hadjivantsides, G., Hussmann, H., Khramova, A., Khristoforova, M., Khromova, I., Kitiashivilli, I., Kozlowski, S., Laakso, T., Laczkowski, T., Lytvinenko, D., Miloni, O., Morishima, R., Moro-Martin, A., Paksyutov, V., Pal, A., Patidar, V., Pečnik, B., Peles, O., Pyo, J., Quinn, T., Rodriguez, A., Romano, C., Saikia, E., Stadel, J., Thiel, M., Todorovic, N., Veras, D., Viera Neto, E., Vilagi, J., von Bloh, W., Zechner, R., and Zhuchkova, E.: 2004, *Stability of Terrestial Planets in the Habitable Zone of Gl 777, HD 72659, Gl 614, 47 UMa and HD 4208*, *astro-ph:* 0403152 v1

Barrow-Green, J.: 1996, *Poincaré and the Three Body Problem*, American Mathematical Society

Blum, J. and Wurm, G.: 2000, *Experiments on Sticking, Restructuring, and Fragmentation of PrePlanetary Dust Aggregates*, *Icarus* **143**, 138

Boccaletti, D. and Puccaco, G.: 1998, *Theory of Orbits. Volume2:Perturbative and Geometrical Methods*, Springer

Bond, I., Udalski, A., Jaroszynski, M., Rattenbury, N., Paczynski, B., Soszynski, I., Wyrzykowski, L., Szymanski, M., M., K., Szewczyk, O., Zebrun, K., Pietrynski, G., Abe, F., Bennett, D., Eguchi, S., Furuta, Y., Hernshaw, J., Kaniya, K., Kilmartin, P., Kuruta, Y., Mazuda, K., Matsubura, Y., Muraki, Y., Noda, S., Okajima, K., Sako, T., Sekiguchi, T., Sullivan, D., Sumi, T., Tristan, P., Yanagisawa, T., and Yock, P.: 2004, *OGLE 2003–BLG–235/MOA 2003–BLG–53: A Planetary Microlensing Event.*, *ApJ Letters* **606L**, 155B

Boulet, D.: First Edition, 1991, *Methods of Orbit Determination for the Microcomputer*, Willman-Bell, Inc.

Brasser, R.: 2003, PhD dissertation, Turku University, Finland, SARJA - SER.A I OSA-TOM. 299, Thesis is available in english

Brasser, R. e.: 2005, *private communication*

Briceño, C., Vivas, A., Calvet, N., Hartmann, N., Pacheco, L., Herrera, D., Romero, L., Berlind, L., Sanchez, G., Snyder, J., and Andrews, P.: 2001, *The CIDA-QUEST large-scale survey of Orion OB1: evidence for rapid disk dissipation in a dispersed stellar population*, *Science* **291**, 93

Butler, R. and Marcy, G.: 1996, *A Planet Orbiting 47 Ursae Majoris*, *ApJ* **464**, L153

Carter, B., Butler, R. P., Tinney, C., Jones, H., Marcy, G., McCarthy, C., Fischer, D., and Penny, A.: 2003, *A Planet in a Cicular Orbit with a 6 Year Period*, *ApJ* **593**, L43

Chambers, J.: 1999, *A hybrid symlpectic integrator that permits close encounters between massive bodies*, *Mon. Not. R. Astron. Soc.* **304**, 793

Chambers, J.: 2001, *Making more Terrestial Planets*, *Icarus* **152**, 205

Chambers, J.: 2003, *The Formation of Life-Sustaining Planets in Extrasolar Systems*, *Lunar and Planetary Science* **34**, 2000C

Chambers, J. and Laughlin, G.: 2001, *Short-Term Dynamical Interactions Among Extrasolar Planets*, *Ap.J. Lett.* **551**, L109

Chambers, J. and Migliorini, F.: 1997, *Mercury - A New Software Packages for Orbital Integrations*, *BAAS* 27-06-P

Chambers, J. E. and Cassen, P.: 2002, *The effect of nebula surface density profile and giant-planet eccentricities on planetary accretion in the inner solar system*, *Meteoritics & Planetary Science* **37**, 1523

Chambers, J. E. and Wetherill, G. W.: 1998, *Making the Terrestial Planets: N-Body Intergrations of Planetary Embryos in Three Dimensions*, *Icarus* **136**, 304

Charbonneau, D., Brown, T., and Latham, D.W.and Mayor, M.: 2000, *Detection of Planetary Transits Across a Sun-like Star*, *ApJ* **529**, L45

Chiang, E., Fischer, D., and Thommes, E.: 2001, *Excitation of Orbital Eccentricities of Extrasolar Planets by Repeated Resonance Crossings*, *ApJ* **564**, L105

Cincotta, P. and Simó, C.: 2000, *Simple tools to study global dynamics in non-axisymmetric galactic potentials - I*, *Astron. Astrophys. Suppl. Ser.* **147**, 205

Clark, S.: 1998, *Extrasolar Planets - The search for new worlds*, John Wiley & Sons

Colwell, P.: 1993, *Solving Kepler's equation over three centuries*, Willman-Bell, Inc.

Contopoulos, G.: 2002, *Order and Chaos in Dynamical Astronomy*, Springer

Contopoulos, G., Galgani, L., and Giorgilli, A.: 1978, *On the number of isolating integrals in Hamiltonian systems*, *Physical Review A* **18,3**, 1183

Danby, J.: Second Edition, revised and enlarged, 1988, *Fundamentals of Celestial Mechanics*, Willman-Bell, Inc.

Diacu, F. and Holmes, P.: 1996, *Celestial encounters - The origin of stability and chaos*, Princeton University Press

Fischer, D., Marcy, G., Butler, R., Laughlin, G., and Vogt, S.: 2002, *A Second Planet Orbiting 47 Ursae Majoris*, *ApJ* **564**, 1028

Gehman, C., Adams, F., and Laughlin, G.: 1996, *The Prospects for Earth-like Planets within known Extrasolar Planetary Systems*, *Publ. Astr. Soc. Pac.* **108**, 1018

Gilmour, I. and Sephton, M. A.: 2004, *An Introduction to Astrobiology*, Cambridge University Press

Gladman, B., Duncan, M., and Candy, J.: 1991, *Symplectic Integrators for Long-Term Integrations in Celestial Mechanics*, *Celestial Mechanics and Dynamical Astronomy* **52**, 221

Goldreich, P. and Tremaine, S.: 1980, *Disk-Satellite Interactions*, *ApJ* **241**, 425

Goldstein, H.: 2nd edition, 1980, *Classical Mechanics*, Addison-Wesley Publishing Company

Goździewski, K.: 2001, *Global dynamics of planetary systems with the MEGNO criterion*, *A & A* **378**, 569

Goździewski, K.: 2002, *Stability of the 47 UMa Planetary System*, *A & A* **393**, 997

Goździewski, K.: 2003, *Stability of the HD 12661 Planetary System*, *A & A* **398**, 1151

Goździewski, K.: 2004, *Dynamical Properties of the Multiplanet System around HD 169830*, *ApJ* **610**, 1093

Gurzadyan, G.: 2002, *Space Dynamics*, Taylor & Francis

Hart, M.: 1979, *Habitable Zones about Main Sequence Stars*, *Icarus* **37**, 351

Hilditch, R.: 2001, *An Introduction to Close Binary Stars*, Cambridge University Press

Hiroshi, K. and Hiroshi, N.: 1989, *Numerical Integration Methods in Dynamical Astronomy*, *Celestial Mechanics* **45**, 231

Huang, S.-S.: 1959, *The Problem of Life in the Universe and the Mode of Star Formation*, *Pub.A.S.P.* **71**, 421H

Ito, T. and Tanikawa, K.: 2002, *Long-term integrations and stability of planetary orbits in our Solar system*, *MNRAS* **336**, 483

Johansen, A., Andersen, A., and Brandenburg, A.: 2004, *Simulations of dust-trapping vortices in protoplanetary discs*, *Astronomy and Astrophysics* **417**, 361

Jones, B. and Sleep, P.: 2002, *The Stability of the Orbits of Earth-Mass Planets in the Habitable Zone of 47 Ursea Majoris*, *A&A* **393**, 1015

Jones, B., Sleep, P., and Chambers, J.: 2001, *The Stability of the Orbits of Terrestial Planets in the Habitable Zones of known Exoplanetary Systems*, *A&A* **366**, 254

Jorissen, A., Mayor, M., and Udry, S.: 2001, *The Distribution of Exoplanet Masses*, *A&A* **379**, 992

Kasting, J., Whitmire, D., and Reynolds, R.: 1993, *Habitable Zones around Main Sequence Stars*, *Icarus* **101**, 108

Kley, W.: 2000, *On the migration of a system of protoplanets*, *MNRAS* **313**, L47

Kokubo, E. and Ida, S.: 2000, *Formation of Protoplanets from Planetesimals in the Solar Nebula*, *Icarus* **143**, 15

Kokubo, E. and Ida, S.: 2002, *Formation of Protoplanet Systems and Diversity of Planetary Systems*, *The Astrophysical Journal* **581**, 666

Kominami, J. and Ida, S.: 2002, *The effect of tidal Interaction with a Gas Disk on the Formation of Terrestial Planets*, *Icarus* **157**, 43

Kominami, J. and Ida, S.: 2004, *Formation of terrestial planets in a dissipating gas disk with Jupiter and Saturn*, *Icarus* **167**, 231

Konacki, M., Torres, G., Jhas, S., and Sasselov, D.: 2003, *A New Transiting Extra-solar Giant Planet*, *Nature* **421**, 507

Laughlin, G. and Adams, F.: 1999, *Stability and Chaos in the υ Andromedae Planetary System*, *The Astrophysical Journal* **526**, 881

Laughlin, G., Chambers, J., and Fischer, D.: 2002, *A Dynamical Analysis of the 47 Ursae Majoris Planetary System*, *Ap.J.* **579**, 455

Lecar, M., Franklin, F., and Holman, M.: 2001, *Chaos in the Solar System*, *Annu.Rev.Astron.Astrophys.* **39**, 581

Lin, D., Bodenheimer, P., and Richardson, D.: 1996, *Orbital Migration of the planetary companion of 51 Peg to its present location*, *Nature* **232**, 606

Lissauer, J.: 1993, *Planet Formation*, *Annu. Rev. Astron. Astrophys.* **31**, 129

Lissauer, J.: 1999, *Three planets for Upsilon Andromedae*, *Nature* **398**, 659

Malhotra, R.: 1998, *Orbital Resonances and Chaos in the Solar System*, *Solar System Formation and Evolution, ASP Conference Series* **149**, 37

Mandell, A. and Sigurdsson, S.: 2003, *Survival of Terrestrial planets in the Presence of Giant Planet Migration*, *ApJ* **599**, L111

Marcy, G. e.: 2005, *private communication*, *email correspondence in 2005, August*

Mayor, M., Naef, D., Pepe, F., Queloz, D., Santos, N. C., and Udry, S.: 2000, in A. Penny, P. Artymowicz, A.-M. Lagrange, and S. S. Russell (eds.), *Planetary Systems in the Universe: Observation, Formation and Evolution*, ASP Conference Series

Mayor, M. and Queloz, D.: 1995, *A Jupiter-mass Companion to a Solar Type Star*, *Nature* **378**, 255

Mikkola, S.: 1997, *Practical symplectic methods with time transformation for the few-body problem*, *Cel.Mech. and Dyn. Astr.* **67**, 145

Mikkola, S.: 2004, *Lecture Notes on Numerical Celestial Mechanics*, *Turku University Observatory, Finland* **23**, 1

Mikkola, S. and Innanen, K.: 1999, *Symplectic Tangent Map for Planetary Motion*, *Cel.Mech.Dyn.Astr.* **74**, 59

Mikkola, S. and Innanen, K.: 2002, *Individual Accuracy Checks for Massive Bodies and Particles in Symplectic Integrations*, *The Astronomical Journal* **124**, 3445

Morbidelli, A.: 2002a, *Modern Celestial Mechanics - Aspects of Solar System Dynamics*, Taylor & Francis

Morbidelli, A.: 2002b, *Modern Integrations of Solar System Dynamics*, *Annual Reviews of Earth and Planetary Sciences* **30**, 1

Morbidelli, A., Chambers, J., Lunine, J., Petit, J., Robert, F., Valsecchi, G., and Cyr, K.: 2000, *Source regions and timescales for the delivery of water on Earth*, *Meteoritics & Planetary Science* **35**, 1309

Morbidelli, A. and Moons, M.: 1993a, *Numerical Evidence on the Chaotic Nature of the 3/1 Mean Motion Commensurability*, *Icarus* **115**, 60

Morbidelli, A. and Moons, M.: 1993b, *Secular Resonances in Mean Motion Commensurabilities: the 2/1 and 3/2 Cases*, *Icarus* **102**, 316

Murray, C. and Dermott, S.: 1999, *Solar System Dynamics*, Cambridge University Press

Murray, N., Hansen, B., Holman, M., and Tremaine, S.: 1998, *Migrating Planets*, *Science* **279**, 69

Naef, D., Latham, D. W., Mayor, M., Mazeh, T., Beuzit, J. L., Drukier, G. A., Perrier-Bellet, C., Queloz, D., Siva, J. P., Torres, G., Udry, S., and Zucker, S.: 2001, *HD 80606b, A Planet on an Extremely Elongated Orbit*, *A&A* **375**, L27

Nelson, R. and Papaloizou, J.: 2004, *The interaction of giant planets with a disc with MHD turbulence - IV. Migration rates of embedded protoplanets*, *MNRAS* **350**, 849

Noble, M., Musielack, Z., and Cuntz, M.: 2002a, *Orbital Stability of Terrestial Planets inside the Habitable Zones of Extrasolar Planetary Systems*, *ApJ* **572**, 1024

Noble, M., Musielak, Z., and Cuntz, M.: 2002b, *Orbital Stability of Terrestial Planets Inside the Habitable Zones of Extrasolar Planetary Systems*, *ApJ* **572**, 1024

Nordström, B., Mayor, M., Andersen, J., Holmberg, J., Pont, F., Jø rgensen, B., Olsen, E., Udry, S., and Mowlavi, N.: 2004, *The Geneva-Copenhagen survey of the Solar neighbourhood - Ages, metallicities and kinematic properties of* ≈ 14000 *F and G dwarfs*, *Astronomy & Astrophysics* **418**, 989

Ott, E.: 1993, *Dynamical Systems*, Cambridge University Press

Owen, T. and Bar-Nun, A.: 1995, *Comets, Impacts and Atmospheres*, *Icarus* **116**, 215

Peale, S.: 1976, *Orbital Resonances in the Solar System*, *Ann. Rev. of Astro. and Astr.* **14**, 215

Perryman, M.: 2000, *Review Article: Extra-solar Planets*, *Rep.Prog.Phys.* **63**, 1209

Peterson, I.: 1993, *Newton's Clock - Chaos in the Solar System*, W.H. Freeman and Company, New York

Pollack, J., Hubickyj, O., Bodenheimer, P., Lissauer, J., Podolak, M., and Greenzweig, Y.: 1996, *Formation of the Giant Planets by Concurrent Accretion of Solids and Gas*, *Icarus* **124**, 62

Press, W., Teukolsky, S. A., Vetterling, W., and Flannery, B.: 1996, *"Numerical Recipes in Fortran 77 - The Art of Scientific Computing"*, Cambridge University Press

Preto, M. and Tremaine, S.: 1999, *A Class of Symplectic Integrators with Adaptive Timestep for Separable Hamiltonian Systems*, *Astronomical Journal* **118**, 2531

Prussing, J. and Conway, B.: 1993, *Orbital Mechanics*, Oxford University Press

Rampino, M. and Caldeira, K.: 1994, *THE GOLDILOCKS PROBLEM: Climatic Evolution and Long-Term Habitability of Terrestial Planets*, *Annu. Rev. Astro. Astrophys.* **32**, 83

Raymond, S., Quinn, T., and Lunine, J.: 2004, *Making other earths: dynamical simulations of terrestial planet formation and water delivery*, *Icarus* **168**, 1

Rivera, E.J.and Lissauer, J.: 2000, *Stability Analysis of the Planetary System orbiting υ Andromedae*, *The Astrophysical Journal* **530**, 454

Roy, A.: 3rd edition, 1988, *Orbital Motion*, Adam Hilger, Bristol and Philadelphia

Sanz-Serna, J. and Calvo, M.: 1994, *Numerical Hamiltonian Problems*, Chapman & Hall

Sleep, P.: 2001, *Orbital Migration of Giant PLanets: Using Numerical Integration to Investigate Consequences for other Bodies*, *earth, Moon and Planets* **87**, 103

Southworth, J. e.: 2005, *private communication*, *2005, August, Astronomical Observatory, Copenhagen*

Sussman, G. and Wisdom, J.: 1988, *Numerical Evidence That the Motion of Pluto Is Chaotic*, *Science* **241**, 433S

Sussman, G. and Wisdom, J.: 1992, *Chaotic Evolution of the Solar System*, *Science* **257**, 56

Szebehely, V. G., M. H.: 1998, *Adventures in Celestial Mechanics*, John Wiley & Sons

Szebehely, V.: 1984, *Review of Concepts of Stability*, *Celestial Mechanics* **34**, 49

Taff, L.: 1985, *Celestial Mechanics*, John Wiley & Sons

Thébault, P., Marzari, F., and Scholl, H.: 2002, *Terrestial planet formation in exoplanetary systems with a giant planet on an external orbit*, *A&A* **384**, 594

Veillet, C., Connors, M., Wiegert, P., Innanen, K., and Mikkola, S.: 2001, *Initial results of a survey of Earth's L4 point for possible Earth Trojan asteroids*, *Icarus, in press (preprint:http://www.astro.uwo.ca/ wiegert/preprints/pp9.html)*

Vogt, S., Butler, P., Marcy, G., Fischer, D., Pourbaix, D., Apps, K., and Laughlin, G.: 2001, *Ten Low Mass Companions from the Keck Precision Velocity Survey*, *The Astrophysical Journal* **568**, 352

Wetherill, G.: 1996, *The Formation and Habitability of Extra-Solar Planets*, *Icarus* **119**, 219

Whiteley, R. J. and Tholen, D. J.: 1998, *A CCD Search for Lagrangian Asteroids of the Earth-Sun System*, *Icarus* **136**, 154W

Whittaker, E.: 1999, *A Treatise on the Analytic Dynamics of Particles and Rigid Bodies*, Cambridge University Press

Wisdom, J.: 1982, *The origin of the Kirkwood gaps: A mapping for the asteroidal motion near the 3/1 commensurability*, *AJ* **87**, 577

Wisdom, J.: 1983, *Chaotic Behavior and the Origin of the 3/1 Kirkwood Gap*, *Icarus* **56**, 51

Zucker, S. and Mazeh, T.: 2001, *Derivation of the mass disribution of extrasolar planets with MAXLIMA, a maximum likelihood algorithm*, *ApJ* **562**, 1038